Hydrogen Storage
In
Graphitic Nanofibres

Simon Roger McCaldin MSci (Hons)

Thesis submitted to the University of Nottingham for the degree of
Doctor of Philosophy, September 2007

Abstract

There is huge need to develop an alternative to hydrocarbons fuel, which does not produce CO_2 or contribute to global warming – 'the hydrogen economy' is such an alternative, however the storage of hydrogen is the key technical barrier that must be overcome. The potential of graphitic nanofibres (GNFs) to be used as materials to allow the solid-state storage of hydrogen has thus been investigated. This has been conducted with a view to further developing the understanding of the mechanism(s) of hydrogen storage in GNFs and modifying the material structure to maximise the amount of hydrogen that can be reversibly stored in the material.

GNFs were synthesised using chemical vapour deposition (CVD) with careful control of temperature and gas mixture to create predominately herringbone GNFs from both Iron and Nickel catalysts. Within this, it was found that once GNF growth has been initiated under certain conditions, alteration of those conditions does not alter the fundamental structure of the GNF synthesised, but can increase the carbon yield, although re-orientation of the surfaces was observed.

The GNFs synthesised were subsequently chemically (acid washed and CO_2 oxidised) and thermally treated to remove the residual CVD catalyst and alter their surface structures in an attempt to allow dihydrogen molecules to penetrate and adsorb onto the internal graphene layers. However, it was found that after initial growth, the surface layers of the GNFs became re-orientated parallel to the fibre axis – representing a large energy barrier to adsorption onto the surfaces of the internal graphene layers. By careful use and control of conditions, this re-orientated layer can be removed to yield GNFs with cleaned surfaces. Once GNFs with cleaned edges had been synthesised, these were modified to remove oxygen species from their surfaces.

To further develop the understanding of the potential hydrogen uptake mechanisms, Pd particles were introduced to the GNF surfaces to act as catalyst gateways. By carefully controlling the variables of the incipient wetness process, a variety of morphologies and structures were synthesised. This allowed the precise determination of the hydrogen uptake mechanism occurring in samples by Kubas binding, Dissociation or Spill-over mechanisms.

All of the GNFs created have had their hydrogen uptake capacities precisely determined using a Sieverts apparatus designed and constructed by the author. None of the samples were found to adsorb any significant levels of hydrogen (>0.1 wt%), regardless of the treatments applied to them – this result has been discussed in light of the existing claims for high hydrogen uptake in GNFs made within the literature. The conclusion of this thesis is that no hydrogen uptake capacity could be observed in the GNFs synthesised during the project, however, the development of the uptake mechanisms and GNF structures has led to suggested modifications that may yield GNFs suitable for storing large quantities of hydrogen (i.e. in excess of US-DOE targets).

Acknowledgements

There are many people who helped and supported me throughout this project. I would like to take this opportunity to thank both my supervisors; Gavin Walker and David Grant for all their helpful discussion and guidance received during the project. Along with these are the post-doc researchers; Neil Bowering, for general discussion and help in the lab and Mohamed Bououdina for introducing me to carbon materials. This project would not have been possible if it had not been for the technical staff in the Wolfson Building, with special thanks going to; Keith Dinsdale for his assistance in TEM and Thermal Analysis, George Anderson for help with the construction my adsorption apparatus and Tom Buss for general sourcing of laboratory equipment.

General discussion within the Carbon/Hydrogen research group is also acknowledged as a helpful forum for the development of the ideas and experiments that have been undertaken during the project. Massive thanks must go to the members of office W204 in the Wolfson building, which have made the whole of the duration of this project more fun, entertaining and insightful that you probably realise!

I must thank my family for their support – most of all my wife; Abi, without how I would never have got this far.

I acknowledge the EPSRC and UK-SHEC for funding this project.

And finally – almighty God – who, without his ingenious imagination in-creation, none of this research would have been possible. All of the questions that have baffled and excited me would not have existed – I have thoroughly enjoyed this journey of discovery!

Content

Select Abbreviations

GNF (or CNF)	Graphitic Nanofibre (or Carbon Nanofibre)
CVD	Chemical Vapour Deposition
CNS	Carbon Nano-structure (filamentous nano-structured carbon of unknown structure)
(HR-)TEM	(High Resolution-) Transmission Electron Microscopy
XRD	(Powder) X-Ray Diffraction
MWNT	Multi-Walled Nanotube
SWNT	Single-Walled Nanotube
CNT	Carbon Nanotube
SA(E)D	Selected Area (Electron) Diffraction
DOE	(US) Department of Energy
TDS	Thermal Desorption Spectroscopy
TPD	Temperature Programmed Desorption
RT	Room Temperature (~298K)
TGA	Thermo-Gravimetric Analysis
MS	Mass Spectroscopy
EDX	Energy Dispersive X-Ray (analysis)
PDF	Powder Diffraction File
BET	Brunauer Emmett Teller
SA	(N_2 BET) Surface Area
-TR	Thermal Reduction (treatment applied)
-HT	Heat Treatment (treatment applied)
-AW	Acid Wash (treatment applied)
PDF	Powder Diffraction File (XRD)
CB	Carbon Black
Max	Maxsorb (activated carbon)
XPS	X-Ray Photoelectron Spectroscopy
sorption	adsorption or absorption (undefined)

1 Introduction

The increased cost, negative environmental impact and dwindling supplies of oil has thrust the search for alternative fuels to the forefront of scientific and technical endeavour.[1] One of the most promising alternatives to oil and hydrocarbon fuels is hydrogen, based around the reaction:

$$H_2 + \tfrac{1}{2}O_2 \rightarrow H_2O \qquad \Delta H = -285 \text{ KJ mol}^{-1}$$

This reaction is completely carbon neutral, only producing water as a reaction by product and is thus environmentally friendly. It is important to note that hydrogen is only acting as an 'energy vector' – a means of moving (chemical potential) energy between geographic locations - energy is still required to synthesise H_2. Currently, this is done by thermal cracking of hydrocarbons at temperatures ~900°C using CH_4 feedstock, but this process produces CO_2, uses up natural gas and is energy intensive. There are alternative methods of H_2 production, such as electrolysis of H_2O, and if the electrical energy required to drive this process is supplied from renewable sources, the process remains carbon neutral and truly environmentally friendly.[2]

The main driving force behind this need for a new energy vector is in the transport sector, specifically automotive applications. Currently the only viable energy source (high enough energy density and low cost) are hydrocarbon products (e.g. petrol, diesel or ethanol) used with an internal combustion engine. This process is only up to 35% efficient - with most of the energy is lost as heat. In contrast, while hydrogen can also be used with an internal combustion engine, it can also be used in a fuel cell which can directly translate up to 70% of the stored energy in electricity. There are other advantages to this method, such as; it is a silent process, no moving parts (reduced maintenance) and no other air pollutants (e.g. NO_x gases).[3]

However, there are several major technical issues associated with using hydrogen as an energy vector, most of which are principally related to the storage (i.e. local supply) of hydrogen. There are two principle issues with using hydrogen; it is a reactive (flammable) gas at room temperature and, most importantly, the volumetric energy density of hydrogen at atmospheric pressure is too low to allow a useful amount of energy to be stored. Thus, there are currently three potential methods being investigated to overcome these storage issues:

- Storage as high pressure gas (>20MPa),
- As a cryogenic liquid (<20 K), or
- Sorption into another material (solid-state)

These different methods are shown comparatively in figure 1.1 – which highlights the relative size of the required storage tank to allow a car to travel the equivalent distance using its existing petrol tank.

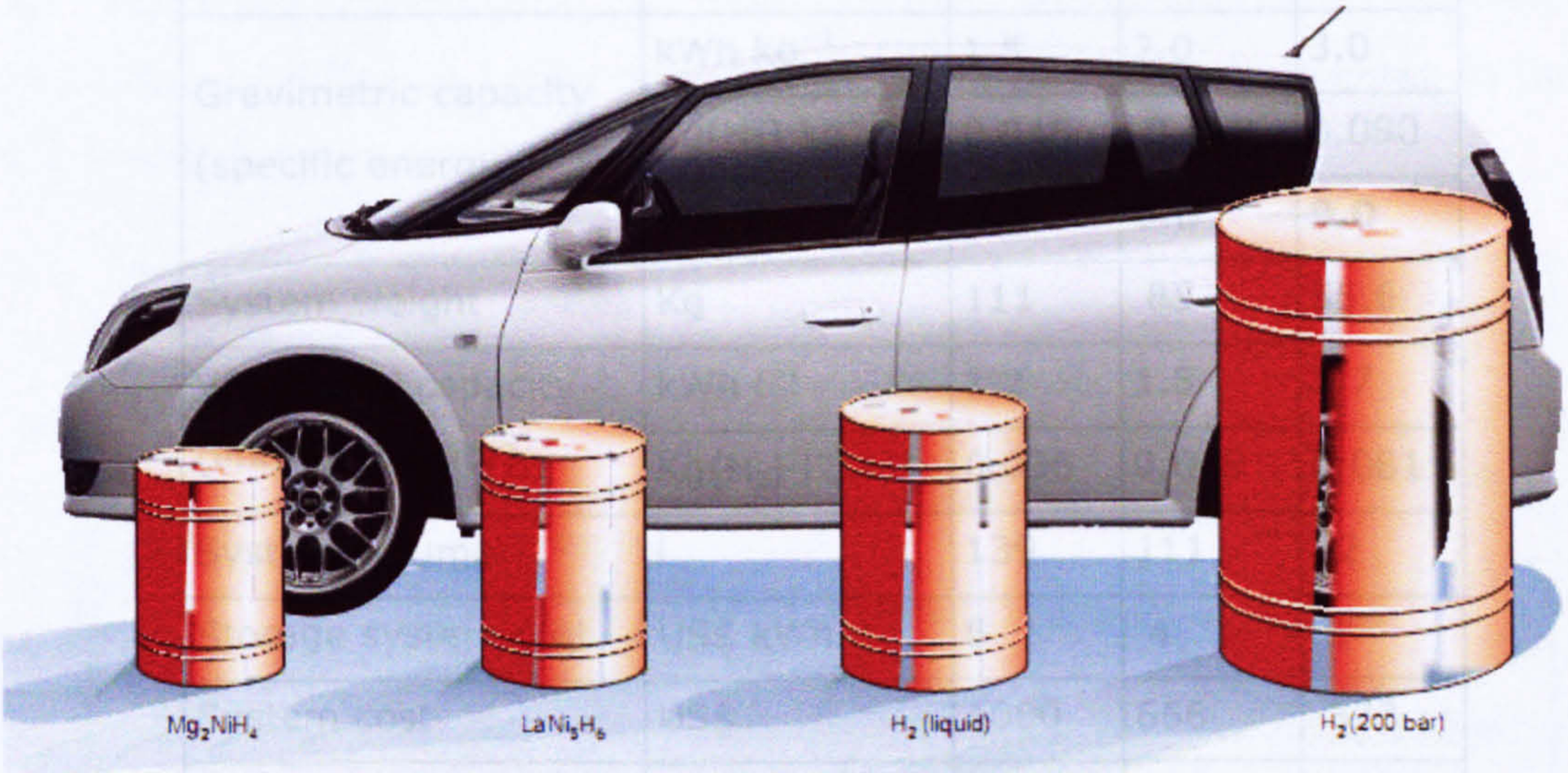

figure 1.1 – The required hydrogen storage tank size for the three types of storage method; (left and left-middle) solid-state storage, (right-middle) liquid, including the energy required for the cooling system and (right) as a pressurised gas (20 MPa).[4]

In order to achieve high enough energy densities, gaseous hydrogen needs to be pressurised to very high pressures (>35 MPa). While this is

technically achievable, it is not cost-effective when considering safety (if tank/container ruptures) or the energy cost associated with compressing the gas.[5] Similarly, while cryogenic hydrogen is technically feasible, around 40% of the energy stored is required to run the cooling system and makes this solution impractical.[6] That leaves solid-state materials solutions to overcome the challenge of hydrogen storage, with the specific challenges of these systems considered below.

1.1 Targets for solid-state hydrogen storage materials

Within the field of solid-state hydrogen storage, the US Department of Energy (US DOE) has released targets that material systems should meet – to enable the wide-spread adoption of hydrogen energy ("the hydrogen economy"). These targets are summarised in table 1.1.

System Parameter	Units	Year		
		2005	2010	2015
Gravimetric capacity (specific energy)	kWh kg^{-1}	1.5	2.0	3.0
	Kg(H_2) kg^{-1}	0.045	0.060	0.090
	Wt %	**4.5**	**6.0**	**9.0**
System weight	Kg	111	83	55.6
Volumetric capacity (energy density)	kWh l^{-1}	1.2	1.5	2.7
	Kg(H_2) l^{-1}	0.036	0.045	0.081
System volume	l	139	111	62
Storage system cost	US$ kWh^{-1}	6	4	2
System cost	US$	1000	666	333
Refuelling rate	kg(H_2) min^{-1}	0.5	1.5	2.0
Refuelling time	min	10	3.3	2.5

table 1.1 – Summary of DOE target for hydrogen storage system.[7]

The most important and widely reported parameter for solid-state storage materials (and/or systems) is the gravimetric capacity (expressed as a wt% - highlighted in bold in table 1.1) and to a lesser extent volumetric capacity. It is important to bear in mind that these US DOE targets are for a

hydrogen storage system, thus realistically most materials will have to exceed the gravimetric and volumetric capacities to compensate for the energy cost in loading and recovering hydrogen from the material. There are also several other considerations that need to be considered for a system such as;

- Stability (e.g. reactivity with air, moisture, temperature, etc)
- Cyclability
- Availability (e.g. of rare elements or compounds)
- Cost (of raw materials and processing)
- Toxicity
- Disposal

While the above is not an exhaustive list, it illustrates how there are many considerations to a hydrogen storage material system, and explains why there are currently no systems which fulfil all of these requirements. This has led to many different storage systems being considered and investigated (detailed further in section 2.6).

An indicative comparison of the current volumetric and gravimetric capacities of different types of hydrogen storage materials is given in figure 1.2 – with further detail given in 2.5 and 2.6.

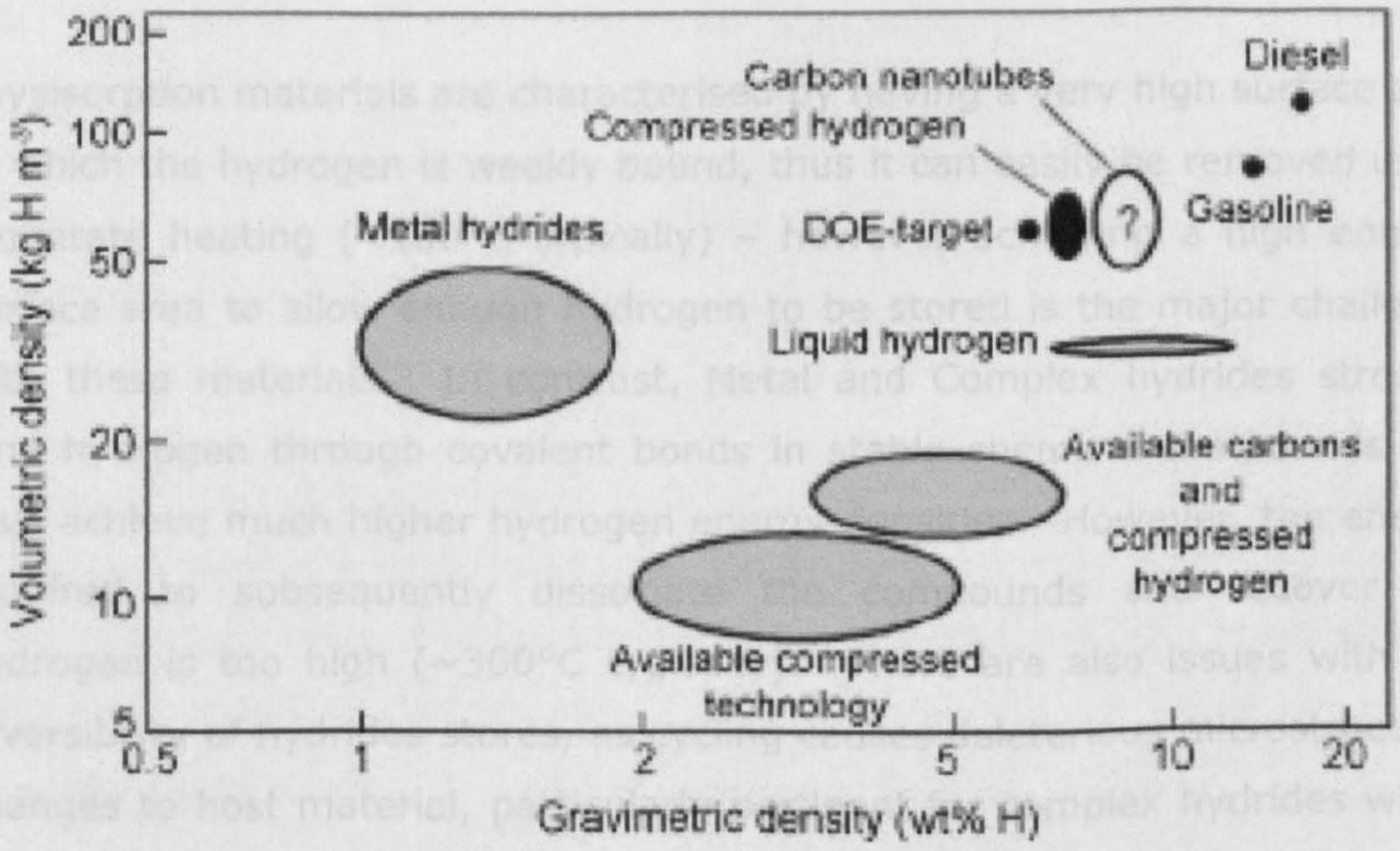

figure 1.2 – Chart illustrating (where) different hydrogen storage capacities of the various types of solid-state hydrogen storage materials.[8]

The different types of hydrogen storage materials are described further in section 1.2. However, there are two critical points shown in figure 1.2; current hydrogen storage material systems currently fail to meet the DOE targets (in respect of gravimetric and volumetric targets), and it shows why gasoline/diesel are such attractive fuels in terms of high energy densities (i.e. both exceed the DOE targets).

1.2 Solid-State Hydrogen Storage Materials

The basic concept of solid-state hydrogen storage is to use a host material to absorb hydrogen by exposure to hydrogen gas, once absorbed the hydrogen can then be transported and released as required by heating the material. The two principal advantages of using this method are; higher volumetric energy densities of hydrogen can be achieved and hydrogen can be stored more safely (compared to compression). There are three different types (classifications) of hydrogen storage materials capable of storing hydrogen in the solid-state:

- Physisorption materials (e.g. Carbons, Zeolites, MOFs)
- Metal hydrides (e.g. MgH_2, $LaNi_5H_6$, $TiMn_2H_{5.5}$)
- Complex hydrides (e.g. Boro-hydrides, Alanates)

Physisorption materials are characterised by having a very high surface area, to which the hydrogen is weakly bound, thus it can easily be removed using moderate heating (<100°C typically) – however achieving a high enough surface area to allow enough hydrogen to be stored is the major challenge with these materials. In contrast, Metal and Complex hydrides strongly bind hydrogen through covalent bonds in stable chemical compounds and thus achieve much higher hydrogen energy densities. However, the energy required to subsequently dissociate the compounds and recover the hydrogen is too high (~300°C typically). There are also issues with the reversibility of hydrides stores, as cycling causes deleterious microstructural changes to host material, particularly pertinent for complex hydrides which undergo a series of different reactions to release the hydrogen. The current understanding of issues surrounding these different material structures and

nature of the bonding of hydrogen is considered in further detail in section 2.7.

1.3 Hydrogen Storage in Graphitic Nanofibres

In 1998, Rodreguiz *et al* reported hydrogen uptake value of 67 wt% for a graphitic nanofibre (GNF) sample, which sparked much interest in this type of physisorption material, as it massively exceeded the US DOE targets.[9] This result has been subsequently been dismissed and accounted for by the original authors as moisture adsorption mistakenly assumed to be hydrogen adsorption.[10] However, subsequent investigation of these materials by several other researchers has resulted in a range of uptakes (anywhere between 0 to 15 wt% - details in section 2.6) being reported.

Most of these results have not been independently reproducible, mainly due to the difficulties in accurately measuring hydrogen uptake capacities and the reluctance of research groups to share samples due to the potential commercial value in these materials. Furthermore, most of the journal papers containing these results have limited detail in the preparation and characterisation of the materials being prepared and examined. Thus, the potential for GNFs to uptake significant levels of hydrogen (i.e. exceed the DOE targets) is still very much an unknown and worthy of further exploration and investigation to precisely determine how much hydrogen can be stored in these materials (and by what mechanism).

1.4 Aims and Objectives

Aim

The overall aim of this thesis shall be the investigation of hydrogen storage in GNFs. There is a clear need and opportunity to clarify whether GNF can store large quantities of hydrogen and if so, to determine (and optimise) the mechanism by which this occurs.

Specific Objectives

Within the general aim of this thesis, several more specific objectives have been identified and shall be investigated;

1. To develop a reproducible method to synthesise high purity GNFs from different catalysts using the CVD method.

2. To further examine the relationship between catalyst morphology and reaction conditions during the CVD growth of GNFs.

3. To develop a method for the successful removal of residual growth catalyst from 'as-grown' GNFs.

4. To post-treat GNFs to alter properties (both surface and bulk) of the GNFs and assess any effect on the hydrogen uptake properties of GNFs.

5. To determine whether the surface state of GNFs has any influence on their hydrogen uptake properties of GNFs.

6. To develop a synthesis method to decorate GNF with metal particles and assess any effect on the hydrogen uptake properties of GNFs.

7. To determine by what mechanism (if applicable) the treatments alter the hydrogen uptake of GNFs.

1.5 Structure and Scope of the Thesis

This thesis is separated into discrete chapters, starting with the current chapter (Introduction) which outlines the background to the work presented and gives the aims and scope of the project. This is followed by a critical literature review of GNFs and hydrogen storage, which illustrates how the aims and objectives of this thesis add to the existing body of knowledge and understanding.

Given that the nature of the specific objectives of the present work, rather than reporting the work in the traditional style (e.g. methods, results, discussion and conclusion covering all the work undertaken), each group of

objectives shall be considered within discrete chapters, with each chapter covering several related objectives;

- Chapter 4 - GNF Synthesis; Objectives 1-2
- Chapter 5 - Post-Treatment of GNFs; Objectives 3-4
- Chapter 6 - Preparation of metal containing GNFs; Objectives 4,6
- Chapter 7 - Hydrogen Storage properties of GNFs; Objectives 5-7

Each chapter consists of a self-contained body of work presented in sections; introduction and aim (of chapter), experimental method(s), results, discussion and conclusion. There will also be a summary section at the end of each chapter to show how the results and conclusions of the chapter contribute to the entire thesis. This is particularly important as the samples prepared in Chapter 4 are used as the starting material for Chapter 5, which are subsequently using in Chapters 6. Thus, Chapters 4-6 will detail the synthesis of the various GNF samples; all of which will have their hydrogen storage properties determined in Chapter 7. As each of the sets of samples synthesised in chapters 4-6 systematically investigate and modify specific properties of the GNFs, collectively testing and comparing these samples (in Chapter 7) will allow the achievement of the overall aim of this thesis - understanding the nature of hydrogen sorption in GNFs.

As several common characterisation methods are used during this thesis in chapters 4-7, an explanation of characterisation methods and experimental methodology used is given in Chapter 3 (Materials Characterisation). Any chapter specific techniques used will be addressed within the methods section for that chapter.

An overall assessment of the thesis aims, summary of the key conclusions and suggestions for future work is presented in Chapter 8.

Scope of the Thesis

This thesis is focused on the synthesis, chemical treatment and metal doping of GNF material, with the aim of being able to systematically investigate the effects of these treatments on the hydrogen sorption

properties of the GNFs. Special attention is paid to the characterisation of samples produced with respect to the surface state of individual GNFs, as well as the bulk properties of samples. As such it is important to consider that there is potential for sampling errors arising from examination of individual nanofibres. The risk of these errors has been minimised by repeating synthesises and microscopic examination of several samples (as indicated in the relevant experimental method descriptions).

In relation to the current literature on GNF and hydrogen storage, parallels and comparisons have been drawn in several instances. However, there is often a lack of detail in much of the work presented in the open literature. As such, the comparisons drawn should be assessed with reference to the original work as some comparisons have been made using inferred conclusions (usually combined from the methods and results presented, along with any relevant comments made during discussion in the work being considered).

2 LITERATURE REVIEW

Introduction

This chapter critically reviews the relevant material available in the open literature related to the aims and objectives of this research. It is split into two sections; carbon materials (2.1-2.4) and hydrogen storage (2.5-2.7) and is followed by a summary of the challenges and opportunities (2.8) that exist within the current body of understanding.

In the carbon section, a brief introduction to carbon materials will be presented, moving onto to discuss in more detail the growth, physical and chemical properties of GNFs and related materials. A brief description of the potential applications of nano-structured carbons shall also be presented.

In the section considering hydrogen storage, the methods of determining hydrogen capacity shall be reviewed, followed by a review of the important results presented in the literature. Then the sorption mechanism(s) of hydrogen shall be reviewed, with particular focus on GNFs and related carbon materials.

To summarise, the challenges and opportunities that exist within nano-structured carbons for use in hydrogen storage will be considered in relation to the aims of this thesis.

2.1 Carbon Materials

This section of the review will concentrate on carbon materials, with specific attention paid towards nano-structured and (nano-) filamentous forms of carbon. The various allotropes and structures of carbon materials are presented (section 2.1). The synthesis of GNFs will then be reviewed (section 2.2), with particular focus on the current understanding of the mechanism(s) of growth (section 2.3). Finally a brief summary of the applications of nano-structured carbon materials will be presented (section 2.4).

Carbon Structures

There are many different forms of carbons, below the major allotropes are defined and described, followed by a more detailed examination of filamentous and nano-structured carbons including a brief history of the landmark discoveries.

2.1.1 DIAMOND

Diamond is the least abundant, naturally occurring allotrope of carbon. It consists of tetragonal sp^3 bonded carbon, arranged in a three dimensional lattice, figure 2.1.

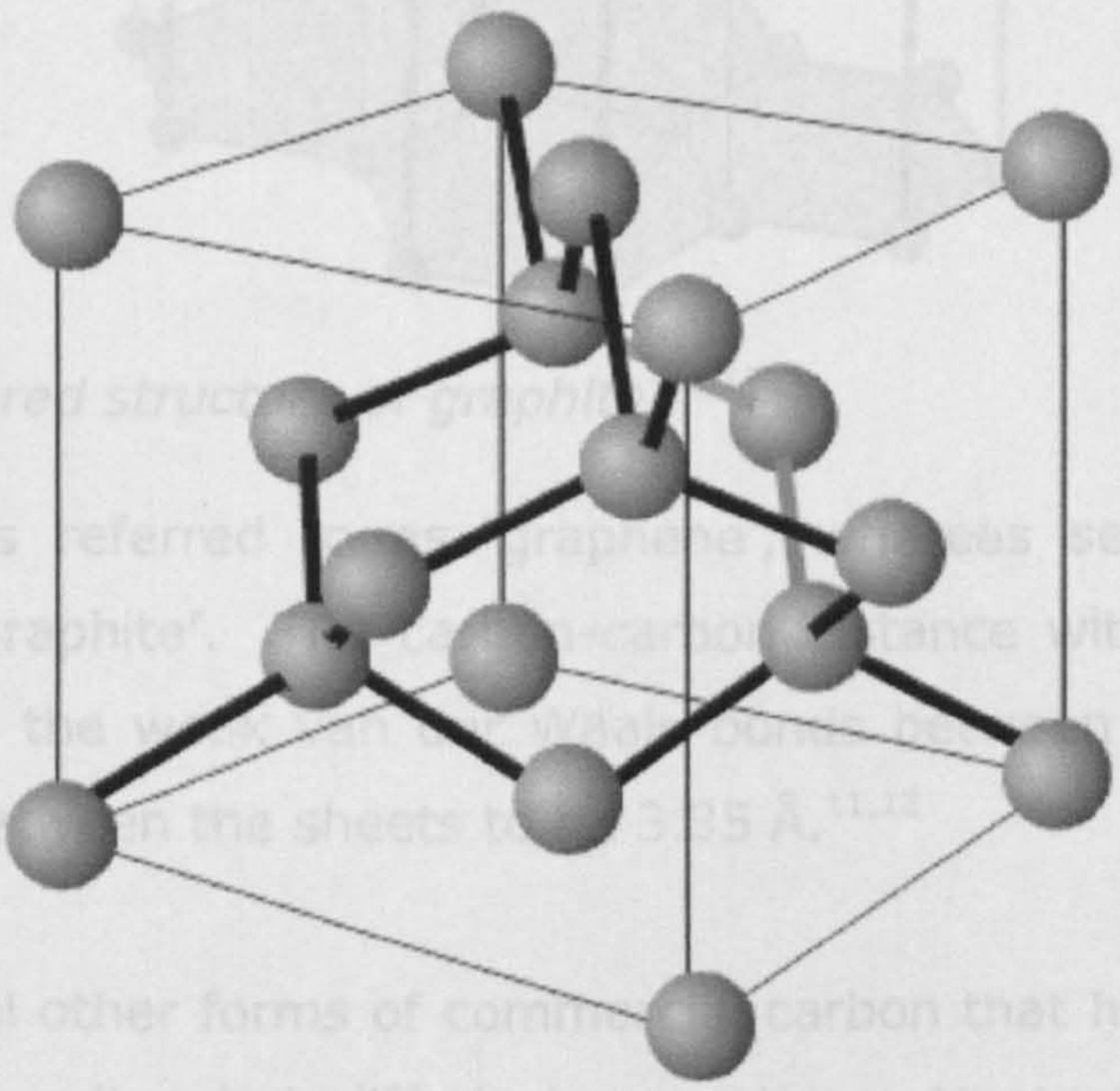

figure 2.1 – FCC Cubic diamond structure.[11,12]

In diamond the carbon-carbon covalent bonds are 1.54 Å. The FCC structure of diamond gives rise to exceptional physical properties, such as; it is the hardest known material (~90 GPa), has the highest melting point of any known solid (>3,500 °C) and has a high refractive index.[11,13,14]

2.1.2 GRAPHITE

This is the most common, naturally occurring allotrope of carbon. It is a layered material and consists of covalently bonded sp^2 hybridised carbon atoms. Each carbon atom is bonded to three other carbon atoms, with the

p_z orbital forming a Π-delocalised electron system. The atoms are arranged in a planer, hexagonal layered arrangement, figure 2.2.

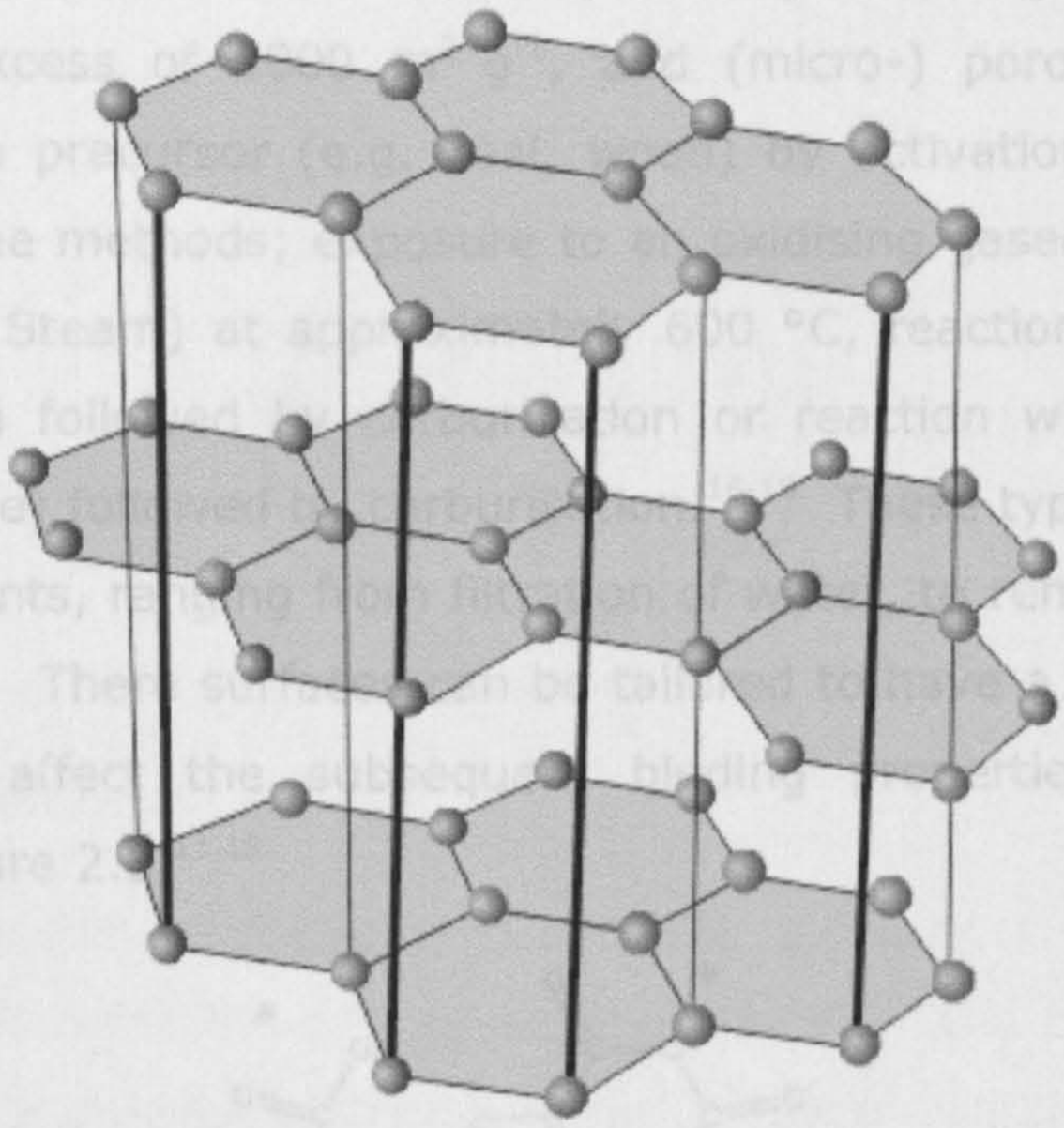

figure 2.2 – Layered structure of graphite.[11,12]

A single layer is referred to as 'graphene', whereas several layers are referred to as 'graphite'. The carbon-carbon distance within the layers is 1.42 Å, whereas the weak van der Waals bonds between the sheet cause the separation between the sheets to be 3.35 Å.[11,12]

There are several other forms of commercial carbon that have graphite-like structures and bonding but differing properties. Most of these forms of carbon are X-ray amorphous, or only exhibit partial crystallinity. A brief summary of these are given below.

Carbon Black

Carbon black (or more commonly soot) has been used commercially for around 100 years and is produced from the thermal oxidative decomposition of hydrocarbons. It contains small particles of graphitic material, typically with particles in the size range 50-500+ nm. Carbon black is cheap to produce and is thus commonly used in printer inks and as a rubber additives; allowing conduction (i.e. removal of static electricity) and as a UV light absorber (i.e. lowers rubber degradation).[11,12,15]

Activated Carbon

Activated carbons are characterised by having very high surface areas, commonly in excess of 1000 $m^2\ g^{-1}$, and (micro-) porosity. They are prepared from a precursor (e.g. coal, wood) by activation, which can be achieved by three methods; exposure to an oxidising gaseous environment (e.g. CO, O_2 or Steam) at approximately 600 °C, reaction with acid (e.g. phosphoric acid) followed by carburisation or reaction with a base (e.g. sodium hydroxide) followed by carburisation.[16-18] These types of carbon are used as adsorbents, ranging from filtration of water, to removal of gases in the atmosphere. There surfaces can be tailored to have a range of oxygen species, which affect the subsequent binding properties for particular applications, figure 2.3.[11,19]

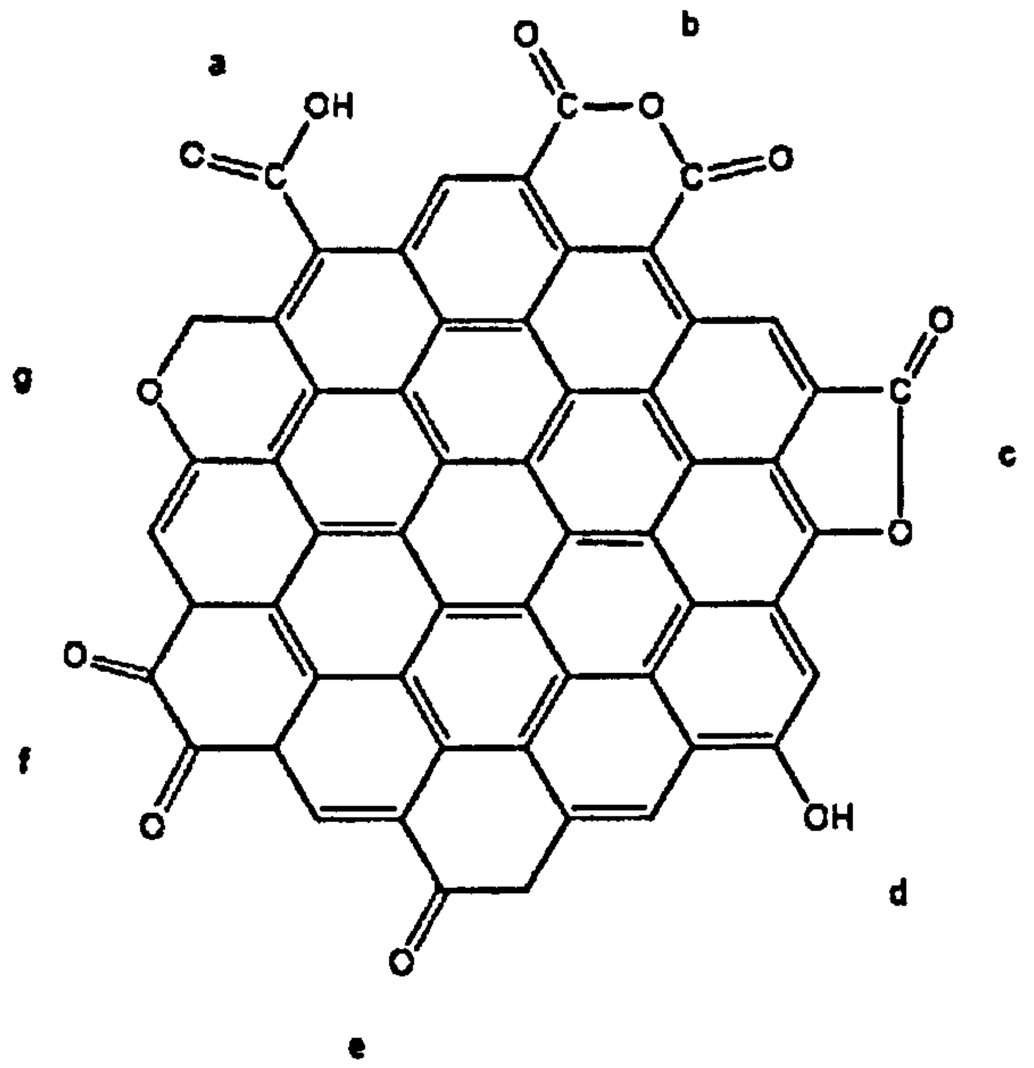

figure 2.3 – Different types of oxygen groups present on the surface of activated carbons/graphitic materials; a) carboxy, b) carboxylic anhydride, c) lactone, d) phenol, e) carbonyl, f) quinone, g) xanthene and ether groups.[11,19]

2.1.3 FULLERENES

C_{60} is the most recently discovered allotrope of carbon and was discovered in 1980s. They consist of sp^2 bonded graphite with a mixture of 5-coordinate and 6-coordinate carbon atoms. The presence of these 5-coordinated carbon rings causes the graphene layer to curve, to the extent

that when 60 carbon atoms are added to the structure, it forms a coherent sphere of atoms – hence C_{60}, figure 2.4.

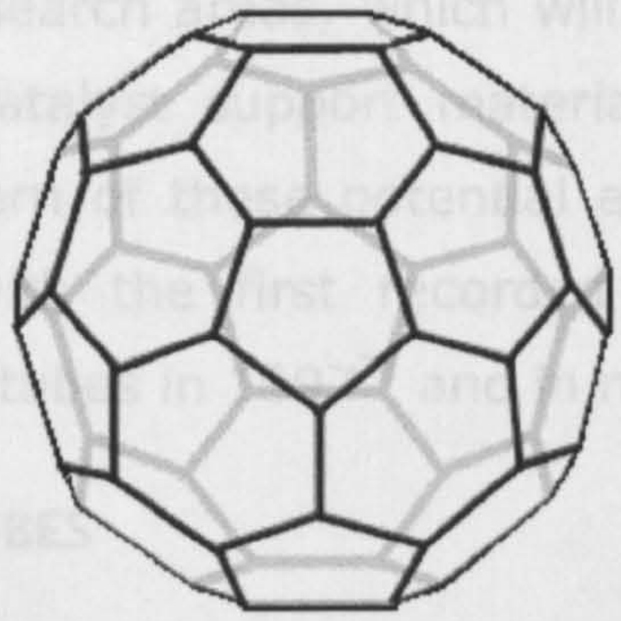

figure 2.4 – Structure of C_{60}.[11,12]

Similar 3-dimensional structures are possible based on C_{70}, C_{108}, C_{120}, etc. Whereas pure fullerenes have found several specific niché applications there is a lot of research interest in the properties of alloys containing C_{60}, such as A_3C_{60} (where A = metal) which exhibit low temperature superconductivity. More interest has been generated for filamentous nanotubes which are based on similar structures, detailed in sections 2.1.5.

2.1.4 History of Filamentous Carbon

Filamentous carbons have been known for over 100 years, with their first reported discovery in a patent in 1889. In the patent they were referred to as carbon filaments and were unintentionally grown on a metallic crucible in the presence of carbon containing gases. For the following 80 years interest in these materials was focused on removing them from industrial processes, as caused coking of catalysts in common synthesis reactions, such as Fischer-Tropsch synthesis.[20,21]

During the 1970-80s the filamentous carbons were more thoroughly investigated for potential applications as additives in polymers and as catalyst support materials. During this period, the first experiments attempting to purposefully grow and control the properties of the filaments were carried out, made possible by advances in electron microscopy techniques allowing more detailed characterisation to be performed.[20-22]

In 1991, Iijima showed that carbon nanotubes were formed during the production of C_{60} via an arc-discharge route.[23] This led to a flurry of new research into the areas of nanotubes and also nanofibres. This research has continued into several research areas, which will be detailed in section 2.4 and include; additives, catalyst support materials and (nano-) electronic devices. The most modern of these potential applications is in hydrogen storage (section 2.5), with the first recorded publication of significant adsorption in carbon nanotubes in 1997[24] and in nanofibres in 1998[9].

2.1.5 Carbon Nanotubes

Carbon nanotubes are based on graphene sheets rolled round to form a tube, often with an end-cap consisting of 'half' a C_{60} structure. There are two varieties; single-walled nanotubes (SWNT) and multi-walled nanotubes (MWNT), referred to generically as CNTs, figure 2.5.

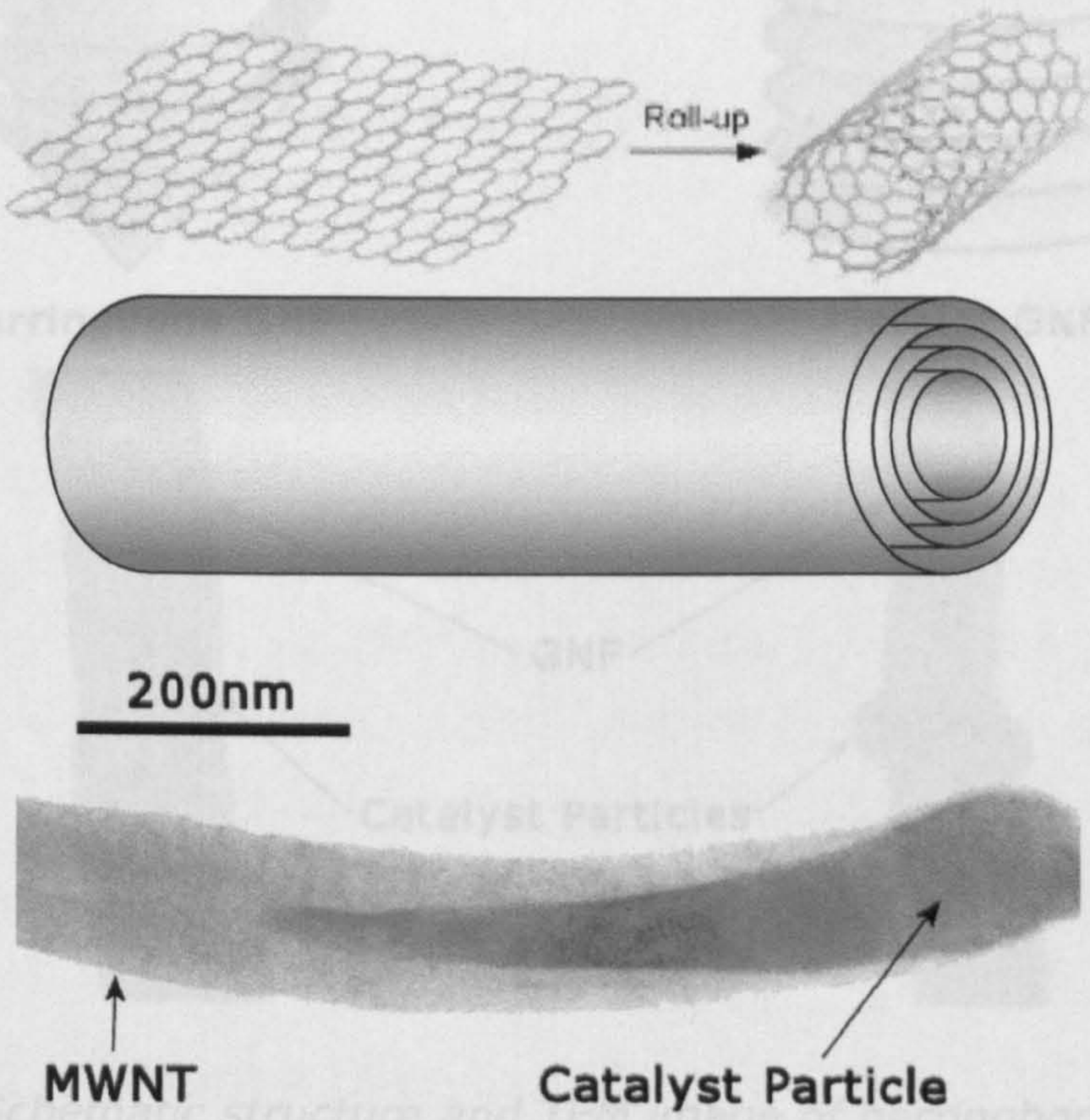

figure 2.5 – Schematic of (top) the construction of a graphene sheet into a SWNT, (middle) structure of a MWNT and (bottom) TEM image showing MWNT and catalyst particle.[25-27]

SWNT have diameters in the range 2-10nm. MWNTs have the same structure as a SWNT, except they consist of several SWNT stacked up inside each other, subsequently having a large range of diameters, from ~10nm

increasing up to (and in excess of) 100nm. The lengths of CNT materials can be from hundreds of nanometres to several millimetres.[27-33]

2.1.6 Graphitic Nanofibres

Graphitic nanofibres (GNFs) are a filamentous form of carbon based on a graphitic-type structure. There are two morphologies of graphitic nanofibres; platelet and herringbone, known generically as graphitic nanofibres (GNFs), figure 2.6.

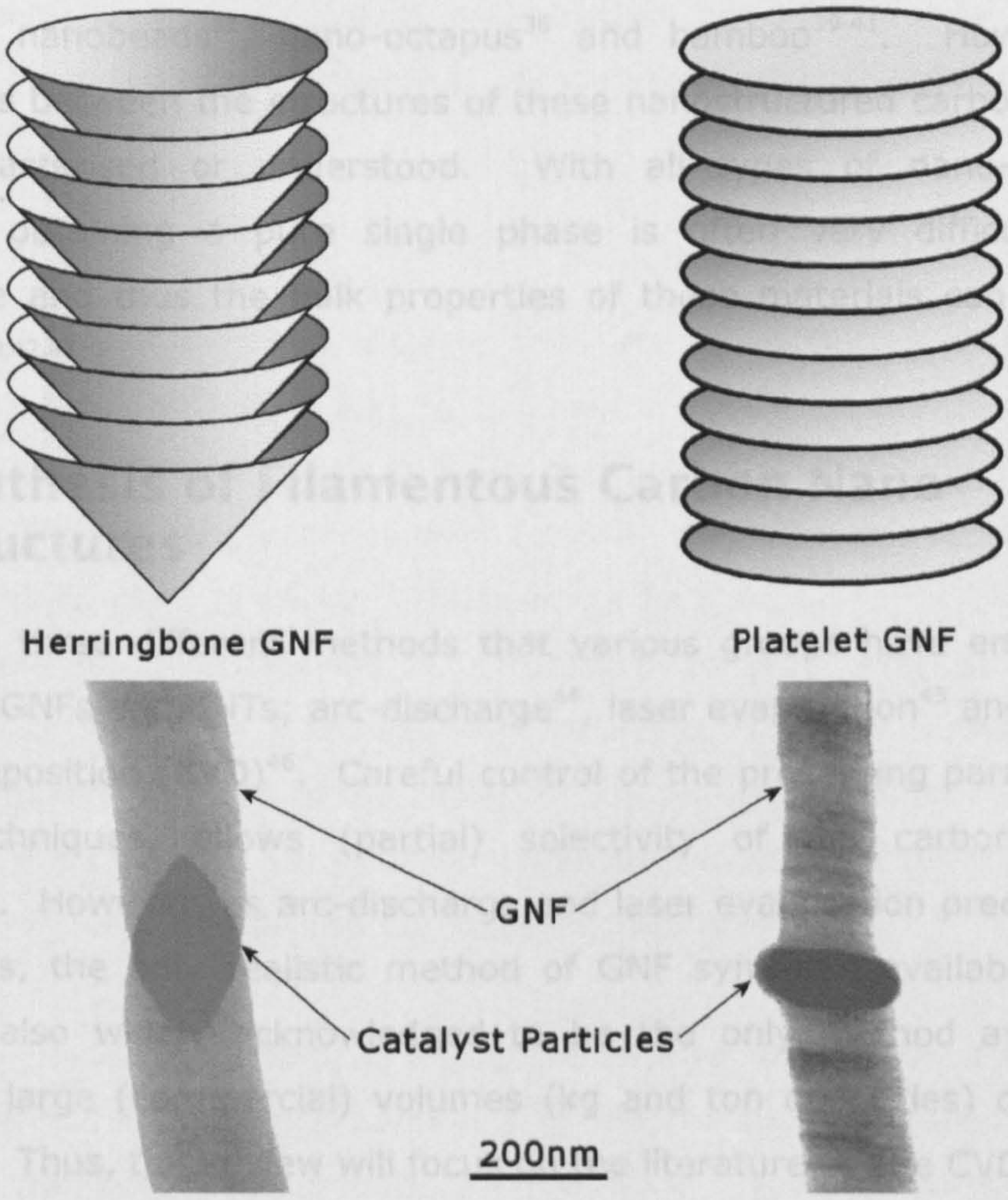

figure 2.6 – Schematic structure and TEM image of herringbone and platelet GNF.[26,27]

Platelet GNFs consist of layers of graphite stacked perpendicular to the fibre axis. Herringbone fibres are very similar to platelet fibres, except that of the graphene planes are aligned at an angle, usually between 30-60°, to the fibre axis.

The GNFs can range in diameter from 50-500nm and can have lengths in the order of 100μm+. The inter-layer spacing in both types of GNFs is often 'turbostratic', with distances of ~3.4 Å commonly being reported, slightly larger than 3.35 Å found in non-turbostratic graphite.[20-22,26,27,34]

Other Nano-structured Carbons

Within the literature there are many other types of nano-structured carbons. These include; peapods[35], CNT bags[36], buckytubes (mix of SWNT and MWNT)[37], nanobeads[31], nano-octapus[38] and bamboo[39-41]. However, the differences between the structures of these nanostructured carbons are not well characterised or understood. With all types of nano-structured graphite, obtaining a pure single phase is often very difficult, if not impossible and thus the bulk properties of these materials can be highly variable.[29,42,43]

2.2 Synthesis of Filamentous Carbon Nano-Structures

There are three different methods that various groups have employed to synthesis GNFs and CNTs; arc-discharge[44], laser evaporation[45] and chemical vapour deposition (CVD)[46]. Careful control of the processing parameters of these techniques, allows (partial) selectivity of the carbon material recovered. However, as arc-discharge and laser evaporation predominately yield CNTs, the only realistic method of GNF synthesis available is CVD, which is also widely acknowledged to be the only method available to synthesis large (commercial) volumes (kg and ton quantities) of GNFs or CNTs.[45-47] Thus, this review will focus on the literature on the CVD process.

2.2.1 Chemical Vapour Deposition

The general process of CVD is to heat a catalyst in a controlled environment and inject reactants, in the form of liquids, gases or mists, which then react with the assistance of a catalyst to form carbon nano-structures. For GNF and CNT synthesis, a carbon containing gas and a transition metal-based catalyst are required; it is also possible to inject the catalyst and reactants into the process simultaneously.[37,40,48,49]

There are many variables that can be altered during the CVD process to alter the properties of the material formed, principally these are; catalyst (material, supported, size, etc), temperature and reactants.[30-32,41,49] Examples of the effect of these principal variables will be discussed below, although several authors have noted that there have been few systematic investigations into the variables with respect to GNF or CNT synthesis. This coupled with the large amount of vague data on GNF and CNT synthesis (with respect to products, yields and reaction conditions) it is difficult to elude a clear or comprehensive explanation of the affect of each variable.[20,30]

2.2.2 Catalyst

The three most common catalysts that are used during CVD are the transition metals, Ni[50], Co[51] and Fe[52]. These metals are often mixed and/or alloyed with other metals such as Mg[53], Mo[33], V[33], Cu[54,55] and Sn[56]. Of these catalysts, Ni is generally considered to offer the highest catalytic activity (greatest mass yield of carbon) followed by Fe then Co.[30,32] While a large carbon yield is advantageous, a catalyst must also offer selectivity of product in order to be effective. For example, work by Rodriguez *et al* showed that over an iron based catalyst they produced almost pure platelet GNFs, using a mixed Fe-Cu catalyst produced a mixture of herringbone and platelet GNFs, using otherwise identical reaction conditions.[21,27]

The other important factors affecting the catalyst behaviour is the size of catalyst particles (detailed in section 2.3) and the support material (if used). The most common support materials are silica[27], zeolites[33] and alumina[48]. Table 2.1 shows the results from Fonseca *et al* and illustrates how the catalytic yield of carbon can be varied using different support material and different catalyst impregnation methods (on the same support).[37]

Support	Graphite	Y	ZSM-5	Silica	Silica	Silica	Silica
Method	impr.	impr.	impr.	impr.	ion-ads.	ion-ads. (pH=7)	ion-ads. (FeCl)
Carbon Yield (%)*	3.4	41.6	21.3	29.5	116.6	160.0	184.0

*30 minutes of synthesis at 700°C.

table 2.1 – Catalytic yield of an Fe-based catalyst on different support materials and impregnation methods.[37]

2.2.3 Reaction Environment

During CVD, the carbon containing (reactant) gas is adsorbed and decomposed on the surface of the catalyst and the carbon re-arranged to form the GNFs or CNTs. Thus the nature of the feedstock gas and temperature has a crucially important role, affecting the adsorption and decomposition behaviour of the system and thus determining the type of carbon synthesised. The most common gases used are short chain hydrocarbons, both saturated and unsaturated, as well as CO.[20,21,43] Ferrocene can also been used as a feedstock, an example of where the catalyst (Fe from the ferrocene) is injected into the reaction along with the carbon containing precursor.[57,58] From a broad examination of the literature, the use of ethylene (C_2H_4) seems to favour GNF formation[27,54,55], whereas other hydrocarbons favour CNT formation[31,39], although some counter examples also exist.[37,56] Although it is difficult to make direct comparisons between systems (due to differing temperatures, catalysts and other experimental variables), these examples (above) show that the specific reaction gas is partially responsible for the type of carbon synthesised. There are several reason(s) for this, which are considered below and in further detail in section 2.3.

As well as the reactant (carbon containing gas), CVD is often conducted with other gases present such as; He[52], N_2[56], Ar[59], H_2[27] NH_3[49] and CO[60]. While the inert species are simple carrier gases, H_2, NH_3 and CO are reducing agents (and a potential source of carbon in the case of CO) and can have a substantial impact on the product formed through their effect on the catalyst in the growth mechanism. Valiente *et al,* showed that due to

the presence of H_2 both prior to and during the reaction causes the iron oxide catalyst to reduce to iron, which allowed (caused) the growth of filamentous carbon.[52] Further to this, Park *et al*, introduced NH_3 prior to and during their reaction, which induced a change in the size of the Fe catalyst (in film form), figure 2.7; producing two catalysts with diameter ranges of 100-150nm and 200-400nm.

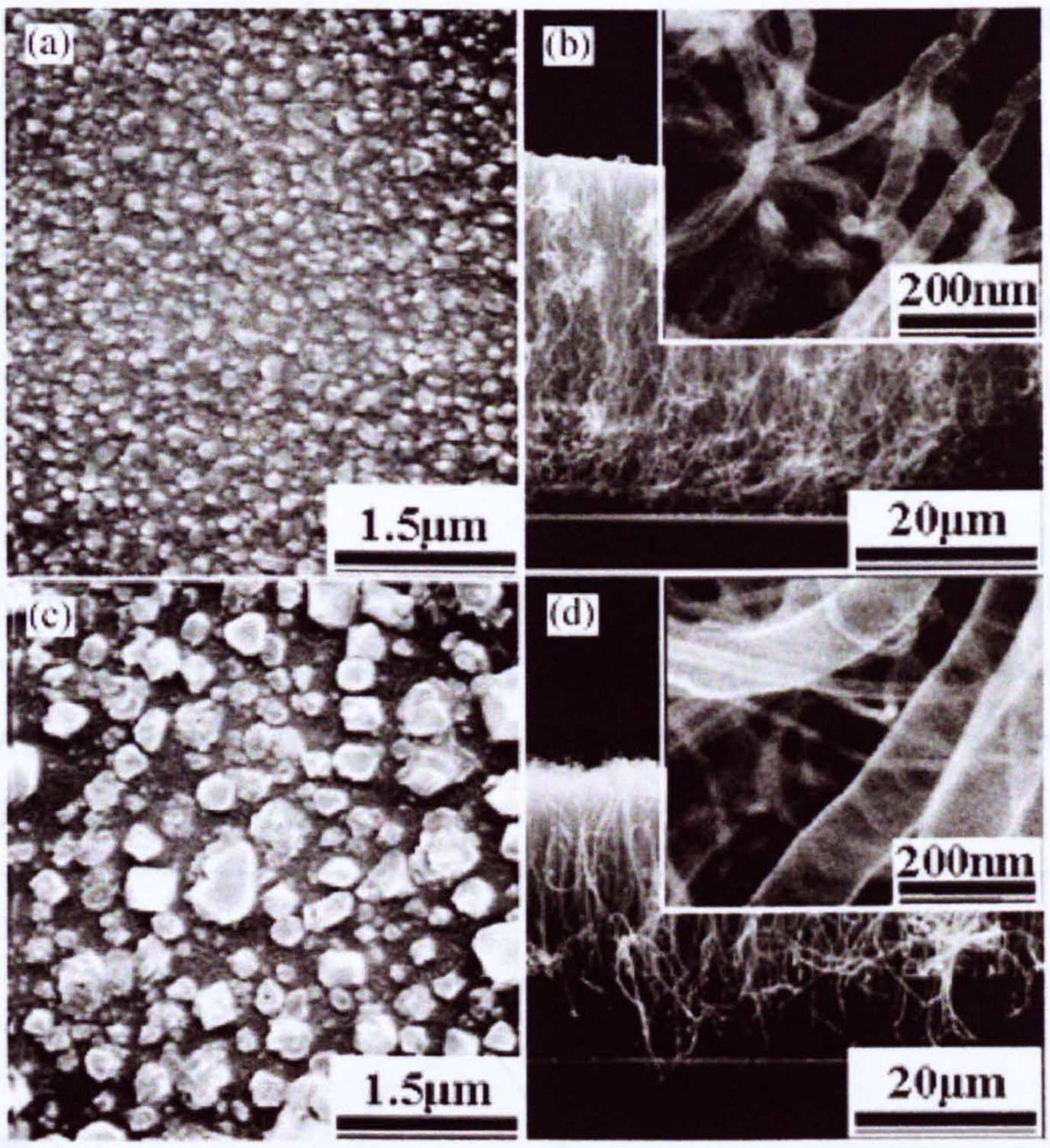

figure 2.7 – (a and b) 100-150nm catalyst which produced CNT of 40nm diameter, (c and d) 200-400nm catalyst produced CNT of 120nm diameter.[41]

Their investigation found that NH_3 was also required, along with carbon containing C_2H_2, to cause carbon growth in their system. The size of the catalyst particles showed good correlation with the diameter of the filamentous carbon formed; 100-150nm catalyst formed CNT with 40nm diameter and 200-400nm catalyst formed CNT with 120nm.[41]

Within the literature gas flow rates vary from as little as 10 ml min^{-1} to over 1,000 ml min^{-1}, however the effect of gas flow rates has not been reported extensively in the literature. However, the effect of gas flow rate has been

shown to be an important variable in other CVD synthesises, due to the effect on the adsorption of the reactant gas onto the catalyst, thus it is likely that a similar effect is occurring in the carbon CVD systems.[49]

To the authors knowledge, only Li *et al* have reported an investigation into the effect of different pressures on filamentous carbon growth.[49] In that work, carbon was synthesised using two pressures investigated (0.6 Torr and 760 Torr), this resulted in different types of carbon being synthesised from otherwise identical reaction conditions (flowing N_2, NH_3 and C_2H_2). At 0.6 Torr, 'high-quality CNTs' were formed, while at 760 Torr, 'bamboo' type filaments were observed. This would be expected, given that different gas partial pressures affect the nature of gas adsorption during synthesis, discussed further in section 2.3.

The reaction temperatures for CVD can vary between 400-1100°C and has a large bearing on both the yield and structure of carbon recovered. Figure 2.8 illustrates work by Li *et al*, investigating how temperature can affect yield on a Ni-based catalyst.[49]

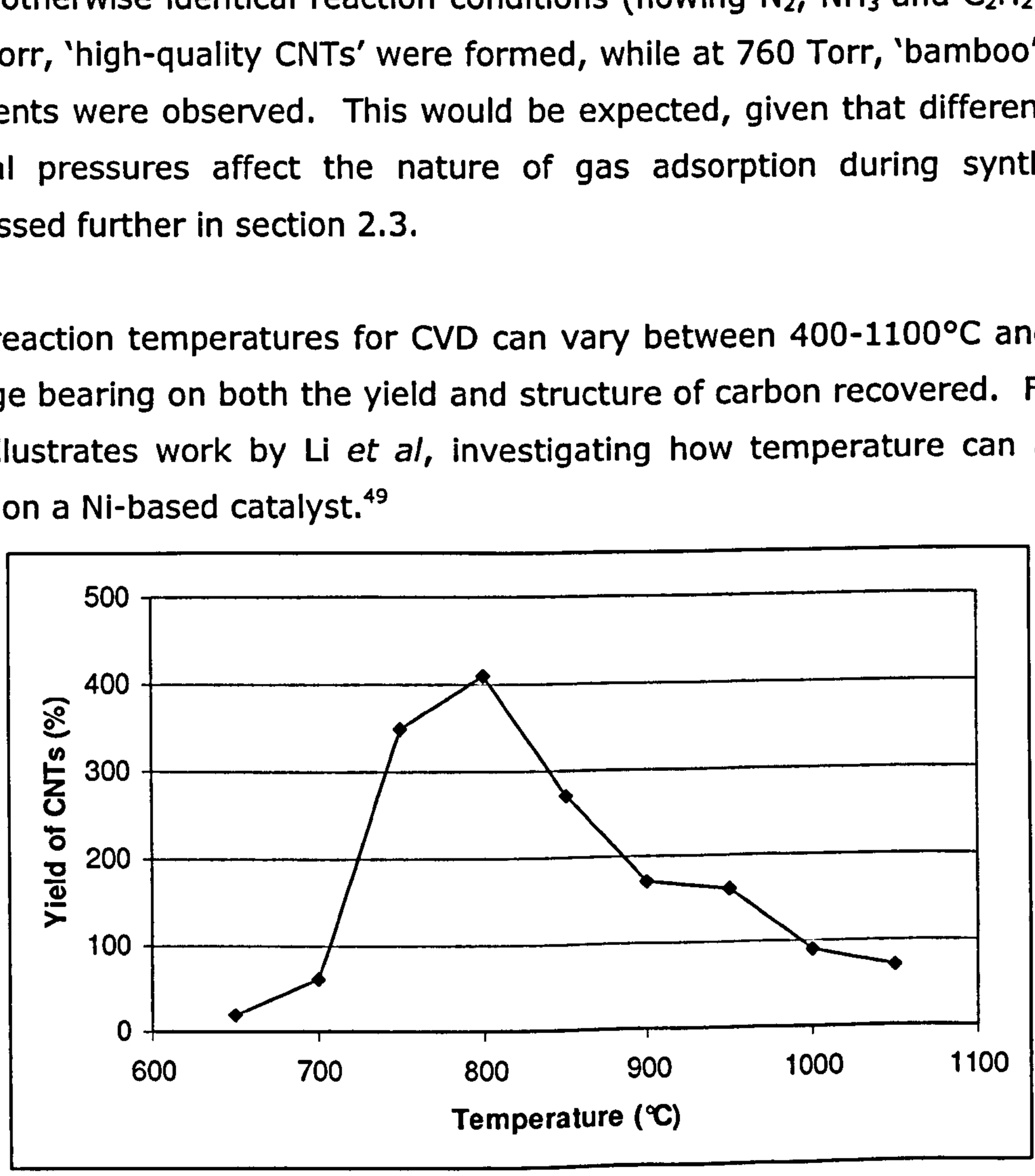

figure 2.8 – Graph of temperature vs. yield for a Ni based catalyst.[49]

As can be seen, the yield of carbon goes through a maximum at 800°C, below this temperature fine and straight CNTs were produced while above 800°C the CNTs become coarse and bent. The authors account for these effects (yield and structure change) by the affect that temperature has on

the rates of diffusion that occurs within the catalyst particles, a principle discussed further in section 2.3.[20,21,49] However, it is also possible that the effect of temperature on the decomposition rates of the hydrocarbon gas (and thus carbon supply) are the critical step in determining the yield and structure of the filament recovered.

2.3 Growth Mechanisms

The precise mechanism of the formation of CNT and GNF has been the subject of debate since these materials were first discovered, with many authors proposing various mechanisms of growth.[20,21,43] The general mechanism of growth is shown in figure 2.9.

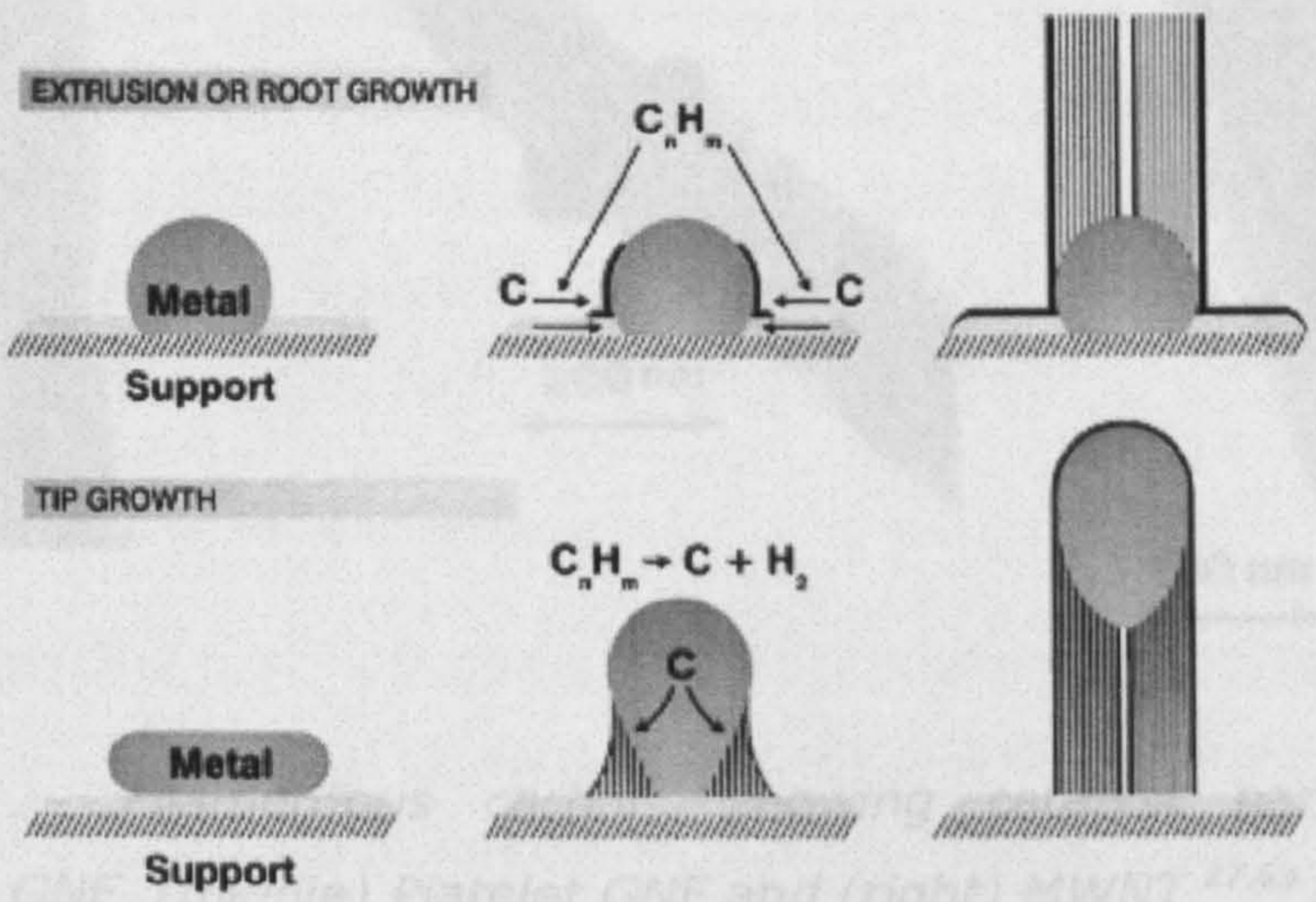

figure 2.9 – General growth mechanism of filamentous carbons.[32]

The growth process consists of several steps; first the hydrocarbon feedstock molecules are adsorbed onto a facet of the catalyst particle and subsequently breaks up to supply carbon. The carbon then diffuses, either through the catalyst particle or around the surface, and is finally deposited on another facet of the particle to yield a filament. Beyond this basic mechanistic explanation, there is a lot of debate as to the precise nature of the processes involved and how different nanostructures are produced (e.g. why GNF are grown instead of CNT). However, within the detailed explanations of growth, mechanisms tend to fall into one of two categories to explain the structure of the recovered product, either; the morphology of the catalyst particle or the reaction conditions, both are considered below.

2.3.1 CATALYST MORPHOLOGY

The influence of the catalyst morphology, specifically its shape and size, was first proposed by Baker *et al* during 1970s.[43,61,62] This was mainly based on close correlation of particle size (diameter) to the diameter of the subsequent filament (either CNT or GNF), observed in the electron microscope, figure 2.10.

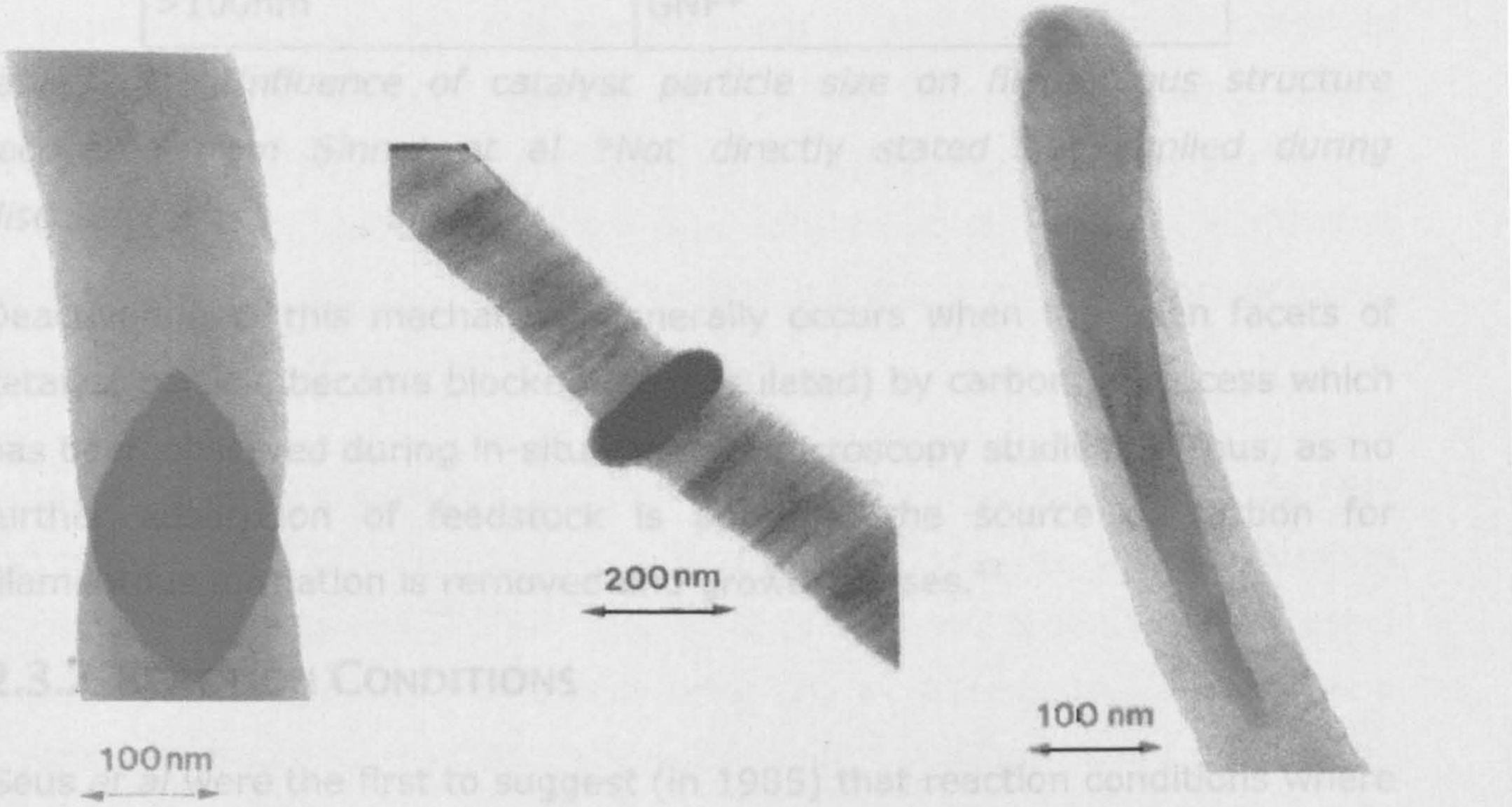

figure 2.10 – Filamentous carbon, showing catalyst particles; (left) Herringbone GNF, (middle) Platelet GNF and (right) MWNT.[27,63]

Furthermore, the shape of the catalyst particle gives rise to the structure observed in the filament; herringbone GNFs have diamond shaped catalyst particles, while platelet GNFs have flat or 'doughnut' shaped particles (figure 2.10).

Sinnot *et al,* have suggested that the size of the particle will actually determine the type of filament produced, as shown in table 2.2. As the curvature of the catalyst particle increases, due to a reduction in its size, the strain on the layers of graphite that form on its surface increases. GNFs have larger particles with (relatively) little curvature, thus graphene sheets are deposited parallel to each other. Eventually it becomes more energetically favourable for the graphite to form a continuous surface, away

from the catalyst particle, rather than sheets on the catalysts surface, thus a MWNT. Extending this further, SWNT will be formed from very small catalyst particles.[32]

Size of Catalyst Particle	Type of filamentous structure
< 20nm	SWNT
20-100nm	MWNT
>100nm	GNF*

*table 2.2 – Influence of catalyst particle size on filamentous structure recovered from Sinnot et al *Not directly stated but implied during discussion.*[32]

Deactivation of this mechanism generally occurs when the open facets of catalyst particle become blocked (encapsulated) by carbon, a process which has been observed during in-situ electron microscopy studies.[64] Thus, as no further adsorption of feedstock is possible, the source of carbon for filamentous formation is removed and growth ceases.[43]

2.3.2 Reaction Conditions

Geus *et al* were the first to suggest (in 1985) that reaction conditions where more important than initial catalyst composition and morphology.[65-69] They argued that the reaction conditions caused reconstruction of catalyst particles, which would in turn adopt the morphologies suitable for filamentous growth. This then explains why it was possible to obtain different filament types from the same catalyst particles by varying the reaction conditions (as shown by the work of Li *et al* in section 2.2.3).

Following on from this, there is much debate as to the precise nature of the active phase during the steady-state growth of filamentous carbon, particularly with Fe based catalysts (due to the ease with which carbides can form given typical CVD reaction conditions[21]). Some authors argue that during formation (using Fe-based catalyst), Fe_3C is the active phase[65-67] while others that $Fe_{2.2}C$ or Fe_2C is the active phase.[70,71] The main issue with determination of the active phase is that most characterisation is performed after the reaction has terminated (i.e. system returned to room

temperature) which makes it difficult to be sure that phases observed are the same as those present during the growth reaction conditions. However, Philip *et al* showed that catalytic activity was gradually lost as a stable carbide was formed during there reactions, determined by stopping the reactions periodically. They also found that activity could be resorted by reduction of the carbide in a hydrogen atmosphere.[43,72] This indicates that the active phase is unlikely to be a carbide, but that the carbides observed at room temperature are due to the effect of the carbon-loaded catalyst cooling after the reaction. Further more, given that many virgin catalysts are oxides (e.g. Fe_2O_3) which transform to carbides (e.g. Fe_3C) during the CVD reaction, indicates that there is a substantial change in the catalyst particles, which will be highly dependent on the prevailing environment, adding credence to the theory of Geus *et al*.

Nolan *et al* have suggested that the presence of hydrogen promotes GNF formation over CNT, due to the hydrogen stabilising the carbon dangling bonds at the surface of GNFs.[73] Delzeit *et al* observed a similar effect using a plasma enhanced CVD synthesis with CH_4 as a feedstock. By varying plasma parameters, the CH_4 feedstock could be decomposed in the gas phase, effectively introducing molecular hydrogen into the system; when this occurred GNFs were formed, otherwise MWNT were recovered.[73,74]

From the available literature and theories discussed in this section (2.3), it is still unclear as to whether the initial state of the catalyst (size, morphology and phase) or the reaction conditions (and their affect on the catalyst) are more important factors in filamentous carbon growth. Further systematic research into the variables discussed is required to gain a more complete understanding of the precise growth mechanisms involved.

2.4 Applications of Nano-Structured Carbon

Due to the relatively new nature of nano-structured carbons and issues with scaling up synthesis, only a few niche commercial applications have been found. However the is a lot of promising research areas being investigated, summarised in table 2.3.

Application	Material(s)	Reference(s)
Atomic Force Microscope Tips	CNT	75
Catalyst Supports	GNF, CNT	76-78
Field Emission Displays	CNT	79-81
Electrodes (in fuel cells and batteries)	GNF, CNT	82-84
Super Capacitors	GNF, CNT	85-87
Nano-electronics	GNF, CNT	88,89
Nano-composites materials	CNT	90
Adsorbents (e.g. hydrogen storage materials)	GNF, CNT	91-93

table 2.3 – Summary of research into potential applications of GNF and CNTs.

Of the potential applications for GNFs (not CNTs), the vast majority of research has been in the area of hydrogen storage; trigger by the claims of 67wt% hydrogen uptake by *Rodriguez et al.*[94] This claimed large uptake has not been subsequently reproduced by any laboratory and has been widely dis-credited, however interest in these materials has continued.

2.5 Hydrogen Storage

The remainder of this review will focus on hydrogen storage and hydrogen interactions with materials. It consists of a review of the current hydrogen uptakes reported in the literature (section 2.6), including a description of the experimental methods used to determine these values (section 2.6.1-2.6.3). This then develops to consider the interaction of materials with hydrogen and hydrogen uptake mechanism(s) in potential carbon-based hydrogen storage materials (section 2.7).

2.6 Current Hydrogen Uptakes

Many groups have published hydrogen uptake results for a range of materials. However, there is a massive problem of un-verified, and un-reproducibility of results between research groups. The main cause of this is largely acknowledged to be due to the experimental difficulties associated with determining the hydrogen uptake in materials. Thus, before considering the hydrogen uptake values reported in the literature, the three

common methods of hydrogen uptake capacity determination shall be described and considered; Volumetric (2.6.1), Gravimetric (2.6.2) and Thermal Desorption (2.6.3).

2.6.1 VOLUMETRIC

The volumetric method is based on exposing a known amount of hydrogen (i.e. pressure in a known volume) to a sample in a container of known volume, observing a pressure drop on exposure to the sample and assuming that the drop is due to adsorption. This method is experimentally straight forward and allows materials to be exposed to relatively high pressures of hydrogen (>10 bar). The method requires relatively large amounts of sample (order of 100's mg), thus allowing large enough amounts of hydrogen to be adsorbed causing large pressure drops, which can then be accurately detected by the pressure transducer(s). There are several problems with the technique, such as; gas leakage and gas purity, both of which can lead to large pressure drops that are mistakenly assumed to be adsorption. The effect of non-stable temperatures on pressure within small volumes can lead to large fluctuations in pressure readings, which in turn will cause error in measuring the 'known' hydrogen volume.[95-98]

2.6.2 GRAVIMETRIC

The gravimetric method uses an increase in sample weight, determined using a micro-balance, to measure the hydrogen capacity of a sample. Due to measuring very small weight variations the average sample required is relatively low, around 10 mg. There are two main errors associated with this method; adsorption of gas impurities can be mistaken for uptake and difficulties in taking account of buoyancy effects (and thus accurate weight changes) when working at elevated pressures.[25,99,100]

2.6.3 THERMAL DESORPTION SPECTROSCOPY

Thermal desorption spectroscopy (TDS) measures the amount of hydrogen desorbed from a sample (during heating) using quantitive mass spectrometry. A sample is loaded (externally or *in-situ*) with hydrogen, then heated to cause desorption. Due to the use of a mass spectrometer, very small amounts of sample are required (<10 mg) and any desorption

products other than hydrogen (e.g. H_2O, hydro-carbons, etc) can also be detected. However, this method can only measure the desorbable uptake of hydrogen from the sample (while under vacuum conditions), which only leads to partial information about the uptake potential.[22,101-103]

2.6.4 Current Hydrogen Uptakes

Table 2.4 gives a range of (gravimetric) hydrogen uptake capacities for nanostructured carbon materials. Similar data tables are available for hydride materials in several good review articles[104,105] and online database[106] but due to the scope of this thesis are not be included here.

While this list is not exhaustive, it does highlight the variety of data that has been presented on hydrogen uptake capacities in nanostructured carbons. The more significant results shall be considered in more detail in the following section, considering the hydrogen uptake mechanism(s) in hydrogen storage materials, focusing on carbon materials.

Sample	T (K)	P (MPa)	Uptake (wt%)	Reference
SWNT	298	0.067	3.5-4.5	8
SWNT (Rice)	298	3.6	0.05	107
MWNT	293	6.5	2	8
MWNT (Non-treated)	300	1.0	5-7	108
MWNT (Acid-treated)	300	1.0	13.8	
SWNT-$TiAl_{0.1}V_{0.04}$	298	0.067	1.5	8
SWNT-Ti-6Al-4V	298	0.08	1.7	109
SWNT-Fe	298	0.08	<0.005	
Doped CNT	-	-	0.5-1.0	8
Li-CNT	473-673	0.1	20	110
K-CNT	<313	0.1	14	
GNF (herringbone)	298	11.35	67.55	94
GNF (platelet)	298	11.35	53.68	
GNF	77-300	0.8-1.8	0.08	111

Sample	T (K)	P (MPa)	Uptake (wt%)	Reference
CNF	300	12	6.5	[112]
Ball Milled GNF	298	0.9	0.5	[113]
Vapour grown carbon fibers	298	3.6	<0.1	[114]
GNF (herringbone)	77-300	1.5	1-1.8	[107]
CNF	300	12	10	[54,55]
CNF	77	12	12.38	[115]

table 2.4 – Summary of selected hydrogen uptakes in filamentous carbons; SWNT, MWNT and GNFs. Samples are described as per the authors in the relevant paper(s).

2.7 Mechanisms for Hydrogen Uptake

Understanding the interaction of hydrogen with materials is vital in the search for hydrogen storage materials. While a good general understanding is present in the literature, novel nanostructured materials exhibit unexpected properties (i.e. higher hydrogen uptakes) that cannot be explained simply, based on current understanding. In this section a brief overview of adsorption theory and adsorption mechanism(s) in (nanostructured) carbons will be presented. Within this, the limitations of knowledge and opportunities for further research and how they relate to the aims of this project will be identified.

2.7.1 Adsorption

When a molecule (adsorbate) approaches a surface (adsorbent) there is a change in their columbic interaction, figure 2.11. There are typically (although not always) two interaction 'wells' where molecules feel a positive attraction towards the surface, such that the adsorbate is then bound to the surface.[116-118]

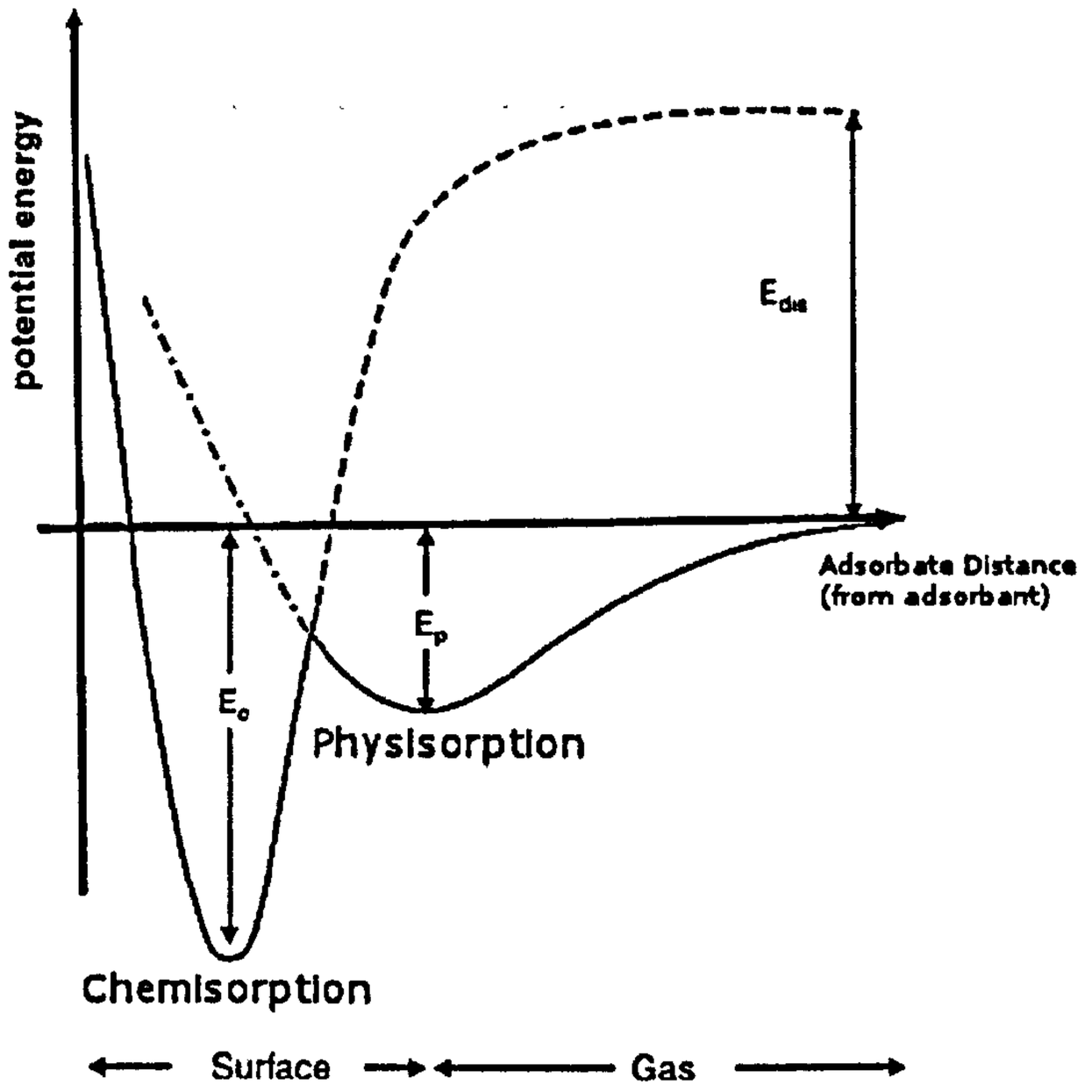

figure 2.11 – Typical potential energy diagram for an adsorbate molecule approaching an adsorbent surface.[116,117,119]

The strength of this interaction can be classified into two general types; physisorption and chemisorption, which are considered below with regards to hydrogen storage materials.

2.7.2 Physisorption and Chemisorption

There are different challenges with hydrogen storage materials; based on whether hydrogen is physisorbed or chemisorbed. The differences between physisorption and chemisorption adsorption mechanisms are summarised in table 2.5.

In chemisorbed materials (i.e. hydrides), due to the strong interaction of hydrogen with the adsorbate, to cause the hydrogen to be adsorbed or desorbed requires heating (to overcome the activation energy of adsorption or desorption) to temperatures above 300°C. This energy requirement lowers the efficiency of the hydrogen store; thus most research in hydrides is focused on introducing catalysts in-order to lower the activation energy for desorption, given that several hydrides have uptakes >6.5 wt% H_2 (up to 18 wt% for $LiBH_4$).

Property	**Physisorption**	**Chemisorption**
Interaction (Bonding)	Weak – Van der Waals	Strong – Chemical (Covalent or Ionic)
Bond Strength ($-\Delta H_{ad}$)	< 10 kJ mol^{-1}	> 50 kJ mol^{-1} (typically 100–400+ kJ mol^{-1})
	< 0.1 eV $atom^{-1}$	> 0.5 eV $atom^{-1}$ (typically 1-4+ eV)
Kinetics	Very Fast	Slow
Surface Coverage	Multilayer (possible)	Monolayer only
Materials	High Surfaces Area Materials; Carbons, Zeolites, MoFs	Hydrides (Metal and Complex)

table 2.5 – Comparison of Physisorption and Chemisorption adsorption.[95,116,117,120]

With physisorbed materials, the interaction between the hydrogen and adsorbent is very weak, thus little (or no) hydrogen is physisorbed at room temperature. However, at liquid nitrogen temperatures (77K) the lower thermal energy of the hydrogen allows adsorption to occur and thus many results for uptakes on physisorption-materials are given at 77K. Again, there is an energy cost in cooling a hydrogen store, which means that efficiency is reduced, however desorption is not an issue, as warming to ambient temperature (298 K) will release the hydrogen. Obtaining high enough hydrogen uptakes (> 6.5 wt% for the entire store from DOE targets), even at low temperatures, remains the principal challenge for these materials.

Given the currently known solid-state hydrogen storage materials, it is not clear whether chemisorbed-type or physisorbed-type materials (or either) will be suitable for large scale solid-state hydrogen stores. It has been postulated that a material that exhibits 'intermediate' binding of hydrogen (in the region of 10-50 kJ mol^{-1}, i.e. between physisorption and chemisorption) could be found, then it may well be able to fulfil the needs for a solid-state hydrogen store, figure 2.12.[8]

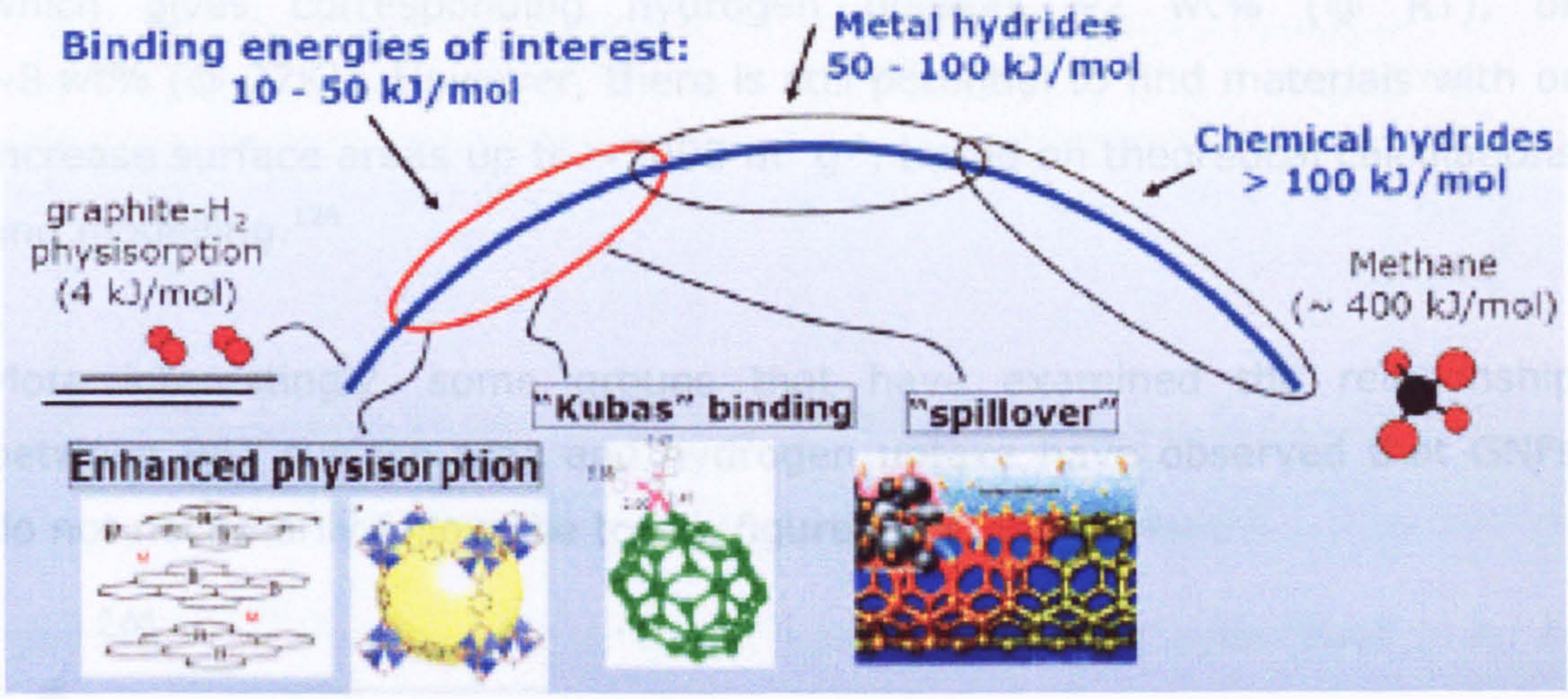

figure 2.12 – Diagram illustrating the range of binding energies of various hydrogen storage materials and potential binding interactions with suitable energies to enhance adsorption.[8,121]

In order to change the binding energy of hydrogen to a material, modification of its (surface) chemistry will be required. Thus given that only the surfaces of physisorption-type materials would need modifying (rather than full chemical properties of chemisorption-type materials), these materials would be more suitable candidates for modification. Thus only physisorption-type materials (carbons, zeolites and MoFs) shall be considered in detail in rest of this section of the literature review, detailing the issues and opportunities that exist for enhancing adsorption.

2.7.3 Physisorption Materials

For physisorption-type materials, there are two principal methods available to increase there hydrogen uptake; increase their surface area or increase the hydrogen binding energy. These two methods shall be considered separately below.

Surface Area

Several authors have published data illustrating how surface area and hydrogen uptake have a directly proportional relationship to N_2 BET surface area. Generally these values approximate to ~0.5 wt% hydrogen uptake per 1,000 m^2 g^{-1} at room temperature, or ~2 wt% per 1,000 m^2 g^{-1} at 77K.[8,25,122,123,123-125] The maximum surface areas for currently known physisorption-type materials (activated carbons and MoFs) are ~4000 m^2 g^1

which gives corresponding hydrogen uptakes ~2 wt% (@ RT), or ~8 wt% (@ 77K). However, there is still potential to find materials with or increase surface areas up to ~7000 $m^2 g^{-1}$, based on theoretical calculations and modelling.[126]

More interestingly, some groups that have examined the relationship between BET surface area and hydrogen uptake have observed that GNFs do not necessarily follow the trend, figure 2.13.

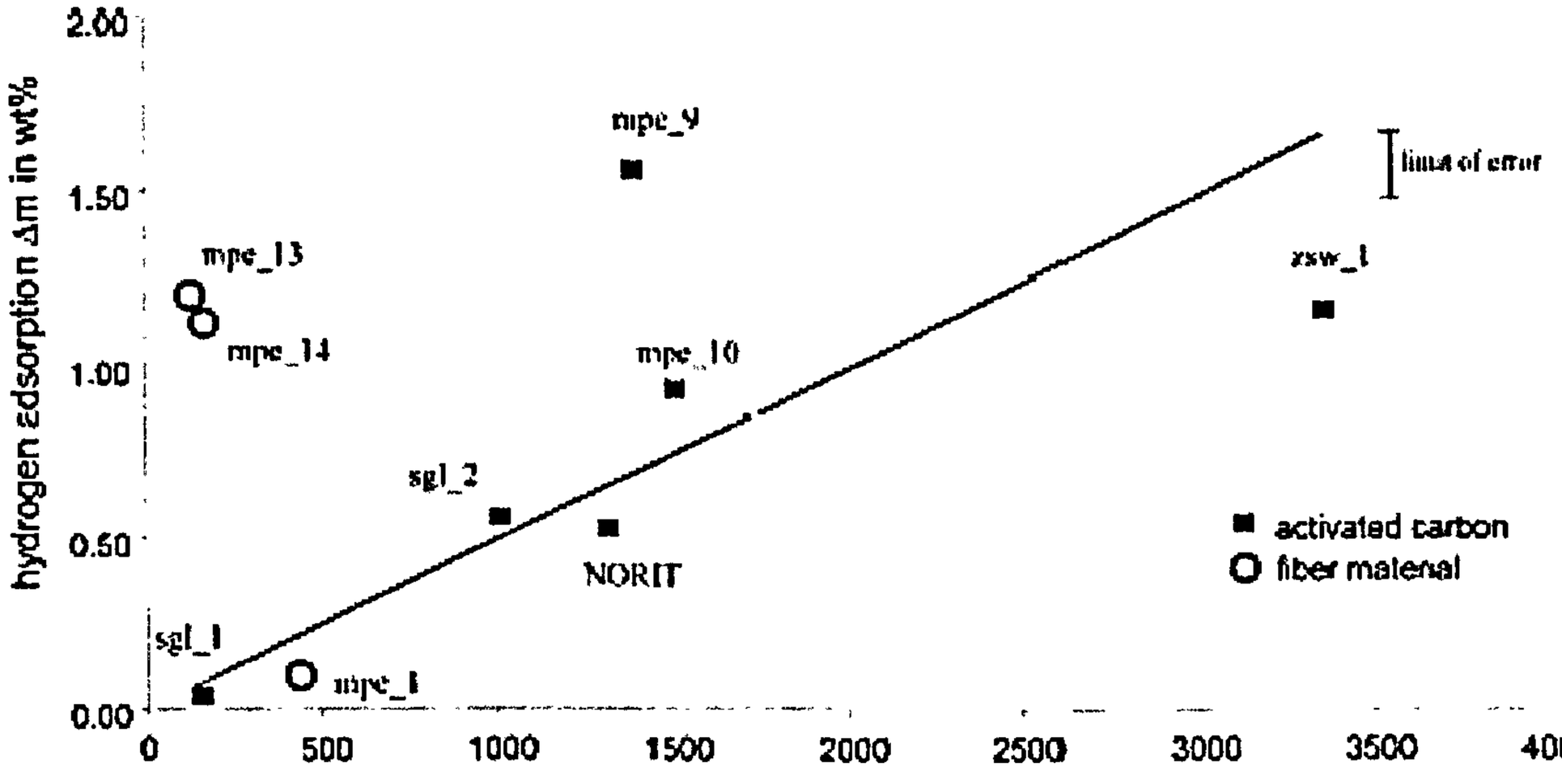

figure 2.13 – Graph showing BET surface area vs. hydrogen uptake results from *Ströbel et al.*[25]

GNF show much higher than expected uptakes, given their lower surface areas; ~1.2 wt% at RT with a surface area of ~300 $m^2 g^{-1}$ from *Ströbel et al*, while *Blackman et al* have observed more modest results, 0.5 wt% for 500 $m^2 g^{-1}$.[25,95]

Work on ball milled GNFs by Orimo *et al* also observed this non-correlation between surface area and hydrogen adsorption for GNF, figure 2.14, although some of the hydrogen uptake is due to chemisorption.[127,128]

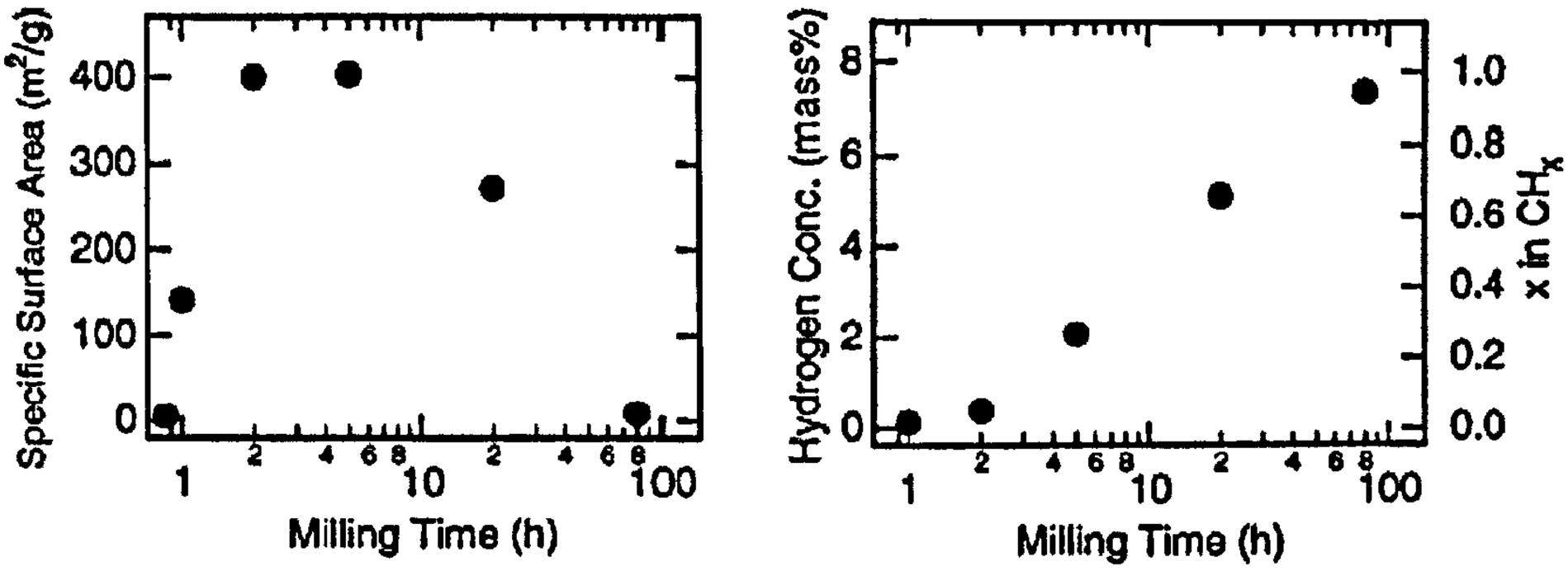

figure 2.14 – Non-correlation of surface area and hydrogen adsorption in ball milled GNF.[127]

Given these unexpected surface area results, the ability of GNF to adsorb hydrogen via physisorption and chemisorption (during ball milling) and the possibilities of surface modification (section 2.1.2), GNF would appear to be ideal candidate hydrogen storage materials. Therefore, the remainder of this review will consider hydrogen uptake in GNFs exclusively and what possibilities exist to maximise their hydrogen uptake potential.

2.7.4 Hydrogen Uptake Mechanisms in GNFs

The original explanation that *Rodreguez et al* gave for the very large hydrogen uptakes (65 wt% @ RT) was that hydrogen molecules (or atoms) were able to intercalate in between the layers of GNFs.[94] *Gupta et al* have also claimed that this is the mechanism of adsorption based on TEM observations of GNFs before and after hydration (15 wt% @ RT) showing damage to the graphene layers and GNF surfaces.[54,55] *Patchkovskii et al* have presented models indicating that pores or channels between graphene sheets could be favourable for hydrogen storage, figure 2.15.[129]

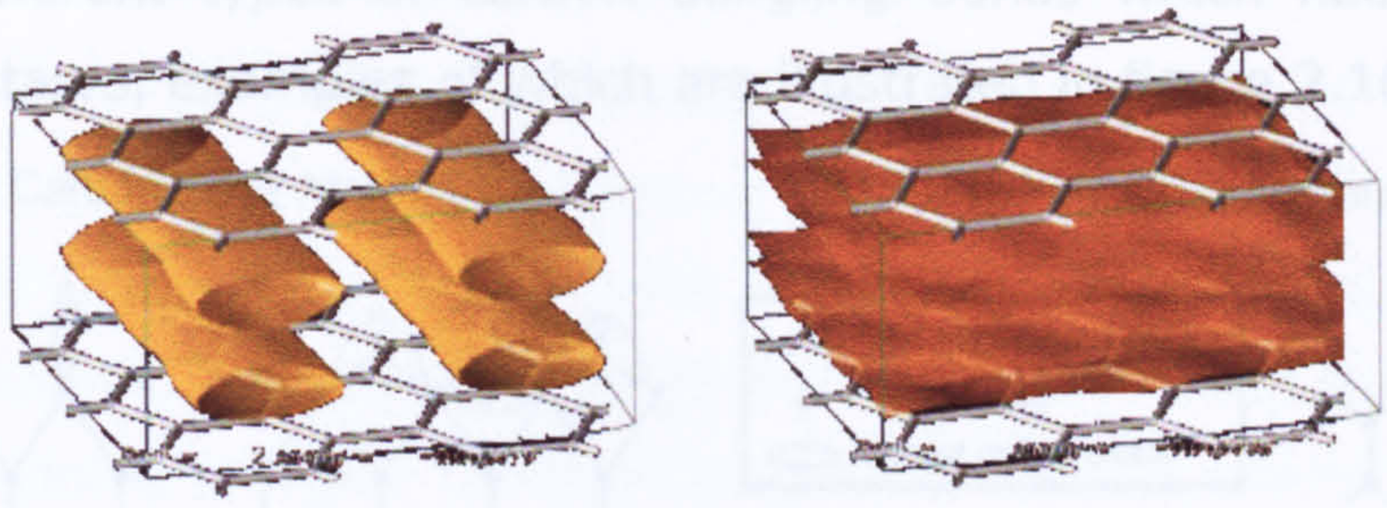

figure 2.15 – Pores and Channels between graphene sheets, proposed by Patchkovskii et al.[129]

However, in this modelling work it was noted that the interlayer separation for the graphene sheets would need to be approximately 0.7 nm in order to obtain hydrogen binding of 13.1 kJ mol^{-1} and potential hydrogen uptake of 6-7 wt%. A simple analysis of the interlayer spacing in GNF (~ 0.34 nm), after accounting for the size of the carbon atoms (r_{cov} ~ 0.07-0.09 nm), leaves a possible space for H_2 to occupy of ~0.27 nm. This distance is almost same (or smaller than) the kinetic diameter of H_2 (~ 0.27-0.29 nm), which could indicate this basic mechanism to be incorrect.[94,116,130] However, given there are only weak Van der Waals forces holding the graphene layers together, expansion of the layers would be relatively easy (low energy) and is easily achieved for other graphitic materials.[131-133]

Carbon Dangling Bonds

Browning et al observed large hydrogen uptakes (6.5 wt% @ RT), but with slow kinetics, suggesting that chemisorption was occurring rather than physisorption. They proposed that in GNFs there were a high proportion of edge sites in GNFs, with large numbers of energetic 'carbon dangling bonds'. These surface sites on the GNFs acted as catalysts to cause dissociation of H_2 to atomic H, which was then small enough to be able to intercalate into the GNFs.[112]

Work by authors in the nuclear industry also supports this more detailed explanation, by examining the detail of adsorption sites and corresponding binding energies.[134-136] Two principle binding energies were proposed; 0.1eV for physisorption sites and 2-4.5+eV for various chemisorption sites.[135,137] The reason for the variation in chemisorption binding energies is

due to different types of carbon dangling bonds which had relaxed into different states, examples of which are illustrated in figure 2.16.[135]

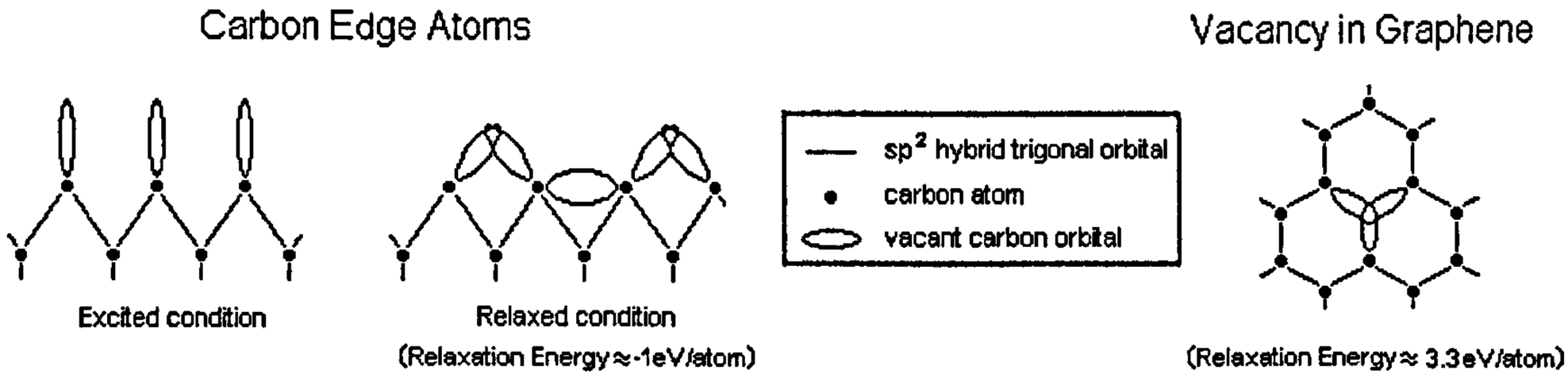

figure 2.16 - Examples of dangling bonds present in graphite structures.[135]

In ball-milling work by *Orimo et al* (figure 2.14) a radial distribution function spectrum a GNF sample with $\sim CD_{0.3}$ was conducted. It indicated that approximately half the deuterium in the sample was located between the graphene layers, which were 6% expanded, indicating intercalation of hydrogen. The remaining deuterium was covalently bonded (chemisorbed) to carbon atoms. The authors proposed that this chemisorbed hydrogen was present on the surface/edge sites of the GNFs, as during the ball milling process, the carbon was 'pulverised', creating dangling bonds which were relaxed by reaction with hydrogen (experiments were conducted under a hydrogen atmosphere).[127,128] This appeared to be confirmed by the observation of two desorption peaks (i.e. edge sites and graphene sites) observed during temperature programmed desorption (TPD), figure 2.17.[128,137-139]

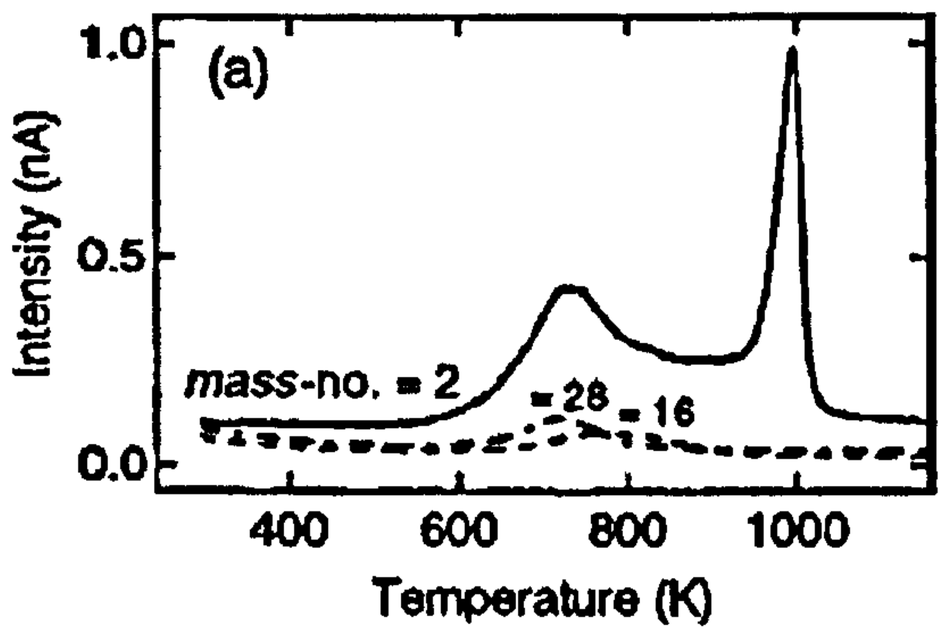

figure 2.17 – TPD results from Orimo et al [128]

Post-Treatments and Surface State of GNFs

Work by *Park et al* (1999) showed that heat-treatment of GNFs can significantly alter the hydrogen uptake properties; uptakes varied from < 5 wt% up to a maximum of 35 wt% depending on the temperature. The authors claimed this was related to the altering the surface of the GNFs from containing oxygen terminated surface carbon atoms to hydrogen terminated surface carbon atoms, based on work by *Murimoto et al* investigating H_2O adsorption on graphite.[140,141] However, there was little definitive supporting experimental evidence to confirm these results (and the hydrogen uptake values have not been reproduced and are widely discredited).

Later work (2004) by *Lueking et al* investigated different post-treatments of GNFs using inert (He), oxidising (Air – O_2) and reducing environments (H_2). These procedures produced a range GNFs with hydrogen uptakes between 0.75 wt% and 3.8 wt%, with largest uptake being observed after treatment in a hydrogen atmosphere at 700°C. The authors referred to the work of *Park et al* (above) as a possible explanation, however also suggested that the GNFs appeared to have a high degree of surface defects after the post-treatment and that this could be the reason for the increased hydrogen uptake, in agreement with the work of *Gupta et al* (mentioned previously).[142] *Marella et al* (2005) have applied similar post-treatments to GNFs at lower temperatures (400°C compared 800-1000°C used above) and found that no samples showed significant hydrogen uptakes (i.e. > 0.2 wt%).[143]

Influence of Metal Particles

In 1999, *Hirscher et al* reported higher than expected hydrogen uptakes (1.5 wt% @ RT) in CNT materials due to the presence of accidentally incorporated Ti from the probe tip during sonification.[109] *Costa et al* observed an identical increase in hydrogen uptake (0.6 wt% @ RT) due to residual Ni catalyst being present in their CNT samples.[102] Both authors concluded that the increase in hydrogen uptake was only due to the uptake in the metal part of the samples, however *Lueking et al* (who observed

similar effects with NiMgO in CNTs) suggested that the metal (oxide) was catalysing 'hydrogen spillover' into the CNTs.[144]

The spillover effect has been well documented (within catalysis) and simply shows that it is possible for hydrogen to adsorb onto a metal particle and then diffuse onto or into a carbon support.[145,146] The significance of this effect is that (potentially) with nano-sized metal particles attached to GNFs, there could be a large amount of hydrogen spillover into and out of the material. It has been noted by *Isobe et al* and *Lee et al* that this effect would be highly dependent on the metal and nature of the contact with the carbon material.[103,147]

In order to investigate this, other authors have impregnated activated carbons and GNFs with various metal particles. Ni has been impregnated onto an activated carbon and GNF by *Zieliński et al* and *Yan et al* respectively, which increased the hydrogen uptake to 0.5 wt% (@ RT) and discharge capacity by 50% (101 mA h g^{-1} to 149 mA h g^{-1}).[148,149] However, more interesting results (on GNFs) have been reported using Pd by *Ansón et al* (0.5 wt% on SWNT)[150], *Back et al* (0.6 wt%)[151] by Marella et al (1.38 wt%)[143] and Lupu et al (1.5 wt%)[152]. These results are different as with *Back et al* and *Marella et al* the Pd was located on the surfaces of the GNFs, whereas with *Lupu et al* the Pd particles where located at the end of the GNFs ('reactivated' residual growth catalyst). It would logical be suggest that the spillover mechanism would be most effective if the hydrogen was able to enter the interlayer space in the GNFs, in which case the metal particles located on the surface of the GNFs would be more effective than particles located at the ends.

Kubas Binding

More recently modelling work by *Yildirim et al, Lee et al and Yang et al* have suggested that transition metals attached to either CNT or C_{60} can bind to several H_2 molecules.[153-156] This is achieved via Kubas binding, common in organo-metallic chemistry, where H_2 is weakly bound to the metal centre, shown in figure 2.18.[157-159]

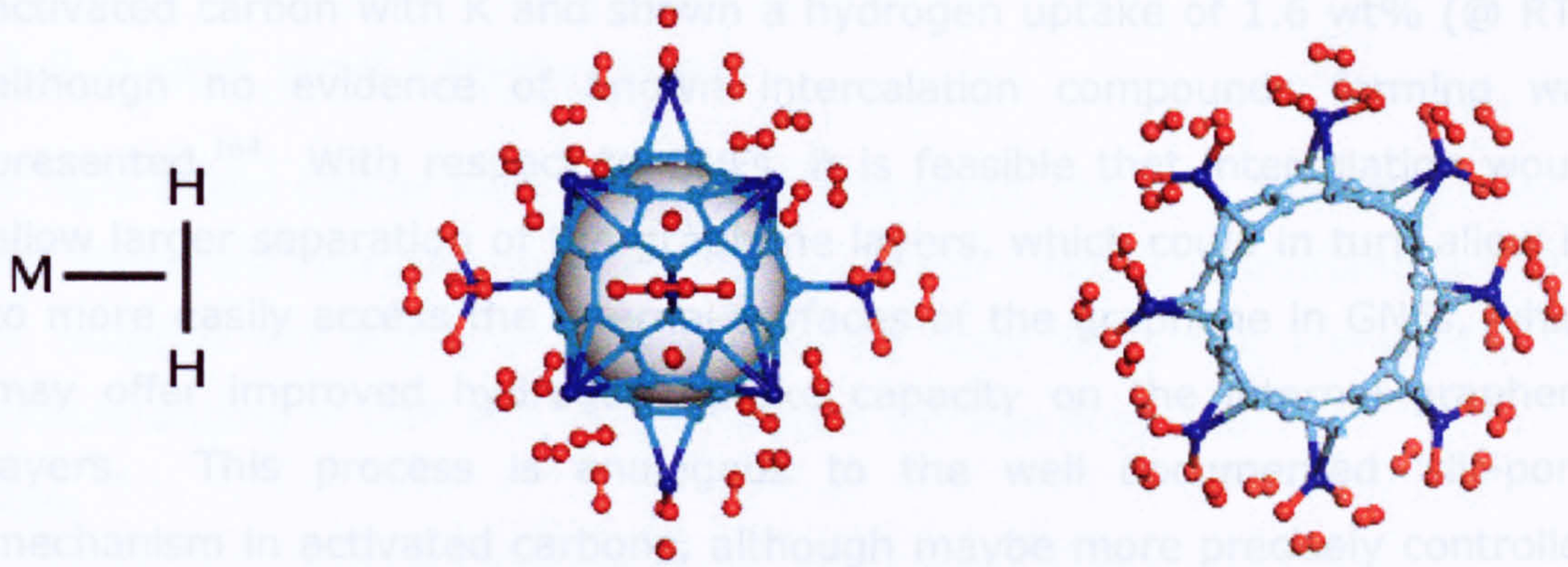

figure 2.18 – Models of; (left) Kubas binding, (centre) Kubas binding of Ti attached to C_{60} and, (right) Kubas biding of Ti attached to a section of a SWNT.[153,154,158]

These structures give theoretical maximum hydrogen uptakes (@ RT) of 6.7 wt% (C_{60}) and 7.7 wt% (SWNT). More interestingly, the binding energy of the hydrogen to the Ti is estimated to be 2-2.5 eV per 4 H_2 molecules, this operates in the region of 10-50 kJ mol^{-1}, due to the interaction of the metal with the de-localised bonding structure of the supporting carbon. To the authors' knowledge, there have been no reports of any experimental work to produce these structures. Given the nature of the interaction, there is no reason why a similar effect could not be observed in metal coated GNFs and may explain why the difference in Pd particle location (in the work by *Marella* and *Lupu*, above) makes little difference to the observed increase in hydrogen uptake.

Intercalation

Chen et al published data that claimed CNTs intercalated with Li or K have hydrogen uptake capacity of 20 wt% and 14 wt% respectively, (casually) suggesting that the spillover.[160] These high values have largely been dismissed as moisture uptake in the hydrogen gas, however *Pinkerton et al* have produced Li intercalated CNT which show more modest hydrogen uptakes of 1.3 wt% (of which only 0.2 wt% is cyclable).[161] *Zhu et al* and *Lee et al* have published theoretical studies indicating that if graphite was intercalated then there could increase the binding energy of hydrogen to graphene, but that the effect would not be significant enough to make any significant difference to the hydrogen uptake.[162,163] *Kojima et al* have doped

activated carbon with K and shown a hydrogen uptake of 1.6 wt% (@ RT), although no evidence of known intercalation compounds forming was presented.[164] With respect to GNFs, it is feasible that intercalation would allow larger separation of the graphene layers, which could in turn allow H_2 to more easily access the internal surfaces of the graphene in GNFs, which may offer improved hydrogen uptake capacity on the internal graphene layers. This process is analogous to the well documented 'slit-pore' mechanism in activated carbons, although maybe more precisely controlled and optimised in GNFs.[165]

Summary

There are several possible different adsorption mechanisms that could occur in GNF materials. The validity of many of these mechanisms is hard to access due to frequently inaccurate hydrogen uptake data often being presented. However, there are some clear areas where opportunities exist for further research and potentially ground breaking discoveries to be made, especially in relation to the surface state and interaction of metals with GNFs and hydrogen.

2.8 Aims and Objectives

In light of the critical literature review presented, the aims and objectives of the thesis will now be presented in more detail – clearly identifying the aims of chapters 4-7 and how they add to the body of current knowledge and understanding of GNF and their hydrogen storage properties.

Aim

The overall aim of this thesis shall be to investigate hydrogen storage in GNFs. There is a clear need and opportunity to clarify whether GNF can storage large quantities of hydrogen and if so, to determine by what mechanism this occurs.

Objectives

The specific objectives of this thesis are given in section 1.4 and are dealt with in the discrete chapters 4-7. Given the more detailed information presented in this literature review, the objectives of each chapter (4-7) shall be consider further below, with reference to how they will be achieved within the relevant chapter and how that chapter contributes to overall aim of this thesis; examining the hydrogen storage properties of GNF, as well as adding to the current body of knowledge and understanding within this field.

Chapter 4 – GNF Synthesis;

1. To develop a reproducible method to synthesise high purity GNFs from different catalysts using the CVD method.
2. To further examine the relationship between catalyst morphology and reaction conditions during the CVD growth of GNFs.

The aim of this chapter is to develop a synthesis method that is reproducible and can be used as a basis for producing high quality GNFs for use in subsequent chapters (5-7) for further treatment and assessment of hydrogen storage properties. Within this, the work presented in the chapters also aims to add to the current understanding of the CVD growth mechanisms of GNFs by conducting a systematic investigation into the CVD variables.

Chapter 5 – Post-Treatment of GNFs;

3. To develop a method for the successful removal of residual growth catalyst from the 'as-grown' GNFs.
4. To post-treat GNF to alter properties (both surface and bulk) of the GNFs and assess any effect on the hydrogen uptake properties of GNFs.

The aim of this chapter is to develop a method that can be used to successfully remove residual CVD catalyst particles from GNF samples produced in Chapter 4, so that any effect of the metal impurity can be removed from any changes observed to the hydrogen uptake properties. Within the method developed, the surface-state of the GNF will also be altered, which will be fully characterised and assessed in terms of the hydrogen uptake properties.

Chapter 6 – Preparation of Metal containing GNFs;

4. To post-treat GNF to alter properties (both surface and bulk) of the GNFs and assess any effect on the hydrogen uptake properties of GNFs.
6. To develop a synthesis method to decorate GNF with metal particles and assess any effect on the hydrogen uptake properties of GNFs.

The aim of this chapter is to prepare GNF samples with further post-treatment (to complement the samples used in Chapter 5) and also create a range of samples decorated with metal particles in various morphologies. This is in order to systematically access the effect of metal particles on the hydrogen uptake properties, adding to the understanding of the potential mechanisms that have been suggested in the open literature (section 2.7).

Chapter 7 – Hydrogen Storage Properties of GNFs;

5. To determine whether the surface state of GNFs has any influence on their hydrogen uptake properties of GNFs.
6. To develop a synthesis method to decorate GNF with metal particles and assess any effect on the hydrogen uptake properties of GNFs.
7. To determine by what mechanism treatments alter the hydrogen uptake of GNFs.

The aim of this chapter is to precisely determine the hydrogen uptake properties of all of the samples produced in chapters 4-6. Due to the

carefully controlled synthesises performed in those chapters, the samples tested will allow for a systematic assessment and clear determination of the hydrogen uptake mechanisms involved.

3 MATERIALS CHARACTERISATION

This chapter will outline the techniques and methods that are used in more than one of the experimental chapters (chapters 4-7) to characterise the materials being investigated. The 4 techniques detailed are;

- Transmission Electron Microscopy (TEM)
- X-Ray Diffraction (XRD)
- Thermo-gravimetric Analysis (TGA)
- Mass Spectrometry (MS)

Any other experimental techniques used in this thesis shall be dealt with in the relevant experimental section, in chapters 4-7. For each technique described; the make and model of the apparatus used, how samples were prepared for analysis and a description of what information was obtained through the characterisation technique is presented, with a description of any relevant theory.

3.1 Transmission Electron Microscopy

Transmission electron microscopy (TEM) was used to give information on the types of nanostructures, morphologies and surfaces features of the different types of carbon investigated. It was used in several different modes; bright field, dark field, phase contrast, selected area electron diffraction (SAED) and energy dispersive X-ray analysis (EDX). Experiments were conducted on two microscopes; (1) a JEOL JEM-2000FX II microscope operating at 200 keV and (2) a JEOL JEM-4000FX microscope operating at 400 keV (used for HR-TEM).

3.1.1 SAMPLE PREPARATION

Samples were prepared by creating a suspension of GNFs in propan-2-ol using an ultrasonic bath. This suspension was then pipetted (approximately 3 drops) onto a copper TEM grid, with a carbon film (Agar Scientific).

3.1.2 Application of TEM

The basic principle of TEM is to examine the interaction between a sample and a 'beam' of accelerated electrons (referred to as Primary Electrons). This produces many different types of interactions that can be examined;

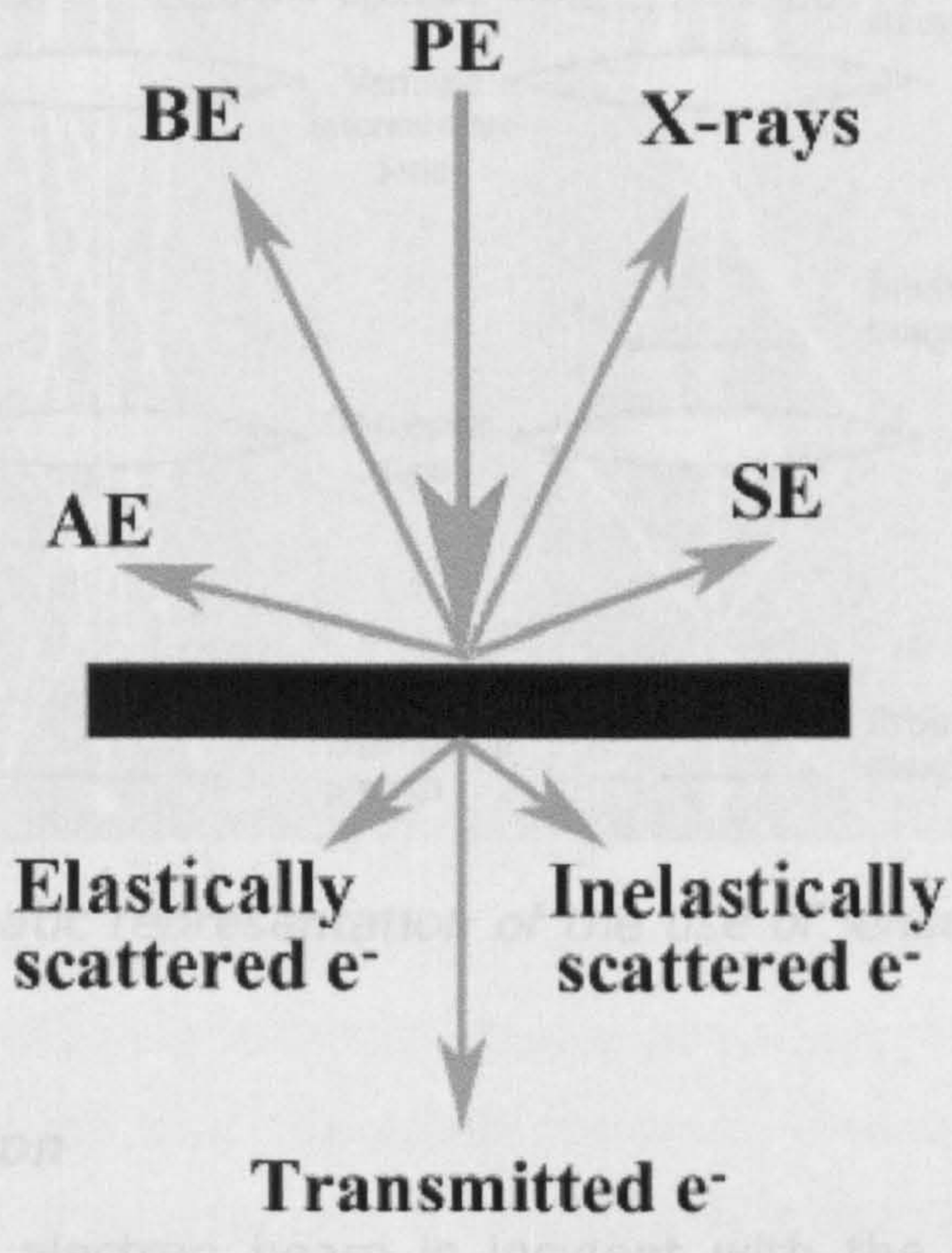

figure 3.1 – Some possible interactions of an electron beam (PE Primary Electrons) and a sample; AE Augur electrons, BE Back-scattered Electrons, SE Secondary Electrons

In TEM the principle interest is to examine the transmitted and scattered electrons to give information regarding the phases, morphologies and surfaces of a sample. By altering electromagnetic lenses and apertures within the microscope, each of these different interactions can be used to investigate different characteristics of the sample. The arrangement of these lenses and apertures are described within the different 'modes' of operation, described below and in reference to figure 3.2.

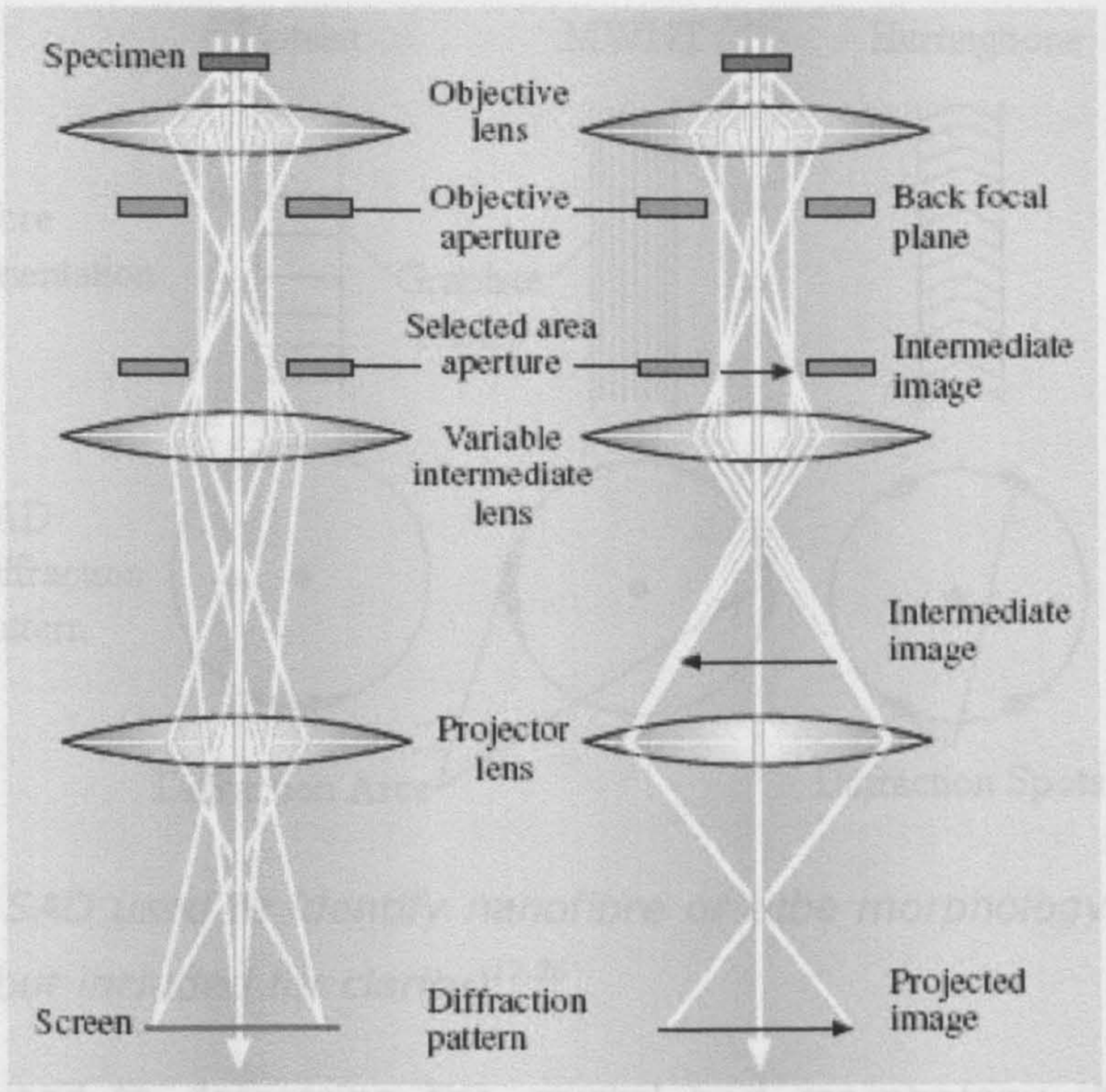

figure 3.2 – Schematic representation of the use of lenses and apertures in a TEM

Electron Diffraction

When the primary electron beam is incident with the sample, diffraction (see section 3.2) occurs through elastic scattering. Inserting the selected area aperture allows these diffracted beams, of an area of the sample, to be focused onto the image screen – selected area electron diffraction (SAED).

When the electron beam passes through filamentous carbon, the diffraction that occurs produces 2 diffraction spots (or more usually, diffraction arcs) opposite each other. The positions of these relative to the fibre axis can then be used to determine the morphology of the filament. If the arcs are parallel to the fibre axis, then the graphite planes must be arranged perpendicular, thus a platelet structure. MWNT are the opposite, the planes run parallel with the fibre, and thus the arcs are perpendicular. Herringbone fibres have two sets of planes at an angle to the fibre axis, each of these orientations cause diffraction and 4 arcs are observed (2 x 2 arcs), the position of these arcs can also be used to calculate the angle of the herringbone planes.[12,26]

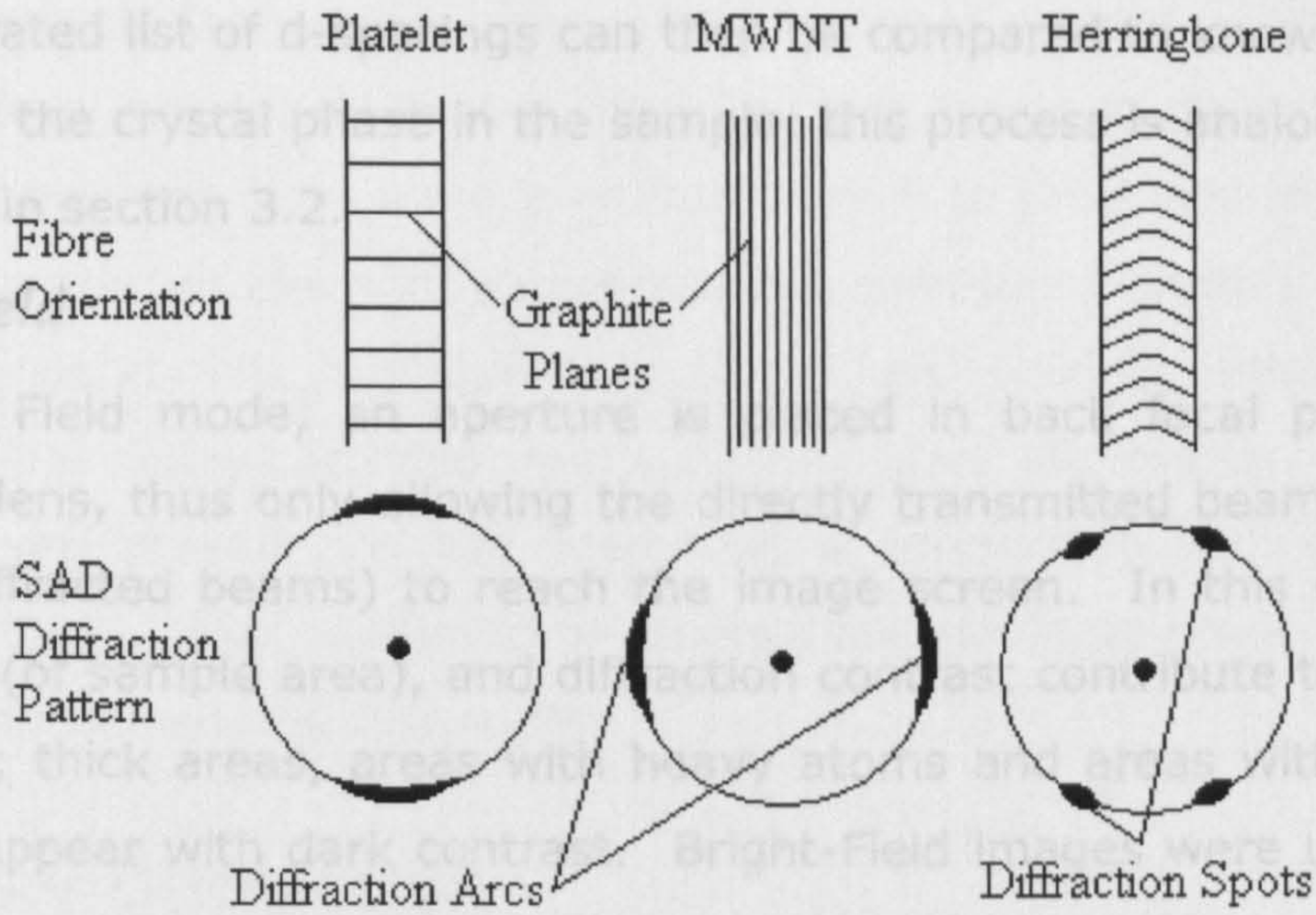

figure 3.3 – SAD used to identify nanofibre or tube morphology (the ring is not present but included for clarity)[12,26]

SAED was used to determine the crystal and morphology (herringbone, platelet or MWNT) of the GNFs via the method described above (figure 3.3). SAED was also used to identify the phases of catalyst particles present in samples, which produce spot diffraction patterns. Measuring the position of these points allows the d-spacing in crystalline material to be calculated using the camera equation:

$$\lambda L = Rd$$

where,

λ is the wavelength electron of the accelerated electrons*

L is the camera length of the microscope*

R is the distance of the diffracted ring, arc or spot from the transmitted centre spot

d is the corresponding lattice d-spacing giving rise to diffraction

---

* The camera constant (λL) was determined through analysis of material of known d-spacing (evaporated Aluminium) performed by Dr H Edwards

The generated list of d-spacings can then be compared to known materials, to identify the crystal phase in the sample; this process is analogous to that described in section 3.2.

Bright Field

In Bright Field mode, an aperture is placed in back focal plane of the objective lens, thus only allowing the directly transmitted beam (and some weakly diffracted beams) to reach the image screen. In this case, mass-thickness (of sample area), and diffraction contrast contribute to the image formation; thick areas, areas with heavy atoms and areas with crystalline material appear with dark contrast. Bright-Field images were used to gain information about the shapes, sizes and surface textures of the GNF samples.

Dark Field

In Dark Field mode, the selected area aperture is used to only allow a specific diffracted beam to reach the image screen (in contrast to Bright Field). In the images formed, areas causing the diffracted beam are contrasted light, while the rest of the image is dark. (Centred) Dark Field images were used to show clear images; highlighting and clarifying the relative positions of GNFs to catalysts particles.

Phase Contrast

When the primary electron beam is diffracted, there is a phase shift in the diffracted beam. Without an aperture to eliminate either the transmitted or diffracted beams (e.g. in Bright Field or Dark Field) destructive interference of the beams at the image screen gives no or limited contrast in the image. However, at higher magnifications, there can be constructive interference between the transmitted electron beam and strongly diffracted beams leading to contrast. This imaging mode is referred to as high resolution (HR-) TEM, lattice fringe or phase contrast imaging. Phase contrast imaging was used to examine the orientation of (crystalline) graphite sheets in GNFs and also explore the crystalline nature of the surface structures in GNFs.

Energy Dispersive X-ray

Energy Dispersive X-Ray (EDX) analysis examines the X-Rays that are emitted from a sample through photoionisation, caused by interaction with

the primary electron beam; the primary beam causes electrons to be removed from the inner shell (K shell) of the atoms in the sample. This causes an electron from a more energetic shell to drop into the K Shell to replace the ejected electron, simultaneously emitting a photon of energy in the X-Ray band. As this transition is element specific, detection of the energy of the X-Rays emitted from a sample gives information about which elements are present (in the area that is interacting with the primary electron beam). EDX was used to confirm the elements present within the samples, specifically Ni, Fe and Pd.

3.2 X-Ray Diffraction

XRD was used to identify the material phases present in samples and calculate average crystallite sizes. XRD patterns were collected on a Bruker D8 diffractometer, using a monochromated Cu Kα radiation source (λ = 0.154 nm), operating at 40 kV and 40 mA.

Sample Preparation

Samples were in powder form and sprinkled onto the sample holder and then flattened using a glass slide. Diffraction patterns were measured from the range 10°- 80°, the step size and dwell time were typically 0.02° and 2 seconds per step, with the samples being rotated within the beam (at approximately 60rpm). When performing scans that were to be analysed to determine particle size (from peak broadening), smaller step sizes and angle ranges were used, typically 0.0005° and 5° range.

3.2.3 Specific Application of XRD

Diffraction occurs when an ordered (i.e. crystalline material) interacts with an electromagnetic wave which has a wavelength approximately equal to that of the inter-atomic distance (i.e. X-Rays). Diffraction occurs when the Bragg condition is met, shown below, with reference to figure 3.4.

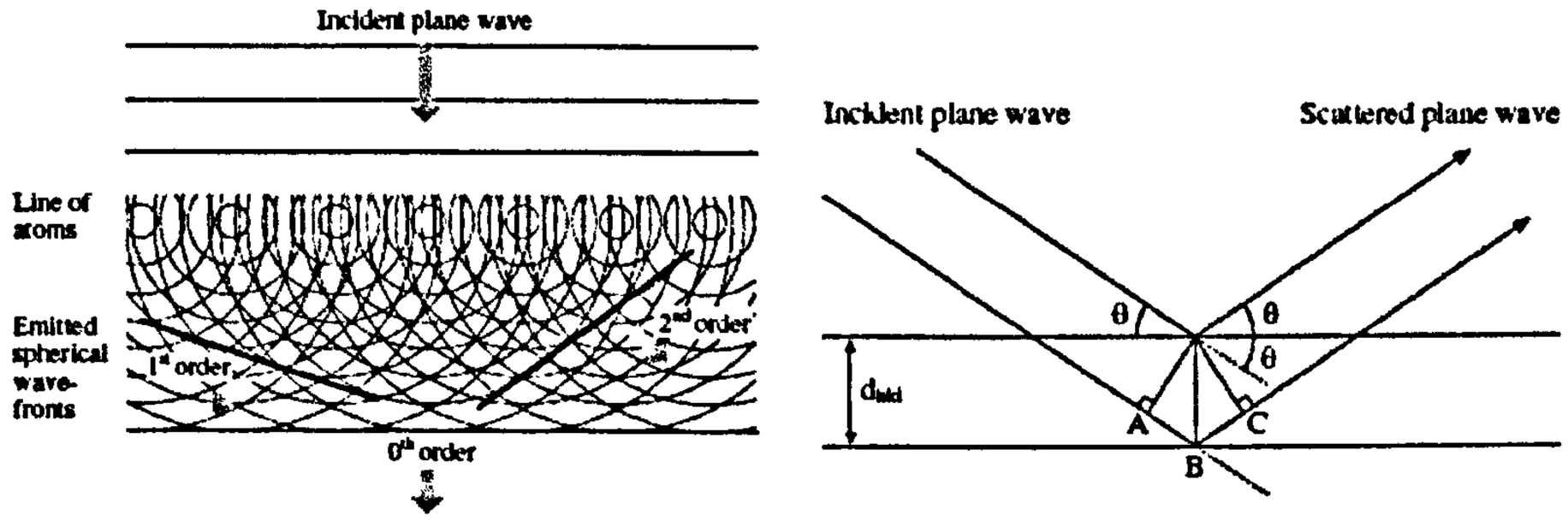

figure 3.4 – (left) Propagation of wave through a crystal lattice (line of atoms), (right) Bragg condition geometry

The Bragg condition;

$$n\lambda = AB + BC = 2\,d\,Sin\theta$$

where,

n is the order of diffraction (taken to be 1)

λ is the wavelength of X-Ray radiation (Cu Kα radiation 0.154 nm)

d is the d-spacing of the crystal plane giving rise to diffraction

θ is the measured Bragg angle

Using a diffractometer, a list of d-spacings for a sample is recorded, called a 'diffraction pattern'. XRD was used to identify which phases were present in a bulk sample by comparing recorded diffraction patterns to published powder diffraction files (PDFs), available in a central database.[166]

In XRD, the angle range over which diffraction is observed (known as the peak width) is determined by several factors; Lattice defects, Residual Lattice strain, Instrument factors and Crystallite (or grain) size. XRD can be used to calculate the average crystallite sizes of particles (below 1 μm) through peak broadening. This is calculated using the Debye-Scherrer equation, given below:

$$B = \frac{k\,\lambda}{D\,Sin\theta}$$

where,

B is the calculated crystallite size

k is an instrument constant

λ is the wavelength of X-Ray radiation

D is the measured diffraction peak width

θ is the measured diffraction angle

By calibrating the diffractometer with a material of known crystallite size (> 1 μm), all of the variables in the peak width can be approximated in a constant (k). Thus, to calculate of crystallite size of a sample requires the width of a samples diffraction peak to be compared with the standard; in the current study Al_2O_3 (supplied by Bruker) was used to determine the standard broadening, used for all the XRD patterns. Peak broadening was used to identify the average crystallite size of Pd in GNF samples (that contain Pd).

3.3 Thermo-Gravimetric Analysis

TGA is a characterisation technique that can be used to identify the temperature at which different, thermally activated reactions occur by monitoring the weight of a sample during heating (weight loss is due to gaseous mass loss). TGA was carried out in a SDT 600 supplied by Universal Instruments, in conjunction with a MS supplied by Hiden Analytical.

3.3.1 Sample Preparation

Samples were prepared for TGA by tarring the micro-balance with two identical pans (Alumina supplied by Universal Instruments). Approximately 10-15mg of sample was then placed into the sample pan.

3.3.2 Application of TGA

TGA has been used in this thesis to determine the reactions of GNFs within various gases environments. The required gas environment was flowed over the sample at 100 cm^3 min^{-1} for 30 mins to ensure that no air was present. The samples were then heated at constant rate (as specified in the relevant experimental chapters) with any mass change being constantly (~1 reading per second) monitored. The gaseous atmosphere was concurrently monitored using MS – details are given in Chapters 5 and 6 on the specific reactions being investigated.

3.4 Mass Spectroscopy

Mass spectroscopy analyses gaseous atmospheres with a very high degree of accuracy. It can be used during reactions to observe changes in the gas atmosphere and can give information about any reactions (temperature, mechanism, intermediate products, etc.) that involve gaseous products or reactants. Several different mass spectrometers were used, all supplied by Hiden Analytical.

3.4.1 Sample Preparation

MS has been used to monitor TGA and heat treatment experiments (Chapters 5 and 6). The MS was attached to apparatus using a heated capillary to sample the gaseous environment just above samples.

3.4.2 Specific Application of Mass Spectroscopy

All analysis was qualitative (rather than quantitative), examining any changes in partial pressure of the gases being monitored to indicate a reaction. Ions with m/z in the range 1-50 were monitored during experiments, with data being collected over approximately a 30 second cycle – details are given in Chapters 5 and 6 on the specific reactions being investigated.

4 GNF SYNTHESIS

4.1 Aim

This chapter will detail the investigation in to the synthesis of the GNFs used throughout this thesis. Samples were synthesised using CVD with two types of catalyst; Fe and Ni based. A detailed study of the Fe-based catalyst system has been undertaken, with the variables of gas mix, temperature and multi-temperature reactions being systematically investigated. Characterisation of both the types and quantities of (nanostructured) carbon synthesised have been undertaken with each of the reaction conditions investigated. The object of this investigation is to elucidate a preparation route for GNFs giving a homogeneous type of nanofibre (either platelet or herringbone), ideally with a large yield of material. An investigation of Ni-based catalyst had been undertaken previously by M Bououdina[167], thus the growth variables of the Ni-catalyst have not been investigated in the study reported here. However, the product(s) of a selected Ni-catalyst synthesis route have been fully characterised, for the purpose of comparison with the Fe-catalyst system. The work in this chapter has also been published in *Carbon,*[26] a copy of which is included in appendix A.

4.2 Experimental

4.2.1 CATALYST PREPARATION

Two types of catalyst were synthesised and used to grow GNFs; based on Ni and Fe. The catalysts were prepared from the precipitation reaction of the nitrate salt (Fisher) and 2 M ammonia solution (Fisher). The dried precipitate was subsequently calcined at 300°C for 3 h to yield either Fe_2O_3 or NiO catalyst precursor.

4.2.2 CVD METHOD FOR GNF SYNTHESIS

Samples were produced by CVD using a controlled environment horizontal tube furnace. Before all reactions, the furnace was purged with Ar and all

temperature changes were performed under a flowing Ar atmosphere (100 ml min^{-1}). All reactions were repeated at least once to ensure consistency and reproducibility. The specific reaction conditions for the Fe system is detailed below and shown schematically in figure 4.1A.

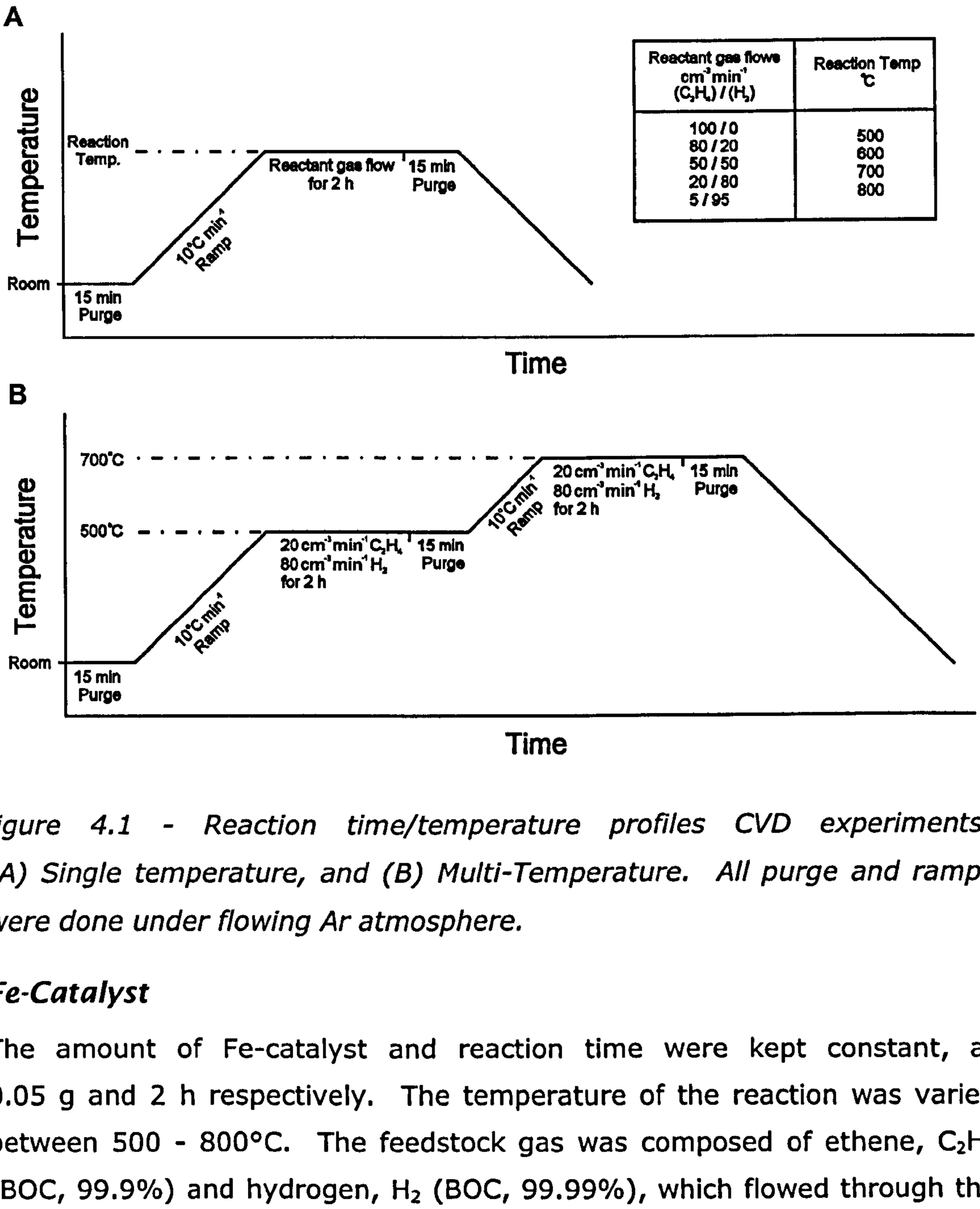

Reactant gas flowe $cm^3 min^{-1}$ $(C_2H_4) / (H_2)$	Reaction Temp °C
100 / 0 80 / 20 50 / 50 20 / 80 5 / 95	500 600 700 800

figure 4.1 - Reaction time/temperature profiles CVD experiments; (A) Single temperature, and (B) Multi-Temperature. All purge and ramps were done under flowing Ar atmosphere.

Fe-Catalyst

The amount of Fe-catalyst and reaction time were kept constant, at 0.05 g and 2 h respectively. The temperature of the reaction was varied between 500 - 800°C. The feedstock gas was composed of ethene, C_2H_4 (BOC, 99.9%) and hydrogen, H_2 (BOC, 99.99%), which flowed through the CVD reactor using mass flow controllers (MKS Instruments ltd). Different mixes of C_2H_4/H_2 where obtained by flowing the gases at different rates; 100/0, 80/20, 50/50, 20/80 and 5/95, maintaining a total flow of 100 cm^3 min^{-1}. Samples produced are referred to as 'CNS-x-y' where x is the synthesis temperature (in °C) and y is percentage of ethene used, e.g.

'CNS-500-80' refers to the sample that was synthesised at 500°C and with a C_2H_4/H_2 mixture of 80/20, respectively.

A second type of synthesis was also performed with the amount of Fe being ~0.25g, a reaction time of 4h, temperature 500°C and a gas mixture of 20/80 (C_2H_4/H_2 respectively). All Fe synthesised samples that were used in subsequent chapters were synthesised using this method and are referred to as 'Fe-GNF-x', were x refers to a subsequent treatment (i.e. no synthesis temperature or ethene percentage specified).

Fe-Catalyst Multi-temperature

A multi-temperature reaction was performed at 500°C for 2 h with 20/80 (C_2H_4/H_2 respectively), having a second stage of carbon deposition at either 600 or 700°C for a further two hours. The two samples are referred to as CNS-500/600 for the 600°C second-stage synthesis or CNS-500/700, for the 700°C second-stage synthesis. A schematic of the reaction time/temperature profile is shown in figure 4.1B.

Ni-Catalyst

Ni-catalyst carbon samples were synthesised using a single set of reaction conditions; 500°C for 2 h with an 80/20 (C_2H_4/H_2 ratio). These samples are referred to as 'Ni-GNF'.

4.2.3 Characterisation

All samples were characterised using TEM and XRD, as described in Chapter 3.

4.3 Results

For the CVD reactions undertaken with the Fe-based catalyst, special attention was focused on the amount of carbon synthesised, the phase of the catalyst and the type(s) of carbon observed. Therefore, the Fe results are collated into those sections (4.3.1-4.3.3), whereas the multi-temperature (4.3.4) and Ni-based experiments (4.3.5) are dealt with separately.

4.3.1 Carbon Yields

The carbon yields[†] deposited for the various gas mixes, at temperatures from 500 to 700°C are shown in figure 4.2. The percentage yield was calculated relative to the mass of elemental iron used. The results show that the carbon deposited increased with increasing hydrogen content in the gas mixture for all temperatures, except CNS-700-5, which produced almost no carbon deposition (this experiment was repeated three times to ensure it was a reproducible result). For samples produced at 500°C and 600°C, the amount of carbon deposited was similar over the range of gas mixes, but for samples produced at 700°C between 100-200% more carbon (at an equivalent gas mixture) was synthesised. Only one gas composition was used at 800°C, sample CNS-800-20, and these conditions gave a yield of 520%, a slightly higher yield than for CNS-700-20, the same gas composition but lower temperature.

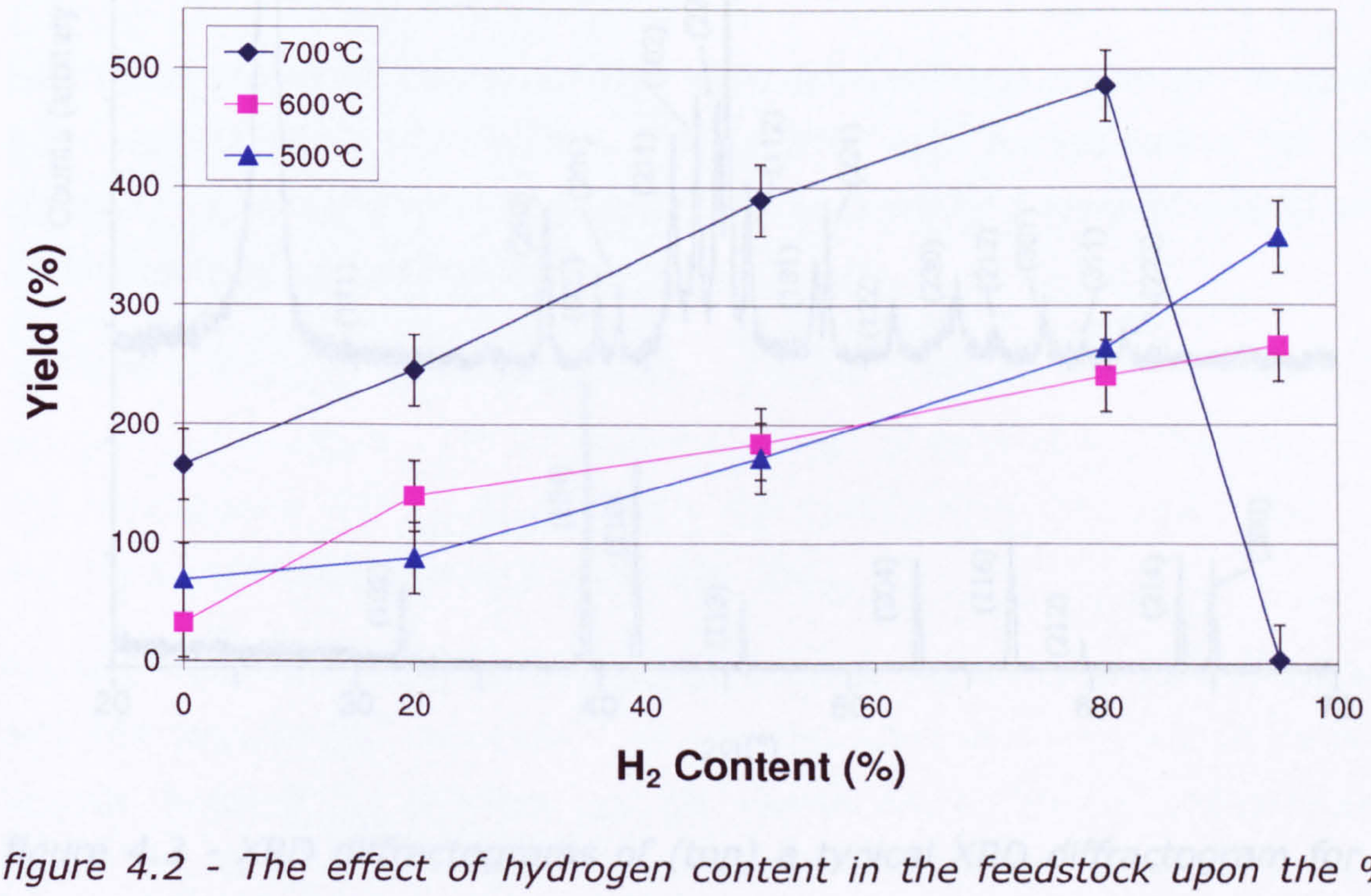

figure 4.2 - The effect of hydrogen content in the feedstock upon the % yield of carbon deposited (gas balance was ethene) for the three reaction temperatures investigated. Error bars are an estimate of errors between repeated experiments.

[†] $Carbon\ \ Yield\ \ = \frac{Mass\ of\ carbon\ + Mass\ of\ any\ \ residual\ catalyst}{Mass\ of\ \ starting\ catalyst} \times \%$

4.3.2 CATALYST PHASE

Figure 4.3 shows the XRD diffraction patterns for the Fe catalyst precursor prior to CVD and after carbon deposition. All the XRD diffractograms recorded after the reactions showed that the XRD pattern of the iron oxide precursor was no longer present; the only phases present were graphite and Fe_3C, figure 4.3.

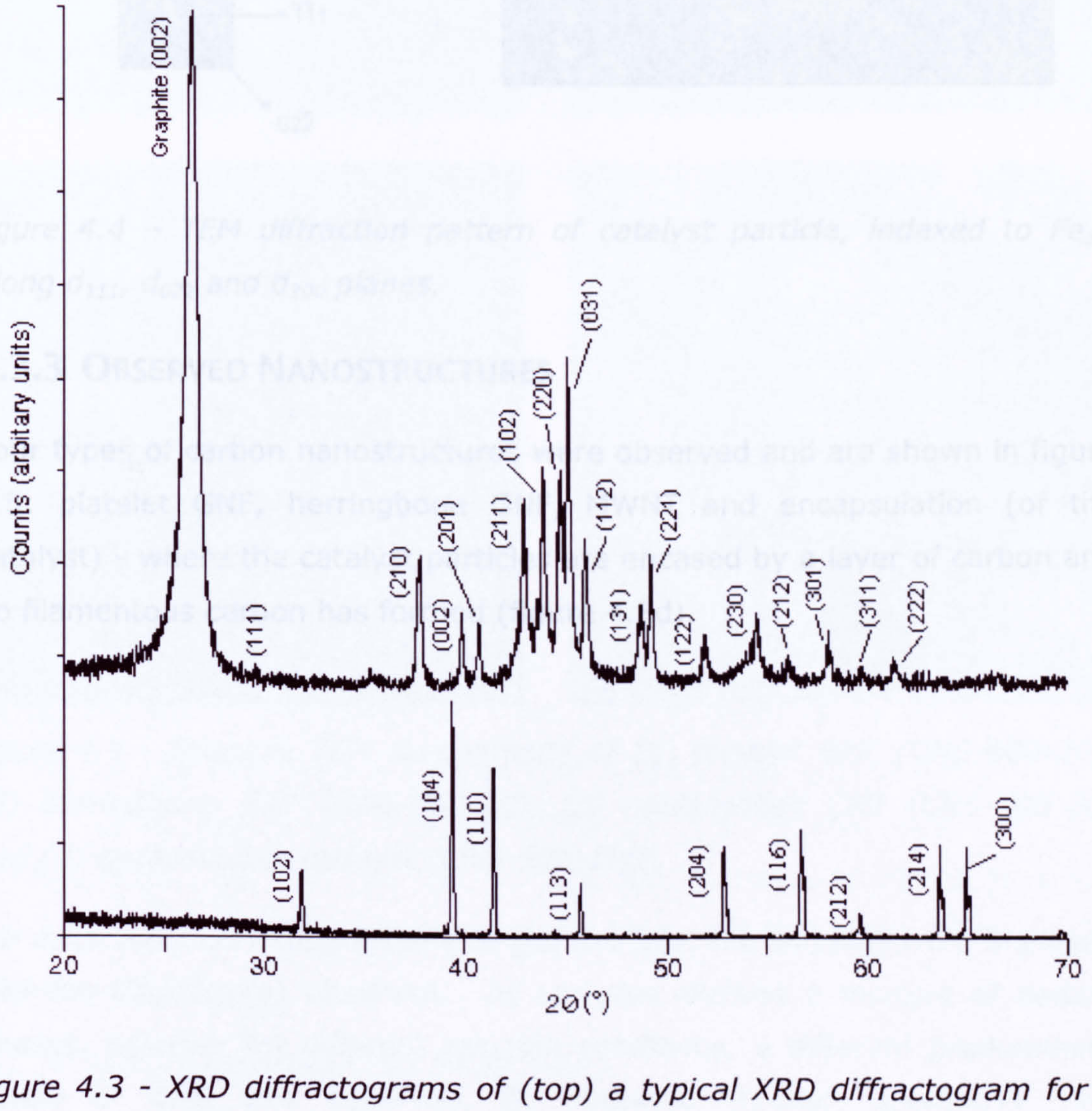

figure 4.3 - XRD diffractograms of (top) a typical XRD diffractogram for a carbon deposition sample (specifically CNS-700-20) indexed to Fe_3C and graphite and (bottom) the Fe catalyst precursor, indexed to Fe_2O_3.

Electron diffraction performed in the TEM on the catalyst particles after CVD have been indexed to be Fe_3C phase, as shown in figure 4.4.

Plane	Calculated d-spacing	PDF d-spacing
111	1.45	1.512
022	1.80	1.879
200	2.30	2.263

figure 4.4 – TEM diffraction pattern of catalyst particle, indexed to Fe_3C along d_{111}, d_{022} and d_{200} planes.

4.3.3 Observed Nanostructures

Four types of carbon nanostructures were observed and are shown in figure 4.5: platelet GNF, herringbone GNF, MWNT and encapsulation (of the catalyst) - where the catalyst particles are encased by a layer of carbon and no filamentous carbon has formed (figure 4.5d).

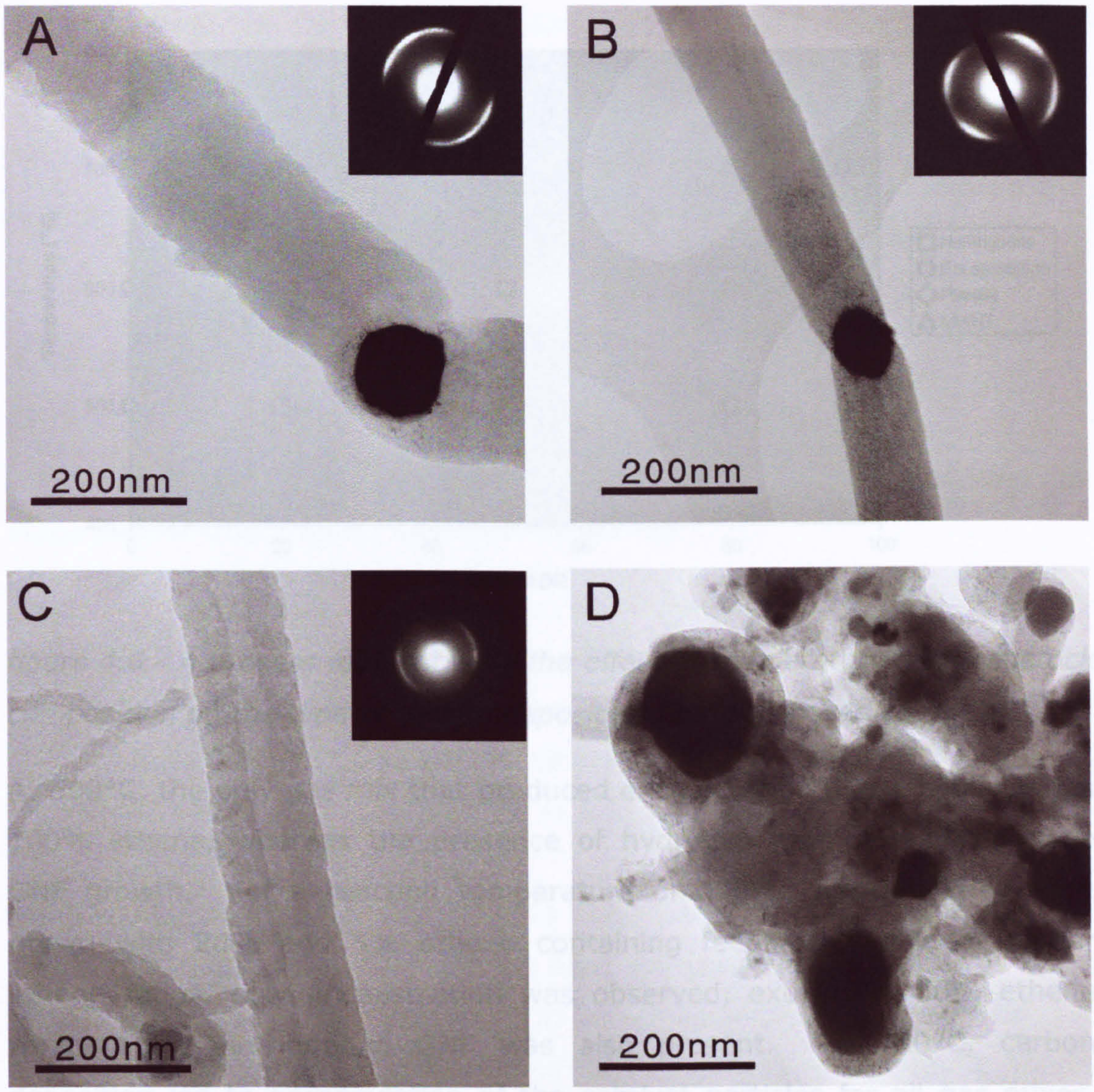

figure 4.5 - Example TEM micrographs of (a) platelet GNF (CNS-600-20), (b) herringbone GNF (CNS-500-20), (c) multi-walled CNT (CNS-700-20) and (d) encapsulated catalyst (CNS-600-100).

For each reaction temperature and gas mixture, the samples were analysed and the structure(s) observed. All samples showed a mixture of carbon phases, however for different reaction conditions, a different predominant phase of CNS was observed, as assessed through qualitative TEM characterisation, the predominate phase for each sample is summarised in figure 4.6.

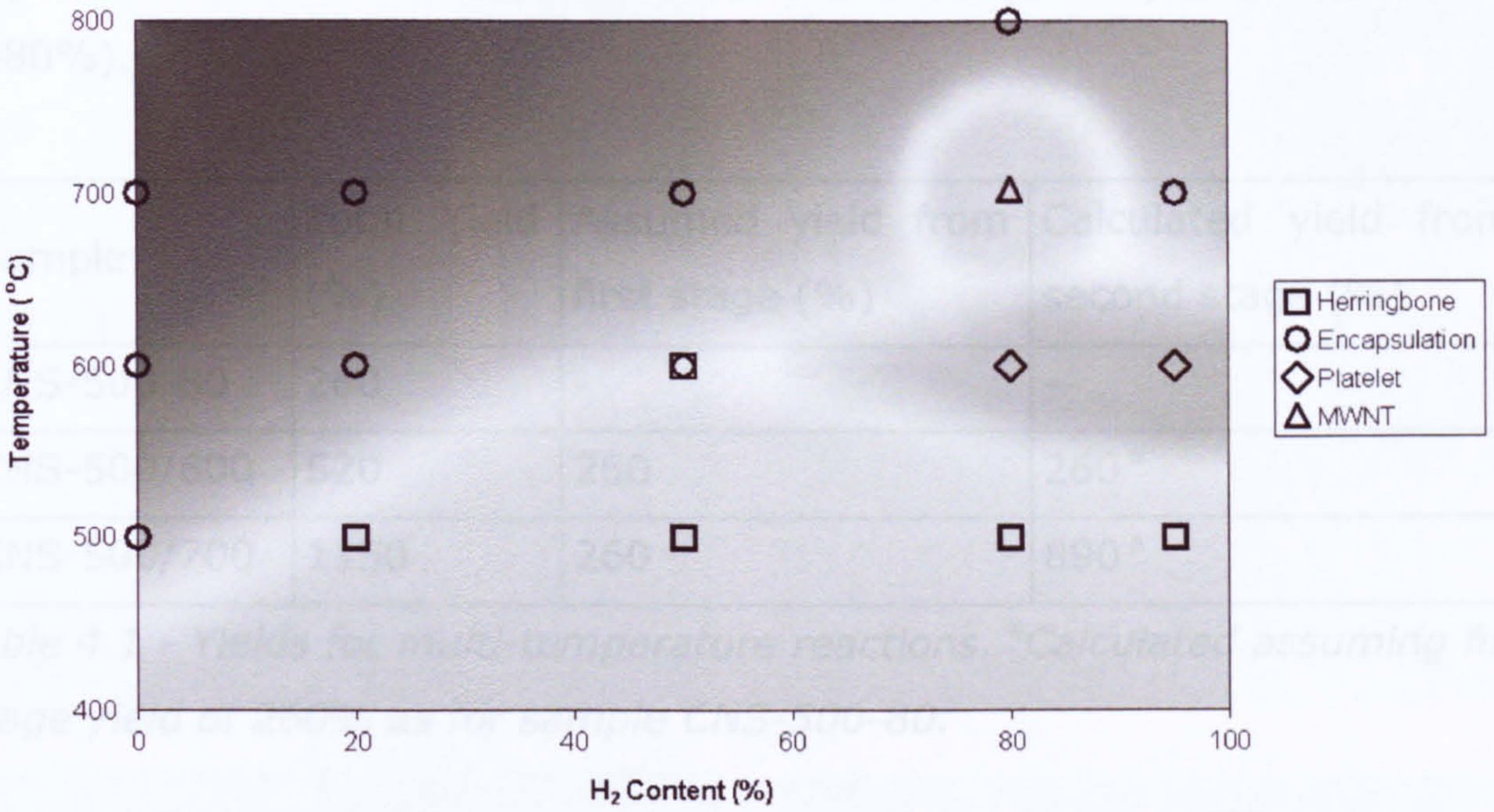

figure 4.6 - A process map showing the effect of temperature and feedstock composition on the type of carbon deposited over iron-based catalysts.

At 500°C, the only gas mix that produced encapsulation of the catalyst was 100% ethene, whereas the presence of hydrogen promoted herringbone GNF growth. For a reaction temperature of 600°C, platelet GNFs were grown with 20% and 5% ethene containing feedstock, while at higher ethene ratios, only encapsulation was observed, except for 50% ethene where some herringbone GNF was also present. At 700°C, carbon deposition led to encapsulation of the catalyst particles for all gas mixes, except for the 20% ethene content that formed poor quality MWNT (figure 4c). Little deposition was observed at 5% ethene and this was encapsulated. For this gas mix, CVD at 800°C was undertaken to see if encapsulation resulted at higher temperature, which was found to be the case, figure 4.6.

4.3.4 Multi-temperature Reactions

The reaction yields for the two sets of multi-temperature CVD reactions (CNS-500/600 and CNS-500/700) given in table 4.1. Whereas the yield for CNS-500/600 (520%) is comparable to the combination of yields in samples CNS-500-80 (260%) and CNS-600-80 (255%). The yield for sample CNS-500/700 (1150%) is significantly higher than the yield that would be

expected from the combination of CNS-500-80 (260%) and CNS-700-80 (480%).

Sample	Total Yield (%)	Assumed yield from first stage (%)	Calculated yield from second stage (%)
CNS-500-80	260	-	-
CNS-500/600	520	260	260 [a]
CNS-500/700	1150	260	890 [a]

table 4.1 - Yields for multi-temperature reactions. [a]Calculated assuming first stage yield of 260% as for sample CNS-500-80.

Figure 4.7 shows both low resolution and high-resolution TEM images for CNS-500-20 and CNS-500/700 (similar TEM images were collected for CNS-500/600). The nanofibres in both samples are observed to be herringbone GNF, as indicated by the inserted SAD image, with CNS-500/700 producing broader SAD arcs than CNS-500-20, as indicated in figure 4.7.

No trace of platelet GNFs or MWNTs were detected in CNS-500/600 and CNS-500/700 as would be expected from the carbon nanostructures found for samples CNS-600-20 and CNS-700-20. However, careful examination of the lattice fringes of the CNS-500/700 nanofibres illustrates a subtle difference from CNS-500-20; the graphene planes appear to re-orientate at the edges of the nanofibre, becoming more parallel with the fibre axis over a distance of between 5-7 nm from the GNF edge. The CNS-500-20 sample showed little (up to 2 nm) or no edge re-orientation. CNS-500/600 and CNS-500/700 also appeared to have broader SAD arcs compared to those observed for CNS-500-20.

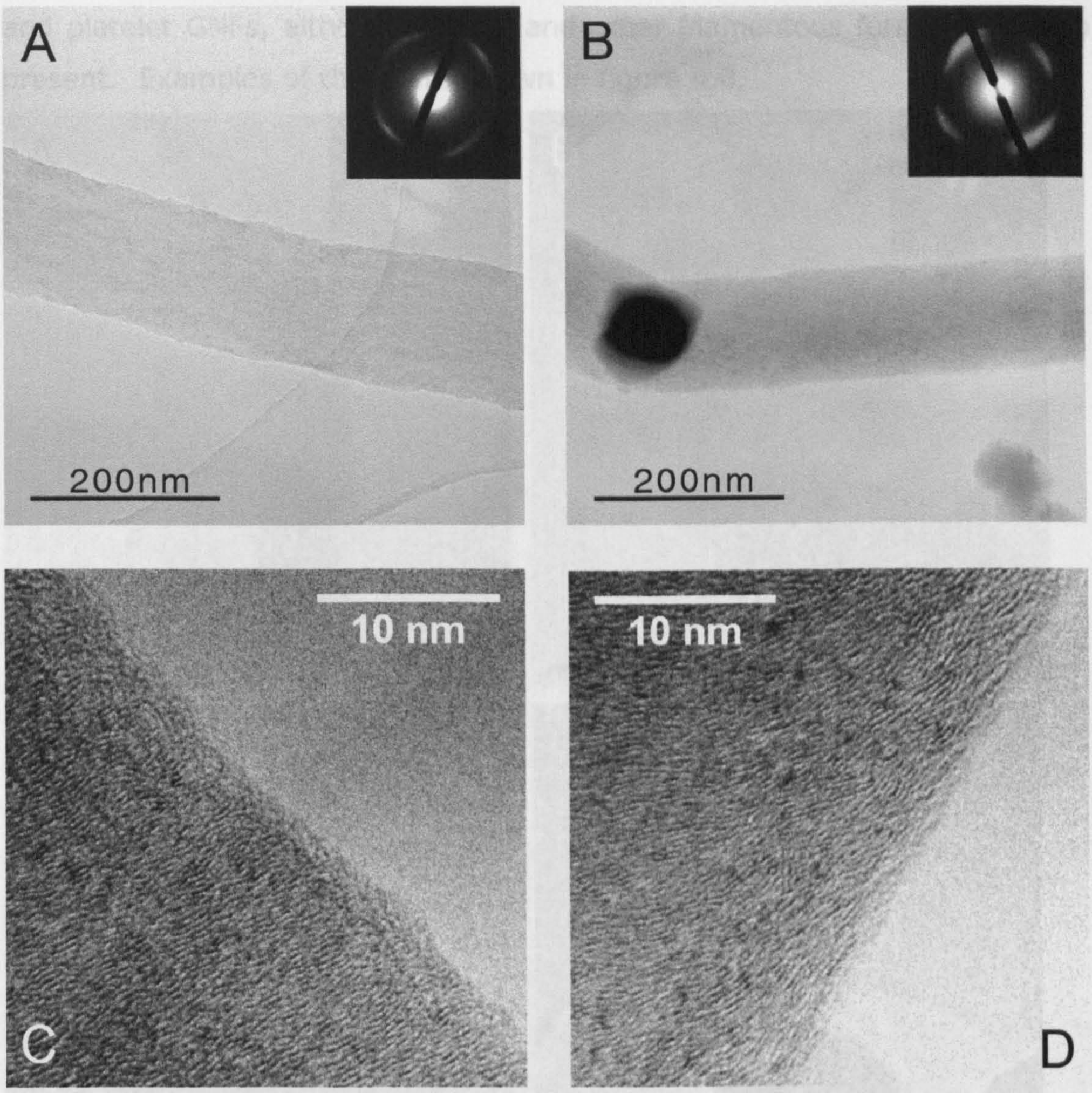

figure 4.7 - TEM images (A and B) with high-resolution TEM images (C and D)[‡]. A and C are for sample CNS-500-20. B and D are for the multi-temperature reaction sample CNS-500/700.

4.3.5 Ni-Catalyst System

GNFs samples synthesised with Ni-based catalyst only performed under a single set of reaction conditions; 80/20 gas mix (C_2H_4/H_2), for 2 h at 500°C. Approximately 5 g of carbon would be synthesised using these conditions (from 0.05 g catalyst) representing a carbon yield of approximately ~10,000%. Samples predominately contained a mixture of herringbone

[‡] High Resolution TEM images were acquired by Dr Mike Fay

and platelet GNFs, although MWNT and other filamentous forms were also present. Examples of these are shown in figure 4.8.

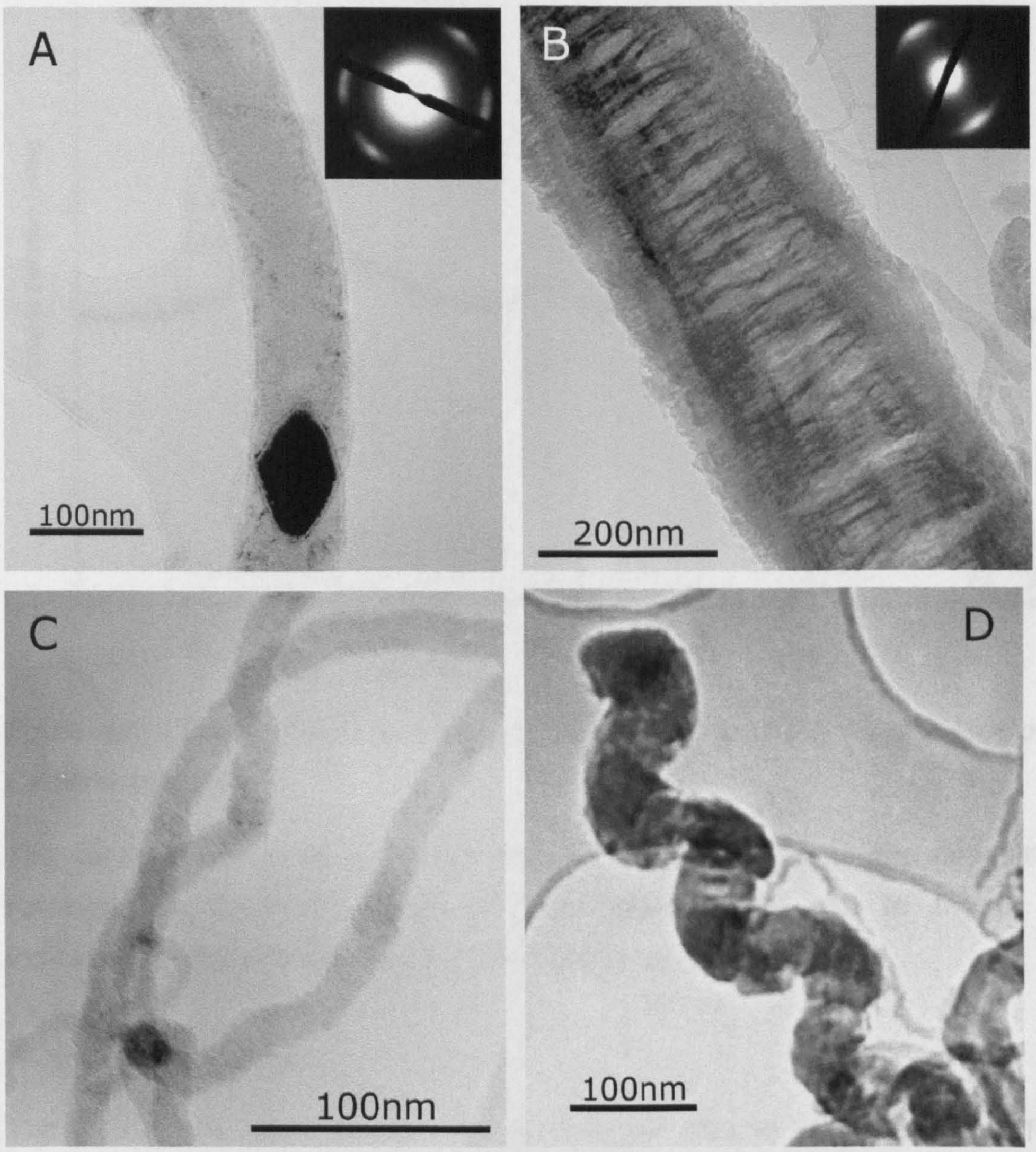

figure 4.8 - Ni-Catalyst synthesised filaments; (A) Herringbone GNF, (B) Platelet GNF, (C) MWNT and (D) Zig-Zag type filament

The XRD of the catalyst precursor and resulting carbon sample is shown in figure 4.9.

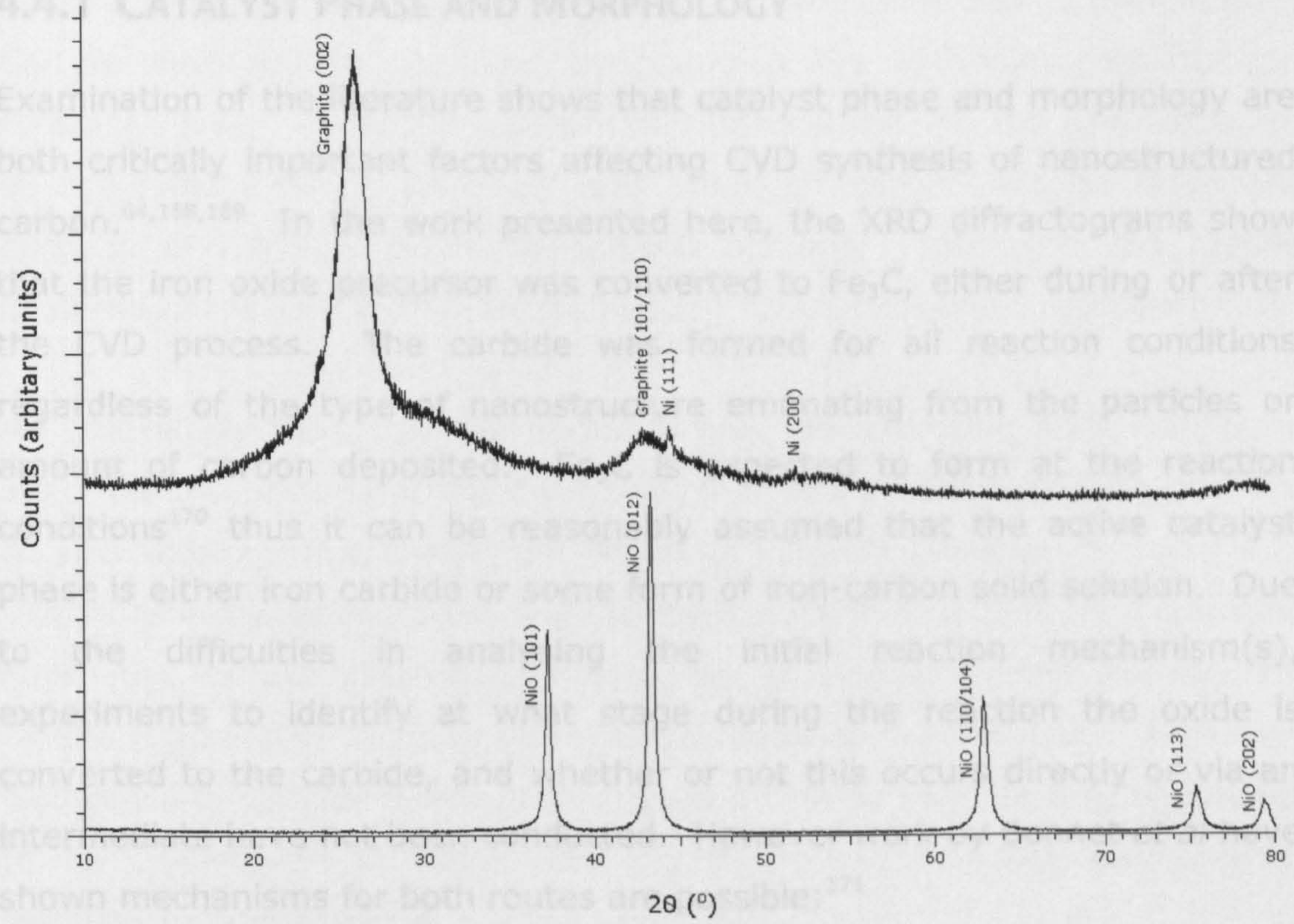

figure 4.9 - XRD diffractogram of (top) Ni-catalyst grown GNF, and (bottom) Catalyst precursor

The catalyst precursor has been indexed to NiO. During the deposition reaction the catalyst appears to have transformed into Ni metal, as indicated by the indexed peaks in the carbon deposited sample.

4.4 Discussion

The aim of the work detailed in this chapter was to identify what affect processing parameters of gas mix and temperature have upon the type and amount of carbon deposited. This includes investigation into the effect of altering the processing conditions during the CVD process. This detailed work has only been undertaken with the Fe-based catalyst, therefore the bulk of the discussion pertains only to the Fe-system and as such when no metal is mentioned in reference to a catalyst, it is referring to the Fe-catalyst. The Ni-system is briefly discussed and compared to the Fe-system at the end of the discussion.

4.4.1 Catalyst Phase and Morphology

Examination of the literature shows that catalyst phase and morphology are both critically important factors affecting CVD synthesis of nanostructured carbon.[64,168,169] In the work presented here, the XRD diffractograms show that the iron oxide precursor was converted to Fe_3C, either during or after the CVD process. The carbide was formed for all reaction conditions regardless of the type of nanostructure emanating from the particles or amount of carbon deposited. Fe_3C is expected to form at the reaction conditions[170] thus it can be reasonably assumed that the active catalyst phase is either iron carbide or some form of iron-carbon solid solution. Due to the difficulties in analysing the initial reaction mechanism(s), experiments to identify at what stage during the reaction the oxide is converted to the carbide, and whether or not this occurs directly or via an intermediate have not been conducted. However work by Bonnet *et al* have shown mechanisms for both routes are possible:[171]

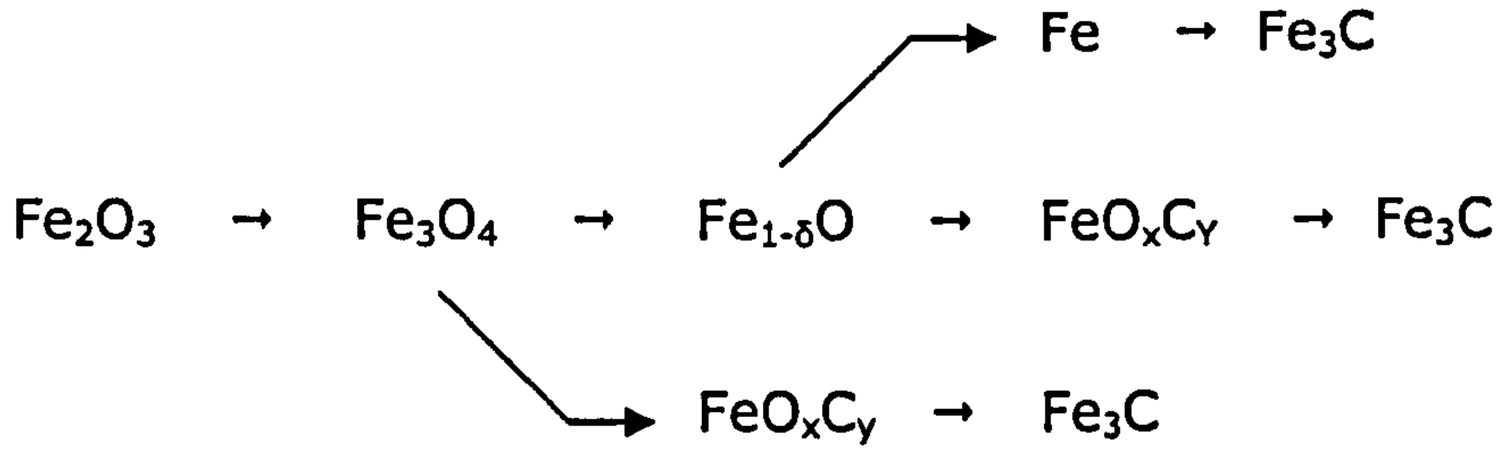

The mechanism (direct conversion or via an intermediate) becomes important when considering the catalyst particle morphology and initiation of carbon deposition, as the catalyst particle morphology will be determined by the surface free energy, which in turn will be affected by the catalyst phase.[43] This also leads to the possibility that the phase of the catalyst during carbon deposition initiation is different to that for the steady state carbon growth.

4.4.2 Influence of Hydrogen Concentration

Other research groups have increased hydrogen content in the feedstock gas to grow preferentially GNFs over CNTs.[73,74] They have proposed the presence of hydrogen acts to promote GNF growth by capping the end of the graphene layer, helping to passivate the edges. As can be seen from

figure 4.6, for the CVD reaction investigated here there was no change from CNT to GNF growth observed by changing the hydrogen content. In contrast, lower hydrogen content feedstocks led to the formation of encapsulated catalyst particles with shells of carbon around them (as opposed to CNTs or other filamentous carbon). Therefore, the results presented here do not offer strong support for this proposed mechanism.

An alternative theory to the above is that the changing CVD conditions affect the morphology of the catalyst particle and subsequent nanostructure. *In situ* studies have shown the shape of catalyst particles changes with variations in the temperature and gas environment.[63] This offers a plausible alternative to the passivation mechanism supported by the *ex-situ* TEM results (figure 4.5) showing characteristic catalyst morphologies. However, further work such as *in-situ* observations of the catalyst morphology needs to be undertaken to obtain the precise relationship between catalyst morphology and deposited carbon structure.

From the experimental data, the rate of carbon deposition increased with increasing hydrogen content (figure 4.2). This indicates that hydrogen plays an important role in the kinetics of the reaction and that the reaction rate is more sensitive to hydrogen partial pressure than the partial pressure of the hydrocarbon feedstock. This effect would appear to be relatively independent of the type of carbon formed (i.e. trends in figure 4.2 are obviously apparent in figure 4.6) and thus is more likely to be influencing one of the earlier mechanistic steps of the reaction. Some possible early mechanistic steps are shown in figure 4.10.

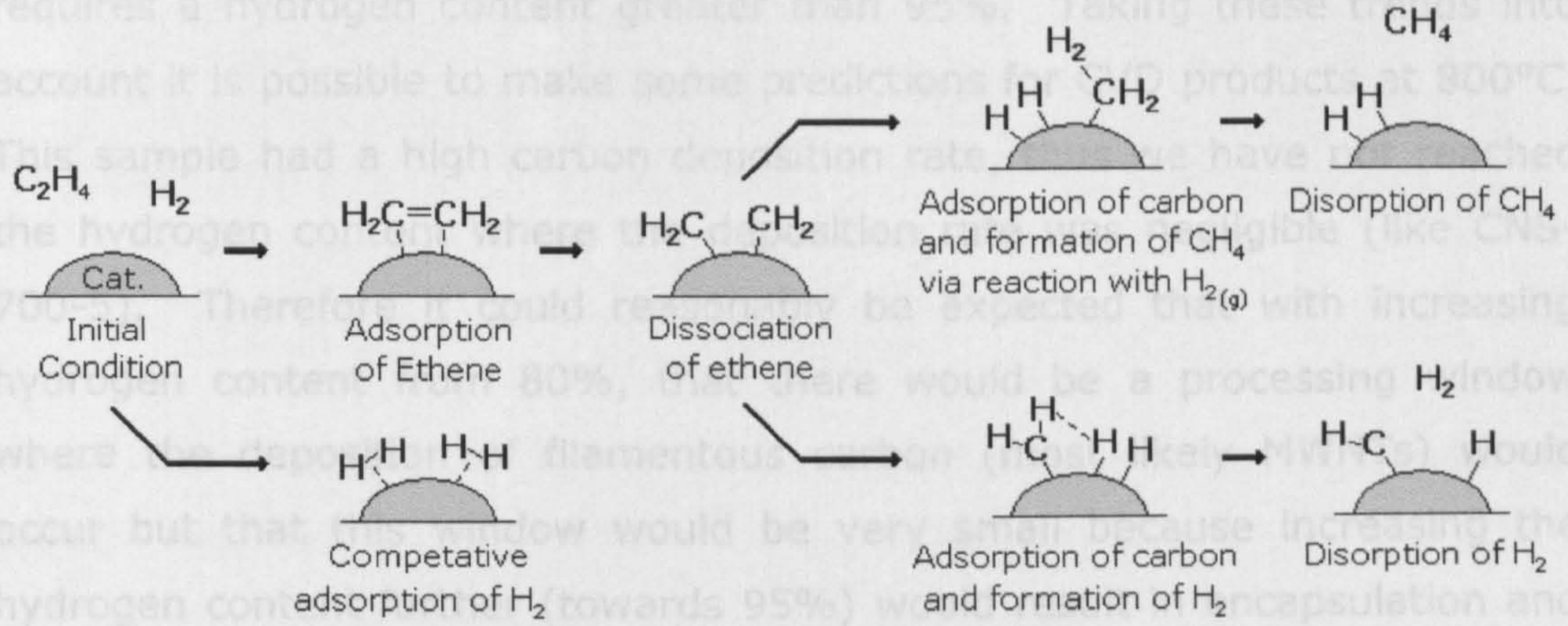

figure 4.10 – Some possible early mechanistic steps in the adsorption and dissociation of C_2H_4 and H_2 on the catalyst surface. Note: Bonds shown are representative rather than being specific.

The dissociative adsorption of the ethene and subsequent dissociation of hydrogen from the adsorbed alkyl moiety (leading to the formation of atomic carbon) is probably likely to be the stage at which the hydrogen partial pressure has the greatest influence. This effect is most likely due to the removal of carbon from the surface of the catalyst particles, via the formation of CH_4 (top mechanism in figure 4.10), as excess carbon formation will deactivate the catalyst particle, as intimated by Park *et al.*[43,172]

Hydrogen effect on encapsulation

An exception to the above trends is sample CNS-700-5 (figure 4.2). Initially a similar trend to that at 500 and 600°C was observed (figure 4.6) with the type of carbon deposited changing from encapsulation to filamentous (note: this transition occurred at higher hydrogen contents as the reaction temperature increased). However, increasing the hydrogen content further at 700°C, led to negligible carbon deposition in sample CNS-700-5. The phase of the catalyst after CVD was still iron carbide, like that of other reactions, which indicates that the reaction(s) of the iron oxide precursor still occurred, but under these conditions the subsequent carbon deposition reaction was severely hindered. This suggests that for the lower temperature CVD reactions there might also be a hydrogen content above which the carbon deposition reaction would become negligible but that

requires a hydrogen content greater than 95%. Taking these trends into account it is possible to make some predictions for CVD products at 800°C. This sample had a high carbon deposition rate, thus we have not reached the hydrogen content where the deposition rate was negligible (like CNS-700-5). Therefore it could reasonably be expected that with increasing hydrogen content from 80%, that there would be a processing window where the deposition of filamentous carbon (most likely MWNTs) would occur but that this window would be very small because increasing the hydrogen content further (towards 95%) would result in encapsulation and negligible carbon deposition.

4.4.3 Influence of Temperature

Liquid-like Growth

As can be seen in figure 4.2 increasing the amount of hydrogen in the gas mix results in a near linear increase in carbon deposition across all temperatures investigated. The growth rates were much higher for samples at 700°C compared to those at 500 and 600°C, which showed no significant difference. This is unexpected as most samples at 700°C are 'encapsulated' and thus should have no apparent route for continuous carbon deposition, unlike the filamentous growth predominately observed at the lower temperature synthesises that keeps some exposed catalyst surface(s). A potential rational for this increase deposition is that the catalyst particles have higher atomic mobility leading to pseudo liquid-like growth, as suggested by Teo et al.[43] Therefore, once carbon has encapsulated a catalyst particle, it is able to 'squeeze' out, leaving a shell/bulb of carbon, the catalyst is then free to become encapsulated once more and the cycle continues. *In situ* electron microscopy studies have observed similar behaviour in a nickel catalyst and methane gas synthesis, resulting in 'bamboo' filaments rather then graphitic bulbs as seen in this system, figure 4.11.[64]

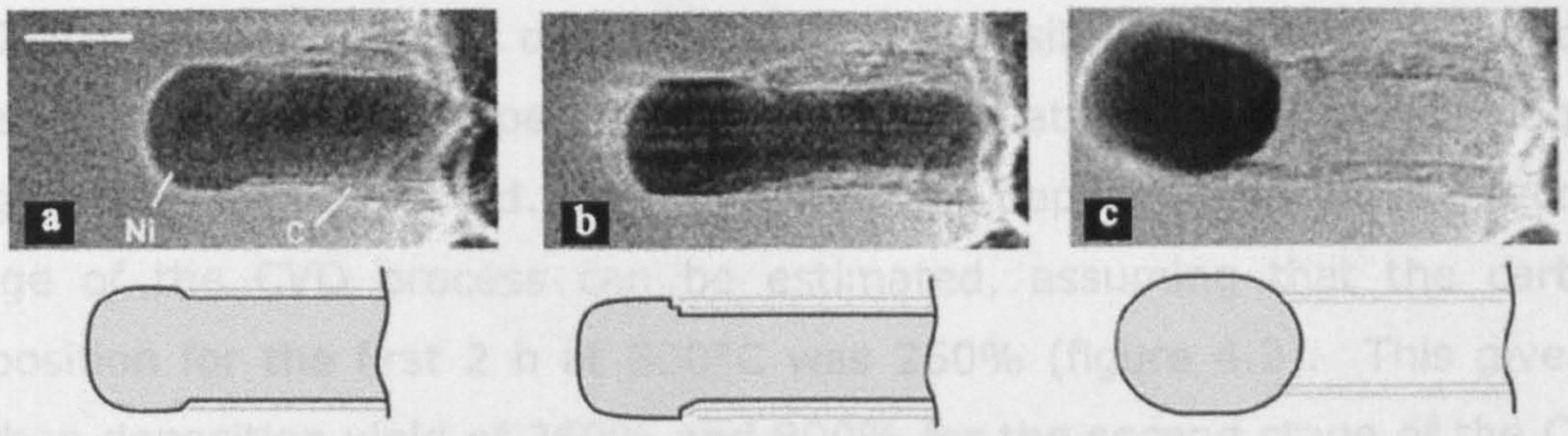

figure 4.11 – Stages of growth of a bamboo nano-filament via liquid-like growth mechanism.[64]

Catalyst Morphology and Constrained Growth

Figure 4.6 shows that the temperature of reaction has an important effect on the type of carbon deposited. For a given gas composition, the general trend is filamentous growth at lower temperatures and encapsulation for the higher temperatures. The most varied changes were identified for the gas mix of 20/80. For this composition, it was found that the carbon deposited changed from herringbone to platelet to MWNT to encapsulation. Comparing the TEM images for these structures (figure 4.5), we can see that the growth from a catalyst particle reflects the morphology/orientation of the graphene layers; diamond shape for herringbone, an oval shape for platelet and pear drop shape for MWNT, consistent with similar systems reported previously.[27] From these changes in catalyst morphology, it is reasonable to assume that the carbon structure that forms is dependent on the initial morphology of the catalyst. Therefore, these results would suggest, for the conditions investigated, temperature played a more important role than gas composition in determining the initial catalyst morphology and subsequent carbon growth.

It has been suggested that the catalyst morphology under different CVD conditions is a result of the nano-sized particle minimising its high surface energy.[43] If this is the only factor to influence catalyst morphology (and therefore the type of carbon formed), it should be possible to produce GNFs with changing structures going from herringbone to either platelet or MWNT depending on the start and end processing conditions. To investigate this, reactions were undertaken using a 20/80 gas mix, with an initial processing temperature of 500°C followed by a second processing stage at either 600

or 700°C. When this was done, the carbon deposited remained herringbone, even at the higher temperatures when the platelet/MWNT morphologies might have been expected. The rate of carbon deposition during the second stage of the CVD process can be estimated, assuming that the carbon deposition for the first 2 h at 500°C was 260% (figure 4.2). This gives a carbon deposition yield of 260% and 890% for the second stage of the CVD process at 600°C and 700°C respectively. Comparison of these yields, with those under comparable conditions shown in figure 4.2, shows that the second stage of processing at 600°C had a comparable rate to that for sample CNS-600-20 (which had a yield of 245%). Undertaking the second stage of processing at 700°C, the deposition rate was almost double that for CNS-700-20 (which had a yield of 480%).

These results show that the surface energy of the catalyst particle under given reaction conditions was not the only factor determining the type of carbon structure grown. It is still likely to be an important factor for the initial type of carbon grown, but these results would suggest that the deposited carbon helps to constrain the catalyst morphology, so that even if the reaction conditions change the carbon nanostructure deposited remains similar. Most Fe-catalyst particles have two GNFs growing from the same particle, which will help constrain the initial catalyst morphology, thereby making the system less susceptible to changes in the CVD conditions. For CVD systems where the catalyst particle is protruding from the end of a single carbon nanostructure (e.g. as is often found when using nickel catalysts[173]), the exposed catalyst facets are more likely to be able to change morphology and therefore maybe more susceptible to changes to the CVD conditions, figure 4.12.

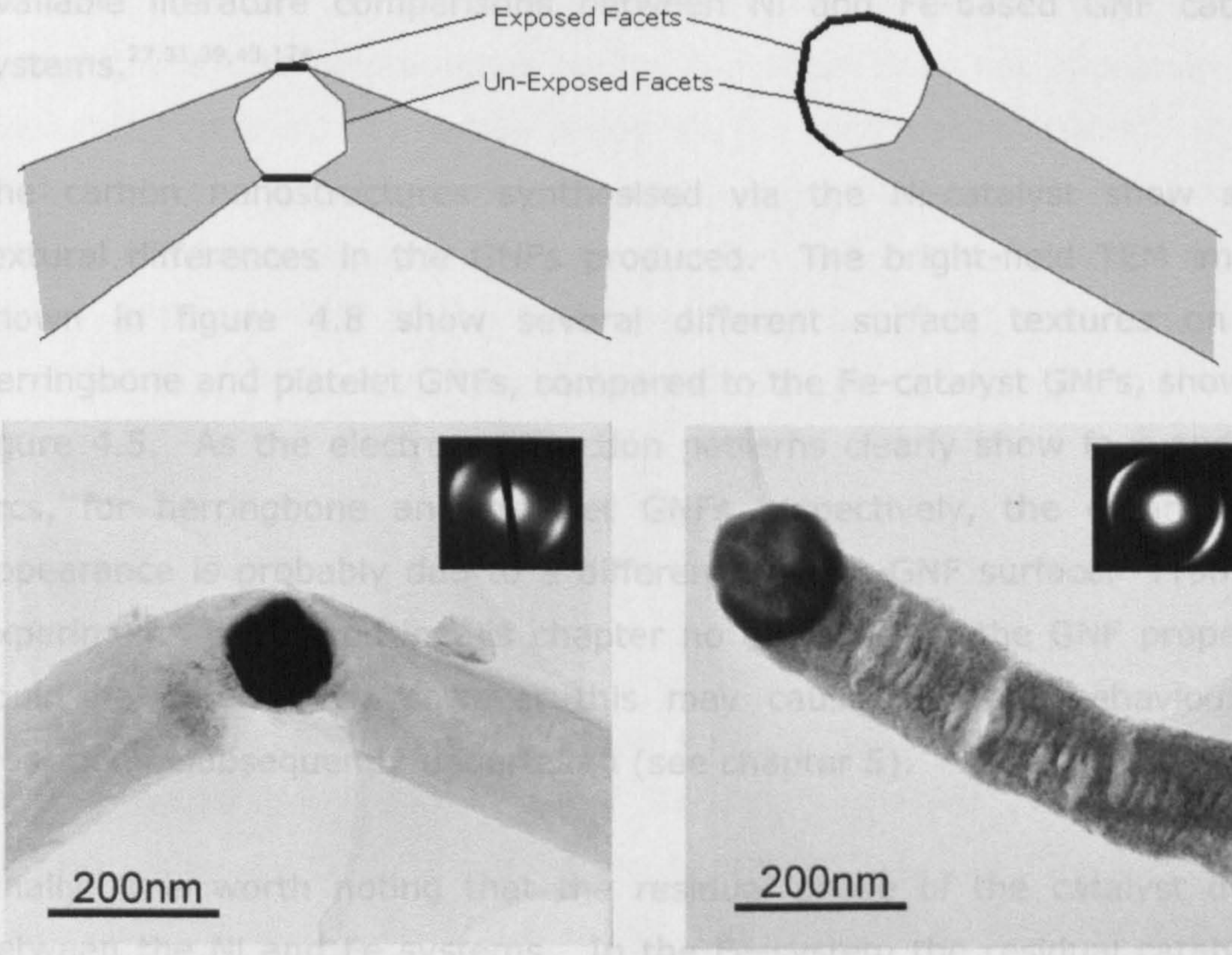

figure 4.12 – Schematic of exposed and un-exposed catalyst particle facets for platelet GNFs synthesised from (left) Fe catalyst and (right) Ni Catalyst.

This two-temperature synthesis method also provides a simple means by which to improve the efficiency of the CVD process (a 3-4 fold increase in the rate demonstrated at 700°C). However, it should be pointed out that this comes at the expense of a reduction in the quality of the herringbone GNFs formed, with both CNS-500/600 and CNS-500/700 showing more diffuse electron diffraction arcs (figure 4.7) and thus less crystalline structures.

4.4.4 Ni-catalyst

Whereas no specific experiments have been undertaken to identify how the reaction conditions of temperature and gas mix affect carbon growth using Ni-catalyst, there are important differences in behaviour between the Ni and Fe systems. The most obvious is the substantial difference in carbon yields, with Ni yielding ~10,000% at 500°C compared to Fe yielding between 80-350% (depending on gas composition). This result is consistent with the

available literature comparisons between Ni and Fe-based GNF catalyst systems.[27,31,39,43,174]

The carbon nanostructures synthesised via the Ni-catalyst show some textural differences in the GNFs produced. The bright-field TEM images shown in figure 4.8 show several different surface textures on the herringbone and platelet GNFs, compared to the Fe-catalyst GNFs, shown in figure 4.5. As the electron diffraction patterns clearly show four and two arcs, for herringbone and platelet GNFs respectively, the difference in appearance is probably due to a difference in the GNF surface. From the experiments conducted in this chapter no difference is the GNF properties could be determined, however this may cause different behaviour for treatments subsequently undertaken (see chapter 5).

Finally, it is worth noting that the residual phase of the catalyst differs between the Ni and Fe systems. In the Fe-system the residual catalyst is present as Fe_3C (figure 4.3 and figure 4.4), whereas with the Ni-system the residual catalyst is present as Ni metal (figure 4.9). Examination of the respective phase diagrams shows that C is readily soluble in Fe, with Fe_3C being the preferred state from the Fe-C phase diagram[170], whereas there is no solubility of C in the Ni-C phase diagram.[175] Thus the phases observed (Fe_3C and Ni) should be expected due to the greater solubility of C into the Fe than Ni.

4.5 Conclusions

In the growth of filamentous carbon, it has been shown that careful control of temperature and gas environment is important in achieving a specifically desired product. The alteration of either or both of these variables will cause a significant change in the type and amount of carbon recovered. The role of hydrogen in this specific catalytic system is very important as it generally encourages the growth of filamentous carbon as opposed to random nano-sized shells of graphite encapsulating catalyst metal particles.

The type of carbon deposited is affected by the initial CVD conditions, but changing the CVD environment during deposition does not appear to alter the fundamental type of carbon deposited (i.e. Herringbone GNFs). It does alter the rate of deposition and presents a convenient route to increase the amount of carbon deposited, providing a 3-4 fold increase in carbon yield. However, the surface of the GNFs can become altered, under going re-construction, which can be detrimental to properties of the carbon recovered.

4.6 Summary

Fe-Catalyst system

The results presented in this chapter have shown the importance of the initial CVD conditions in synthesis of GNFs. Figure 4.6 illustrated the range of processing conditions that gave rise to the formation of different types of carbon structures. Increasing the deposition rate for a given nanostructure can be achieved, by initiating growth of a desired nanostructure and then increasing the temperature to increase the growth rate, although the surfaces of the GNFs maybe detrimentally affected.

Owing to the (relative) purity of the GNFs synthesised using the Fe-based catalyst, the selected reaction conditions that will be used for subsequent investigation is:

500°C, 20/80 (C_2H_4/H_2), 6 hrs to produced Herringbone GNFs

In order to increase the yield of carbon, 0.25 g of the Fe_2O_3 precursor was used to prepare the GNFs, typically producing ~1 g of carbon per run. Nomenclature for these GNFs in following chapters will be Fe-GNF-x, where x refers to subsequent treatments.

Ni-Catalyst System

Ni-catalyst grown GNFs will be investigated in subsequent chapters, and are synthesised using the reaction conditions:

500°C, 80/20 (C_2H_4/H_2), 0.05 g, 2 hrs to produced Herringbone GNFs

Nomenclature for these GNFs in the following chapters will be Ni-GNF-x, where x refers to subsequent treatments.

5 Catalyst Removal and CO_2 Oxidation

5.1 Aim

This chapter will detail the investigation into removal of residual CVD catalyst from the as-prepared Ni-GNF and Fe-GNF, described in Chapter 4. This has been achieved using a combination of post synthesis acid and heat treatments. The surface of as synthesised GNFs (figure 4.7) exhibit defects such as carbon caps, re-oriented and amorphous carbon, due to surface re-arrangement to minimise surface energy. However, this surface layer represents a large energy barrier to hydrogen being able to access the internal surface area of GNFs. Therefore, removing this surface layer should be beneficial for hydrogen storage in GNFs. The removal of surface carbon can be achieved using CO_2 oxidation, shown schematically in figure 5.1. From HR-TEM data (figure 5.4), removing around ~5 nm of GNF surface should ensure that any surface defects are removed, leaving a cleaned GNF surface.

In order to be able to carefully control the oxidation rate, CO_2 was chosen because it has a relatively large (compared to other oxidising gases) activation energy, thus allowing the precise removal of the small amount (~5 nm) of dis-ordered surface carbon in the GNFs. The use of CO_2 to oxidise graphitic materials is a common process and much previous work has been performed to understand the precise physical mechanism(s) of the process.[176-178] Several authors have investigated the oxidation for GNFs, often observing differences in oxidation properties compared to other graphite morphologies (e.g. PAN fibres, bulk graphite, etc).[179-182] From this work, it has been shown that the presence of transition metals, Ni, Co and Fe, (often residual after CVD growth) act as catalysts for CO_2 oxidation of GNFs and other forms of filamentous carbon. However, the precise effect of the oxidation process on GNF morphology and surfaces has not been fully investigated.[179,183-185] Given that residual catalyst can also act as oxidation

catalyst, it is very important to ensure all CVD catalyst residues are removed from the samples, in order to avoid any complications in the interpretation of possible CO_2 oxidation mechanisms.

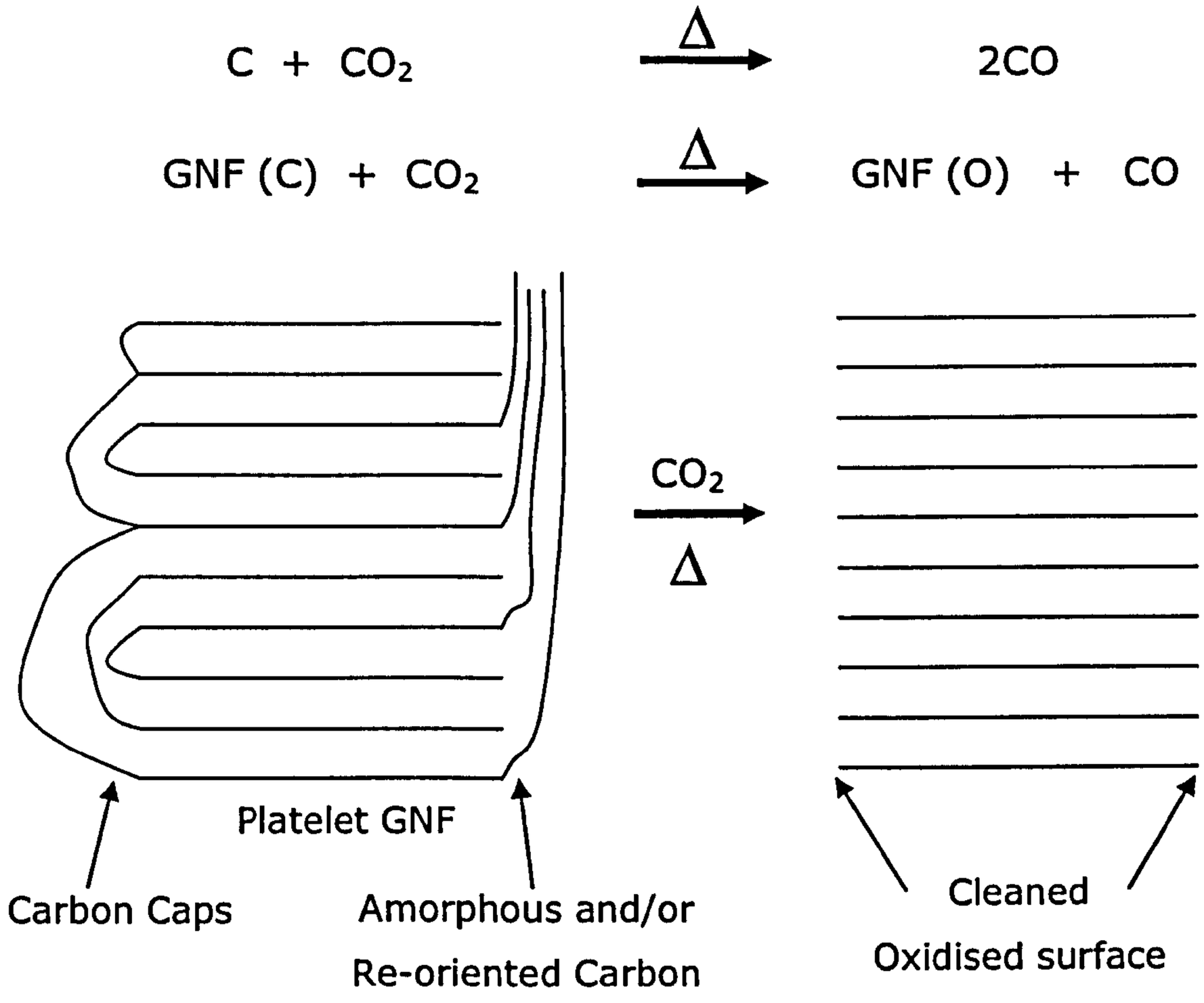

figure 5.1 - Schematic of CO_2 treatment of GNFs, (top) chemical reaction(s) (bottom) effect on platelet GNF.

This chapter will detail the investigation into how Ni-GNFs, Fe-GNFs, Maxsorb (an activated carbon) and carbon black oxidise in a CO_2 environment. The investigation focuses on how the different types of carbon structures affect both the reaction onset temperature and subsequent mass loss (which is also known as the degree of burn off[180,181]). The effectiveness of the applied acid and heat treatments at removing residual catalyst particles is also assessed. Special attention was given to the oxidation behaviour of the GNFs after each process, with a detailed study of any surface and dimension changes in the GNFs.

Some of the work presented here was undertaken in conjunction with Dr Neil Bowering, who has been acknowledged where relevant data he

collected has been presented. Furthermore, this work was presented at 'Carbon' conference (2006), a copy of which is presented in Appendix B.

5.2 Experimental

5.2.1 Carbon Materials

Details of different carbon samples under investigation are given below, table 5.1 .

Type of Carbon	**Description**	**Nomenclature**
Carbon Black	Amorphous particulate carbon	CB
Maxsorb	High surface area activated carbon	Max
Ni catalysed GNFs	GNF synthesised via NiO catalyst – Herringbone and Platelet fibres	Ni-GNF
Fe catalysed GNFs	GNF synthesised via Fe_2O_3 catalyst – Herringbone fibres	Fe-GNF

table 5.1 - Four different types of carbon materials investigated

The carbon black (CB) and Maxsorb (Max) were used as received (Degussa and Kansai Coke and Chemicals, respectively) and are used as graphitic carbon references.

The GNFs were synthesised using the optimised preparation detailed in chapter 4. Briefly, Ni-catalyst GNFs were synthesised at 500°C from C_2H_4 and H_2 flowing at 80 and 20 cm^3 min^{-1}, respectively, for 2 hours using 0.05 g of NiO catalyst precursor. Fe-catalysed GNFs were synthesised at 500°C from C_2H_4 and H_2 flowing at 20 and 80 cm^3 min^{-1}, respectively, for 6 hours using 0.2 g of Fe_2O_3 precursor.

In order to remove residual catalyst particles from the GNF samples an acid treatment was applied; samples were mixed with 2M nitric acid solution and stirred overnight (~16 h), then filtered and washed with water. Samples were then heated in an induction furnace at 1,500°C for 30 min under an Ar environment. A second acid wash was then applied to the GNF samples. Table 5.2 summaries the chemical and heat treatments applied to the GNFs,

including the short hand nomenclature used to subsequently describe samples.

Treatment	**Description**	**Ni-Catalyst Grown GNFs**	**Fe-Catalyst Grown GNFs**
-	As-prepared (AP) GNFs	Ni-GNF-AP	Fe-GNF-AP
Acid Wash 1	Nitric acid wash (AW) applied to the –AP GNFs	Ni-GNF-AW	Fe-GNF-AW
Heat Treatment	Heat treatment (HT) to 1500°C applied to -AW GNF samples	Ni-GNF-HT	Fe-GNF-HT
Acid Wash 2	Nitric acid wash applied to –HT GNF samples	Ni-GNF-HT-AW	Fe-GNF-HT-AW

table 5.2 - Summary of chemical and thermal treatments applied to GNF samples and sample nomenclature.

5.2.2 CO_2 Treatment

The CO_2 treatment was performed in a thermogravimetric analyser (TGA) (SDT Q600 – TA Instruments) fitted with a mass spectrometer (Hidden Analytical) to analyse the exhaust gases. Between 10-20 mg of sample were used for each experimental run. The sample chamber was purged for 30 min with a 100 cm^3 min^{-1} flow of CO_2 and then ramped at 20°C min^{-1} from room temperature to 1,000°C. Mass spectrum data were collected for m/z values 44 and 28, corresponding to CO_2 and CO respectively, mass 32 was also monitored to ensure that no atmospheric O_2 was present in the system.

GNF samples were only ever CO_2 treated once, with new samples being prepared to allow CO_2 treatment at different stages of post-treatment. Samples that have been CO_2 treated are referred to with $-CO_2$ to indicate the treatment was applied (e.g. Fe-GNF-AP-CO_2, Ni-GNF-HT-AW-CO_2, etc).

5.2.3 Characterisation

All samples were characterised using the following methods, described in detail in Chapter 3; TEM, XRD and TGA-MS.

Further to the standard characterisation techniques, GNF diameters were analysed using TEM. This was done statistically by measuring at least 70 random GNF diameters, to the nearest nm, and then calculating the mean diameter value. Filaments below 50nm were ignored as they are assumed to be SWNT or MWNT (section 4.4).

5.3 Results

The results of the experiments are presented with characterisation data first (5.3.1 TEM and 5.3.2 XRD), followed by TGA data, separated into 3 sections (5.3.4 Comparison of Carbons, 5.3.5 Ni-GNFs and 5.3.6 Fe-GNFs), followed by 5.3.7 GNF Diameters.

5.3.1 TEM

Figure 5.2 shows example GNF structures observed. The Ni-GNF samples showed a mixture of predominately platelet and herringbone type GNFs, with a small fraction of other filaments carbon such as zigzag, multi-walled nanotubes. The Fe-GNFs samples contained herringbone GNFs, with a small fraction of other types of carbon.

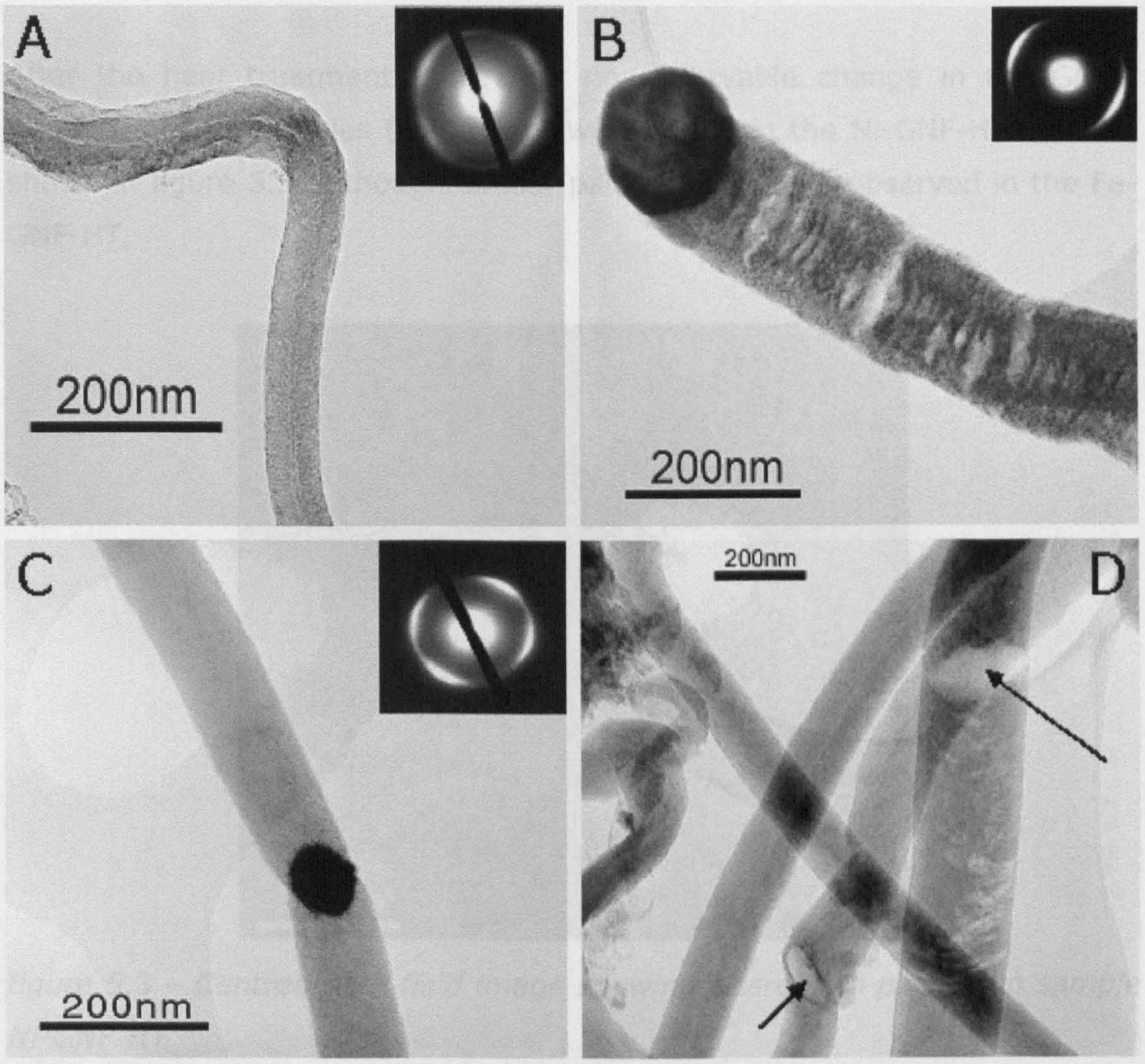

figure 5.2 – TEM images of GNF samples (A) Herringbone fibre in Ni-GNF-AP (B) Platelet fibre in Ni-GNF-AP (C) Herringbone fibre in Fe-GNF-AP and (D) several GNFs from Fe-GNF-AW.

After the first acid wash had been applied, only a very small number of catalyst particles could be observed in either the Ni-GNFs or Fe-GNFs. In the Fe-GNFs, there was evidence of catalyst particle removal where two GNFs had grown from a single particle, as indicated by the arrows in figure 5.2d.

Furthermore, the only catalyst particles observed in the acid washed samples were found in the centre of large areas of carbon, where the catalyst was encapsulated. The presence of catalyst was only confirmed by the presence of Ni or Fe in the energy dispersive X-ray analysis (EDX) rather than by indexed spots in the SAED images.

After the heat treatment there was no observable change in the GNFs. Some larger Ni-particles (>200 nm) were found in the Ni-GNF-HT sample, shown in figure 5.3, although similar particles were not observed in the Fe-GNF-HT.

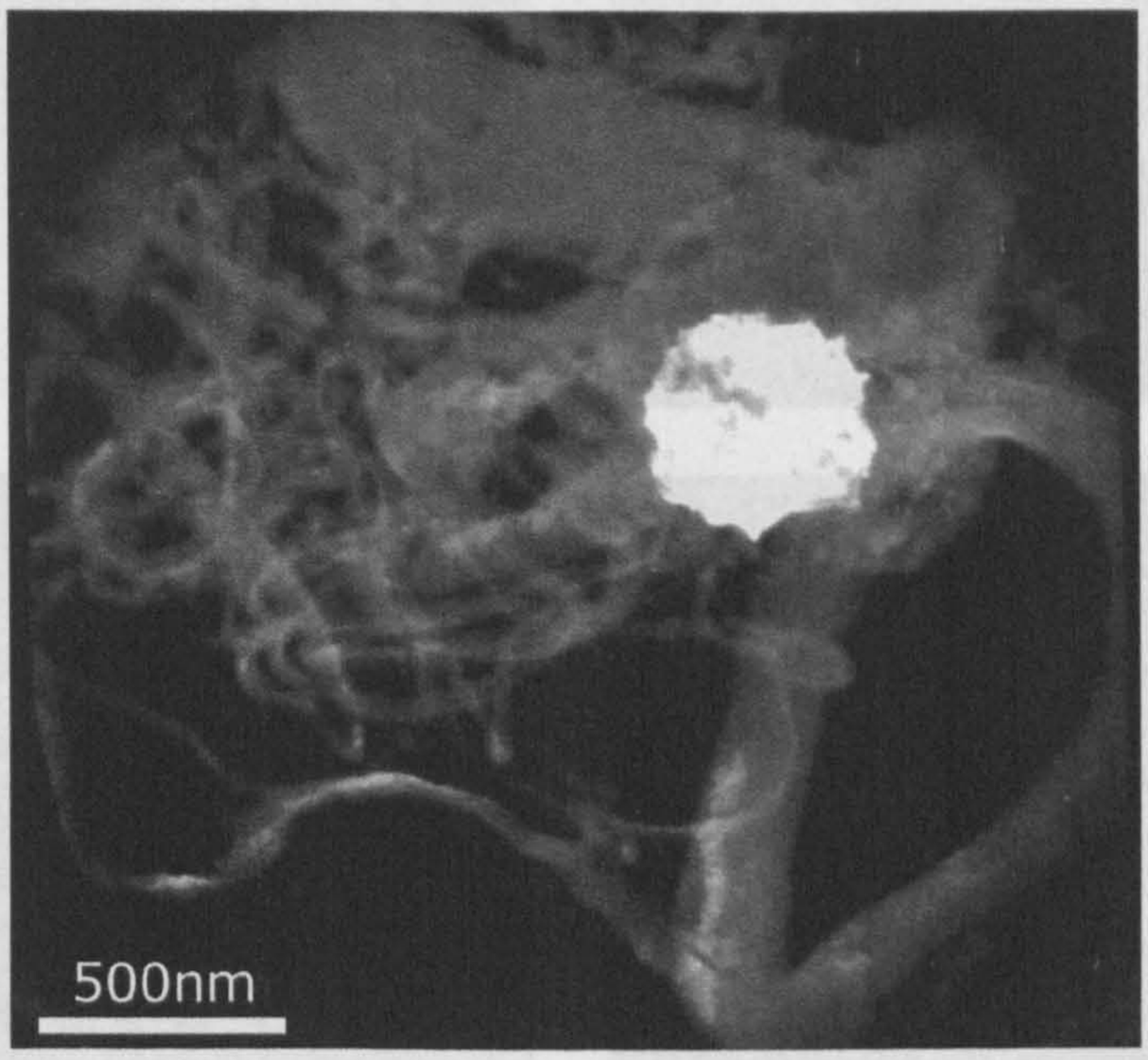

*figure 5.3 – Centred dark field image showing a larger Ni particle in sample Ni-GNF-HT**

After the second acid wash had been applied, no catalyst particles could be observed in the TEM in either the Ni-GNF or Fe-GNF samples.

* TEM image courtesy of Neil Bowering

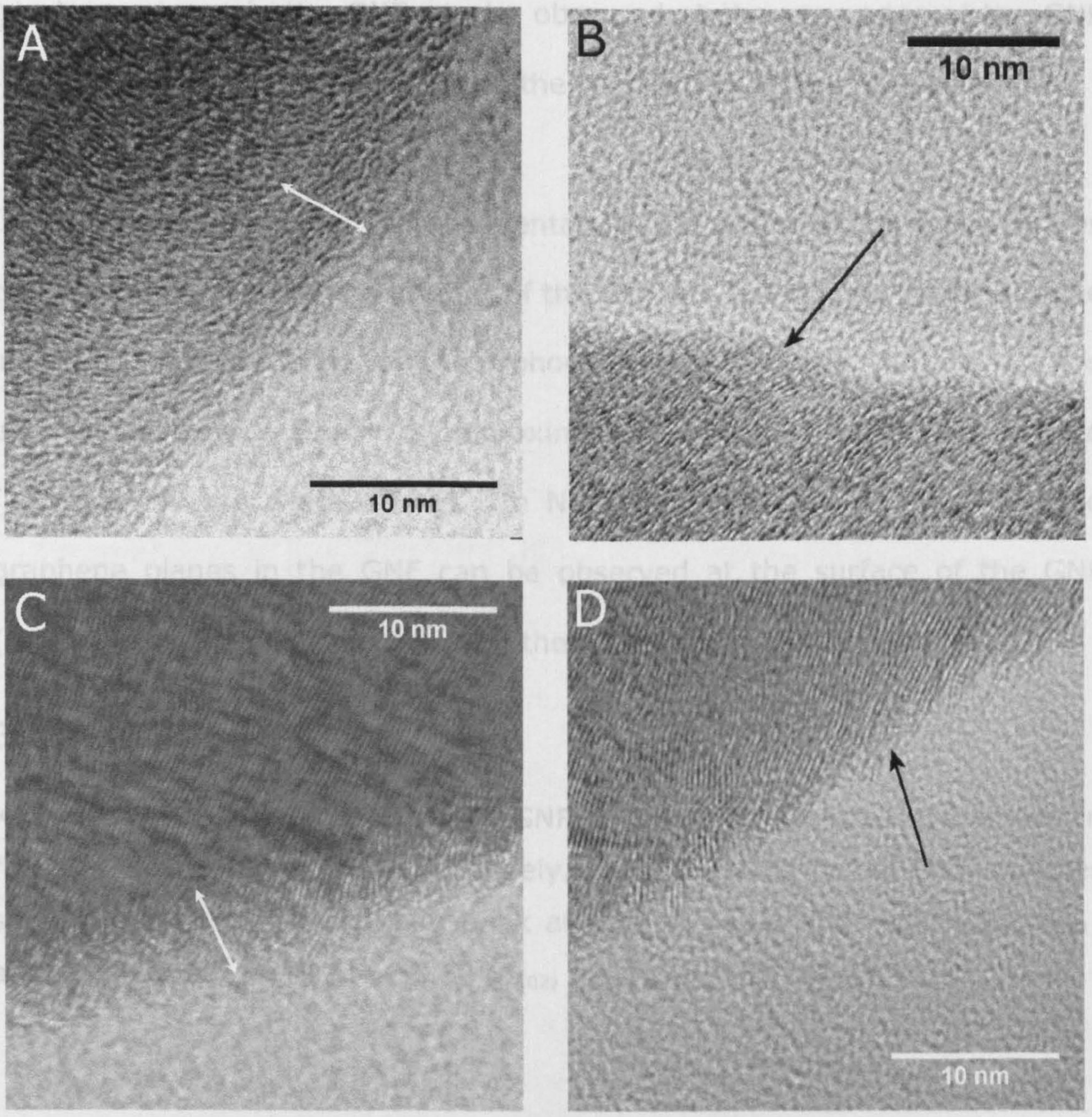

figure 5.4 – HR-TEM [§] of (A) Fe-GNF-AP (B) Fe-GNF-HT-AW-CO_2 (C) Ni-GNF-AP and (D) Ni-GNF-HT-AW-CO_2.

Figure 5.4 shows HR-TEM images of -AP and –HT-AW-CO_2. In the Fe-GNFs, the graphene planes in the –AP state have re-oriented from being at an angle (~30°) to the fibre axis to being parallel. The re-orientation of the graphene fringes start to occur approximately 5 nm from the GNF surface (shown by the white arrow). After the oxidation has been performed, the

[§] High Resolution TEM images were acquired by Mike Fay

graphene planes in the GNF can be observed at the very edge of the GNF (indicated by the black arrow), with the re-oriented planes removed.

In the Ni-GNF-AP, rather than reorientation, the well ordered lattice fringes that are present within the interior of the GNF are not present at the surface, indicating less ordered or amorphous carbon at the surface. This amorphous surface region is approximately 5 nm from the GNF surface (indicated by the white arrow). In Ni-GNF-HT-AW-CO_2, the well ordered graphene planes in the GNF can be observed at the surface of the GNF (indicated by the black arrow), with the amorphous carbon removed.

5.3.2 XRD

XRD diffraction patterns of the Ni-GNF and Fe-GNF samples are shown in figure 5.5 and figure 5.6, respectively. XRD patterns for all GNF samples show the characteristic carbon peak at ~26.5° (d_{002}) and ~43° (d_{100}, d_{101}) and less intense peaks at ~53.5° (d_{102}, d_{004}) and ~78° (d_{110}).

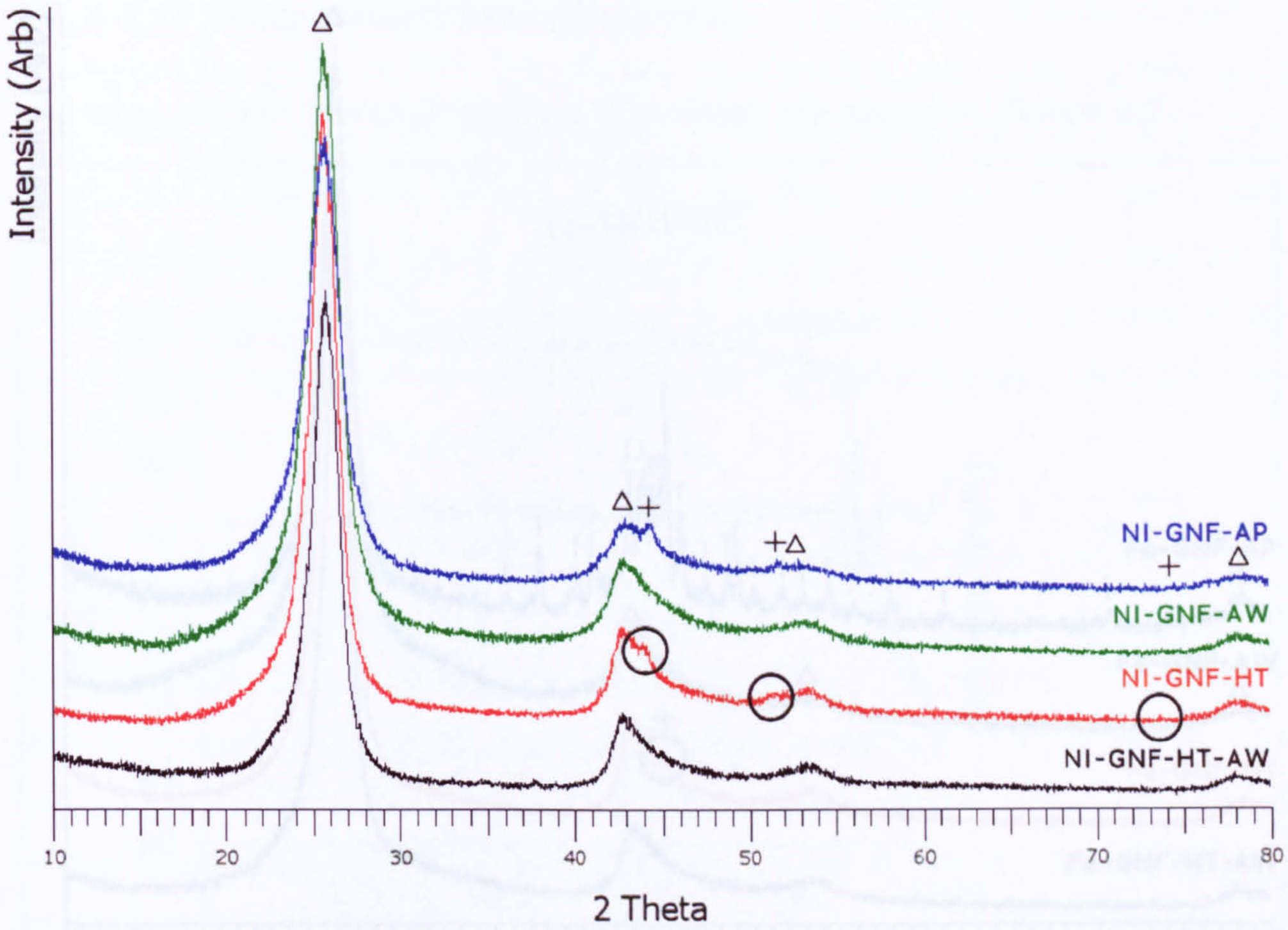

figure 5.5 - XRD for Ni-GNF samples. Symbols are indexed to phases; Δ to GNF and + to Ni metal.

For the Ni-GNFs, figure 5.5, there is a peak at ~44° and a smaller peak at ~52° in Ni-GNF-AP. These coincide with the d_{111} and d_{200} reflections for Ni metal, respectively. These peaks were not present after the first acid wash (Ni-GNF-AW). The peaks then re-appeared after heat-treatment had been applied (Ni-GNF-HT), albeit with lower relative intensities, as well as a third peak corresponding to Ni metal (d_{220}), circled in figure 5.5. After the second acid wash (Ni-GNF-HT-AW), these peaks were not observed in the XRD diffractogram.

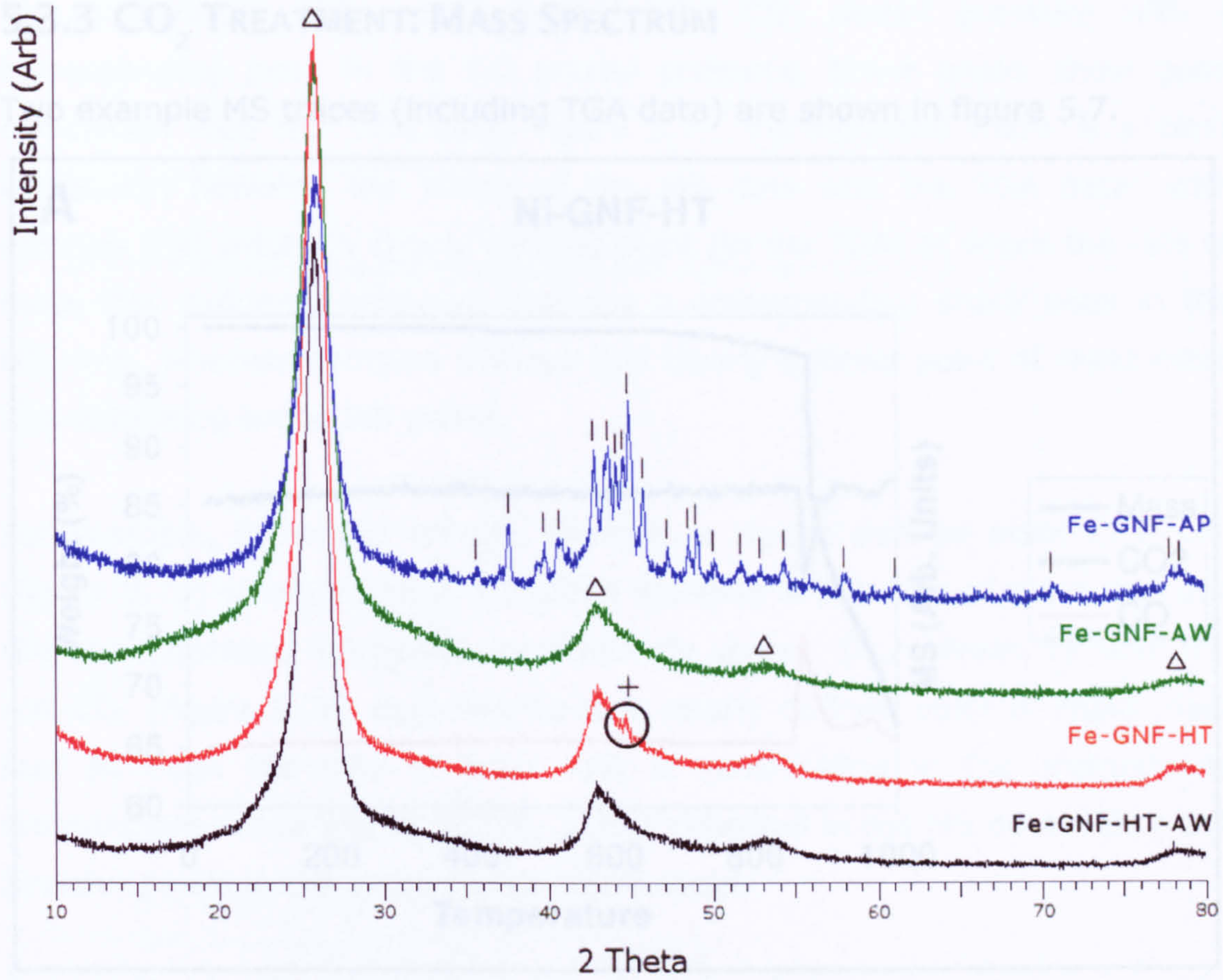

figure 5.6 - XRD for Fe-GNF samples. Symbols are indexed to phases; I to *Fe_3C, Δ to GNF and + to Fe metal.*

In the Fe-GNF samples, figure 5.6, the Fe-GNF-AP sample showed Fe_3C present, as would be expected from this system (Chapter 4). After acid washing Fe-GNF-AW, the Fe_3C peaks were no longer present with only the GNF peaks observed. After the heat treatment Fe-GNF-HT, a small peak was observed at ~45°, corresponding to the strongest reflection for Fe metal (d_{110}). This peak was not present after the second acid wash, Fe-GNF-HT-AW.

5.3.3 CO_2 Treatment: Mass Spectrum

Two example MS traces (including TGA data) are shown in figure 5.7.

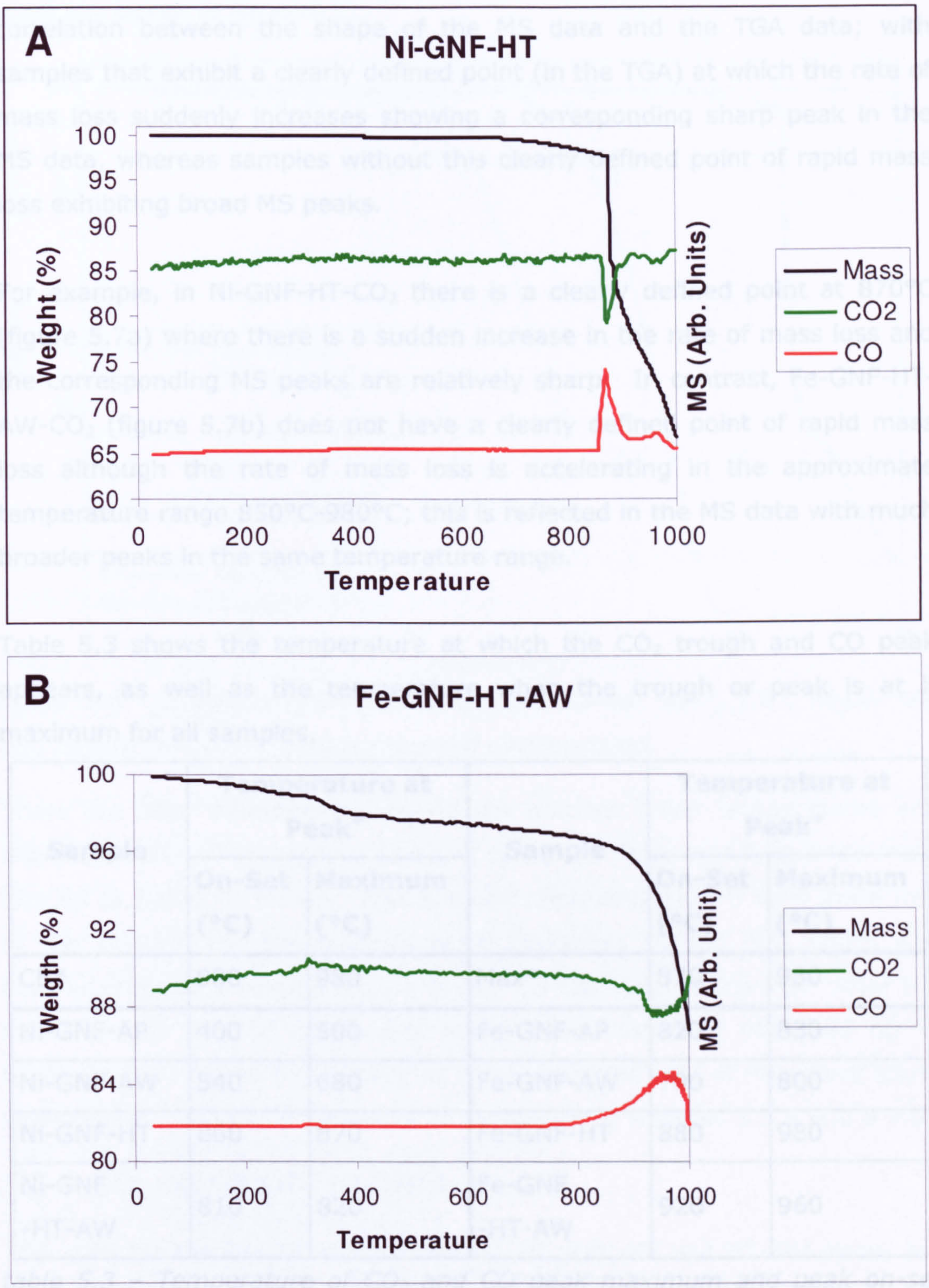

figure 5.7 – Example TGA and MS data for (top-A) Ni-GNF-HT and (bottom-B) Fe-GNF-HT-AW.

For all samples, there is a drop in the CO_2 partial pressure with a corresponding peak in the CO partial pressure, these peaks show good correlation with the TGA data, figure 5.7. Furthermore there is a clear correlation between the shape of the MS data and the TGA data; with samples that exhibit a clearly defined point (in the TGA) at which the rate of mass loss suddenly increases showing a corresponding sharp peak in the MS data, whereas samples without this clearly defined point of rapid mass loss exhibiting broad MS peaks.

For example, in Ni-GNF-HT-CO_2 there is a clearly defined point at 870°C (figure 5.7a) where there is a sudden increase in the rate of mass loss and the corresponding MS peaks are relatively sharp. In contrast, Fe-GNF-HT-AW-CO_2 (figure 5.7b) does not have a clearly defined point of rapid mass loss although the rate of mass loss is accelerating in the approximate temperature range 850°C-980°C; this is reflected in the MS data with much broader peaks in the same temperature range.

Table 5.3 shows the temperature at which the CO_2 trough and CO peak appears, as well as the temperature when the trough or peak is at it maximum for all samples.

Sample	Temperature at Peak+		Sample	Temperature at Peak+	
	On-Set (°C)	Maximum (°C)		On-Set (°C)	Maximum (°C)
CB*	880	980	Max*	870	980
Ni-GNF-AP	400	500	Fe-GNF-AP	820	830
Ni-GNF-AW	540	680	Fe-GNF-AW	790	800
Ni-GNF-HT	860	870	Fe-GNF-HT	880	980
Ni-GNF -HT-AW	810	820	Fe-GNF -HT-AW	920	960

*table 5.3 – Temperature of CO_2 and CO peak maximum and peak on-set from MS data. +Accurate to the nearest 10°C *Data supplied by Neil Bowering*

5.3.4 CO_2 Treatment: Reference TGA

The TGA data for the CO_2 treatments of the CB, Max and GNFs in the –AP state are shown in figure 5.8.

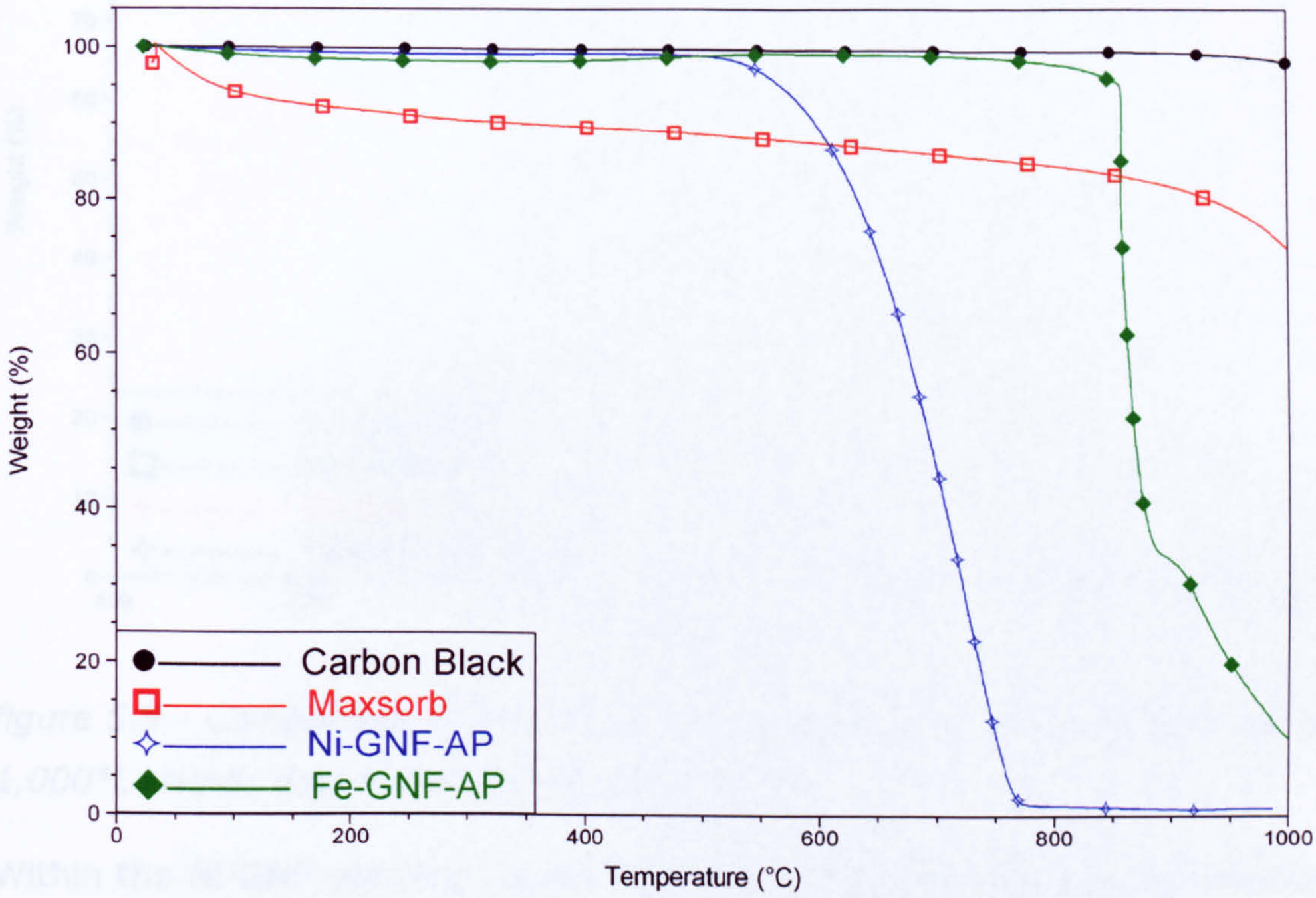

figure 5.8 - Comparison of CO_2 treatment between Max, CB*, Ni-GNF-AP and Fe-GNF-AP. Note: data is recorded every second.*

There are clear differences between the reaction onset temperatures and mass loss rates of the various forms of carbons. There was little or no mass loss up to 1,000 °C for CB. Max showed approximately ~8 wt% mass loss at the start of the temperature ramp (between 30-150 °C), which was accompanied by a small increase in m/z 18 observed in the MS. After the initial weight loss, a continuous linear mass loss was observed up to approximately 900°C (~ 8 wt%), at which point the rate of mass loss starts to increases. The GNFs behaviour is considered is sections 5.3.5 and 5.3.6.

5.3.5 CO_2 Treatment: Ni-GNFs

TGA data for the Ni-GNF samples in the AP, AW, HT and HT-AW states are shown in figure 5.9.

---

* TGA data for Maxsorb and Carbon Black was supplied by Neil Bowering

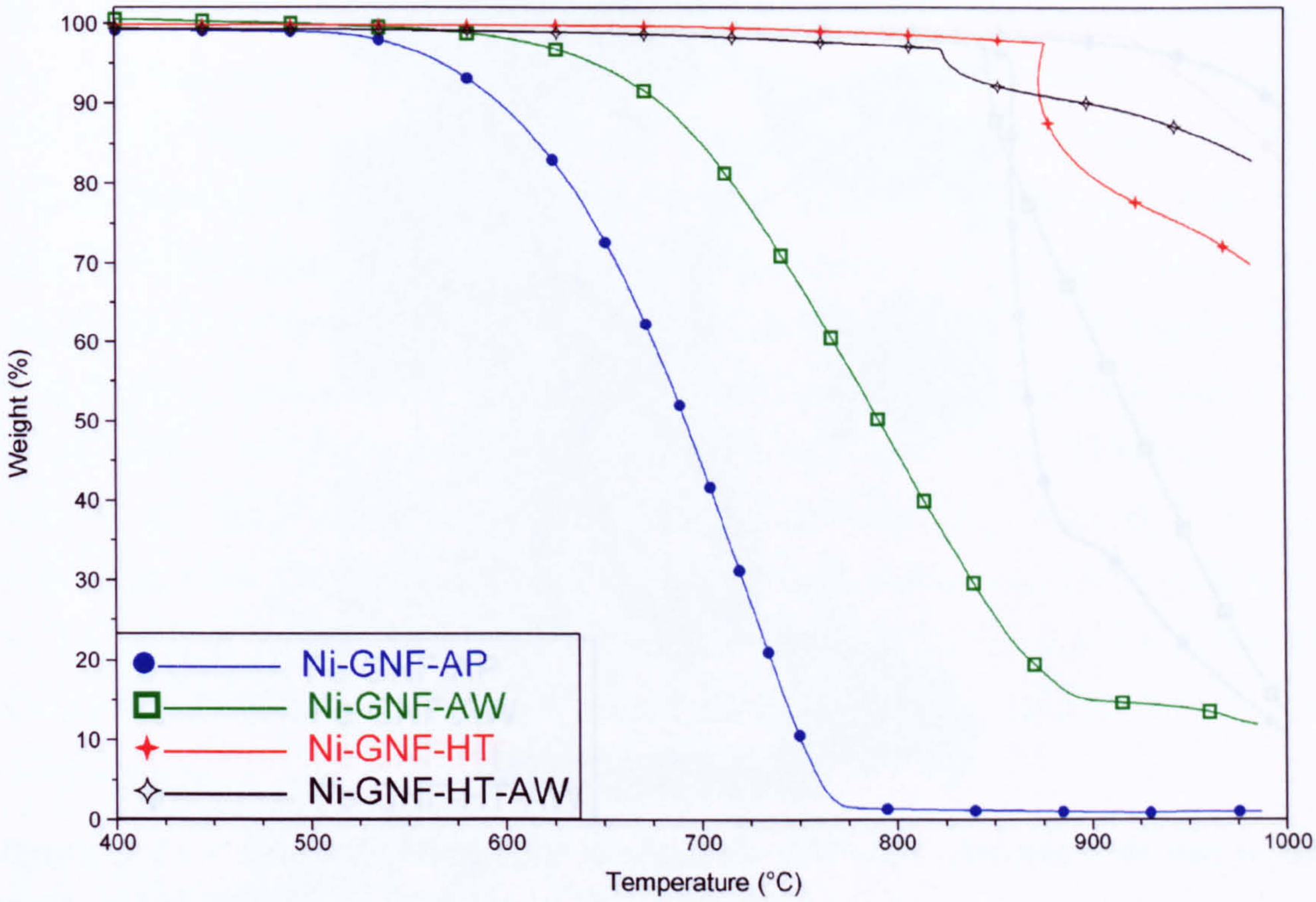

figure 5.9 - Comparison of Ni-GNF samples during CO_2 temperature ramp to 1,000°C. Note: data is recorded every second.

Within the Ni-GNF samples, there are large differences in the CO_2 oxidation behaviour, depending on the post-treatment. In Ni-GNF-AP state, the reaction onset temperature is ~530°C and resulted in rapid sample mass loss, with the entire sample oxidised by 780°C. After the first acid wash, the onset temperature was slightly higher at ~580°C after which point a moderate continuous mass loss between 600-850°C can be observed, at which point the rate mass loss stops with ~15% of the sample remaining. For Ni-GNF-HT, there was no mass loss in the sample until a sudden rapid mass loss at 870°C of ~15 wt%, after which the mass loss rate slows, becoming linear and causing a further ~15 wt% mass loss up to 1,000°C. In Ni-GNF-HT-AW, there was a small sudden mass lost at 820°C (~10 wt%), then slow mass loss (~5 wt%) up to 1,000°C.

5.3.6 CO_2 TREATMENT: FE-GNFS

TGA data for the Ni-GNF samples in the AP, AW, HT and HT-AW states are shown in figure 5.10.

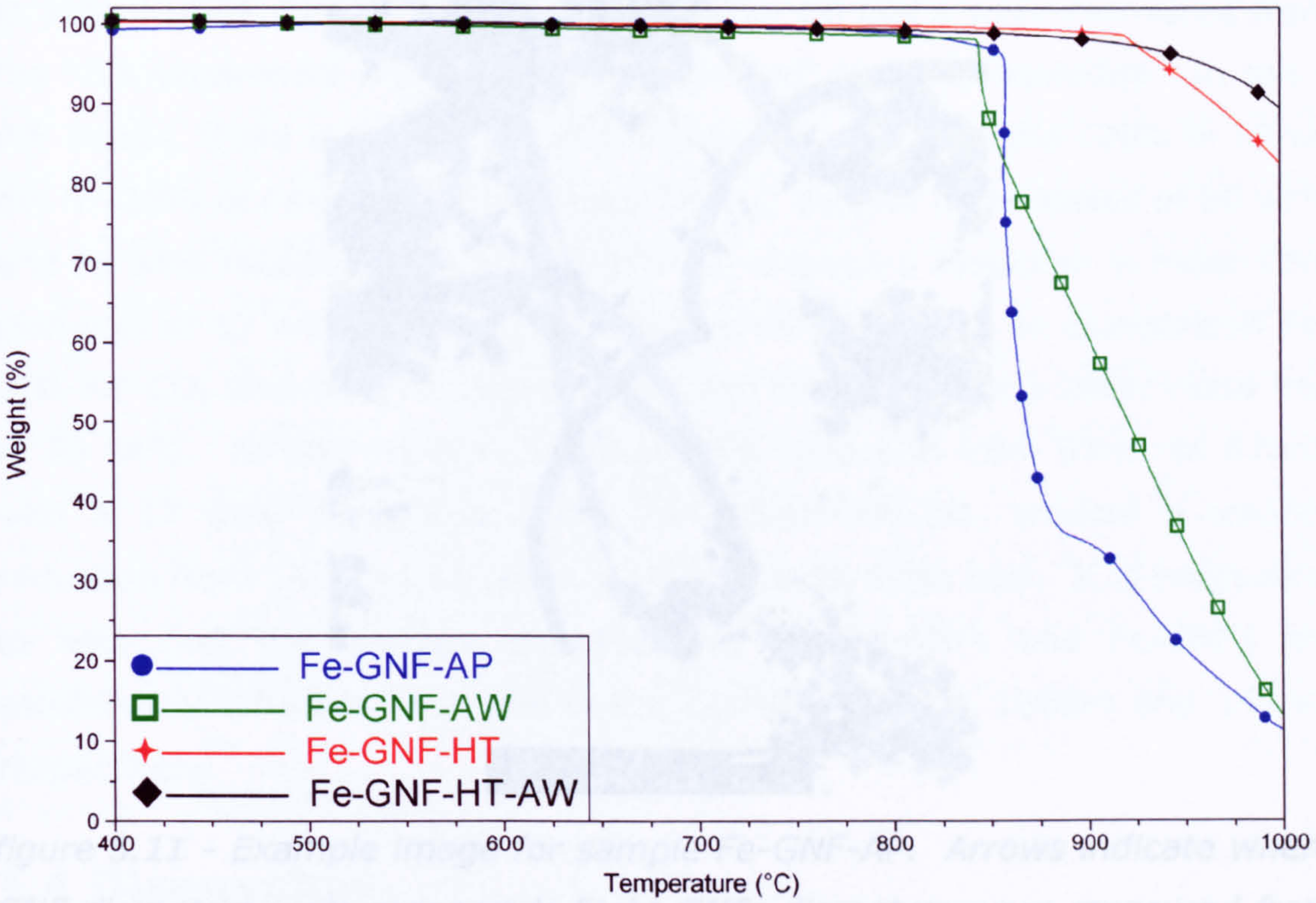

figure 5.10 - Comparison of Fe-GNF samples during CO_2 temperature ramp to 1,000°C. Note: data is recorded every second.

For the Fe-GNF samples, the range in on-set temperatures is small, with all samples showing the onset of oxidation in the range 850°C-950°C. Fe-GNF-AP shows a sudden rapid mass loss at 860°C, then rapid mass loss until ~30 wt% of sample is remaining, at which point the rate of mass loss slows. Fe-GNF-AW exhibits similar behaviour with the onset being sudden at 850°C, followed by rapid linear mass loss until 1,000°C. Fe-GNF-HT displays a sudden mass loss at 920°C, followed by linear mass loss. Fe-GNF-HT-AW does not show a sudden point at which the rate of mass loss changes, however a gradual increase in the mass loss rate can be observed over the range of ~900-950°C.

5.3.7 GNF Diameters

For GNF samples, the diameters of the fibres were measured using several images of each sample, an example image is shown in figure *5.11*.

figure 5.11 - Example image for sample Fe-GNF-AP. Arrows indicate where GNF diameters were measured; Eight GNFs diameters were measured from this image.

Table 5.4 shows the mean (of n≥70 fibres) diameters for some GNF samples, as well as the sample mass loss if CO_2 treated.

Sample	**Mean GNF Diameter before CO_2 /nm[a]**	**Mass Loss after CO_2 /wt%**	**Mean GNF Diameter after CO_2 /nm[a]**	**Theoretical Diameter /nm**
Ni-GNF-AP	103	>99[d]	-	-
Ni-GNF-AW	100	90	100	30[b]
Ni-GNF-HT	97	30	89	81[b]
Ni-GNF-HT-AW	97	17	87	88[b]
Fe-GNF-AP	142	>99[d]	-	-
Fe-GNF-AW	140	95	144	53[c]
Fe-GNF-HT	141	20	134	126[c]
Fe-GNF-HT-AW	138	14	133	128[c]

table 5.4 - Mean diameters of GNFs. [a]Standard error is ±5 nm. The theoretical diameter is the expected diameter if mass was removed from the surface of a rod of fixed length and diameter of [b]103nm or [c]142nm. [d]No GNFs present in sample.

In both Ni-GNF-AP-CO_2 and Fe-GNF-AP-CO_2, no GNFs were recovered from the TGA experiment and thus no average GNF diameter recorded. In the –AW states, there is no change in the mean diameter of the GNFs in either the Ni-GNFs or Fe-GNFs (within error limits), despite mass losses of 90 wt% and 95 wt% respectively. Ni-GNF-HT-CO_2 showed a reduction in mean GNF diameter of 97 nm to 89 nm, with a 30 wt% mass loss, in comparison Fe-GNF-HT-CO_2 showed a reduction of 141 nm to 134nm, for a lower mass loss of 20 wt%. Ni-GNF-HT-AW-CO_2 showed a reduction from 97nm to 87nm, with a 17 wt% mass loss, while Fe-GNF-HT-AW-CO_2 showed a smaller reduction from 138nm to 133nm, with a 14 wt% mass loss. It is interesting to note that the average diameters of the Ni-GNFs and Fe-GNFs are consistently different, with the mean diameters being 100nm and 140nm respectively.

5.4 Discussion

5.4.1 Carbon Oxidation

The CO_2 oxidation behaviour of the reference carbons examined was quite different to the GNF samples, as shown in figure 5.8. CB showed no significant mass loss up to 1,000°C, although there was a small weight loss (~2-3 wt%) observed over the temperature range ~ 920-1,000°C. There was also a change in the CO_2 and CO levels in the MS over a similar range indicating that there is the onset of an oxidation reaction with the CB. Maxsorb showed some initial mass loss up to 150°C due to the loss of absorbed water – as evidenced by the increase in H_2O signal in the mass spectrum (m/z 18), a common feature in porous, high-surface area materials. The sample then continued to show a slow linear mass loss up to ~900°C without any obvious signal changes in the MS. The final accelerated weight loss indicates that there was the on-set of the CO_2 reaction, confirmed by a change in the CO_2 and CO levels in the MS data at between ~900-1,000°C. The onset of CO_2 oxidation at just below 1,000°C is in broad agreement with the available literature for both CB and Max.[21,186] From figure 5.8 it is clear the GNF samples do not show a similar trend, with their CO_2 behaviour being considered below in sections 5.4.2 and 5.4.3.

5.4.2 Ni-GNF Oxidation

The presence of Ni in GNF samples has a clear effect on the CO_2 oxidation behaviour of the samples, as shown in figure 5.9. Ni-GNF-AP and -AW show the onset temperature of oxidation being 530°C and 600°C respectively, much lower than that for Ni-GNF–HT and -HT-AW, with onset being at 870°C and 830°C, respectively. It is expected that acid washing removes residual CVD catalyst in samples[142,187], although not completely, thus the amount of catalyst in GNF sample would be expected to follow the order: AP>AW≈HT>HT-AW. This is also supported by XRD (figure 5.5) and TEM (figure 5.2 and figure 5.3) data. As this shows a similar trend to the CO_2 oxidation behaviour, it is likely that residual catalyst particles are allowing carbon to be catalytically oxidised at lower temperatures, as could be expected (section 5.1).

In Ni-GNF-AP, there is Ni present from the residual catalyst particles, predominately located at the end of the GNFs (figure 5.2). Due to the mechanism GNF growth (section 2.3) requiring exposed catalyst facets in order to absorb reactant gases, it is reasonable to assume that after growth, these facets were still exposed and are thus able to absorb CO_2 gas directly onto the particle that was in contact with the end of the GNF.[43] If this process then allows catalytic oxidation the GNF, it will be along the GNF length (i.e. where the GNF is in contact with the catalyst particle). In order to determine if this process is occurring, diameter analysis of the GNF samples before and after CO_2 oxidation was performed, table 5.4. Figure 5.12 shows a graph illustrating how a GNFs diameter will decrease with % mass, assuming all carbon is removed from the surface/diameter of the GNF, as opposed to along the length (basal plane oxidation), which is the conjectured mechanism.

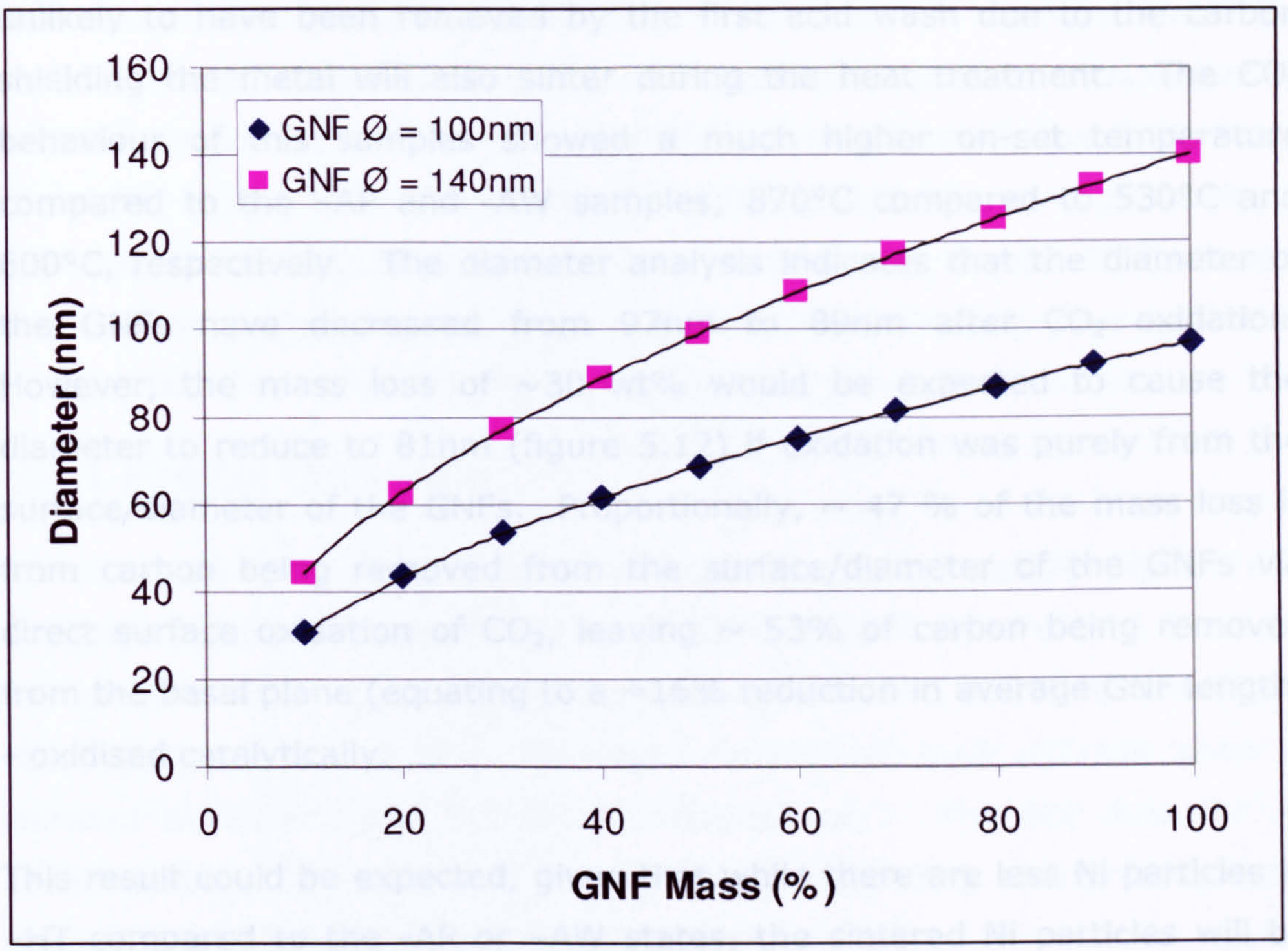

figure 5.12 – Theoretical GNF Diameter Vs Mass, assuming carbon is removed from the surface/diameter of the fibre.

After the first acid wash (Ni-GNF-AW), a large quantity of the Ni particles appear to have been removed, as shown by the removal of Ni peaks in the XRD (figure 5.5). The CO_2 reaction onset temperature was increased from 530°C to 600°C for Ni-GNF-AP and Ni-GNF-AW, respectively. However, even after the sample had lost 90% of its mass, the mean diameter was 100 nm, unchanged after CO_2 treatment. According to figure 5.12, the diameter of the GNFs in Ni-GNF-AW-CO_2 should have been approximately 30nm, thus indicating that carbon is only being removed along the basal plane of the GNFs.

After the heat treatment has been applied (Ni-GNF-HT), the Ni peak at ~46° re-appears in the XRD. This is complemented by the observation of large (~400nm in diameter) Ni particles in the TEM (figure 5.3). This could be expected as any residual Ni particles will become molten and have high atomic mobility during the heat-treatment, therefore sintering into larger particles.[188] Furthermore, any carbon encapsulated Ni particles, which are

unlikely to have been removed by the first acid wash due to the carbon shielding the metal will also sinter during the heat treatment. The CO_2 behaviour of this samples showed a much higher on-set temperature compared to the –AP and -AW samples; 870°C compared to 530°C and 600°C, respectively. The diameter analysis indicates that the diameter of the GNFs have decreased from 97nm to 89nm after CO_2 oxidation. However, the mass loss of ~30 wt% would be expected to cause the diameter to reduce to 81nm (figure 5.12) if oxidation was purely from the surface/diameter of the GNFs. Proportionally, ~ 47 % of the mass loss is from carbon being removed from the surface/diameter of the GNFs via direct surface oxidation of CO_2, leaving ~ 53% of carbon being removed from the basal plane (equating to a ~16% reduction in average GNF length) - oxidised catalytically.

This result could be expected, given that while there are less Ni particles in –HT compared to the -AP or –AW states, the sintered Ni particles will be particularly active (i.e. fully exposed facets) and will readily oxidise carbon that it is in contact with. However, it is also important to consider that the sintered particles are less likely to be located at the ends of GNFs, due to mobility during sintering; thus it could be expected that basal oxidation is more rapid for GNFs in contact with particles, but less GNFs will be in contact. This would explain the rapid weight loss at 870°C (~15 wt%) as being catalytic oxidation of GNFs in contact with sintered particles, while the slower mass loss (~15 wt%) up to 1,000°C is due to non-catalytic oxidation which causes the average diameter reduction in Ni-GNF-HT-CO_2.

After the second acid wash, it appears that all or nearly all the residual Ni was removed from the sample. There is no peak in the XRD and no Ni particles (large or small) could be observed the TEM. The onset temperature for this reaction was slightly lower than that for the Ni-GNF-HT sample, however the overall mass loss for the sample (up to 1,000°C) was smaller, 17 wt% compared to 30 wt% respectively, indicating that CO_2 reaction was not occurring as rapidly. The GNF diameter analysis shows that the diameter reduced from 97nm to 87nm, which is in good agreement with the theoretically predicted reduction to 88nm, for the 17 wt% mass

loss observed. This indicates that all the carbon is loss from the surface/diameter, with no (or little) catalytic basal oxidation. This reduction in diameter corresponds to ~5 nm of the surface carbon in the GNFs being removed, which is the approximate thickness of the amorphous layer observed in the Ni-GNF-AP, figure 5.4. As shown in the HR-TEM images, this amorphous layer is not present in Ni-GNF-HT-AW-CO_2, thus indicating that at least 5 nm of carbon has been removed.

5.4.3 Fe-GNF Oxidation

With the Fe-GNF system, there are much smaller differences in CO_2 oxidation behaviour compared to the Ni-GNF system. The Fe-GNF-AP and –AW samples show a clear reaction on-set temperature at 850°C and 860°C respectively, figure 5.10. Whereas, Fe-GNF-HT and -HT-AW show a reaction at 920°C and 900-950°C, respectively. The MS data for all samples shows the CO_2 and CO peaks corresponding to the TGA data, indicating that in each case the oxidation is occurring.

The XRD data (figure 5.6) shows the Fe_3C residue in the Fe-GNF-AP sample is removed after the first acid wash (Fe-GNF-AW). Due to two GNFs usually growing from one catalyst particle in Fe-GNFs, it is clear that catalyst particles (located at the end of two GNFs) are removed by this treatment, shown in figure 5.2. After the heat treatment, a single peak appears ~46° and which is likely to correspond to Fe metal. However, there was no peak observed at ~65° corresponding to the d_{200} reflection, as might be expected, although this can be accounted for as the relative intensity of d_{200} is 34% with respect to d_{110}. This indicates that the Fe present in the Fe_3C catalyst residue is presumably sintering during the heat treatment to give Fe metal. However, no particles, large sintered (>200 nm) or small catalyst (<200 nm) could be observed in the TEM in Fe-GNF-HT. The Fe metal peak was not present in the XRD after the second acid wash.

The TEM diameter analysis (table 5.4) indicates that in Fe-GNF-AW the GNF diameter is unchanged (140 nm before CO_2 and 144 nm after CO_2), indicating that carbon is only being removed from the basal plane of the GNFs. In both the Fe-GNF–HT and Fe-GNF-HT-AW, there is a reduction in

GNF diameter, however this is smaller than would be expected if carbon was only being removed from the surface/diameter (figure 5.12). In Fe-GNF-HT the diameter is reduced from 141nm to 134nm for a mass loss of 20 wt%, lower than the expected theoretical reduction to 125nm (for 20 wt% mass loss). This indicates that oxidation is occurring ~45 % via the surface/diameter mechanism and ~55 % from basal oxidation (equating to ~11 % reduction in GNF length). For Fe-GNF-HT-AW the diameter analysis shows a reduction from 138 nm to 133 nm, again lower than the theoretically expected 128 nm, for a 14 wt% mass loss. Oxidation in this sample again shows both surface/diameter and basal, but with ~60% of the carbon being oxidised from the surface/diameter and ~40 % being removed from the basal plane (equating to ~6 % reduction in GNF length). Given this analysis for Fe-GNF-HT-AW-CO_2, is would be expected that approximately 2.5 nm of the diameter should be removed from the surface of the GNFs. However, figure 5.4 indicates that the re-oriented carbon surface has been completely removed from the GNFs, despite being ~5 nm thick.

5.4.4 Oxidation Mechanisms in GNFs

Considering the temperatures of the CO_2 oxidation onset reactions, it is clear that there are significant differences between the effect of residual Ni and Fe catalyst. In samples where the CVD catalyst is still present in relatively high levels (i.e. –AP and –AW states) the difference in onset temperatures between the Ni and Fe are 530°C and 600°C, and, 860°C and 850°C for the Ni-GNF-AP and -AW and Fe-GNF-AP and -AW samples respectively. Once the majority of catalyst particles have been removed (i.e. in the –HT and –HT-AW states), the range of reaction on-set temperatures become much similar; 870°C and 820°C, and, 920°C and 900-950°C for the Ni-GNF-HT and -HT-AW, and, Fe-GNF-HT and -HT-AW, respectively. These reaction temperatures are also much closer to those for the standard carbon materials investigated (CB and Maxsorb). It can therefore be concluded that the residual catalyst is causing catalysed oxidation of GNFs and that Ni is more catalytically active than Fe. This is in agreement with other studies present in the literature that compares the general oxidation activity of Ni and Fe[21,189]. However, with regards to

activity, in Fe-GNF-AP, Fe is present as Fe_3C, rather than the more reactive metallic Fe (which is observed in the Fe-GNF-HT); this makes precise comparison of the catalytic activities difficult.

Given the evidence presented, it would appear that the presence of residual catalyst particles causes CO_2 oxidation of GNFs to occur along the lengths of the GNFs – termed 'Basal' oxidation. In contrast, when the majority of the catalyst has been removed, carbon is oxidised from the surfaces/diameters of the GNFs – termed 'Edge' oxidation. These two mechanisms are shown schematically in figure 5.13.

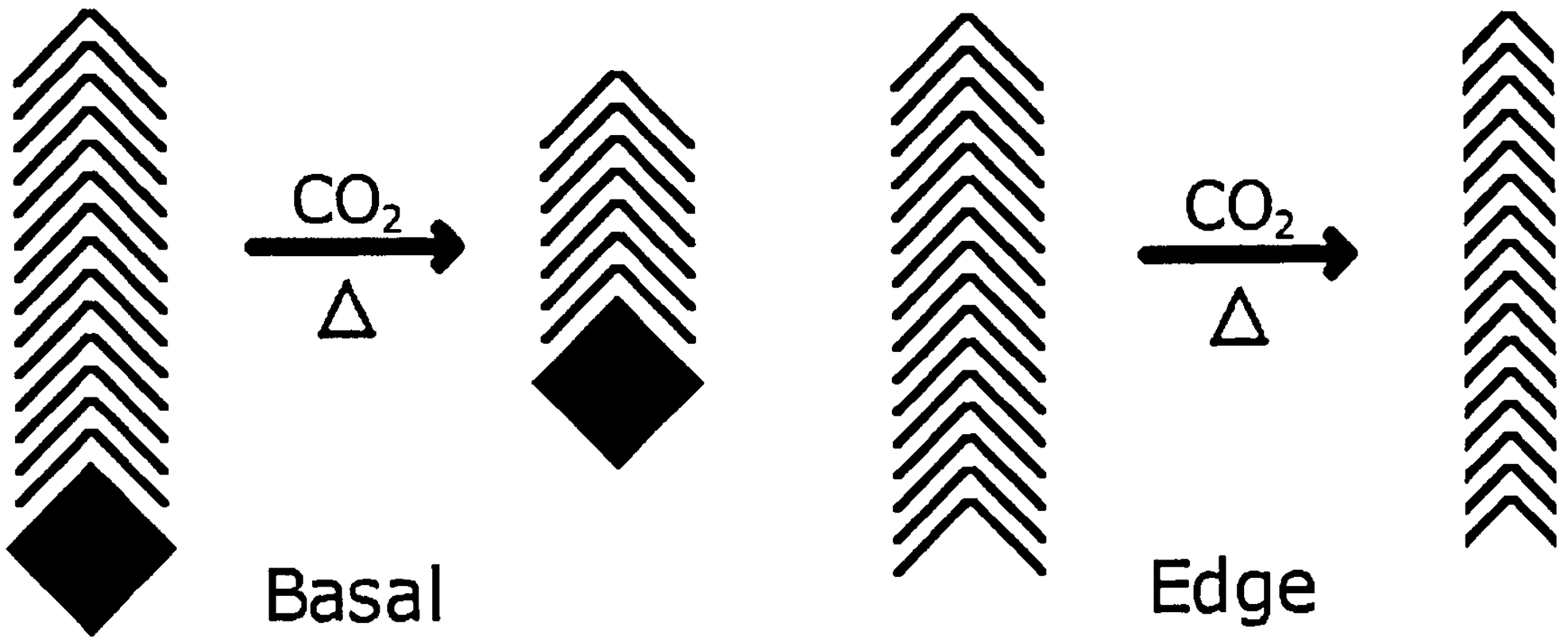

figure 5.13 - Schematic of Basal and Edge oxidation mechanisms in GNFs

In Fe-GNF-HT-AW, some basal oxidation was occurring (simultaneously with edge oxidation) indicating that some catalyst residues were still present in the sample. There are (at least) two possibilities for this; 1) that it is easier to fully remove Ni catalyst residue from GNF samples than residual Fe catalyst particles (thus promoting edge oxidation in Ni-GNFs), or 2) Fe-GNFs are more generally susceptible to basal oxidation instead of edge oxidation (regardless of residual catalyst), due to a structural differences in the GNFs. Given the similarity of the GNF samples (Chapter 4) is more reasonable that residual catalyst is most important factor determining the oxidation mechanism. However, the lack of supporting evidence (XRD, TEM, etc) for residual catalyst being present in Fe-GNF-HT-AW, coupled with the difference in mean diameter (Fe-GNFs being 140nm, Ni-GNFs being 100nm)

means that possibility (2) still exists – further investigation would be required to more fully elude this effect.

5.5 Conclusions

The removal of residual CVD catalyst and the CO_2 oxidation behaviour of GNFs synthesised from Ni and Fe catalysts has been investigated. It was found that any residual catalyst particles (Ni or Fe) remaining in GNF samples will change the mechanism of CO_2 oxidation. If any residual catalyst particles are present a sample, a 'basal' mechanism – removal of carbon along the lengths of the GNFs – is prevalent, catalysed by the residual CVD catalyst particles. Full removal of catalyst residues causes oxidation to occur via the 'edge' mechanism – removal of carbon along the surface/diameters of the GNFs.

Careful removal of catalyst particles can be achieved, in the Fe and Ni systems investigated here, by the use an acid wash, followed by a heat treatment and subsequent acid wash. However, even using this process, it would appear that not all of the residual Fe catalyst can be removed from the Fe-GNFs.

The method presented here allows for any amorphous or re-orientated carbon on the surface of GNFs to be removed (oxidised), thus allowing cleaned and lower energy access for potential sorbate molecules to the 'internal' surface area of GNFs.

5.6 Summary

From the work presented in this chapter it has been shown that the use of appropriate post synthesis treatments residual CVD catalyst particles can be removed from GNFs. Therefore, for the subsequent work presented in the rest of this thesis all samples have been acid washed, followed by a heat-treatment followed by further acid wash in ordered to remove any residual catalyst.

In order to allow larger quantities (>0.5 g) of GNF samples to be CO_2 treated, a controlled environment tube furnace has been used (as opposed to the TGA apparatus used in this chapter, sample weights ~0.15 g). Thus samples used subsequent have been CO_2 treated using the following procedure;

- Evacuation of Air from the tube furnace
- Fill with Ar (1000 cm^3 min^{-1}), then follow Ar at 100 cm^3 min^{-1} once filled to atmospheric pressure
- Heat to 1,200°C at 10°C min^{-1}
- Evacuate furnace (while at 1,200°C)
- Flow CO_2 (into sealed atmosphere furnace) at 200 cm^3 min^{-1} for 5 mins (note this does not fill the furnace to atmospheric pressure)
- Evacuate furnace
- Fill with Ar (1000 cm^3 min^{-1}), then follow Ar at 100 cm^3 min^{-1} (once atmospheric pressure is achieved)
- Cool to room temperature

Samples that have undergone this treatment show a weight loss of ~10 wt% and show typical oxidised surfaces similar to those presented in figure 5.4.

Given that the removal of all residual Fe-catalyst traces appears to be less efficient than that for the Ni-catalyst, coupled with relatively very small carbon yields of the Fe-catalyst (Chapter 4), all future investigations (Chapter 6) will be done purely on Ni-GNFs. Samples will subsequently be referred to as Ni-GNF-x, although are equivalent to sample 'Ni-GNF-HT-AW'-x, where x is a further post-treatments of the GNFs.

6 Pd LOADING

6.1 Introduction

Several research groups have proposed that the presence of transition metals (Ti, Pd, Pt amongst others) on various nanostructured carbons can have a positive effect on the hydrogen storage capacity of the materials.[143,150-152] Between these groups, there have been several different theories as to the precise mechanism by which this occurs (outlined below and in detail in section 2.7). However, there have been few detailed investigations into the area and doubt still exists as to whether or not the uptakes reported are reproducible. Thus, the current chapter will detail the synthesis of GNFs with a variety of Pd particles on their surfaces, with the aim to determine what affect Pd has on the hydrogen storage properties of GNFs.

Dissociation catalyst

It has been proposed that Pd could act as a dissociation catalyst; allowing smaller (relative to H_2 molecules) H atoms or H^+ ions to diffuse into the inter-layer spacing of the GNFs, facilitating hydrogen uptake.[150,151,190] Thus the Pd particles are acting as gateways, facilitating the reaction scheme:

$$H_2\,(g) \longleftrightarrow H_2\,(ad) \longleftrightarrow H_2\,(ad\text{-}Pd) \xleftrightarrow{Pd} 2H\,(abs\text{-}Pd) \longleftrightarrow 2H\,(abs\text{-}GNF)$$

Hydrogen Spillover

The hydrogen spillover effect is another possible theory and is similar to the dissociation mechanism above, as the Pd particles act catalytically to dissociate H_2. The key difference with the spillover effect is that the hydrogen atoms (or ions) then diffuse onto the surface of the GNFs, rather than into the bulk of the GNF (as in the dissociation mechanism).[146,191,192]

Kubas Binding

A more distinct alternative mechanism has been proposed based on Kubas binding, where several H_2 molecules (rather than atoms) are bonded to a transition metal atom, as shown in figure 2.18 (section 2.7.4). The

interaction of the metal centre and delocalised electron system of the GNF is critical in this mechanism in order to allow or promote Kubas binding.[153-156]

The precise determination of the interaction mechanism of the hydrogen-metal and metal-carbon has been hard to elucidate to date. This is due to two principal reasons; the variability and accuracy in the determination of hydrogen uptake capacities and precise characterisation of the nanostructured carbon support. Because of this, making meaningful comparison of the results of different groups is very difficult - to the point of not being viable.

Thus, the aim of this chapter is to investigate the preparation of GNFs with Pd particles and then accurately determine if these particles have any effect of their hydrogen storage properties (in Chapter 7). By careful design of the experiments it shall also be possible to determine by which hydrogen uptake mechanism any improvement in hydrogen storage capacity is achieved. For all the proposed mechanisms, the distribution of Pd particles is very important; there should be a large numbers of small particles, homogeneously dispersed on the surface of GNFs.[143] Thus this investigation may also have further relevance to the application of GNFs as catalyst support materials, as the requirements of particle size and distribution described above are analogous to those required in heterogeneous catalysts. This is especially pertinent, as Pd and Pd alloys are commonly used as catalysts in many different hydro-carbon and organic chemistry reactions.[193]

To investigate the preparation of Pd particles on GNFs, the incipient wetness impregnation technique will be employed. Two principle experimental variables (of incipient wetness impregnation) will be investigated; GNF surface state (achieved through post-synthesis treatments) and loading level (concentration) of Pd.

GNF Surface State

It is proposed that GNFs with different surface states can be synthesised by application of different post-synthesis treatments. It is anticipated that this will then affect the shape, size or distribution of Pd particles on the GNFs,

which will enable determination of the mechanism of adsorption; if Kubas binding is occurring, samples with (a higher number of) smaller particles of Pd on the GNF surface will allow more H_2 to bind to the Pd, causing a larger hydrogen uptake capacity to be observed. It is also possible that Kubas binding may only occur in select samples due to the dependence of the mechanism on the interaction between the Pd particles and the GNFs, which will be affected by the different surface states of the GNFs.

Pd Loading Level

By changing the concentration of Pd present within a sample, assessment of whether the dissociation or spillover mechanisms are occurring will be possible. As both of these mechanisms are essentially catalytic, with the Pd acting as gateways, increasing the Pd concentration (i.e. increasing the number of gateways) should have a directly proportional effect on the observed hydrogen uptake capacity. It is possible that this effect may only be kinetic rather than increasing the maximum hydrogen storage capacity, but this would still be relevant due to the information that can be gained about the proposed mechanism.

The hydrogen storage properties (and mechanisms) of these materials shall be considered in detail in Chapter 7, along with the materials synthesised in Chapters 4 and 5. The current chapter only details the investigation in to the preparation and characterisation of the Pd loaded GNFs.

6.2 Experimental

Three sets of experiments have been performed within this chapter, all using similar experimental procedures. This section will detail the general synthesis methods used, with the specific sets of experiments being detailed in the results sections. With the three sets of experiments referred to as; 'Surface Treatment', 'Pd-Loading: GNF Surfaces' and 'Pd-Loading: Loading Level'.

The section on Surface Treatment details how different chemical and thermal post-treatments were applied to GNF samples, which were then subsequently used in the Pd-loading experiments. The 'Pd-loading: GNF

Surfaces' section describes how the effect of the GNF surface alters the morphology and distribution of the Pd deposited - to access the Kubas binding mechanism. For the 'Pd-Loading: Loading Level' section, a single (post-treated) GNFs sample was selected and loaded with different levels (concentrations) of Pd, to examine any catalytic effect of Pd on hydrogen uptake properties of GNFs.

All of the GNF samples were synthesised using Ni catalyst, thus within this chapter samples will simply be referred to as 'GNF-x', as opposed to 'Ni-GNF-x', where x indicates subsequent treatment(s) applied to the sample.

6.2.1 Surface Treatment

Preparation details of GNF-HT-AW and GNF-CO_2 are given in Chapter 5. A further H_2 treatment was also applied, with the aim to remove any surface oxygen that is likely to be present on the surface of the GNF-HT-AW and GNF-CO_2 samples. The H_2 treatment was performed in an environmentally controlled tube furnace; samples were heated at 10°C min^{-1} under flowing Ar (100 ml min^{-1}) to 800°C. A mixture of hydrogen and argon was then flowed at 50 ml min^{-1} each (total flow 100 ml min^{-1}) for one hour at constant temperature, after which the furnace was cooled to room temperature under a pure Ar flow (100 ml min^{-1}). During the treatment the gas environment was analysed using MS, with m/z values between 1 and 50 being monitored.

This provided three GNF samples, each with a different surface state, summarised in table 6.1.

Treatment	**Details**	**Nomenclature**
Ni-GNF-AP with acid wash, heat treatment and second acid wash applied	Chapter 5 (5.2.1)	GNF-HT-AW
GNF-HT-AW with a CO_2 treatment applied	Chapter 5 (5.2.2)	GNF-CO_2
GNF-CO_2 with a H_2 treatment applied	Chapter 6 (6.2.1)	GNF-CO_2-H_2

table 6.1 – Summary of the different surface treatments applied to GNF samples, reference to detailed procedure and nomenclature.

6.2.2 Pd Coating

Samples were coated with Pd particles using the 'incipient wetness' technique. Approximately 0.5 g of GNFs was mixed with 200 ml of distilled water and then the appropriate quantity of Pd nitrate was added to the mixture. The mixture was then stirred and heated on a hot-plate stirrer, set at 200°C until all the liquid was evaporated. The solid was recovered and placed in a drying oven (70°C) over night (~16 h). Two sets of samples were synthesised using this method, in order to access the hydrogen uptake capacity and mechanism. Set 1 used GNFs with different surface states and set 2 using different Pd loading levels applied to GNF-CO_2-H_2, summarised in table 6.2.

Set	GNF	Pd Loading level (wt% Pd)	Nomenclature
1	GNF-HT-AW	5.0	GNF-HT-AW-5Pd
	GNF-CO_2	5.0	GNF-CO_2-5Pd
	GNF-CO_2-H_2*	5.0	GNF-CO_2-H_2-5Pd
2	GNF-CO_2-H_2	0.5	GNF-0.5Pd
	GNF-CO_2-H_2	1.0	GNF-1Pd
	GNF-CO_2-H_2*	5.0	GNF-5Pd
	GNF-CO_2-H_2	10.0	GNF-10Pd

*table 6.2 – Pd coated samples synthesised. *equivalent sample*

After the samples were loaded with Pd, they underwent a heat treatment, referred to as a thermal reduction for clarity. The treatment temperature was determined by multiple TGA experiments, an example TGA experiment plot is shown in figure 6.1.

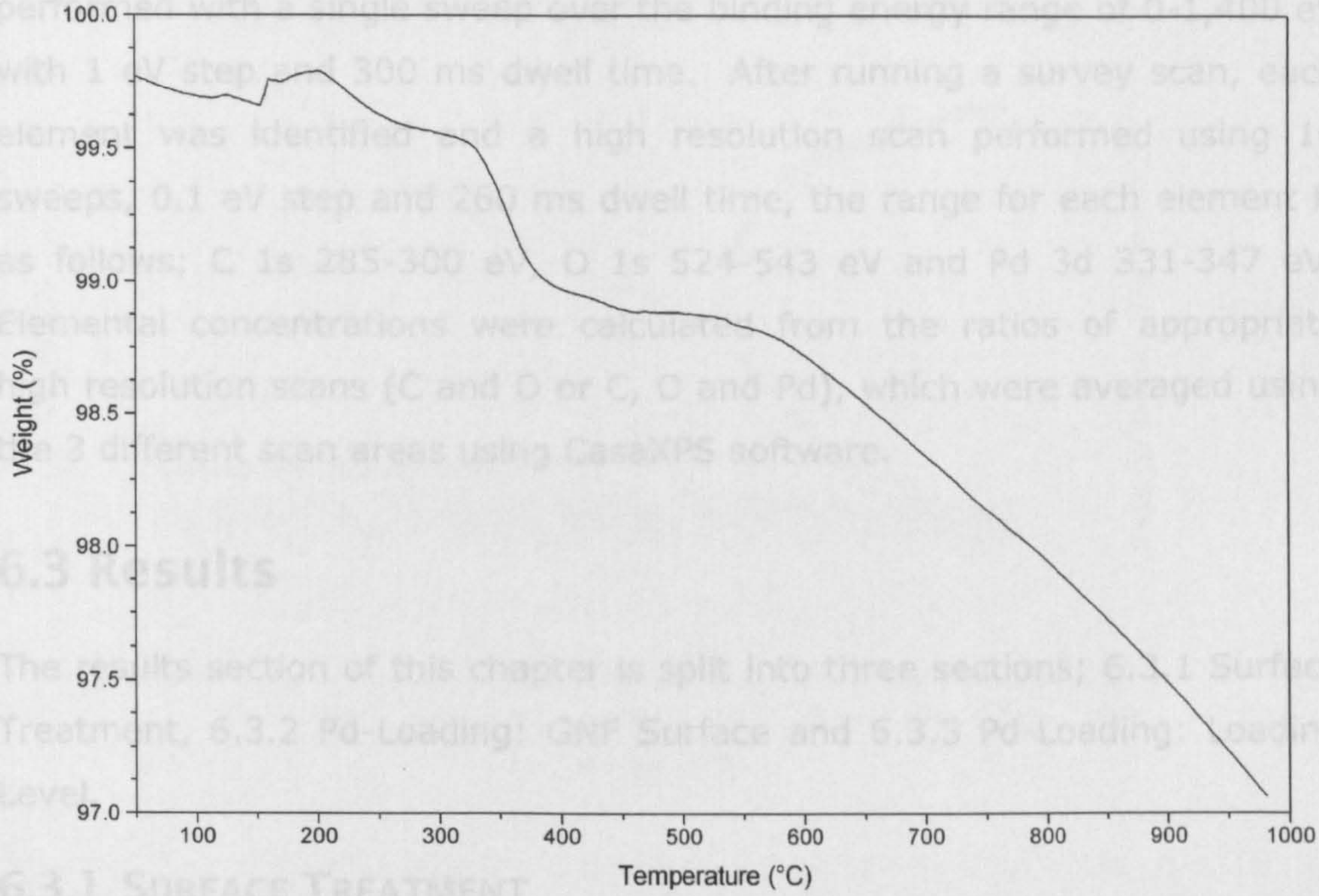

figure 6.1 - Example TGA data for GNF-HT-AW-5Pd heated at 10°C min^{-1} under flowing Ar.

The rapid mass loss at ~350°C was reproducible, thus samples were thermally reduced in a controlled environment tube furnace heated at 10°C min^{-1} to 400°C under flowing Ar (100 ml min^{-1}), then held isothermally for 1 hour and then cooled to room temperature. Samples that have undergone this thermal reduction are referred to with a '-TR', for example GNF-CO_2-5Pd-TR.

6.2.3 Characterisation

TEM, XRD and TGA were used to characterise the samples synthesised in this chapter, as described in Chapter 3. X-Ray Photoelectron Spectroscopy was also employed to determine the elemental compositions and bonding information of the different samples, as described below.

XPS experiments were performed using an 'Axis Ultra' (Kratos Ltd) with a monochromated Al X-ray source. Samples were pressed onto a loading bar (approximately 5 mm x 10 mm). Spectra were recorded at 3 different physical areas per sample. For each area, a wide-energy survey scan was

performed with a single sweep over the binding energy range of 0-1,400 eV with 1 eV step and 300 ms dwell time. After running a survey scan, each element was identified and a high resolution scan performed using 10 sweeps, 0.1 eV step and 260 ms dwell time, the range for each element is as follows; C 1s 285-300 eV, O 1s 524-543 eV and Pd 3d 331-347 eV. Elemental concentrations were calculated from the ratios of appropriate high resolution scans (C and O or C, O and Pd), which were averaged using the 3 different scan areas using CasaXPS software.

6.3 Results

The results section of this chapter is split into three sections; 6.3.1 Surface Treatment, 6.3.2 Pd-Loading: GNF Surface and 6.3.3 Pd-Loading: Loading Level.

6.3.1 Surface Treatment

This section gives the TGA-MS data for GNF-CO_2-H_2, along with XPS and XRD data for the three samples with different post-treatments; GNF-HT-AW, GNF-CO_2 and GNF-CO_2-H_2.

TGA-MS

A H_2 treatment was applied to GNF-CO_2, with the aim to remove any surface oxygen. The precise reaction conditions (800°C under flowing H_2/Ar at 50 ml^{-1} min^{-1}) were selected based on the TGA data presented in figure 6.2. In order to protect the Pt heating elements in the TGA apparatus reacting with H_2 gas, the flowing gas was 5% H_2 in 95% N_2 rather than pure hydrogen, thus this results are considered within that context.

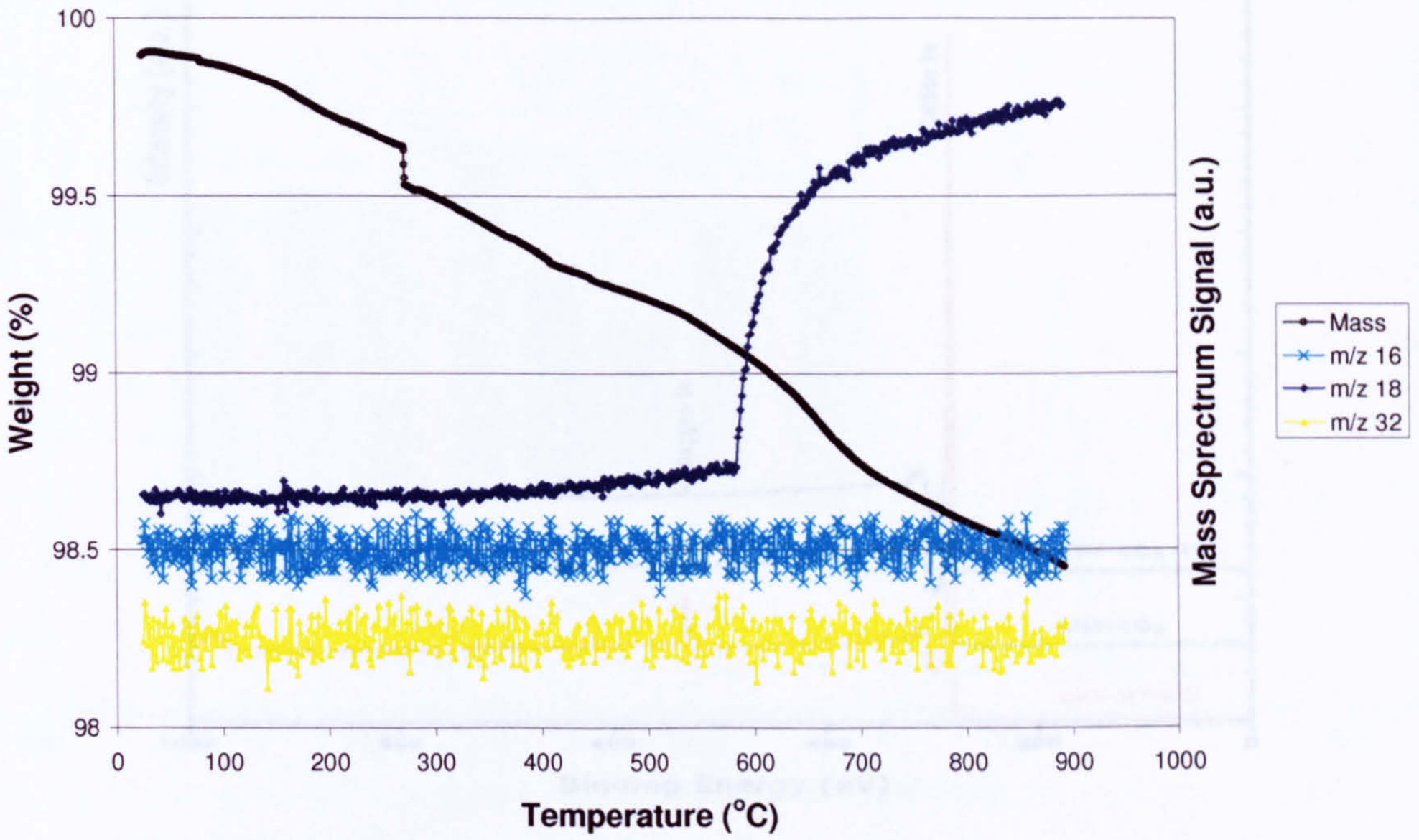

figure 6.2 – TGA-MS data for GNF-CO_2 including MS signal for m/z 16, 18 and 32. m/z 16 and 32 has been off-set for clarity.

From figure 6.2, it appears that GNF-CO_2 shows little or no reaction with the flowing (5%) H_2 atmosphere up to 900°C; evidenced by the small mass loss (1.5 wt%) observed over the temperature range investigated. There appears to be a sudden mass loss at ~280°C, although this not accompanied by a change in the partial pressures in any of the MS in any fragments (for m/z 1 to 50). At ~580°C there was a sharp increase in the m/z 18 level, coupled with a slight change slope in the otherwise linear mass loss trace. However, while the m/z 18 signal started to level off by the end of the experiment (at 900°C), the mass loss trace had returned to a linear continuous mass loss by 700°C. There was no change observed in the m/z 16 or m/z 32 fragments which where only detected at trace levels compared to m/z 18, as shown by the larger amount of noise in the signals in figure 6.2.

XPS

XPS of GNF–HT-AW, GNF-CO_2 and GNF–CO_2-H_2 samples only showed peaks corresponding to C 1s and O 1s in the survey scans, figure 6.3.

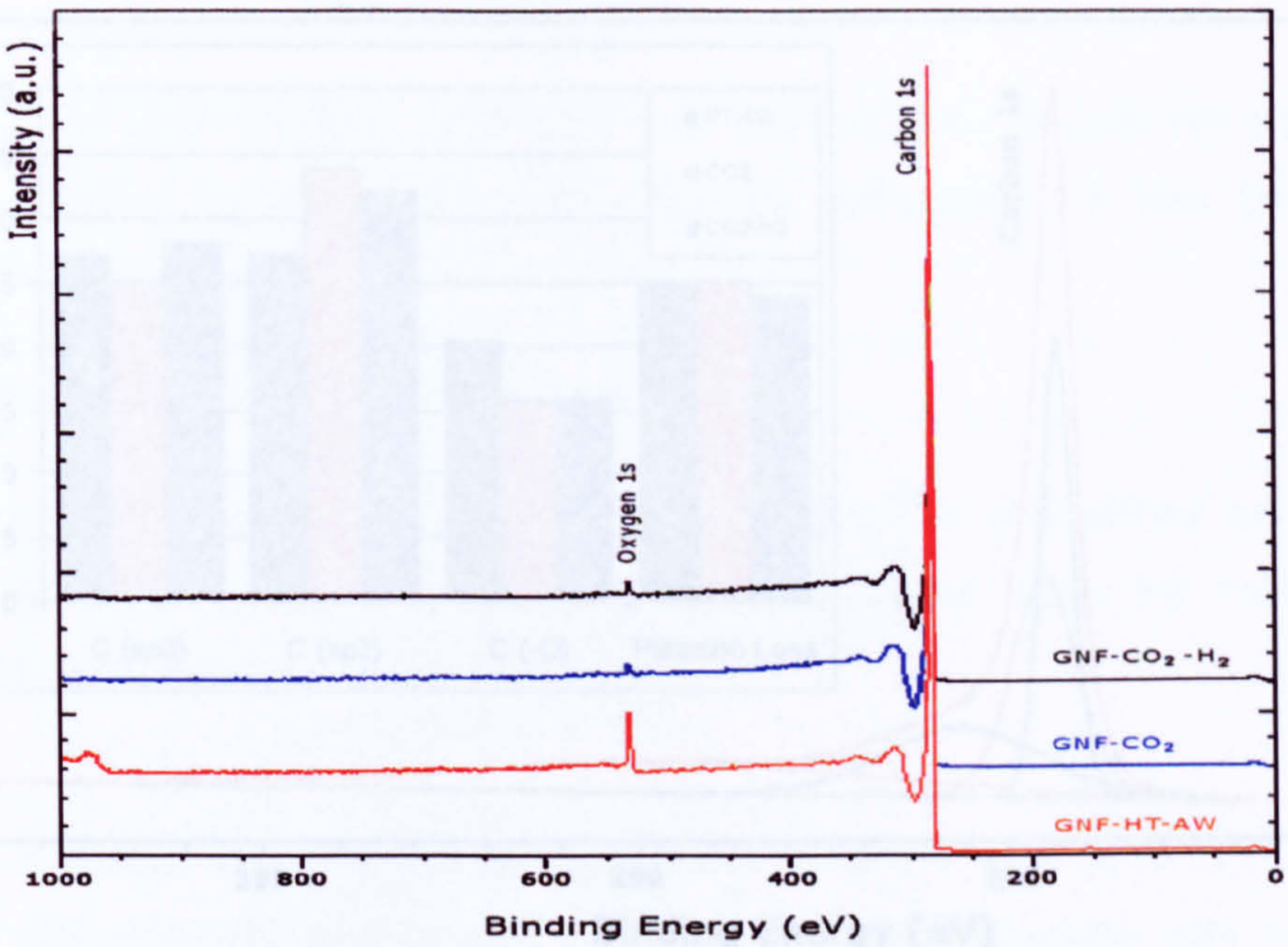

figure 6.3 - XPS Survey scan of GNF-HT-AW, GNF-CO_2 and GNF-CO_2-H_2.

From the high resolution scan of these peaks, the atomic and weight % of C and O in the samples has been calculated, present in table 6.3.

Sample	**Atomic (%)**		**Weight (%)**	
Element	Carbon 1s	Oxygen 1s	Carbon 1s	Oxygen 1s
GNF-HT-AW	85.4	14.6	81.4	18.6
GNF-CO_2	97.6	2.4	96.8	3.2
GNF-CO2-H_2	97.2	2.8	96.3	3.7

table 6.3 – XPS data showing atomic % and calculated weight % of C and O in GNF samples.

There is a large difference in the amount of oxygen present in GNF samples, depending on their previous treatment(s). GNF-HT-AW shows the largest concentration of oxygen in the sample of ~ 18 wt%, GNF-CO_2 and GNF-CO_2-H_2 show much lower concentrations, 3.2 and 3.7 wt% respectively.

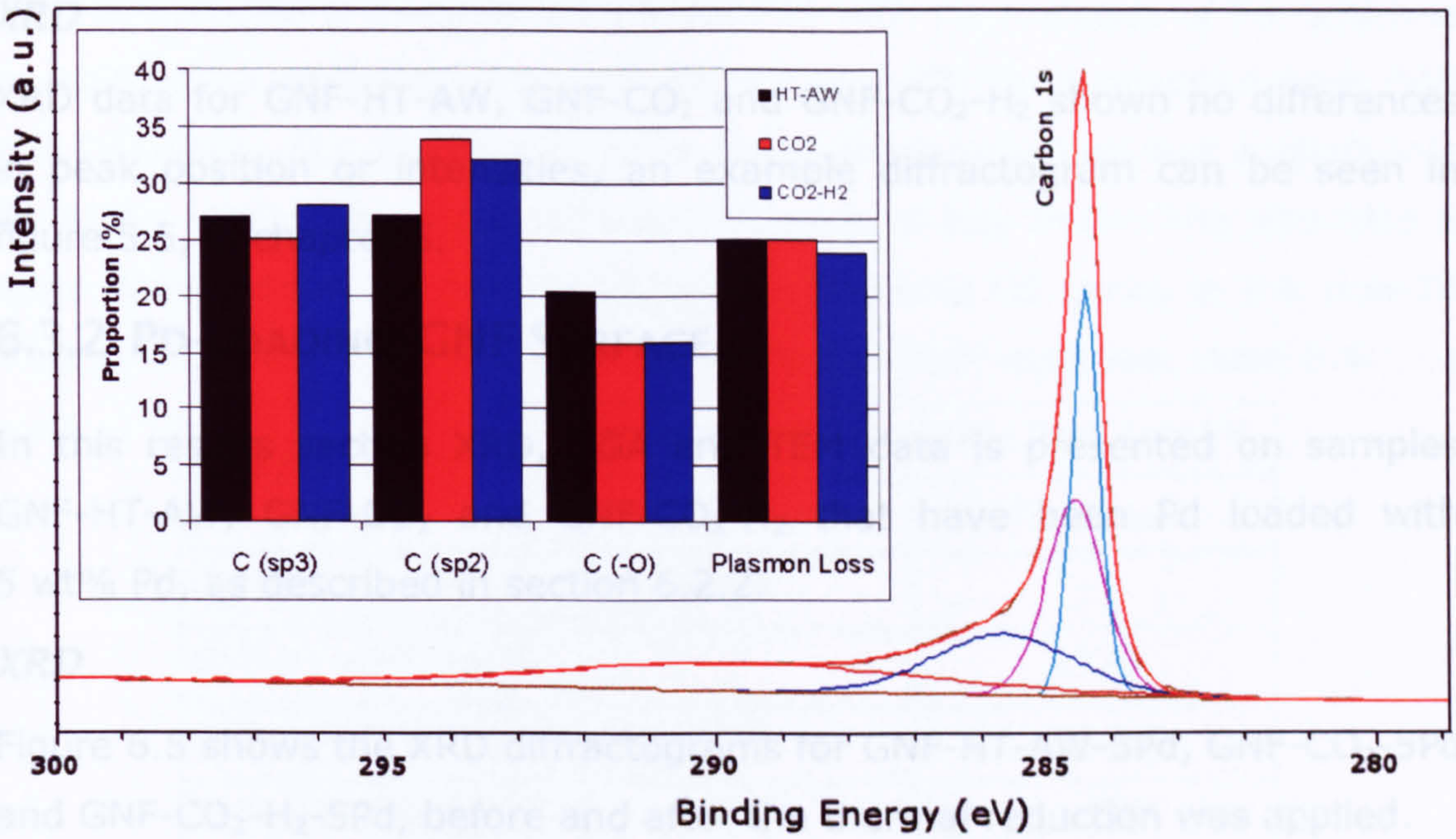

figure 6.4 – Example high resolution scan and peak fitting for Carbon 1s peak, (insert) comparison of proportion of components fitted to GNF-HT-AW, GNF-CO_2 and GNF-CO_2-H_2.

The model for C 1s was based on 4 different components (at binding energy); C sp^2 (284.4 eV), C sp^3 (284.6 eV), C bound to O (C-O, 285.6 eV) and Plasmon-loss (289.9 eV) and agrees with other authors who have undertaken XPS on GNFs.[194-197] The same peak positions were applied to each sample, with a comparison of the proportions of the samples shown in this insert in figure 6.4. Due to the broad π-π^* tail (component fitted to 289.9 eV), the presence of any C=O or C-O-x is masked, as these bonds introduce a small amount of asymmetry into the C 1s peak, thus distinguishing between C-O-x and C=O has not been undertaken. The single component (fitted at 285.6 eV) used to assess the carbon-oxygen interaction does indicate that there is more oxygen bound to carbon in GNF-HT-AW > GNF-CO_2 ≈ GNF-CO_2-H_2. In all three samples, the O 1s peak (not shown) was fitted with a single component (C-O), centred at 532.5 eV, with only the intensities of the peaks changing between samples, as shown in table 6.3.

XRD

XRD data for GNF-HT-AW, GNF-CO_2 and GNF-CO_2-H_2 shown no differences in peak position or intensities, an example diffractogram can be seen in figure 5.5, in chapter 5.

6.3.2 Pd-Loading: GNF Surface

In this results section XRD, TGA and TEM data is presented on samples GNF-HT-AW, GNF-CO_2 and GNF-CO_2-H_2 that have been Pd loaded with 5 wt% Pd, as described in section 6.2.2.

XRD

Figure 6.5 shows the XRD diffractograms for GNF-HT-AW-5Pd, GNF-CO_2-5Pd and GNF-CO_2-H_2-5Pd, before and after the thermal reduction was applied.

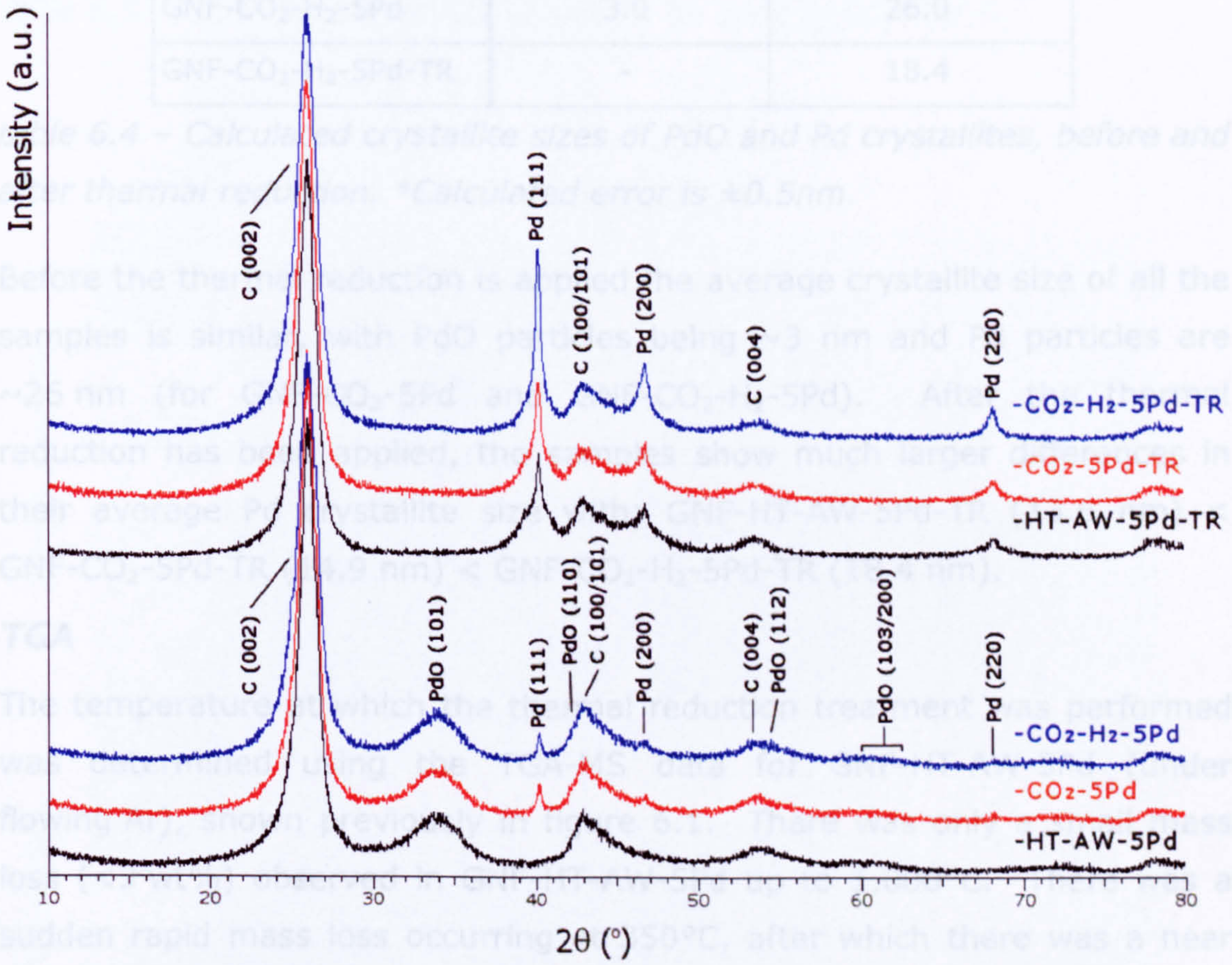

figure 6.5 – XRD diffractograms of GNF–HT-AW-5Pd, GNF-CO_2-5Pd and GNF–CO_2-H_2-5Pd before and after the thermal reduction treatment. Peaks are indexed to C, PdO and Pd, as indicated.

GNF-HT-AW-5Pd showed only PdO (and C) with no evidence of Pd, which is in contrast to GNF–CO_2-5Pd and GNF–CO_2-H_2-5Pd that exhibited both PdO and Pd peaks. For all samples, after the thermal reduction was applied only Pd peaks where observed, with no evidence of any PdO. The was also a large difference in the broadness of the PdO and Pd peaks in the non-TR state, which have been analysed using the Scherrer equation, table 6.4

Sample	Calculated Crystallite Size (nm)*	
	PdO (d_{101})	Pd (d_{111})
GNF-HT-AW-5Pd	2.8	-
GNF-HT-AW-5Pd-TR	-	13.6
GNF-CO_2-5Pd	2.8	25.4
GNF-CO_2-5Pd-TR	-	14.9
GNF-CO_2-H_2-5Pd	3.0	26.0
GNF-CO_2-H_2-5Pd-TR	-	18.4

*table 6.4 – Calculated crystallite sizes of PdO and Pd crystallites, before and after thermal reduction. *Calculated error is ±0.5nm.*

Before the thermal reduction is applied the average crystallite size of all the samples is similar, with PdO particles being ~3 nm and Pd particles are ~26 nm (for GNF-CO_2-5Pd and GNF-CO_2-H_2-5Pd). After the thermal reduction has been applied, the samples show much larger differences in their average Pd crystallite size with; GNF-HT-AW-5Pd-TR (13.6 nm) < GNF-CO_2-5Pd-TR (14.9 nm) < GNF-CO_2-H_2-5Pd-TR (18.4 nm).

TGA

The temperature at which the thermal reduction treatment was performed was determined using the TGA-MS data for GNF-HT-AW-5Pd (under flowing Ar), shown previously in figure 6.1. There was only a small mass loss (<3 wt%) observed in GNF-HT-AW-5Pd up to 1,000°C. There was a sudden rapid mass loss occurring at 350°C, after which there was a near linear mass loss up to 1,000°C.

TEM

The following three figures (figure 6.6, figure 6.7 and figure 6.8) show example TEM images from samples GNF–HT-AW-5Pd-TR, GNF-CO_2-5Pd-TR and GNF-CO_2-H_2-5Pd-TR. The figures show representative images of each

GNF sample (both low and high magnification), between 8-12 images per sample were collected and analysed with the GNFs being put into one of four categories; herringbone GNFs (with a diameter of 200-450 nm or 50-199 nm), and platelet GNFs (with diameters 200-450 nm or 50-199 nm), summarised in table 6.5. No GNFs were observed with diameters outside of these ranges (50-450 nm) and approximately 50 GNFs were observed for each sample.

GNF Type	**GNF Diameter Range**	**Nomenclature**
Herringbone	200-450 nm	Large Herringbone
Herringbone	50-199 nm	Small Herringbone
Platelet	200-450 nm	Large Platelet
Platelet	50-199 nm	Small Platelet

table 6.5 – Classification of GNF types to be used in Chapter 6.

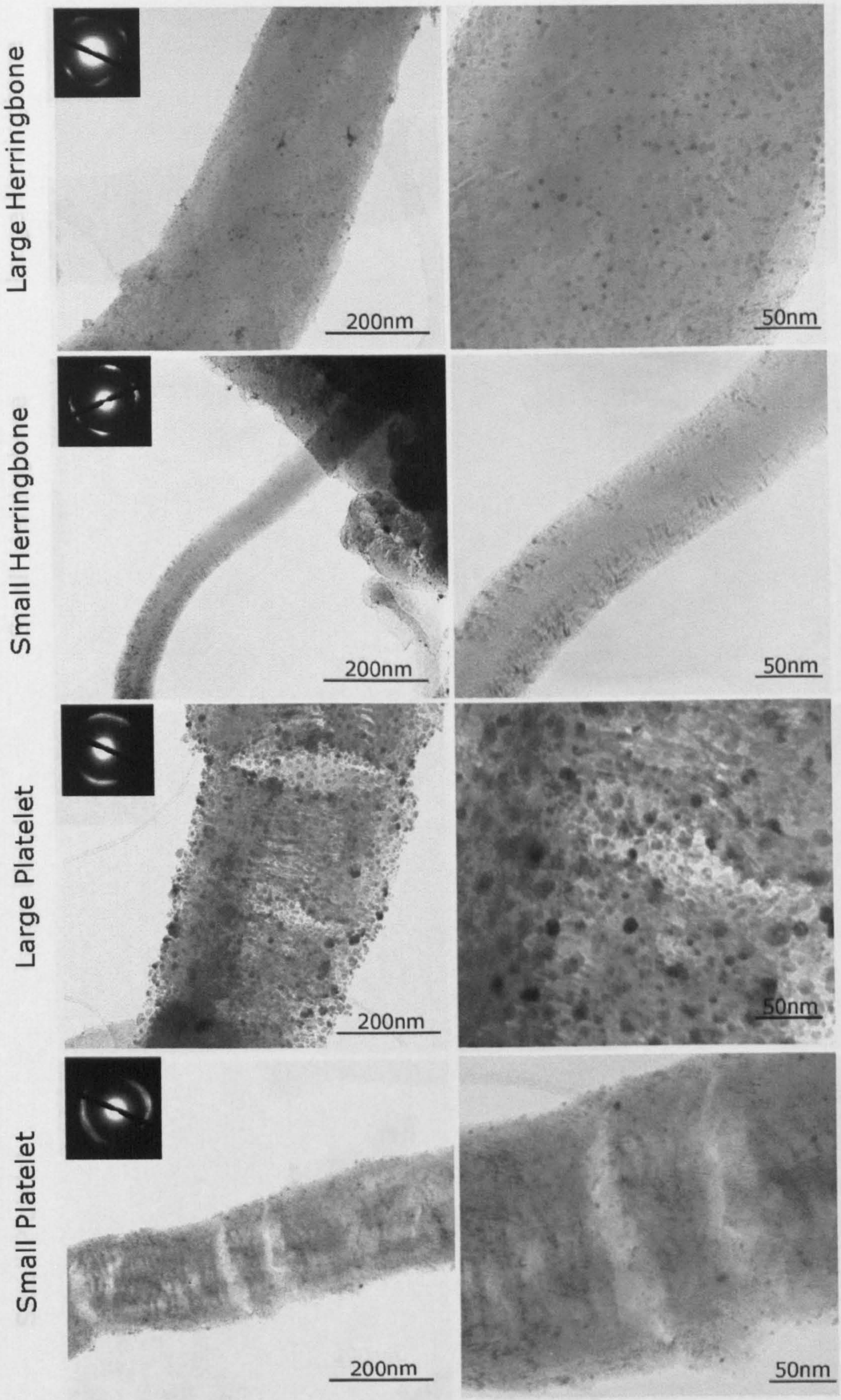

figure 6.6 – TEM images of GNF-HT-AW-5Pd-TR.

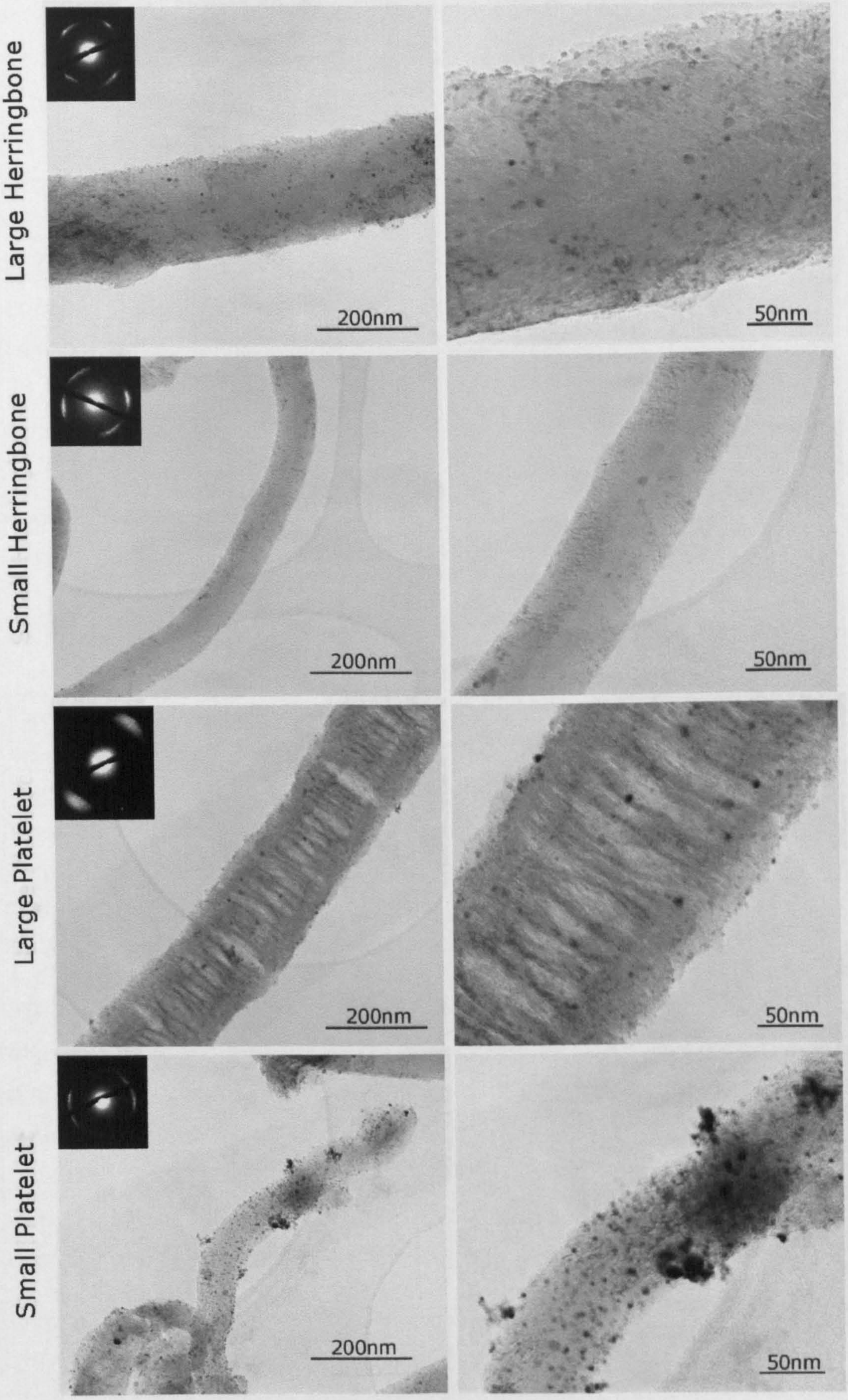

figure 6.7 – TEM images of GNF-CO_2-5Pd-TR.

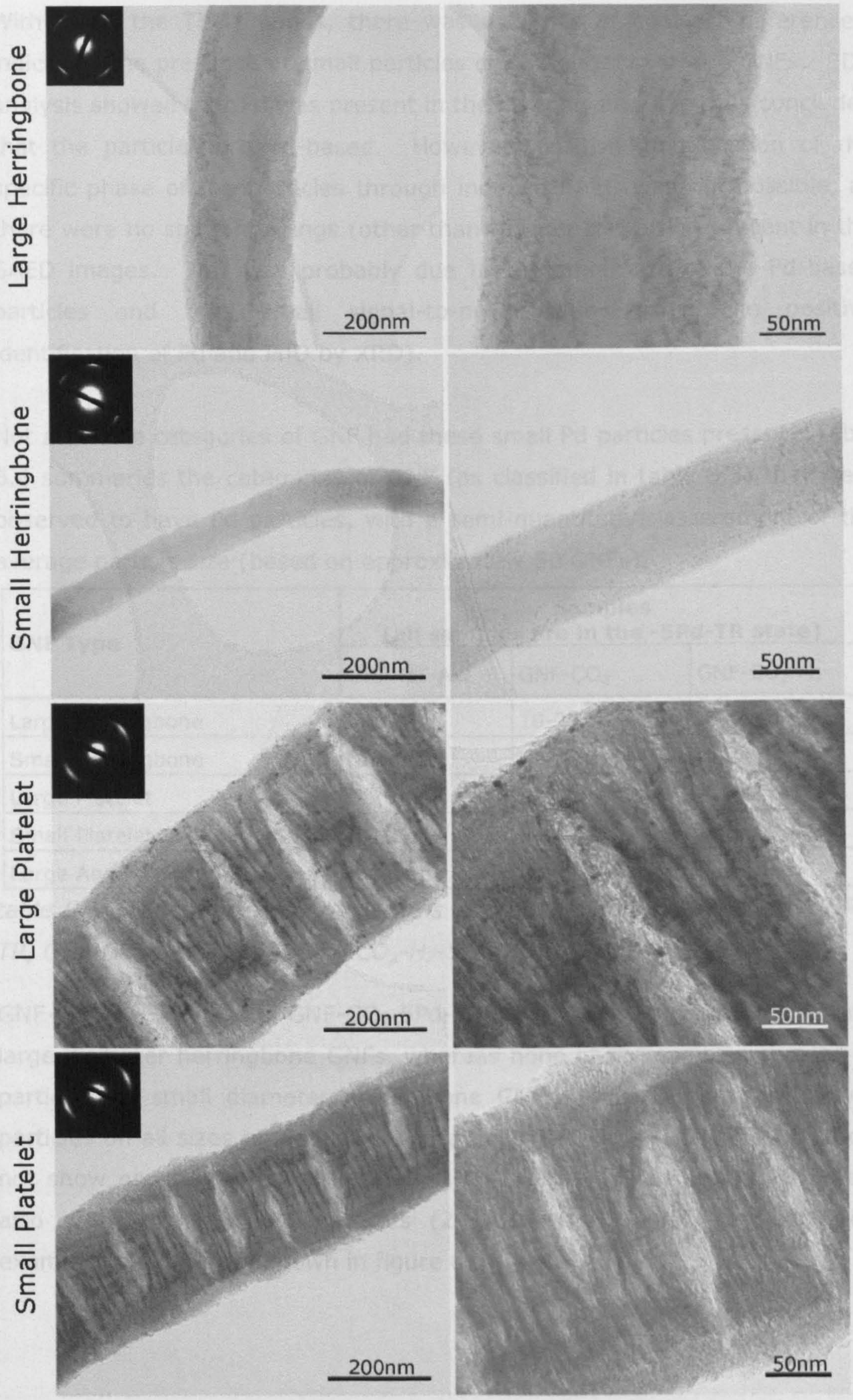

figure 6.8 – TEM images of GNF-CO_2-H_2-5Pd-TR.

With all of the TEM images, there was evidence of contrast differences, indicating the presence of small particles on the surfaces of the GNFs. EDX analysis showed that Pd was present in the samples and it is thus concluded that the particles are Pd-based. However, positive identification of the specific phase of the particles through indexed SAED was not possible, as there were no spots nor rings (other than that for the GNFs) present in the SAED images. This was probably due to the small size of the Pd-based particles and thus small signal-to-noise ratio (given the positive identification of Pd and PdO by XRD).

Not all of the categories of GNF had these small Pd particles present. Table 6.6 summaries the categories of GNF (as classified in table 6.5) that were observed to have Pd particles, with a semi-quantitative assessment of the average particle size (based on approximately 50 GNFs).

GNF Type	**Samples (all samples are in the -5Pd-TR state)**		
	GNF-HT-AW	GNF-CO_2	GNF-CO_2-H_2
Large Herringbone	5-10 nm	10-20 nm	None
Small Herringbone	None	None	None
Large Platelet	5-20 nm	5-10 nm	5-10 nm
Small Platelet	5-10 nm	5-10 nm	None
Large Agglomerated Particles	Present	Present	Present

table 6.6 – Summary of particle sizes and distribution in GNF-HT-AW-5Pd-TR, GNF-CO_2-5Pd-TR and GNF-CO_2-H_2-5Pd-TR.

GNF-HT-AW-5Pd-TR and GNF-CO_2-5Pd-TR showed some Pd particles on only large diameter herringbone GNFs, whereas none of the samples showed Pd particles on small diameter herringbone GNFs. All the samples showed particles on all sizes of platelet GNFs, except GNF-CO_2-H_2-5Pd-TR which did not show particles on small platelet GNFs. In all the samples there were also areas of larger Pd particles (20-200+ nm) found, representative examples of which are shown in figure 6.9.

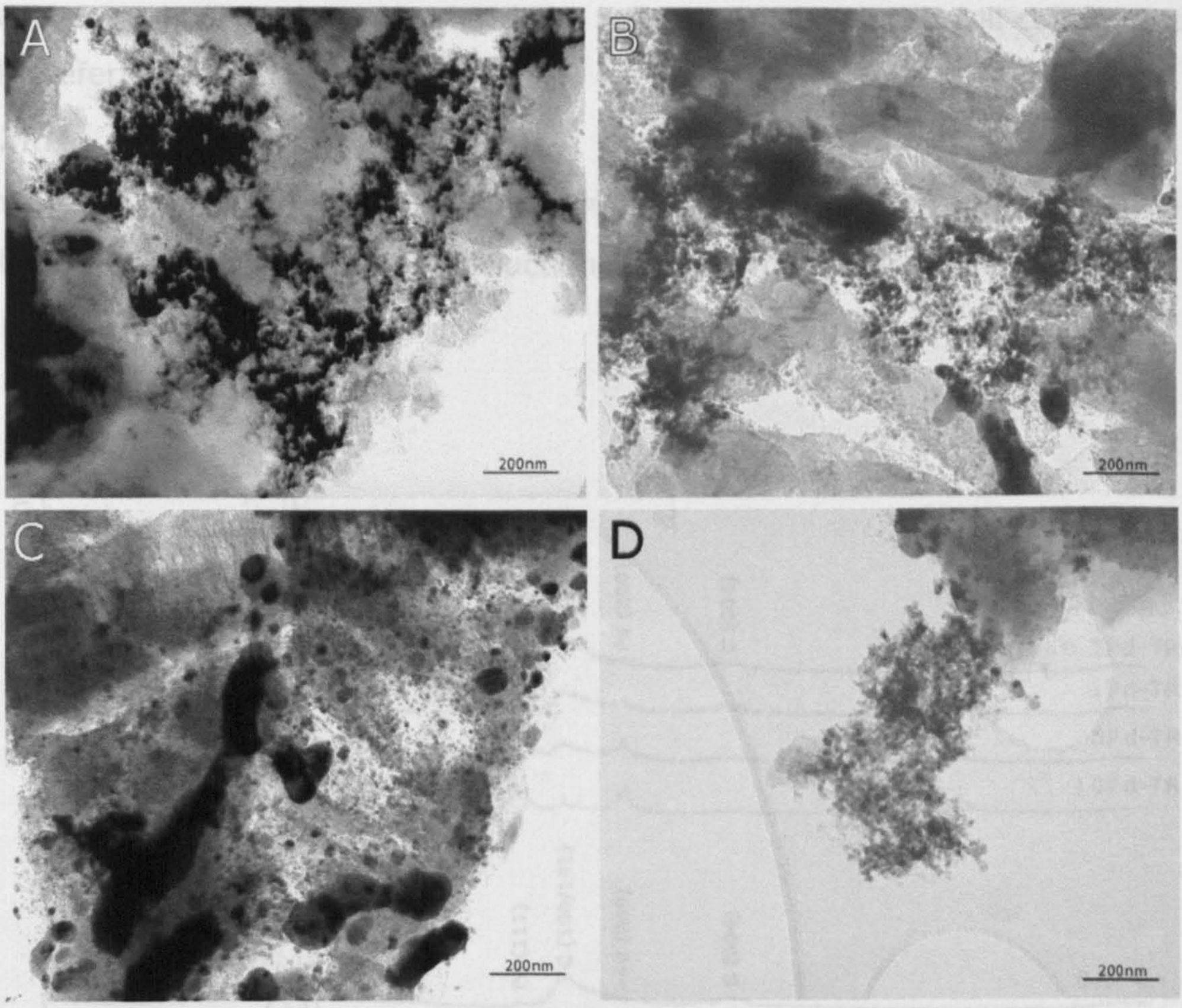

figure 6.9 – TEM images of large and agglomerated Pd particles in samples; (A) GNF-HT-AW-5Pd-TR, (B) GNF-CO_2-5Pd-TR, (C) GNF-CO_2-5Pd-TR and (D) GNF-CO_2-H_2-5Pd-TR.

All of the agglomerated Pd particles appeared to be deposited on regions of amorphous carbon present within the samples, rather than GNFs. Coherent large Pd particles (>200 nm in size) were present in GNF-HT-AW-5Pd-TR and GNF-CO_2-5Pd-TR but were not observed in GNF-CO_2-H_2-5Pd-TR. All three samples showed smaller (20-200 nm), interconnected Pd particles; images (C) and (D) illustrate these coherent and interconnected types of Pd particles, respectively.

6.3.3 Pd-Loading: Loading Level

In this section of the results XRD, XPS and TEM data for samples with different Pd loading levels (0.5, 1, 5 or 10 wt%) loaded onto GNF-CO_2-H_2 will be presented. The nomenclature for these samples is GNF-xPd, where x is the Pd loading level, for example, sample GNF-5Pd is equivalent to

GNF-CO_2-H_2-5Pd. Samples that have been thermal reduced will continue to be referred to with '–TR'.

XRD

The XRD diffractograms for GNF-0.1Pd, GNF-1Pd, GNF-5Pd and GNF-10Pd, before and after the thermal reduction, are shown in figure 6.10.

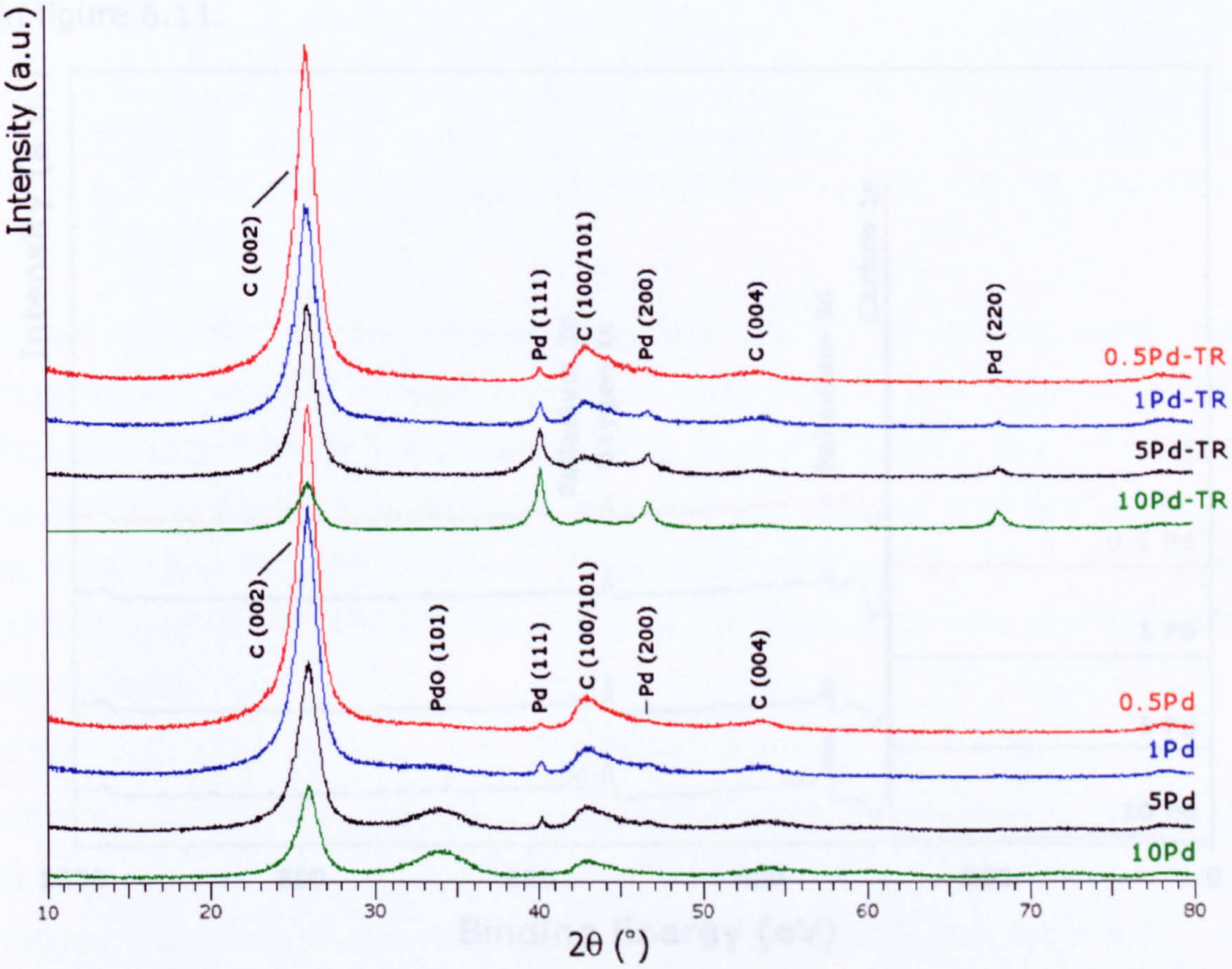

figure 6.10 – XRD for samples GNF-0.5Pd, GNF-1Pd, GNF-5Pd and GNF-10Pd before and after thermal reduction.

As seen in section 6.3.2 (figure 6.5), before the thermal reduction the loaded samples show a mixture of both Pd and PdO phases in their XRD diffractograms. For GNF-10Pd, there is a large PdO (d_{101}) reflection, with only a very small Pd (d_{111}) reflection. GNF-5Pd exhibited a smaller PdO reflection (d_{101}) but clear Pd (d_{111}) reflection. This trend was continued in sample GNF-1Pd, with there being only a very small PdO (d_{101}) reflection and clear Pd (d_{111}) reflection. However, for sample GNF-0.5Pd, there was no evidence of any PdO reflections and only a very small Pd (d_{111}) reflection.

After the thermal reduction, all samples show only Pd reflections; d_{111}, d_{200} and d_{220}. The intensity of these peaks relative to the graphite d_{002} peak follows the order GNF-10Pd > -5Pd > -1Pd > -0.5Pd.

XPS

XPS survey scans showed the presence of C, O and Pd in all samples, shown in figure 6.11.

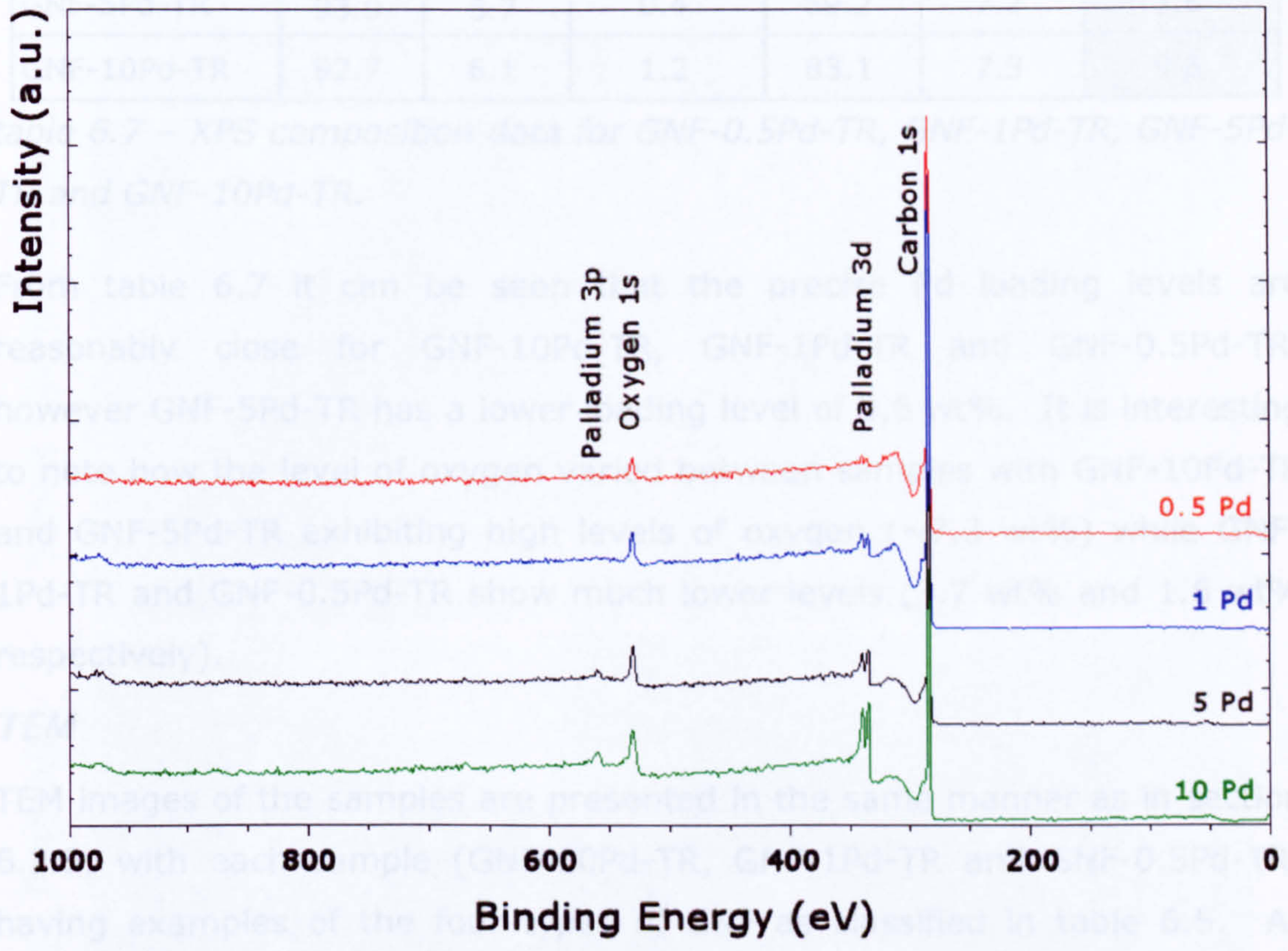

figure 6.11 – XPS Survey scans of Pd samples GNF-0.5Pd, GNF-1Pd, GNF-5Pd and GNF-10Pd (all in –TR state).

The atomic and weight composition data for the samples from the high resolution scans are shown in table 6.7.

Sample	**Atomic (%)**			**Weight (%)**		
Element (shell)	Carbon (1s)	Oxygen (1s)	Palladium (3d)	Carbons (1s)	Oxygen (1s)	Palladium (3d)
GNF-0.5Pd-TR	98.7	1.2	0.1	97.9	1.6	0.5
GNF-1Pd-TR	97.0	2.8	0.2	95.0	3.7	1.3
GNF-5Pd-TR	93.9	5.7	0.4	89.2	7.2	3.6
GNF-10Pd-TR	92.7	6.1	1.2	83.1	7.3	9.6

table 6.7 – XPS composition data for GNF-0.5Pd-TR, GNF-1Pd-TR, GNF-5Pd-TR and GNF-10Pd-TR.

From table 6.7 it can be seen that the precise Pd loading levels are reasonably close for GNF-10Pd-TR, GNF-1Pd-TR and GNF-0.5Pd-TR, however GNF-5Pd-TR has a lower loading level of 3.6 wt%. It is interesting to note how the level of oxygen varied between samples with GNF-10Pd-TR and GNF-5Pd-TR exhibiting high levels of oxygen (~7.3 wt%) while GNF-1Pd-TR and GNF-0.5Pd-TR show much lower levels (3.7 wt% and 1.6 wt% respectively).

TEM

TEM images of the samples are presented in the same manner as in section 6.3.3, with each sample (GNF-10Pd-TR, GNF-1Pd-TR and GNF-0.5Pd-TR) having examples of the four types of GNF as classified in table 6.5. As samples GNF-CO_2-H_2-5Pd-TR and GNF-5Pd-TR are equivalent samples, the TEM data in figure 6.8 shall also be take into consideration within this section as GNF-5Pd-TR and GNF-CO_2-H_2-5Pd-TR are equivalent.

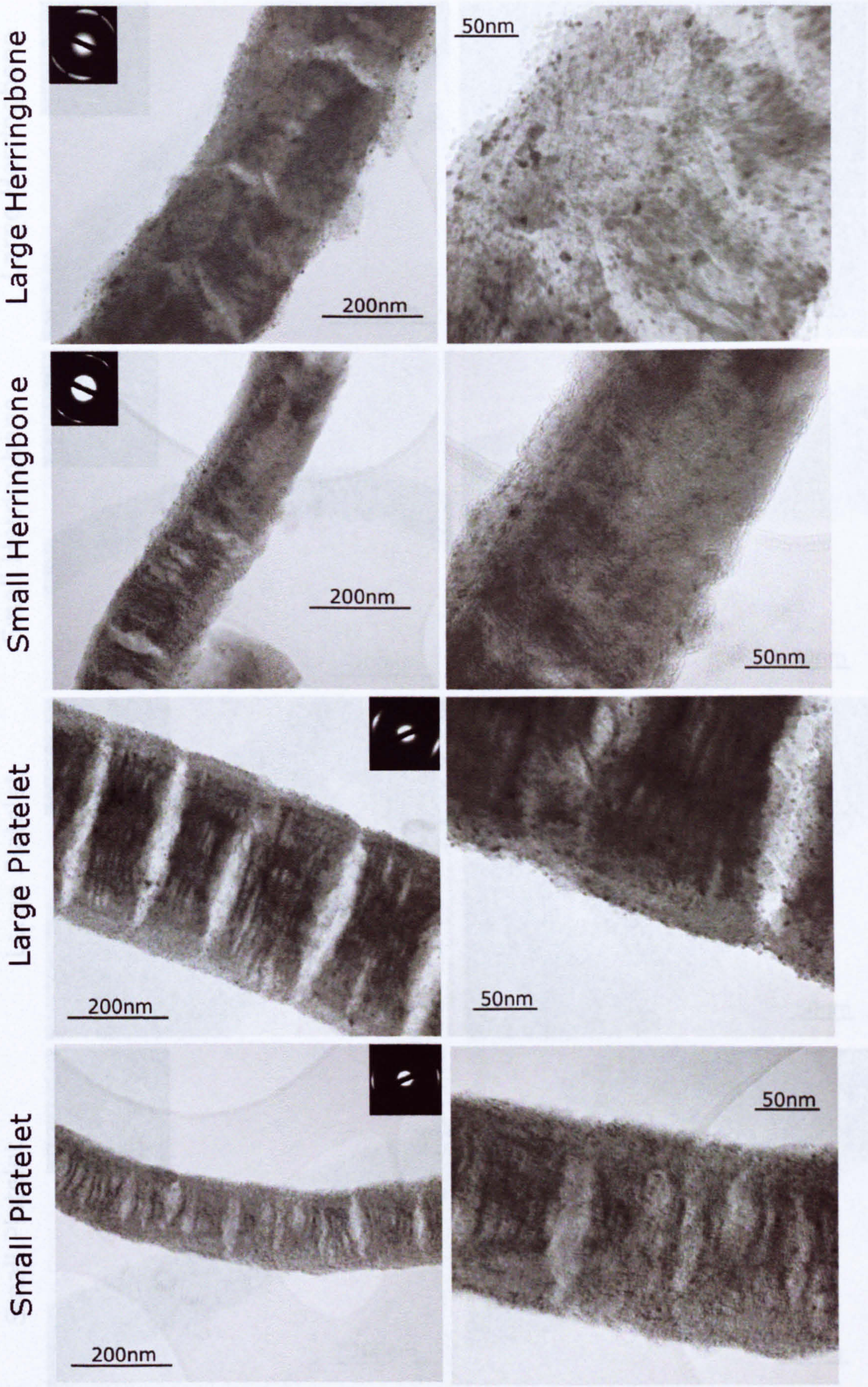

figure 6.12 – TEM images of GNF-10Pd-TR.

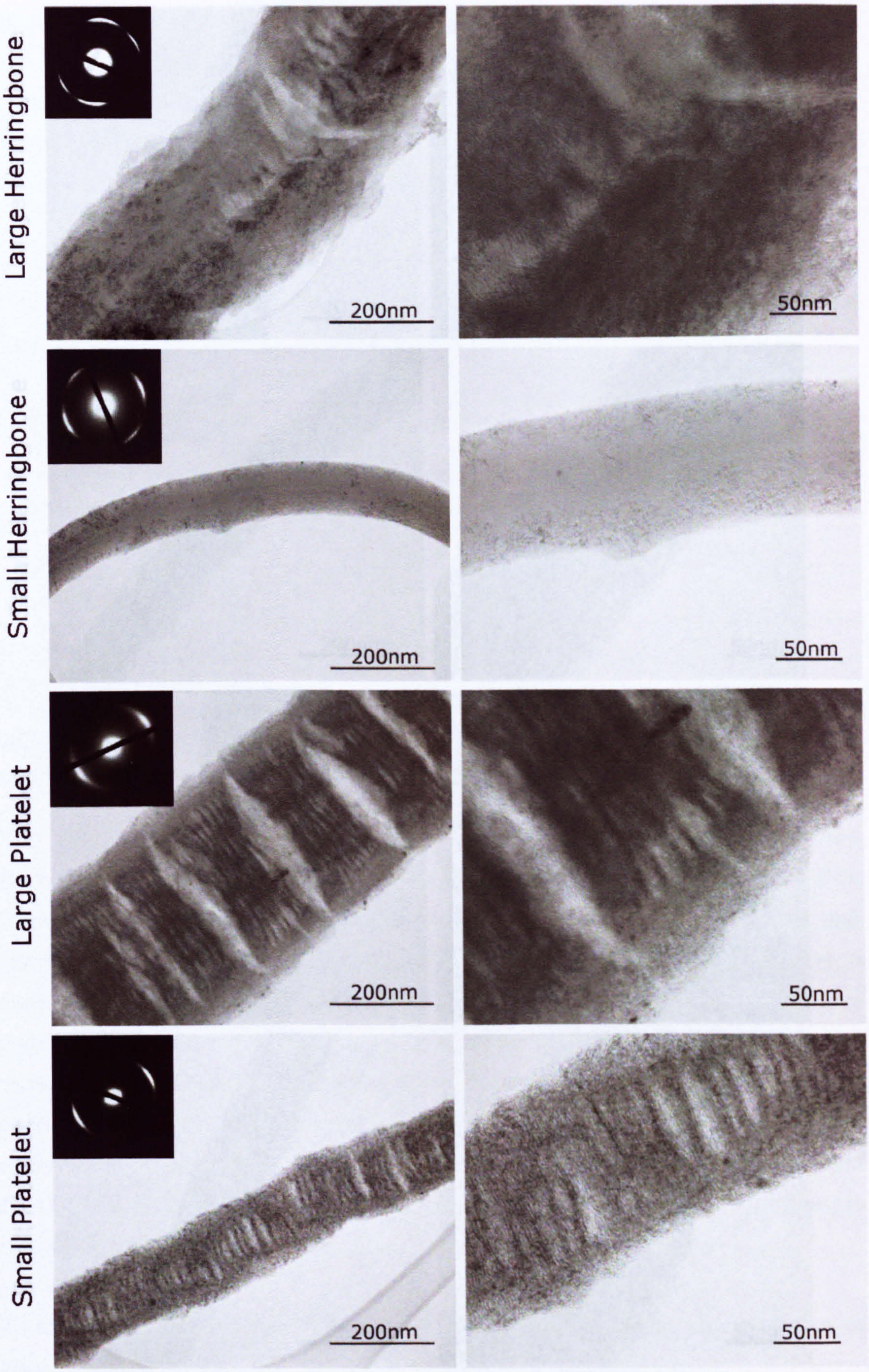

figure 6.13 – TEM images of GNF-1Pd-TR.

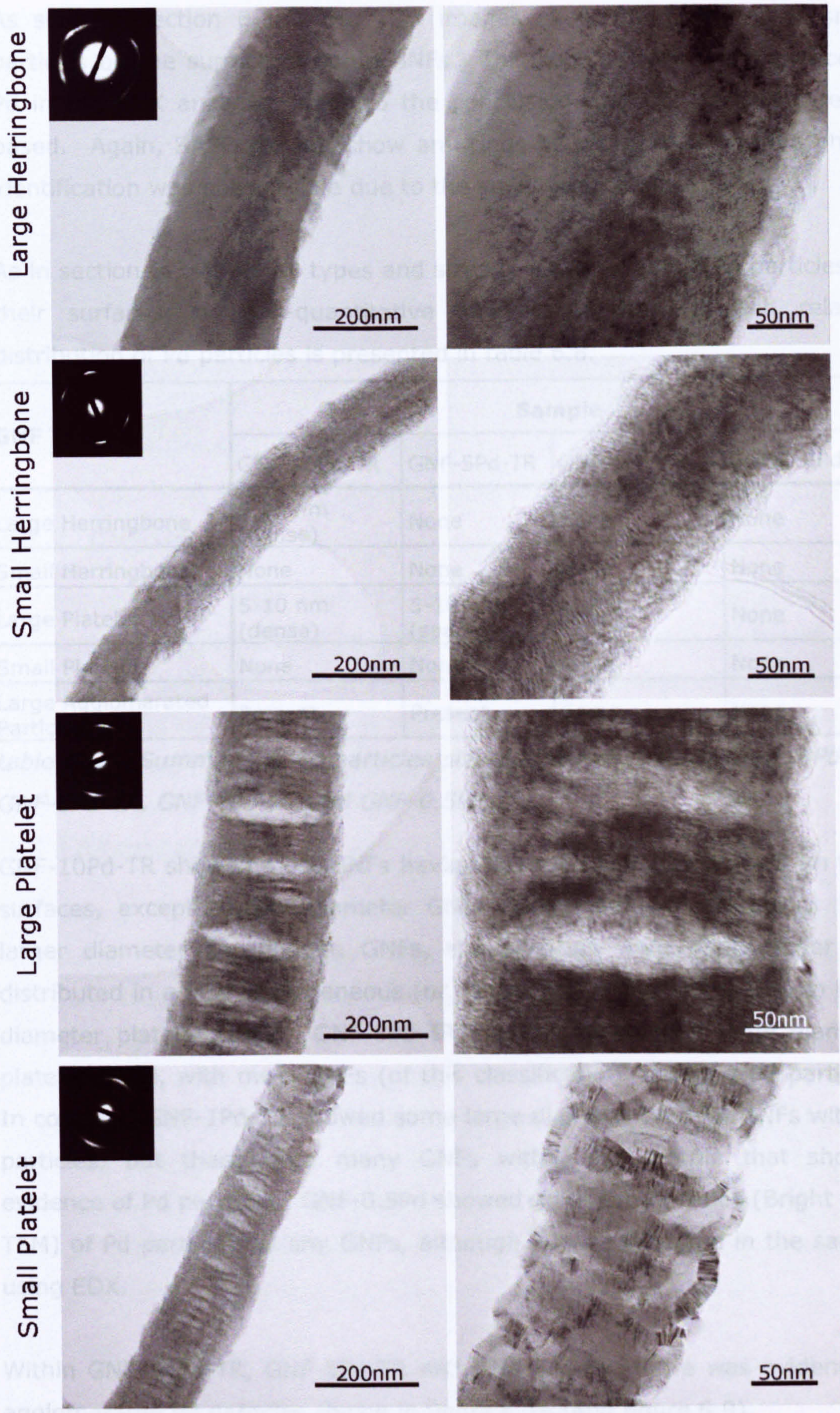

figure 6.14 – TEM Images of GNF-0.5Pd-TR.

As seen in section 6.3.2, the TEM images show the presence of small particles on the surface of some GNFs. This coupled with the presence of Pd in the EDX analysis, leads to the conclusion that the particles are Pd based. Again, SAED did not show any rings or spots, thus positive phase identification was not possible due to the small particle size.

As in section 6.3.2, not all types and sizes of GNFs exhibited Pd particles on their surfaces; a semi-quantitative analysis of the size and relative distribution of Pd particles is presented in table 6.8.

GNF Type	**Sample**			
	GNF-10Pd-TR	GNF-5Pd-TR	GNF-1Pd-TR	GNF-0.5Pd-TR
Large Herringbone	5-20 nm (dense)	None	None	None
Small Herringbone	None	None	None	None
Large Platelet	5-10 nm (dense)	5-10 nm (sparse)	Some	None
Small Platelet	None	None	None	None
Large Agglomerated Particles	Present	Present	Some	None

table 6.8 – Summary of Pd particles size and distribution in GNF-10Pd-TR, GNF-5Pd-TR, GNF-1Pd-TR and GNF-0.5Pd-TR.

GNF-10Pd-TR showed most GNFs having some Pd particles present on their surfaces, except smaller diameter GNFs (herringbone or platelet). With larger diameter herringbone GNFs, the particles were often larger and distributed in a less homogeneous (or consistent) manor compared to large diameter platelet GNFs. GNF-5Pd-TR showed Pd on only large diameter platelet GNFs, with most GNFs (of this classification) showing Pd particles. In contrast, GNF-1Pd-TR showed some large diameter platelet GNFs with Pd particles, but there were many GNFs within the sample that showed evidence of Pd particles. GNF-0.5Pd showed no direct evidence (Bright Field TEM) of Pd particles on any GNFs, although Pd was detected in the sample using EDX.

Within GNF-10Pd-TR, GNF-5Pd-TR and GNF-1Pd-TR, there was evidence of agglomerated Pd particles shown in figure 6.15 (and figure 6.9).

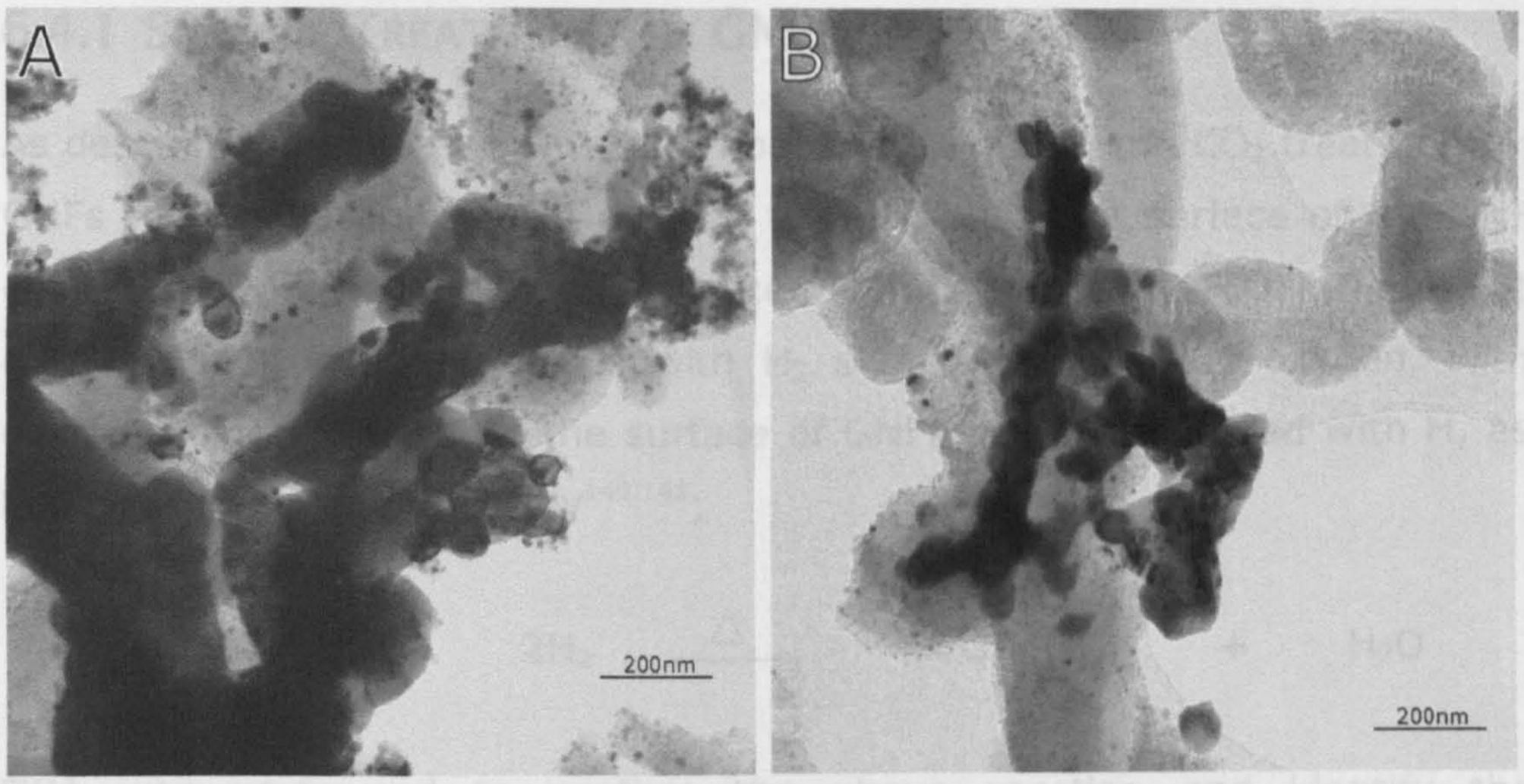

figure 6.15 – TEM images of agglomerated Pd particles in (a) GNF-10Pd-TR and (b) GNF-1Pd-TR.

In GNF-10Pd-TR and GNF-5Pd-TR several areas of coherent and non-coherent agglomerated Pd particles were present (see section 6.3.2). However, for GNF-1Pd-TR only a single example of an area of agglomerated particles could be found, shown in figure 6.15. There was no evidence of any Pd particles either agglomerated or attached to GNFs in GNF-0.5Pd-TR.

6.4 Discussion

The aim of this investigation was to prepare GNFs with Pd particles distributed onto their surfaces (using the incipient wetness technique) for the purpose of accessing their hydrogen uptake capacity (and adsorption mechanism). Two parameters were varied for difference purposes; GNF surface states were used to investigate the effect on the distribution of the Pd particles, while the level of Pd loading was varied so that the effect on hydrogen uptake can be assessed (chapter 7). Thus the following discussion will focus on (and sectioned into); structure(s) of GNF after surface treatments (6.4.1), the effect of surface state on Pd distribution (6.4.2) and the Pd distribution at different loading levels (6.4.3).

6.4.1 Surface Treatments of GNFs

As described in chapter 5, it was proposed that during the CO_2 treatment of GNFs to remove amorphous carbon, that the resultant surface of the GNF consisted of graphene edges terminated with O groups [GNF(O)], figure 5.1 (page 76). Reacting GNF(O) with H_2 should remove any oxygen, with oxygen being replaced on the surface of GNFs being terminated with H, as has been reported previously[140,141];

$$GNF(O) + 2H_2 \xrightarrow{\Delta} GNF(H) + H_2O$$

TGA was performed to confirm the above reaction and identify the temperature at which it occurs for sample GNF-CO_2. However, the TGA data (figure 6.2) does not show conclusive results. Only a very small mass loss (~1.5 wt%) up to 900°C, albeit with a 5% hydrogen gas environment (due to limitations of the TGA apparatus). There was an observed increase in the m/z = 18 fragment, corresponding to H_2O, observed at ~550°C. However, there was no obvious mass change (or heat flow differential), which would be expected with a reaction, although there was a subtle increase in gradient indicating a possible reaction. It is more likely that there was a small proportion of oxygen in the TGA atmosphere and that at 550°C the gaseous reaction of H_2 and O_2 was occurring, however there was no trace of m/z 32 (O_2) in the mass spectrum data. The only sudden mass loss observed was at 280°C over a 20 second period, which is most likely to be an instrument error (glitch), especially given that there was not change in the m/z values.

Considering the XPS elemental composition data; GNF-CO_2 shows only a small amount of oxygen ~3.2 wt% present in the sample, the same oxygen content as GNF-CO_2-H_2 (~3.7 wt%) when considering experimental limits. This would indicate that there was no reaction or no removal of surface oxygen, or that there was no surface oxygen present after the CO_2 treatment.

Given the uncertainty of the hydrogen reaction and thus precise reaction temperature, samples were treated under flowing Ar at 800°C as up to this temperature direct carbon gasification of the GNF is unlikely to occur ($\Delta G \sim -14$ kJ mol^{-1} at 800°C). Especially as the reaction was conducted using a relatively short exposure time and that there was no catalyst present.[198,199] The mass spectrum data (not shown) for the bulk hydrogen treatment of GNF did not show any trace of m/z 13-16, which would correspond to CH_4, the most likely gasification products (mass spectrum fragments; CH_4, CH_3, CH_2 and CH).

6.4.2 Effect of Surface State on Pd Distribution

The use of the three samples; GNF-HT-AW, GNF-CO_2 and GNF-CO_2-H_2, was undertaken to examine if different Pd distributions on the GNFs would be produced. A 5 wt% loading level was chosen to be a large enough quantity to observe any catalytic effect of Pd on hydrogen storage properties of GNFs, while there would be a negligible effect if $PdH_{0.67}$ was formed during hydrogenation.[200,201]

XRD data (figure 6.5) shows that for all samples, after the deposition of Pd, PdO was shown to be present, with a broad reflection corresponding to the d_{101} reflection. For GNF-CO_2-5Pd and GNF-CO_2-H_2-5Pd there are also peak corresponding to Pd metal, which indicates that the deposited Pd was present in two phases (Pd metal and PdO) in those samples. A possible explanation for this would be that the formation of PdO is due to reaction with surface oxygen present in the GNF. As GNF-HT-AW has a much larger surface oxygen content (18.6 wt% for XPS data, table 6.3) only PdO was deposited, whereas both Pd and PdO were deposited in GNF-CO_2 and GNF-CO_2-H_2, both of which had much lower surface oxygen content (3.3 wt% and 3.7 wt% respectively). This would also explain why it is necessary to acid wash GNFs (thus introducing oxygen species[202]) as has been reported by *Marella et al* and *Baker et al.*[143,197]

After the thermal reduction treatment had been applied, the XRD data indicated that only Pd was present in all three samples. The TGA data for the reaction shows a clear and reproducible sudden mass loss (albeit small

at only ~0.5 wt%) at ~350°C followed by a steady mass loss. Thus, it is reasonable to assume that using the given reaction conditions and PdO is converted in Pd.

The TEM data showed that for all samples, Pd particles have been deposited onto the surface of some of the GNFs. However, the TEM also showed larger agglomerated particles present in the three samples. From a general assessment of the size of the Pd particles (using the TEM), it is clear that small particles (<20 nm, attached to the GNF surfaces) and larger 'agglomerated' particles (>100 nm) are present, both before (not shown) and after the thermal reduction (figure 6.6 - figure 6.9). However, from the XRD crystallite size calculation, upon initial deposition; PdO particles are small (3 nm), while Pd particles are much larger (26 nm). This would indicate that while some Pd particles were directly deposited onto the GNF surface, a proportion was deposited as agglomerated particles (as no particles larger than 20 nm were observed on the GNF surface in the TEM). This further validates the need for surface oxygen in deposition process.

The TEM data (figure 6.6 - figure 6.8) also indicates that the Pd particles adhere preferentially to different types and sizes of GNFs, as well as in different quantities depending on the surface treatment. For GNF-HT-AW-5Pd-TR, there is some adhesion of Pd particles to larger herringbone GNFs but with the highest density of particles being adhered to larger platelet GNFs. A similar observation can be seen with GNF-CO_2-5Pd-TR, although there also appears to be adhesion of particles to smaller platelet GNFs and less dense distribution of particles in larger (platelet and herringbone) GNFs. In further contrast, GNF-CO_2-H_2-5Pd-TR shows only large platelet GNFs having any Pd particle attachment. Assuming that surface oxygen is the critical requirement in order to obtain Pd particles on the surface of GNFs, these results would indicate that amount of (effective) surface oxygen on each sample is ordered; GNF-HT-AW-5Pd-TR > GNF-CO_2-5Pd-TR > GNF-CO_2-5Pd-TR. The difference in adhesion between GNF-CO_2-5Pd-TR and GNF-CO_2-H_2-5Pd-TR indicates that the hydrogen treatment is having some effect on the surface of the GNFs, despite them having very similar oxygen contents. Unfortunately, due to the inconclusive data that is available for

the treatment, it is difficult to draw any meaningful conclusions. However, it is likely to be due to the re-ordering of the oxygen species, for example from C=O to C-OH. It is clear that the treatment does effect the distribution of Pd particles and effectively only adheres particles to large diameter platelet GNFs. This is not an un-desired effect, as it allows any difference between herringbone and platelet GNFs to be assessed if the Kubas uptake mechanism is prevalent.

6.4.3 Pd Coating Level

In order to investigate the potential for Pd to act catalytically on the hydrogen uptake in GNF, samples were prepared with varying levels of Pd loading. GNF-CO_2-H_2-5Pd-TR was chosen as it offers selectivity of the Pd particle adhesion and thus any hydrogen uptake effects would only be due to large diameter platelet GNFs. The use of the four different Pd concentrations (0.5 wt%, 1 wt%, 5 wt% and 10 wt%) should allow any catalytic effect to be observed, but again with little influence from any $PdH_{0.67}$ that maybe formed during hydration.

The XRD data for the four samples GNF-10Pd-TR, GNF-5Pd-TR and GNF-1Pd-TR and GNF-0.5Pd-TR show only Pd peaks. The GNF-1Pd and GNF-0.5Pd samples also only showed Pd metal (i.e. no PdO) before the thermal reduction. This could imply that Pd is able to adhere to the GNFs without reacting with surface oxygen, however the TEM evidence shows that no Pd particles were being adhered to the surface of the GNF in these samples. However, GNF-10Pd shows only PdO before the thermal reduction, which indicates that oxygen is being obtained from a source other than the GNFs surface when (relatively) large quantities of Pd are involved.

The XPS data in table 6.7 shows that the actually achieved concentrations of the samples is roughly in line with expected coating levels, although slightly lower (3.6 compared 5.0) for GNF-5Pd-TR. For the purposes of investigation the catalytic effect of Pd on hydrogen uptake, there is significant difference between the samples prepared. It is also found when examining the TEM data that the Pd particles only adheres to large platelet GNFs in GNF-5Pd-TR and GNF-1Pd-TR, with GNF-0.5Pd-TR showing no

direct evidence of the location of any Pd in the sample (only its presence from EDX and XPS). Unfortunately, for GNF-10Pd there is also some adhesion of particles to large herringbone GNFs, which will need to be considered when making comparisons with regards to hydrogen uptake mechanisms. The reason for this adhesion cannot be fully eluded to based on the experiment data collected, although it probably due to another mechanism of Pd attachment in which oxygen is involved but from a source other than the GNF surface (see above).

6.5 Conclusion

In has been shown that it is possible to coat GNFs with Pd particles, and that through control of the GNF surfaces this can be done preferentially into platelet GNFs. Using the incipient wetness technique, the amount of Pd and the amount of surface oxygen present in the GNF will determine whether Pd or PdO phase is formed in the coating; any PdO can be reduced to Pd using a simple heat treatment.

6.6 Summary

Two sets of Pd-doped samples have been prepared as detailed in table 6.2 and will be used in Chapter 7 to determine the uptake mechanism prevalent in Pd-coated GNFs.

7 Hydrogen Storage in GNFs

7.1 Aim

This chapter will report the hydrogen uptake capacity of the GNFs prepared and described in Chapters 4-6. As described in section 2.7 and there are several proposed mechanisms by which hydrogen can be adsorbed or adsorbed onto GNFs. By carefully selecting and synthesising different GNF materials in chapters 4-6, any hydrogen uptake observed should allow a much greater insight and understanding into the hydrogen uptake mechanisms in GNFs to be gained. There are principally 2 sets of samples which have been synthesised, with associated mechanisms that are relevant outlined below.

Surface State

The first set of samples will allow the effect of surface state to be assessed. This is achieved through applying several post-treatments to GNF samples, creating various surface states; as-prepared GNFs, removal of re-orientated graphitic surface (from as-prepared state), introduction of surface oxygen functional groups and removal of these groups with hydrogen. These sample should show an improvement in hydrogen uptake if adsorption is via simple adsorption onto the internal surfaces of the graphene layers within the GNFs ('slit-pore' mechanism).[203-205] These samples will also allow any effect of residual Fe (Fe_3C) or Ni from the CVD growth catalyst to be assessed (with GNFs in the as-prepared state), which some groups have suggested can occur.[206,207]

Effect of Pd

The second set of samples will allow the effect of Pd on GNFs to be assessed. Within this, different distribution of Pd on the GNFs surfaces and different levels of Pd loading shall be investigated. This will identify whether or not the hydrogen is bound only to the Pd (i.e. producing a higher hydrogen uptake with a large surface-area of Pd particles) or if the Pd acts as a catalyst to allow hydrogen to be bound to the internal layers of the GNFs

(i.e. the hydrogen uptake increases over a given time relative to the amount of Pd present).

For all samples, the hydrogen uptake measurements will be determined using the volumetric method, on apparatus designed and constructed by the author. In order to ensure any effects due to high (nitrogen) surface area physisorption, the BET surface area of samples will also be measured. The results of these measurements will subsequently be discussed in light of the current literature and conclusions drawn.

7.2 Experimental

As all of the samples used here have been characterised in chapters 4, 5 and 6, only BET surface area and hydrogen uptake capacity shall be reported in the present chapter. The details of these experiments are given below; all samples are referred to as-per the nomenclature described in chapters 5 and 6.

7.2.1 BET Surface Area

BET analysis was carried out on an automated 'Autosorb-1' supplied by Quantachrome. Samples were prepared by placing a known mass of sample into a sample tube, then degassing at 300°C overnight (~16 h) under vacuum, achieving a pressure around $1x10^{-9}$ bar. The adsorption measurement was then undertaken at 77K using N_2 as adsorbate gas.

BET was run on all samples prior to hydrogen uptake measurements being carried out. A full adsorption and desorption isotherm was recorded for each sample, however, only the linear proportion of the isotherm with P/P_0 = 0.05, 0.08, 0.11, 0.13, 0.15, 0.18, 0.20, 0.23, 0.25, 0.28 and 0.30 was used to determine the BET surface area. An example of the full isotherm and region where the BET surface area was determined from is given below in figure 7.1.

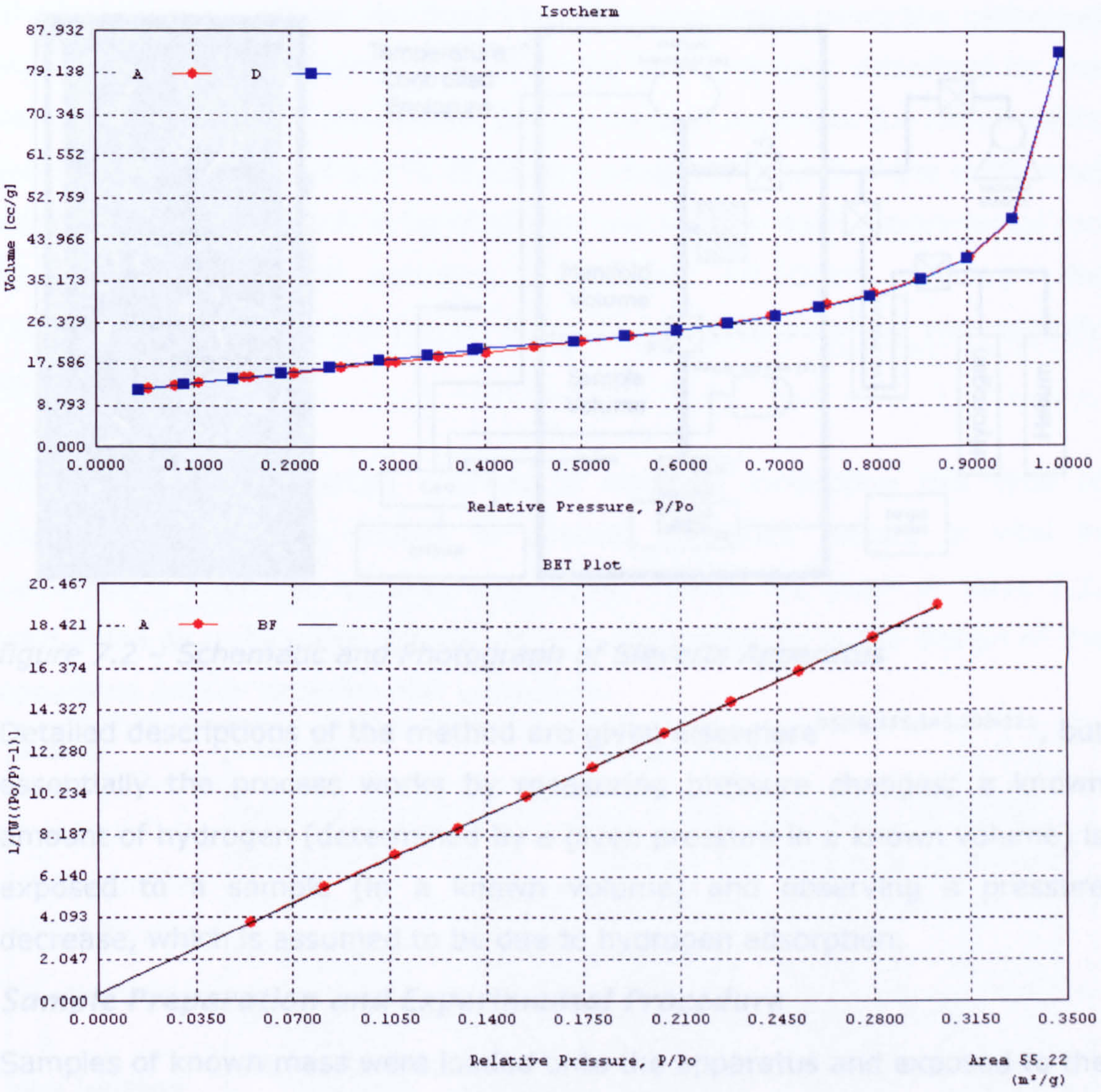

figure 7.1 – Example isotherm for Ni-GNF-HT-AW and BET plot showing P/Po points used for BET surface area.

7.2.2 Hydrogen Uptake Measurement - Sieverts

The Sieverts method was used to volumetrically determine the hydrogen uptake capacity of samples. Experiments were carried out on a personally constructed Sieverts apparatus, shown in figure 7.2.

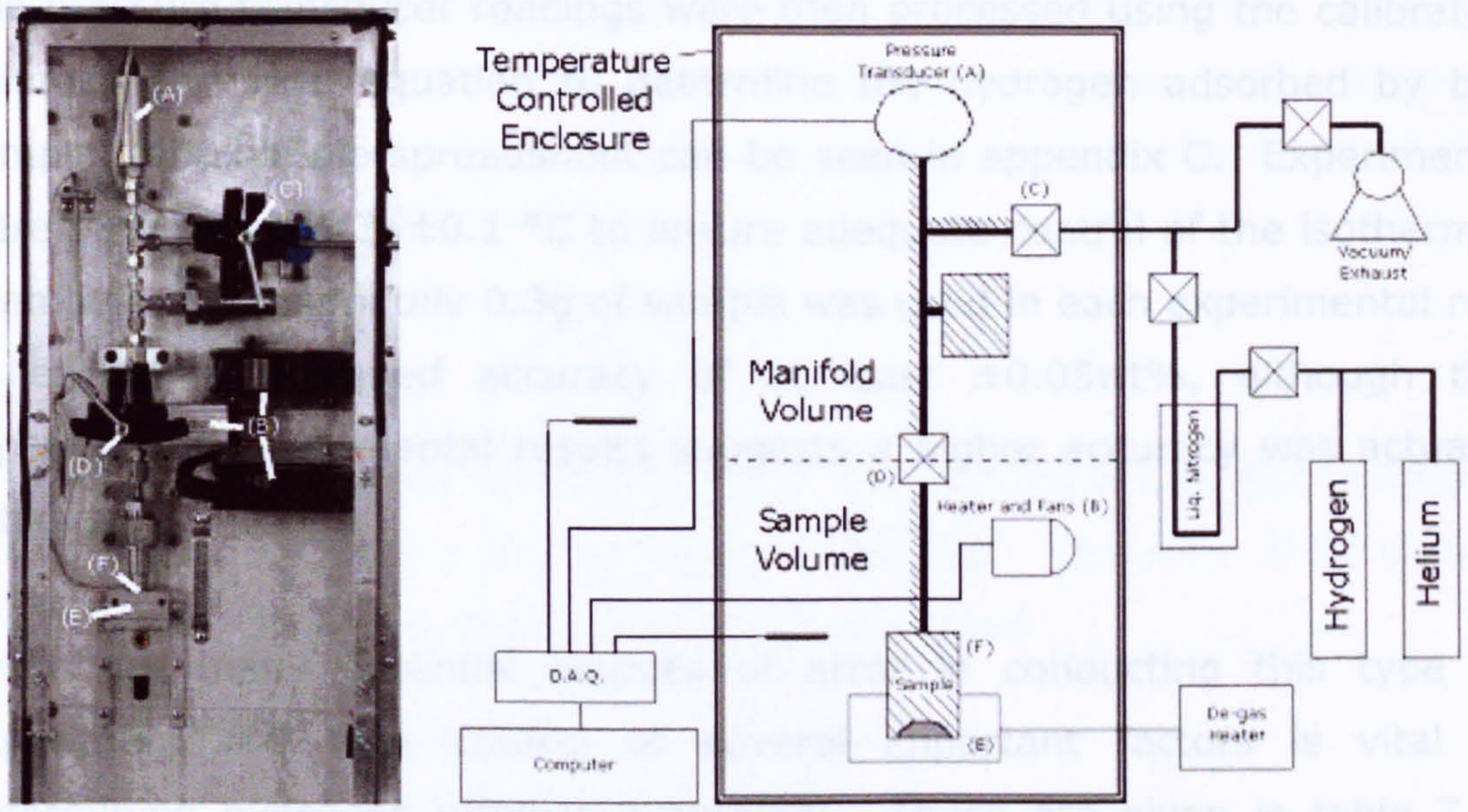

figure 7.2 – Schematic and Photograph of Sieverts Apparatus

Detailed descriptions of the method are given elsewhere[95,98,115,143,208-211], but essentially the process works by measuring pressure changes; a known amount of hydrogen (determined by a given pressure in a known volume) is exposed to a sample (in a known volume) and observing a pressure decrease, which is assumed to be due to hydrogen adsorption.

Sample Preparation and Experimental Procedure

Samples of known mass were loaded onto the apparatus and exposed to the following procedure; all pressure readings were taken after pressures were stable for at least 30 minutes to allow for equilibrium to occur:

1. Load Sample, put under vacuum and de-gas at 300°C overnight (~16 h).
2. Close Sample Vol. and load manifold Vol. with He (to approximately 8-10 MPa) and record pressure.
3. Open Sample Vol. and record pressure.
4. Evacuate system (minimum of 2 h)
5. Close Sample Vol. and load manifold Vol. with H_2 with approximately 11.5 MPa and record pressure.
6. Open Sample Vol. and record pressure.

The pressure transducer readings were then processed using the calibrated volumes and viral equation to determine the hydrogen adsorbed by the sample, an example spreadsheet can be seen in appendix C. Experiments were performed at 35±0.1 °C to ensure adequate control of the isothermal chamber. Approximately 0.3g of sample was used in each experimental run to ensure a designed accuracy of at least ±0.05wt%, although the repetition of experimental results suggests a higher accuracy was actually achieved.

There are many potential sources of error in conducting this type of experiment[95,212], thus control of several important factors is vital in determining hydrogen uptakes accurately. These are given in table 7.1, with detail as to how the specific issue is accounted for in the design of the apparatus and/or experimental procedure.

Issue	**Problem**	**Design Factor**
Moisture contamination in gases	Moisture adsorption will cause pressure drop, which can be mistaken for hydrogen adsorption.	Use of ultra high purity (99.999%) hydrogen and passing of gas through a liquid nitrogen trap prior to exposure to the apparatus.
Gas Leakage	Will produce pressure drops, which can be mistaken for hydrogen adsorption.	Once sample is loaded, He is exposed to the entire system and left overnight (~ 16 hours) to ensure pressure does not change.
Temperature Variations	Will cause fluctuations in pressure reading	Entire system is kept in an isothermal chamber (in an air-conditioned lab). Pressure must be (perfectly) stable for at least 30 minutes before reading is accepted.

table 7.1 – Issues with volumetric hydrogen capacity determination and design considerations in overcoming issues.

The system volumes (manifold and sample) were calibrated using stainless steel ball bearings, using both hydrogen and helium gas, at 2 different (initial manifold) pressures. The calibrated volumes of the manifold and sample chambers were 21.41 cm^3 and 13.41cm^3 respectively. The accuracy

of the apparatus was also verified using a standard carbon material; 'Maxsorb' – an activated carbon with a measured surface area of ~ 3200 m^2 g^{-1} and reproducible maximum hydrogen uptake of between 0.6-0.8 wt% (at up to ~14 MPa).[98,150,213,214]

7.3 Results

This section reports the determined and BET surface areas and hydrogen uptake capacities of the GNF materials examined. The XRD of Pd loaded samples after hydrogen exposure are also presented.

7.3.1 BET Surface Area

The BET surface areas of the Ni-GNFs are shown in figure 7.3.

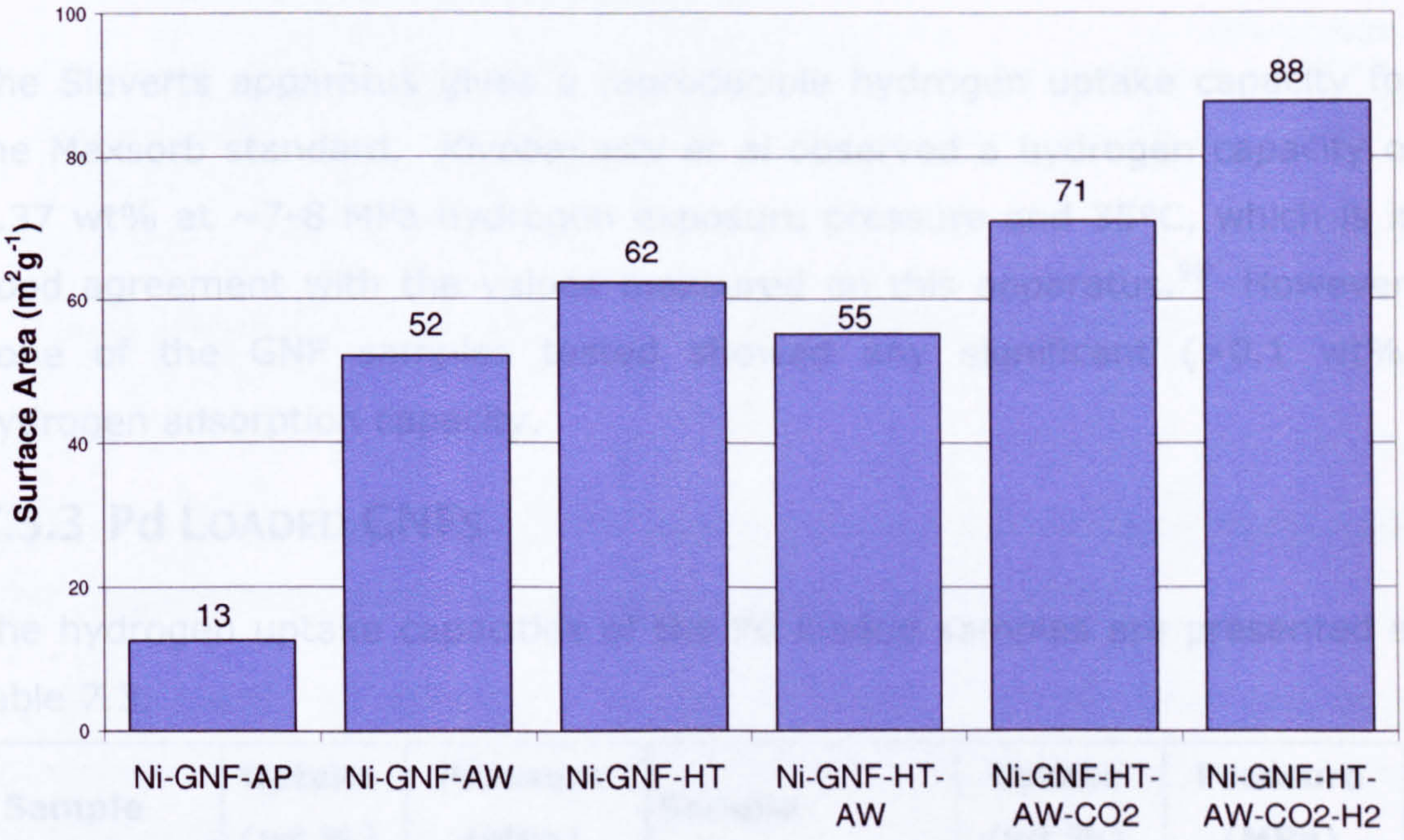

figure 7.3 – BET surface areas for Ni-GNF samples. Estimated accuracy from repeated experiments is ±10 m^2 g^{-1}.

For all the GNF samples (Fe-GNFs, Ni-GNFs and Pd loaded) the BET surface area was consistently determined to be in the range of 50-90 m^2 g^{-1}, except for Ni-GNF-AP which showed a lower surface area outside this range of 13 m^2 g^{-1}.

7.3.2 Hydrogen Uptake Capacities

Sample	Uptake (wt %)	Pressure (MPa)	Sample	Uptake (wt %)	Pressure (MPa)
Maxsorb	0.33	7.3	-	-	-
Ni-GNF-AP	0.02	8.0	Fe-GNF-AP	0.01	8.2
Ni-GNF-HT-AW	0.03	8.1	Fe-GNF-HT-AW	0.03	8.0
Ni-GNF-HT-AW-CO_2	0.01	7.6	Fe-GNF-HT-AW-CO_2	0.02	7.9
Ni-GNF-HT-AW-CO_2-H_2	0.01	8.0	-	-	-

table 7.2 – Hydrogen uptake data for Ni-GNFs and Fe-GNFs. Estimated error in measurements is ±0.05 wt%.

The Sieverts apparatus gives a reproducible hydrogen uptake capacity for the Maxsorb standard. *Kiyobayashi et al* observed a hydrogen capacity of 0.37 wt% at ~7-8 MPa hydrogen exposure pressure and 35°C, which is in good agreement with the values measured on this apparatus.[98] However, none of the GNF samples tested showed any significant (>0.1 wt%) hydrogen adsorption capacity.

7.3.3 Pd Loaded GNFs

The hydrogen uptake capacities of the Pd loaded samples are presented in table 7.3.

Sample	Uptake (wt %)	Pressure (MPa)	Sample	Uptake (wt %)	Pressure (MPa)
0.5Pd-TR	0.02	8.1	HT-AW-5Pd-TR	0.03	8.1
1Pd-TR	0.02	8.2	CO_2-5Pd-TR	0.03	8.1
5Pd-TR	0.02	8.1	CO_2-H_2-5Pd-TR	0.02	8.1
10Pd-TR	0.03	8.1	-	-	-

table 7.3 – Hydrogen uptake data for Pd loaded samples. Error in measurements is ±0.05 wt%.

None of the Pd loaded samples showed any significant (>0.1 wt%) hydrogen uptake. The XRD diffractograms before and after hydrogen uptake are shown in figure 7.4.

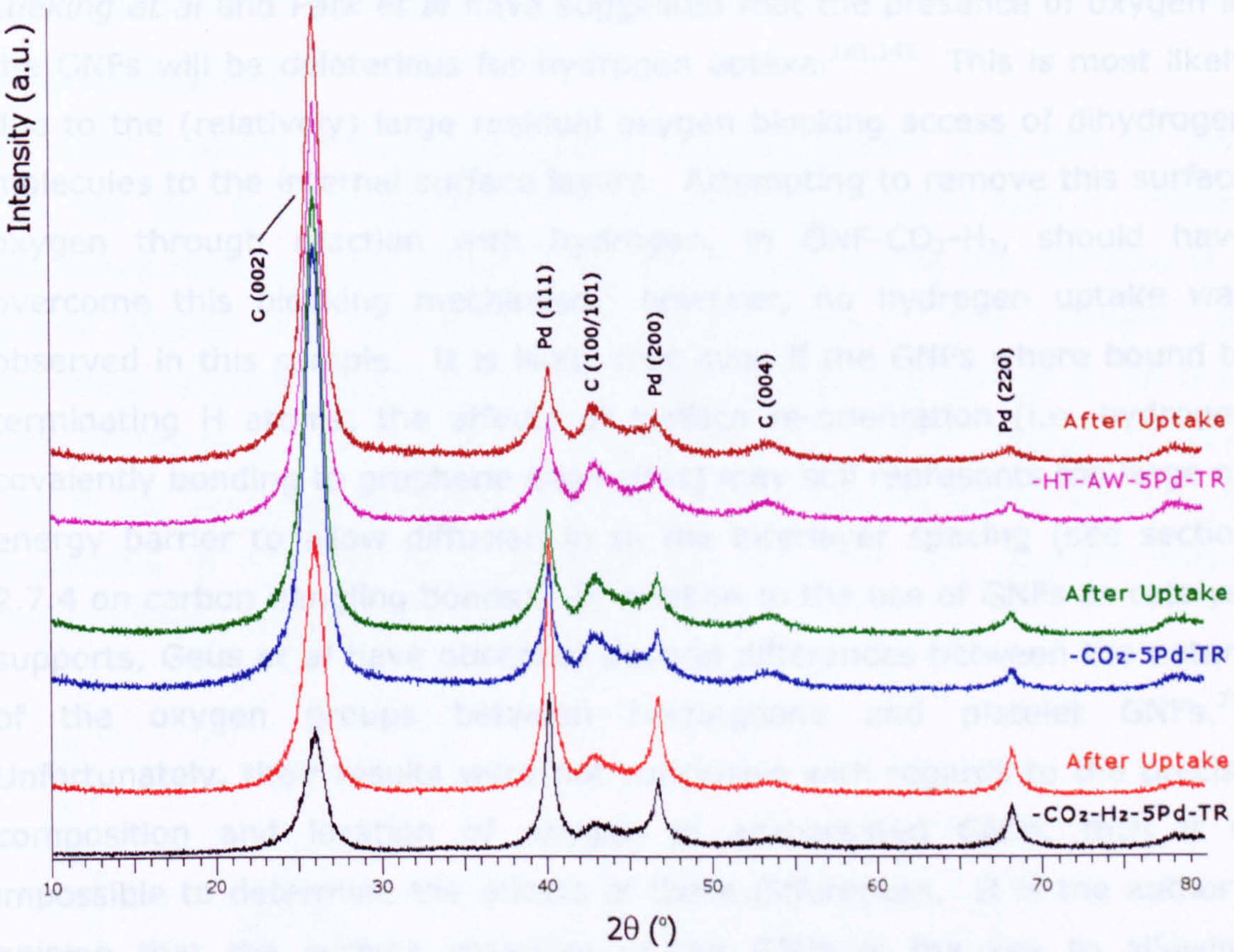

figure 7.4 – Examples XRD of Pd loaded samples before (lower trace) and after (higher trace) hydrogen uptake capacity determination.

The XRD shows no difference in any Pd loaded sample after hydrogen uptake capacity was measured, with all diffraction peaks being due to either the GNF or Pd.

7.4 Discussion

The aim of this chapter was to assess the hydrogen storage capacities of the GNFs synthesised in the previous chapters of this thesis. However, as shown in table 7.2 and table 7.3 no significant levels (>0.1 wt%) of hydrogen uptake could be observed in any of the samples tested. Therefore, it is difficult to make a detailed assessment of any of the hydrogen uptake mechanisms that have been discussed in section 2.7 or 6.1, as none of the GNFs showed any hydrogen uptake capacity. Thus, these results appear to

agree with the growing consensus that significant levels of hydrogen storage (at room temperature) in GNFs is not possible[10,211,215,216].

Lueking et al and *Park et al* have suggested that the presence of oxygen in the GNFs will be deleterious for hydrogen uptake.[141,142] This is most likely due to the (relatively) large residual oxygen blocking access of dihydrogen molecules to the internal surface layers. Attempting to remove this surface oxygen through reaction with hydrogen, in GNF-CO_2-H_2, should have overcome this blocking mechanism; however, no hydrogen uptake was observed in this sample. It is likely that even if the GNFs where bound to terminating H atoms, the affects of surface re-orientation (i.e. hydrogen covalently bonding to graphene edge sites) may still represents too large an energy barrier to allow diffusion in to the interlayer spacing (see section 2.7.4 on carbon dangling bonds). In relation to the use of GNFs as catalyst supports, Geus *et al* have observed several differences between the nature of the oxygen groups between herringbone and platelet GNFs.[217] Unfortunately, their results were not conclusive with regards to the precise composition and location of oxygen in acid-treated GNFs, thus it is impossible to determine the effects of these differences. It is the author's opinion that the surface structure of the GNFs is the key to allowing hydrogen uptake in GNFs (if at-all possible), and that the structure of these surfaces is often neglected when characterising GNF materials.

The Pd loaded samples showed no significant hydrogen uptake. XRD after hydrogen exposure showed no change in the samples and no presence of $PdH_{0.67}$ which may have formed, indicating that the interaction of the Pd and GNF was preventing $PdH_{0.67}$ forming, in-line with other author's views.[152,218]

Given that the GNFs synthesised here have some surface oxygen, necessary for Pd loading using the incipient wetness technique (Chapter 6), the presence of this oxygen maybe blocking access of hydrogen to the interior graphene surfaces of the GNFs, thus explaining why no hydrogen uptake was observed. However, other groups have used similar methods to prepare Pd loaded GNFs, which will also contain surface oxygen, but showed significant levels of hydrogen uptake. Further investigation would be

required to ascertain the precise influence of oxygen in hydrogen uptake in GNFs.[143,152] From the expected outcomes of the designed experiments and materials synthesised, no hydrogen uptake mechanism was prevalent via Pd particles.

Intercalated GNF

An initial experiment investigating in to the intercalation of Ni-GNF-HT-AW-CO_2 has also been undertaken. The sample was synthesised by mixing potassium metal and the GNFs in the ratio of C_8K, sealing the reactants in a quartz ampule and heating to 600°C for 2 weeks. The resultant (air sensitive) material hydrogen uptake capacity was determined to be 0.55 wt% for the first cycle, with subsequent cycles (2nd and 3rd) being 0.07 wt%. Due to the air-sensitive nature of the material, characterisation was largely impossible to transfer the sample inertly, thus the only characterisation possible was XRD, shown in figure 7.5.

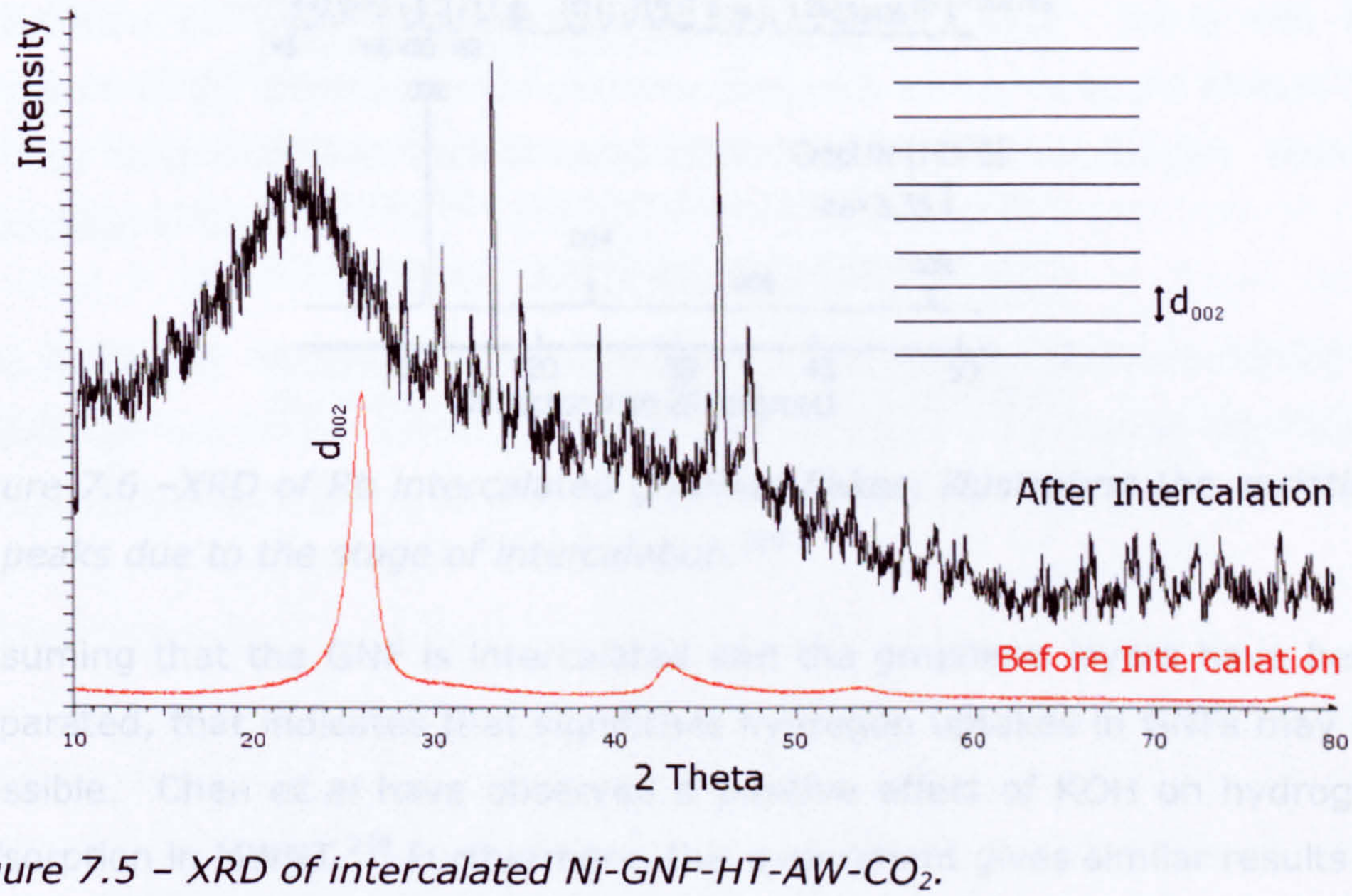

figure 7.5 – XRD of intercalated Ni-GNF-HT-AW-CO_2.

There are several interesting features in the XRD. Firstly, the main GNF diffraction at ~26.5° (d_{002}) is not present in the intercalated sample and secondly there are many more peaks in the sample than would be expected from either carbon or potassium. If potassium is intercalating into the structure, the d_{002} diffraction is likely to shift to a lower angle. However,

this is difficult to determine as the sample was covered by amorphous tape (to prevent contact with air), which produces a broad amorphous peak centred at ~22°. The large number of other peaks between 30-80°, would also indicate that intercalation has occurred, observed by *Leung et al* for Rb intercalated graphite, figure 7.6.[219]

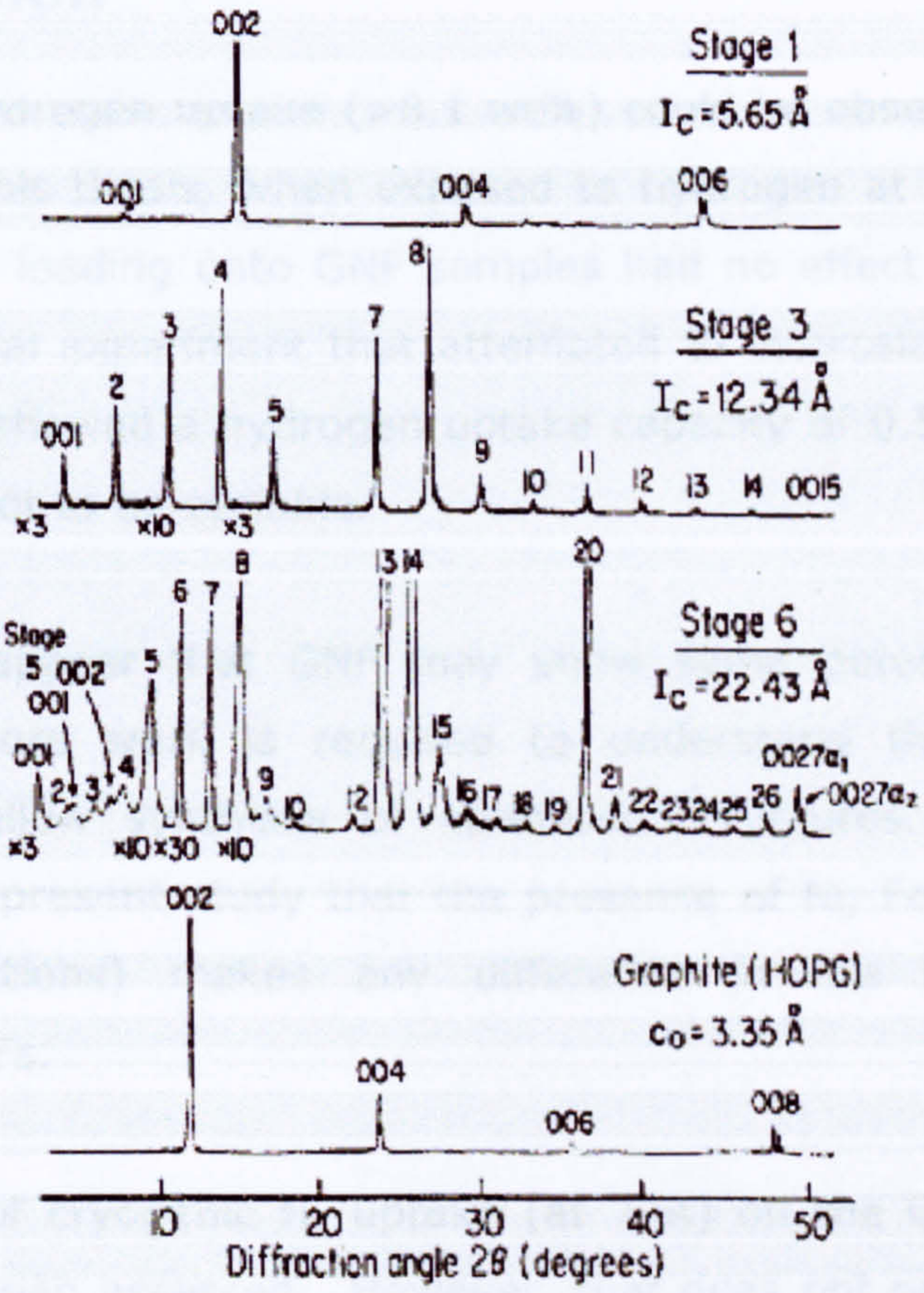

figure 7.6 –XRD of Rb intercalated graphite flakes, illustrating the variation in peaks due to the stage of intercalation.[219]

Assuming that the GNF is intercalated and the graphene layers have been separated, that indicates that significant hydrogen uptakes in GNFs may be possible. Chen *et al* have observed a positive effect of KOH on hydrogen adsorption in MWNT.[220] Furthermore, this experiment gives similar results to *Pinkerton et al*; a large amount of hydrogen was adsorbed (1.3 wt%) but on subsequent cycles only nominal amounts of hydrogen were adsorbed (0.2 wt%).[161] This would indicate that the hydrogen adsorbed is not being released under moderate heating (200°C), which indicates that it is being chemisorbed into the structure. However, this would also be an interesting effect as there is no published data concerning pure potassium hydride in

the Sandia hydride database[106], thus the effect of potassium is allowing hydrogen to chemisorb onto the GNF. Further investigation into this effect may lead to another potential interaction between hydrogen and GNF, not already reported, as discussed in section 2.10 and 6.1.

7.5 Conclusion

No significant hydrogen uptake (>0.1 wt%) could be observed in any GNFs synthesised in this thesis, when exposed to hydrogen at ~8 MPa at 35°C. The effect of Pd loading onto GNF samples had no effect on the hydrogen uptake. An initial experiment that attempted to intercalate a GNF sample with potassium showed a hydrogen uptake capacity of 0.55 wt%, although this was found not to be cyclable.

Thus it would appear that GNF may show some potential in hydrogen storage, but more work is required to understand the mechanism of adsorption to allow synthesis of optimised structures. There was no evidence in the present study that the presence of Ni, Fe or Pd metals (in various distributions) makes any difference in the hydrogen uptake capacities in GNFs.

The possibility of cryogenic H_2 uptake (at 77K) on the GNFs examined in thesis has not been assessed. However, that does not preclude significant levels of hydrogen being able to be absorbed on to the GNFs.

8 CONCLUSIONS

In light of the structure of this thesis, each of the conclusions shall be dealt with relevant to the chapter in which they were made.

Chapter 4 - GNF Synthesis

In the growth of filamentous carbon, it has been shown that careful control of temperature and gas environment is important in achieving a specifically desired product. The alteration of either or both of these variables will cause a significant change in the type and amount of carbon recovered. The role of hydrogen in this specific catalytic system is very important as it generally encourages the growth of filamentous carbon as opposed to random nano-sized shells of graphite encapsulating catalyst metal particles.

The type of carbon deposited is affected by the initial CVD conditions, but changing the CVD environment during deposition does not appear to alter the fundamental type of carbon deposited (i.e. Herringbone GNFs). It does alter the rate of deposition and presents a convenient route to increase the amount of carbon deposited, providing a 3-4 fold increase in carbon yield. However, the surface of the GNFs can become altered, under going re-construction, which can be detrimental to properties of the carbon recovered.

Chapter 5 – Post-Treatment of GNFs

The removal of residual CVD catalyst and the CO_2 oxidation behaviour of GNFs synthesised from Ni and Fe catalysts has been investigated. It was found that any residual catalyst particles (Ni or Fe) remaining in GNF samples will change the mechanism of CO_2 oxidation. If any residual catalyst particles are present a sample, a 'basal' mechanism – removal of carbon along the lengths of the GNFs – is prevalent, catalysed by the residual CVD catalyst particles. Full removal of catalyst residues causes oxidation to occur via the 'edge' mechanism – removal of carbon along the surface/diameters of the GNFs.

Careful removal of catalyst particles can be achieved, in the Fe and Ni systems investigated here, by the use an acid wash, followed by a heat treatment and subsequent acid wash. However, even using this process, it would appear that not all of the residual Fe catalyst can be removed from the Fe-GNFs.

The knowledge developed allows for method of successfully removing any amorphous or re-orientated carbon on the surface of GNFs to be removed (oxidised), thus allowing cleaned and lower energy access for potential sorbate molecules to the 'internal' surface area of GNFs.

Chapter 6 – Preparation of Metal containing GNFs;

In has been shown that it is possible to coat GNFs with Pd particles through control of the GNF surfaces and that this can be achieved preferentially onto platelet GNFs. Using the incipient wetness technique, the amount of Pd and the amount of surface oxygen present in the GNF will determine whether Pd or PdO phase is formed in the coating; any PdO can be reduced to Pd using a simple heat treatment.

Chapter 7 – Hydrogen Storage Properties of GNFs;

No significant hydrogen uptake (>0.1 wt%) could be observed in any GNFs synthesised in this thesis, when exposed to hydrogen at ~8 MPa at 35°C. The effect of Pd loading onto GNF samples had no effect on the hydrogen uptake, indicating that hydrogen uptake is not possible in GNFs via the Kubas, Dissociation or Spill-Over mechanisms – when catalysed through Pd. An initial experiment that attempted to intercalate a GNF sample with potassium showed a hydrogen uptake capacity of 0.55 wt%, although this was found not to be cyclable.

Thus it would appear that GNF show some potential in hydrogen storage, however more work is required to understand the mechanism of adsorption to allow synthesis of optimised structures. There was no evidence in the present study that the presence of Ni, Fe or Pd metals (in various

distributions) makes any difference in the hydrogen uptake capacities in GNFs. However, the initial work undertaken to expand the inter-layer spacing using potassium has shown some success – thus could be concluded that mechanisms investigated, may still be applicable (to maximise the hydrogen uptake capacity), if applied to GNFs with an expanded inter-layer spacing.

8.1 Suggested Future Work

As a result of the work undertaken during this thesis there are several further investigations that could be undertaken to further enhance understanding in the area of GNFs and there use as hydrogen storage materials.

Despite having investigated the variables in CVD growth of GNFs, there is still a mixture of products recovered, with a single type of GNF being nearly impossible to obtain. In addition to this, there is a wide difference in the average diameters of GNFs produced from Ni and Fe catalysts. Both of these facts make determination of the GNFs bulk properties very challenging – with several variables causing conflicting characterisation data to be obtained. Whereas there are many groups investigating methods to selectively synthesise one type of GNF using various methods, it is also important to ensure that the internal structure of the GNFs be carefully examined and modelled to determine whether the efforts should be concentrated in synthesis conditions or post-synthesis GNF selection. Only once an optimised GNF structure can be synthesised will the full extent of these materials be realised.

For the purposes of hydrogen storage, there are two key areas that would need to be more fully understood and could build on the presented in this project. It would also be note worthy to examine and model the surfaces of GNFs, in order to precisely determine the GNF interaction with hydrogen – especially as surface re-construction/relaxation/ad-atoms appears to 'block' the internal surface area of the graphene sheets. Exposing those surfaces would potentially yield a material with potential to exceed the DOE

hydrogen storage targets and revolutionise energy transport. Secondly, in order to expose the internal graphene surfaces the layer separation within the GNFs will need to expand beyond 0.34 nm. This may be possible using 'standard' intercalation methods, such as potassium or lithium intercalation. However, authors that have tried this have had many problems with moisture adsorption.[220,221] It is probably un-necessary to expand the layers by more than 0.1 nm to ~ 0.5 nm, thus intercalation is probably excessive. A more sensible method would be to use a large hetro-atom e.g. N or P substituted in to the GNF lattice to increase the inter-layer separation. This could be achieved by adding a N or P containing feedstock in to the CVD synthesis reaction.

9 REFERENCES

1 UK Energy White Paper. Dept for Transport, London, **2003**, ISBN 0-10-157612-9

2 S Massey. Report *'Future of the hydrogen economy'*, Business Insights, London, UK **2005**,

3 L Schlapbach, A Zuttel. *Nature.* **2001,** 414 pg 353-358

4 S Satyapal, J Petrovic, C Read, G Thomas, G Ordaz. *Catalysis Today.* **2007,** 120 (3-4) pg 246-256

5 A Sarkar, R Banerjee. *Int J Hydrogen Energy.* **2005,** 30 (8) pg 867-877

6 US DOE. **2007,**

7 R Strobel, J Garche, PT Moseley, L Jorissen, G Wolf. *Journal of Power Sources.* **2006,** 159 (2) pg 781-801

8 A Chambers, C Park, RTK Baker, NM Rodriguez. *Journal of Physical Chemistry B.* **1998,** 102 (22) pg 4253-4256

9 C Zandonella. *Nature.* **2001,** 410 (6830) pg 734-735

10 Shriver DF, Atkins PW. *Inorganic Chemistry,* Oxford University Press, Oxford **1999**, pg 351-357

11 H Marsh, F Rodriquez-Reinoso. *Sciences of Carbon Materials,* Universidad de Alicante, Alicante, Spain, **2000**,

12 Anderson JC, Hayman CC. *Science.* **1988,** 241 pg 913-921

13 Geis MN, Angus JC. *Scientific American.* **1992,** 267 (4) pg 64-65

14 GSJ Perrott, R Thiessen. *Journal of Industrial and Engineering Chemistry-Us.* **1920,** 12 pg 324-331

15 PA Gauden, AP Terzyk, G Rychlicki, P Kowalczyk, MS Cwiertnia, JK Garbacz. *Journal of Colloid and Interface Science.* **2004,** 273 (1) pg 39-63

16 TH Usmani, MT Motan, AHK Yousufzai. *Journal of the Chemical Society of Pakistan.* **2000,** 22 (1) pg 73-78

17 F Rodriguezreinoso, A Linaressolano. *Chemistry and Physics of Carbon.* **1989,** 21 pg 1-146

18 TG Ros, AJ van Dillen, JW Geus, DC Koningsberger. *Chemistry-A European Journal.* **2002,** 8 (5) pg 1151-1162

19 KP De Jong, JW Geus. *Catalysis Reviews - Science and Engineering.* **2000,** 42 (4) pg 481-510

20 NM Rodriguez. *Journal of Materials Research.* **1993,** 8 (12) pg 3233-3250

21 M Hirscher, M Becher, M Haluska, A Quintel, V Skakalova, YM Choi, U Dettlaff-Weglikowska, S Roth, I Stepanek, P Bernier, A Leonhardt, J Fink. *Journal of Alloys and Compounds.* **2002,** 330 pg 654-658

22 S Iijima. *Nature.* **1991,** 354 (6348) pg 56-58

23 AC Dillon, KM Jones, TA Bekkedahl, CH Kiang, DS Bethune, MJ Heben. *Nature.* **1997,** 386 (6623) pg 377-379

24 R Strobel, L Jorissen, T Schliermann, V Trapp, W Schutz, K Bohmhammel, G Wolf, J Garche. *Journal of Power Sources.* **1999,** 84 (2) pg 221-224

25 S McCaldin, M Bououdina, DM Grant, GS Walker. *Carbon.* **2006,** 44 (11) pg 2273-2280

26 NM Rodriguez, A Chambers, RTK Baker. *Langmuir.* **1995,** 11 (10) pg 3862-3866

27 RH Baughman, AA Zakhidov, WA de Heer. *Science.* **2002,** 297 (5582) pg 787-792

28 FL Darkrim, P Malbrunot, GP Tartaglia. *International Journal of Hydrogen Energy.* **2002,** 27 (2) pg 193-202

29 CJ Lee, J Park, Y Huh, JY Lee. *Chemical Physics Letters.* **2001,** 343 (1-2) pg 33-38

30 D Pradhan, M Sharon. *Materials Science and Engineering B-Solid State Materials for Advanced Technology.* **2002,** 96 (1) pg 24-28

31 SB Sinnott, R Andrews, D Qian, AM Rao, Z Mao, EC Dickey, F Derbyshire. *Chemical Physics Letters.* **1999,** 315 (1-2) pg 25-30

32 I Willems, Z Konya, JF Colomer, G Van Tendeloo, N Nagaraju, A Fonseca, JB Nagy. *Chemical Physics Letters.* **2000,** 317 (1-2) pg 71-76

33 M Endo, K Takeuchi, T Hiraoka, T Furuta, T Kasai, X Sun, CH Kiang, MS Dresselhaus. *Journal of Physics and Chemistry of Solids.* **1997,** 58 (11) pg 1707-1712

34 M Shiraishi, T Takenobu, A Yamada, M Ata, H Kataura. *Chemical Physics Letters.* **2002,** 358 (3-4) pg 213-218

35 JJ Schneider, J Engstler, S Franzka, K Hofmann, B Albert, J Ensling, P Gutlich, P Hildebrandt, S Dopner, W Pfleging, B Gunther, G Muller. *Chemistry-A European Journal.* **2001,** 7 (13) pg 2888-2895

36 A Fonseca, K Hernadi, JB Nagy, D Bernaerts, AA Lucas. *Journal of Molecular Catalysis A-Chemical.* **1996,** 107 (1-3) pg 159-168

37 D Pradhan, M Sharon, M Kumar, Y Ando. *Journal of Nanoscience and Nanotechnology.* **2003,** 3 (3) pg 215-217

38 CJ Lee, J Park, JA Yu. *Chemical Physics Letters.* **2002,** 360 (3-4) pg 250-255

39 C Park, MA Keane. *Journal of Colloid and Interface Science.* **2002,** 250 (1) pg 37-48

40 JB Park, GS Choi, YS Cho, SY Hong, D Kim, SY Choi, JH Lee, KI Cho. *Journal of Crystal Growth.* **2002,** 244 (2) pg 211-217

41 HS Youn, H Ryu, TH Cho, WK Choi. *International Journal of Hydrogen Energy.* **2002,** 27 (9) pg 937-940

42 K Teo, C Singh, M Chhowalla, W Milne. *Encyclopedia of Nanoscience and Nanotechnology.* American Scientific Publishers, USA **2004,** ISBN 1-58883-001-2 pg 665-686

43 Y Ando, XL Zhao. *New Diamond and Frontier Carbon Technology.* **2006,** 16 (3) pg 123-137

44 C Baddour, C Briens. *International Journal of Chemical Reactor Engineering.* **2005,** 3

45 C Oncel, Y Yurum. *Fullerenes Nanotubes and Carbon Nanostructures.* **2006,** 14 (1) pg 17-37

46 K Awasthi, A Srivastava, ON Srivastava. *Journal of Nanoscience and Nanotechnology.* **2005,** 5 (10) pg 1616-1636

47 A Chambers, T Nemes, NM Rodriguez, RTK Baker. *Journal of Physical Chemistry B.* **1998,** 102 (12) pg 2251-2258

48 WZ Li, JG Wen, ZF Ren. *Applied Physics A-Materials Science & Processing.* **2002,** 74 (3) pg 397-402

49 JR Rostrup-Nielsen. *J Catal.* **1972,** 27 (3) pg 343-356

50 K Hernadi, A Fonseca, P Piedigrosso, M Delvaux, JB Nagy, D Bernaerts, J Riga. *Catalysis Letters.* **1997,** 48 (3-4) pg 229-238

51 AM Valiente, PN Lopez, IR Ramos, AG Ruiz, C Li, Q Xin. *Carbon.* **2000,** 38 (14) pg 2003-2006

52 SW Liu, XH Tang, Y Mastai, I Felner, A Gedanken. *Journal of Materials Chemistry.* **2000,** 10 (11) pg 2502-2506

53 BK Gupta, ON Srivastava. *International Journal of Hydrogen Energy.* **2000,** 25 (9) pg 825-830

54 BK Gupta, ON Srivastava. *International Journal of Hydrogen Energy.* **2001,** 26 (8) pg 857-862

55 K Hernadi, A Fonseca, JB Nagy, A Fudala, D Bernaerts, I Kiricsi. *Applied Catalysis A-General.* **2002,** 228 (1-2) pg 103-113

56 AY Cao, HW Zhu, XF Zhang, XS Li, DB Ruan, CL Xu, BQ Wei, J Liang, DH Wu. *Chemical Physics Letters.* **2001,** 342 (5-6) pg 510-514

57 S Collins, R Brydson, B Rand. *Carbon.* **2002,** 40 (7) pg 1089-1100

58 ML Toebes, JH Bitter, AJ van Dillen, KP De Jong. *Catalysis Today.* **2002,** 76 (1) pg 33-42
59 NM Rodriguez, MS Kim, RTK Baker. *Journal of Catalysis.* **1993,** 144 (1) pg 93-108
60 RTK Baker, PS Harris, RB Thomas, RJ Waite. *J Catal.* **1973,** 30 (1) pg 86-95
61 RTK Baker, MA Barber, RJ Waite, PS Harris, FS Feates. *J Catal.* **1972,** 26 (1) pg 51-&
62 RTK Baker, MS Kim, A Chambers, C Park, NM Rodriguez. *Catalyst Deactivation,* Elsevier Science Publ B V, Amsterdam, Netherlands, **1997**, pg 99-109
63 S Helveg, C Lopez-Cartes, J Sehested, PL Hansen, BS Clausen, JR Rostrup-Nielsen, F Abild-Pedersen, JK Norskov. *Nature.* **2004,** 427 (6973) pg 426-429
64 E Boellaard, PK Debokx, AJHM Kock, JW Geus. *J Catal.* **1985,** 96 (2) pg 481-490
65 PK Debokx, AJHM Kock, E Boellaard, W Klop, JW Geus. *J Catal.* **1985,** 96 (2) pg 454-467
66 AJHM Kock, PK Debokx, E Boellaard, W Klop, JW Geus. *J Catal.* **1985,** 96 (2) pg 468-480
67 JW Geus, PB Wells. *Applied Catalysis.* **1985,** 18 (2) pg 231-242
68 AJHM Kock, HM Fortuin, JW Geus. *J Catal.* **1985,** 96 (1) pg 261-275
69 A Oberlin, M Endo, T Koyama. *Carbon.* **1976,** 14 (2) pg 133-135
70 A Oberlin, M Endo, T Koyama. *Journal of Crystal Growth.* **1976,** 32 (3) pg 335-349
71 J Philip, L Walker, P Thrower. *Chemistry and Physics of Carbon,* Basel, New York, **1978**,
72 PE Nolan, DC Lynch, AH Cutler. *Journal of Physical Chemistry B.* **1998,** 102 (21) pg 4165-4175
73 L Delzeit, I McAninch, BA Cruden, D Hash, B Chen, J Han, M Meyyappan. *Journal of Applied Physics.* **2002,** 91 (9) pg 6027-6033
74 M Yasutake, Y Shirakawabe, T Okawa, S Mizooka, Y Nakayama. *Ultramicroscopy.* **2002,** 91 (1-4) pg 57-62
75 ML Toebes, FF Prinsloo, JH Bitter, AJ van Dillen, KP De Jong. *Synthesis and characterization of carbon nanofiber supported ruthenium catalysts,* **2002**, pg 201-208
76 K Kaneko. *Colloids and Surfaces.* **1989,** 37 pg 115-124
77 NM Rodriguez, MS Kim, RTK Baker. *Journal of Physical Chemistry.* **1994,** 98 (50) pg 13108-13111
78 T Ikuno, T Yamamoto, M Kamizono, S Takahashi, H Furuta, S Honda, S Ohkura, M Katayama, T Hirao, K Oura. *Physica B-Condensed Matter.* **2002,** 323 (1-4) pg 171-173
79 H Furuta, T Ikuno, N Shikina, S Honda, T Hirao, K Oura. *Physica B-Condensed Matter.* **2002,** 323 (1-4) pg 299-302
80 YW Jin, JE Jung, YJ Park, JH Choi, DS Jung, HW Lee, SH Park, NS Lee, JM Kim, TY Ko, SJ Lee, SY Hwang, JH You, JB Yoo, CY Park. *J. Appl. Phys.* **2002,** 92 (2) pg 1065-1068
81 CA Bessel, K Laubernds, NM Rodriguez, RTK Baker. *J Phy. Chem. B.* **2001,** 105 (6) pg 1115-1118
82 ES Steigerwalt, GA Deluga, CM Lukehart. *J Phy. Chem. B.* **2002,** 106 (4) pg 760-766
83 B Gao, A Kleinhammes, XP Tang, C Bower, L Fleming, Y Wu, O Zhou. *Chem Phy Lett.* **1999,** 307 (3-4) pg 153-157
84 PV Adhyapak, T Maddanimath, S Pethkar, AJ Chandwadkar, YS Negi, K Vijayamohanan. *Journal of Power Sources.* **2002,** 109 (1) pg 105-110
85 GL Che, BB Lakshmi, CR Martin, ER Fisher. *Langmuir.* **1999,** 15 (3) pg 750-758
86 CM Niu, EK Sichel, R Hoch, D Moy, H Tennent. *App. Phys. Lett.* **1997,** 70 (11) pg 1480-1482

87 M Terrones, WK Hsu, HW Kroto, DRM Walton. *Fullerenes and Related Structures.* **1999,** 199 pg 189-234
88 PG Collins, A Zettl, H Bando, A Thess, RE Smalley. *Science.* **1997,** 278 (5335) pg 100-103
89 CY Wei, D Srivastava, KJ Cho. *Nano Letters.* **2002,** 2 (6) pg 647-650
90 BJ Kim, SJ Park. *Nanotechnology.* **2006,** 17 (17) pg 4395-4398
91 GP Dai, M Liu, MZ Wang, HM Cheng. *New Carbon Materials.* **2002,** 17 (3) pg 70-74
92 M Jacoby. *Chemical & Engineering News.* **1998,** 76 (21) pg 6
93 A Chambers, C Park, RTK Baker, NM Rodriguez. *J Phy. Chem. B.* **1998,** 102 (22) pg 4253-4256
94 J Blackman, PhD Thesis; *High Pressure Hydrogen Storage on Carbon Materials for Mobile Applications*, University of Nottingham, **2005**.
95 JM Blackman, JW Patrick, CE Snape. *Carbon.* **2006,** 44 (5) pg 918-927
96 JM Blackman, JW Patrick, A Arenillas, W Shi, CE Snape. *Carbon.* **2006,** 44 (8) pg 1376-1385
97 T Kiyobayashi, HT Takeshita, H Tanaka, N Takeichi, A Zuttel, L Schlapbach, N Kuriyama. *Journal of Alloys and Compounds.* **2002,** 330 pg 666-669
98 JM Blackman, JW Patrick, CE Snape. *Carbon.* **2006,** 44 (5) pg 918-927
99 K Hanada, H Shiono, K Matsuzaki. *Diamond and Related Materials.* **2003,** 12 (3-7) pg 874-877
100 S Isobe, T Ichikawa, JI Gottwald, E Gomibuchi, H Fujii. *Journal of Physics and Chemistry of Solids.* **2004,** 65 (2-3) pg 535-539
101 PMFJ Costa, KS Coleman, MLH Green. *Nanotechnology.* **2005,** 16 (4) pg 512-517
102 YW Lee, R Deshpande, AC Dillon, MJ Heben, H Dai, BM Clemens. *Mat. Res. Soc. Symp. Proc.* **2005,** 837 N3.18
103 W Grochala, PP Edwards. *Chemical Reviews.* **2004,** 104 (3) pg 1283-1315
104 DG Ivey, DO Northwood. *Journal of Materials Science.* **1983,** 18 (2) pg 321-347
105 G Sandrock, G Thomas. Sandia National Laboratory - Online Database http://hydpark.ca.sandia.gov/dbsummary.html, last accessed March 2008
106 GG Tibbetts, GP Meisner, CH Olk. *Carbon.* **2001,** 39 (15) pg 2291-2301
107 Y Chen, DT Shaw, XD Bai, EG Wang, C Lund, WM Lu, DDL Chung. *App. Phys. Lett.* **2001,** 78 (15) pg 2128-2130
108 M Hirscher, M Becher, M Haluska, U ttlaff-Weglikowska, A Quintel, GS Duesberg, YM Choi, P Downes, M Hulman, S Roth, I Stepanek, P Bernier. *Applied Physics A-Materials Science & Processing.* **2001,** 72 (2) pg 129-132
109 P Chen, X Wu, J Lin, KL Tan. *Science.* **1999,** 285 (5424) pg 91-93
110 CC Ahn, Y Ye, BV Ratnakumar, C Witham, RC Bowman, B Fultz. *Applied Physics Letters.* **1998,** 73 (23) pg 3378-3380
111 DJ Browning, ML Gerrard, JB Lakeman, IM Mellor, RJ Mortimer, MC Turpin. *Nano Letters.* **2002,** 2 (3) pg 201-205
112 E Poirier, R Chahine, TK Bose. *International Journal of Hydrogen Energy.* **2001,** 26 (8) pg 831-835
113 M Hirscher, M Becher, M Haluska, A Quintel, V Skakalova, YM Choi, U ttlaff-Weglikowska, S Roth, I Stepanek, P Bernier, A Leonhardt, J Fink. *J Alloy and Compounds.* **2002,** 330 pg 654-658
114 YY Fan, B Liao, M Liu, YL Wei, MQ Lu, HM Cheng. *Carbon.* **1999,** 37 (10) pg 1649-1652
115 Atkins PW. *Physical Chemistry,* Oxford University Press, Oxford, **1998,**
116 G Attard, C Barnes. *Surfaces,* Oxford University Press, Oxford, **1998,**
117 M Hirscher, B Panella. *Journal of Alloys and Compounds.* In Press, Corrected Proof
118 M Hirscher, B Panella. *IPHE International Hydrogen Storage Technology Conference.* **2005,**

119 Y Kojima, Y Kawai, A Koiwai, N Suzuki, T Haga, T Hioki, K Tange. *J Alloy and Compounds.* **2006,** 421 (1-2) pg 204-208
120 A Zuttel, P Sudan, P Mauron, C Emmenegger, T Kiyobayashi, L Schlapbach. *Electrochemical and Chemical Reactivity of Amorphous and Nanocrystalline Materials.* **2001,** 377 pg 95-102
121 A Zuttel, P Sudan, P Mauron, T Kiyobayashi, C Emmenegger, L Schlapbach. *International Journal of Hydrogen Energy.* **2002,** 27 (2) pg 203-212
122 HK Chae, DY Siberio-Perez, J Kim, Y Go, M Eddaoudi, AJ Matzger, M O'Keeffe, OM Yaghi. *Nature.* **2004,** 427 (6974) pg 523-527
123 S Orimo, G Majer, T Fukunaga, A Zuttel, L Schlapbach, H Fujii. *Applied Physics Letters.* **1999,** 75 (20) pg 3093-3095
124 S Orimo, T Matsushima, H Fujii, T Fukunaga, G Majer. *Journal of Applied Physics.* **2001,** 90 (3) pg 1545-1549
125 S Patchkovskii, JS Tse, SN Yurchenko, L Zhechkov, T Heine, G Seifert. *Proceedings of the National Academy of Sciences of the United States of America.* **2005,** 102 (30) pg 10439-10444
126 G Kaye, T Lady. *Tables of Physical and Chemical Constants,* Longman, London, **1995,**
127 M Inagaki, R Tashiro, Y Washino, M Toyoda. *Journal of Physics and Chemistry of Solids.* **2004,** 65 (2-3) pg 133-137
128 A Magasinski, G Furdin, JF Mareche, G Medjahdi, A Albiniak, E Broniek, M Jasienko-Halat. *Fuel Processing Technology.* **2002,** 79 (3) pg 259-264
129 M Toyoda, Y Kaburagi, A Yoshida, H Iwata, M Inagaki. *Carbon.* **2002,** 40 (4) pg 628-629
130 H Atsumi, M Iseki, T Shikama. *Journal of Nuclear Materials.* **1994,** 215 pg 1478-1482
131 SL Kanashenko, AE Gorodetsky, VN Chernikov, AV Markin, AP Zakharov, BL Doyle, WR Wampler. *Journal of Nuclear Materials.* **1996,** 237 pg 1207-1212
132 H Atsumi, K Tauchi. *Journal of Alloys and Compounds.* **2003,** 356 pg 705-709
133 A Zuttel, S Orimo. *Mrs Bulletin.* **2002,** 27 (9) pg 705-711
134 T Fukunaga, K Itoh, S Orimo, M Aoki, H Fujii. *Journal of Alloys and Compounds.* **2001,** 327 (1-2) pg 224-229
135 K Itoh, Y Miyahara, S Orimo, H Fujii, T Kamiyama, T Fukunaga. *Journal of Alloys and Compounds.* **2003,** 356 pg 608-611
136 K Miura, T Morimoto. *Langmuir.* **1991,** 7 (2) pg 374-379
137 C Park, PE Anderson, A Chambers, CD Tan, R Hidalgo, NM Rodriguez. *J Phy. Chem. B.* **1999,** 103 (48) pg 10572-10581
138 AD Lueking, RT Yang, NM Rodriguez, RTK Baker. *Langmuir.* **2004,** 20 (17) pg 7346
139 M Marella, M Tomaselli. *Carbon.* **2006,** 44 (8) pg 1404-1413
140 A Lueking, RT Yang. *J Catal.* **2002,** 206 (1) pg 165-168
141 M Boudart, AW Aldag, MA Vannice. *J Catal.* **1970,** 18 (1) pg 46-51
142 AJ Robell, EV Ballou, M Boudart. *Journal of Physical Chemistry.* **1964,** 68 (10) pg 2748-&
143 S Isobe, T Ichikawa, JI Gottwald, E Gomibuchi, H Fujii. *Journal of Physics and Chemistry of Solids.* **2004,** 65 (2-3) pg 535-539
144 M Zielinski, R Wojcieszak, S Monteverdi, M Mercy, MM Bettahar. *Int J Hydrogen Energy.* In Press, Corrected Proof
145 XQ Yan, XP Gao, Y Li, ZQ Liu, F Wu, YT Shen, DY Song. *Chemical Physics Letters.* **2003,** 372 (3-4) pg 336-341
146 A Anson, E Lafuente, E Urriolabeitia, R Navarro, AM Benito, WK Maser, MT Martinez. *J Phy. Chem. B.* **2006,** 110 (13) pg 6643-6648
147 CK Back, G Sandi, J Prakash, J Hranisavljevic. *J Phy. Chem. B.* **2006,** 110 (33) pg 16225-16231
148 D Lupu, AR Biris, I Misan, A Jianu, G Holzhuter, E Burkel. *Int J Hydrogen Energy.* **2004,** 29 (1) pg 97-102
149 T Yildirim, J Iniguez, S Ciraci. *Physical Review B.* **2005,** 72 (15)

150 T Yildirim, S Ciraci. *Physical Review Letters.* **2005,** 94 (17)
151 JW Lee, HS Kim, JY Lee, JK Kang. *App. Phys. Lett.* **2006,** 88 (14)
152 WH Shin, SH Yang, WA Goddard, JK Kang. *App. Phys. Lett.* **2006,** 88 (5)
153 YF Zhao, YH Kim, AC Dillon, MJ Heben, SB Zhang. *Physical Review Letters.* **2005,** 94 (15)
154 GJ Kubas. *Journal of Organometallic Chemistry.* **2001,** 635 (1-2) pg 37-68
155 D Michael, P Mingos. *Journal of Organometallic Chemistry.* **2001,** 635 (1-2) pg 1-8
156 FE Pinkerton, BG Wicke, CH Olk, GG Tibbetts, GP Meisner, MS Meyer, JF Herbst. *Journal of Physical Chemistry B.* **2000,** 104 (40) pg 9460-9467
157 ZH Zhu, GQ Lu, SC Smith. *Carbon.* **2004,** 42 (12-13) pg 2509-2514
158 EC Lee, YS Kim, YG Jin, KJ Chang. *Physical Review B.* **2002,** 66 (7)
159 Y Kojima, N Suzuki. *Applied Physics Letters.* **2004,** 84 (20) pg 4113-4115
160 PA Sermon, GC Bond. *Journal of the Chemical Society-Faraday Transactions I.* **1980,** 76 pg 889-900
161 ISCD Database. **2007,**
162 M Bououdina, D Grant, G Walker. *Carbon.* **2005,** 43 (6) pg 1286-1292
163 C Park, MA Keane. *Journal of Catalysis.* **2004,** 221 (2) pg 386-399
164 N Krishnankutty, NM Rodriguez, RTK Baker. *Journal of Catalysis.* **1996,** 158 (1) pg 217-227
165 American Society for Metals.Handbook Committee. *Metals handbook / prepared under the direction of the ASM Handbook Committee. Vol.8, Metallography, structures and phase diagrams,* Metals Park, Ohio : American Society for Metals., **1973,**
166 F Bonnet, F Ropital, Y Berthier, P Marcus. *Materials and Corrosion-Werkstoffe und Korrosion.* **2003,** 54 (11) pg 870-880
167 C Park, RTK Baker. *Journal of Catalysis.* **2000,** 190 (1) pg 104-117
168 S McCaldin, M Bououdina, DM Grant, Walker. *Carbon.* **2006,** 44 pg 2273-2280
169 *Binary Alloy Phase Diagrams,* ASM International, **1996,**
170 SG Chen, RT Yang, F Kapteijn, JA Moulijn. *Industrial & Engineering Chemistry Research.* **1993,** 32 (11) pg 2835-2840
171 JA Moulijn, F Kapteijn. *Carbon.* **1995,** 33 (8) pg 1155-1165
172 HJ Grabke. *Materials and Corrosion-Werkstoffe und Korrosion.* **1999,** 50 (12) pg 686-688
173 P Serp, JL Figueiredo, P Bertrand, JP Issi. *Carbon.* **1998,** 36 (12) pg 1791-1799
174 LB Avdeeva, TV Reshetenko, VB Fenelonov, AL Chuvilin, ZR Ismagilov. *Carbon.* **2004,** 42 (12-13) pg 2501-2507
175 A Arenillas, S Cuervo, A Dominguez, JA Menendez, F Rubiera, JB Parra, C Merino, JJ Pis. *Thermochimica Acta.* **2004,** 423 (1-2) pg 99-106
176 G Mul, F Kapteijn, C Doornkamp, JA Moulijn. *Journal of Catalysis.* **1998,** 179 (1) pg 258-266
177 RTK Baker, RD Sherwood. *Journal of Catalysis.* **1981,** 70 (1) pg 198-214
178 JL Figueiredo, CA Bernardo, J Chludzinski, RTK Baker. *Journal of Catalysis.* **1988,** 110 (1) pg 127-138
179 PJ Goethel, RT Yang. *Journal of Catalysis.* **1987,** 108 (2) pg 356-363
180 PJ Mather, KM Thomas. *Journal of Materials Science.* **1997,** 32 (7) pg 1711-1715
181 P Wu, SZ Deng, J Chen, JC She, NS Xu. *Surface and Interface Analysis.* **2004,** 36 (5-6) pg 497-500
182 D Askeland. *The Science and Engineering of Materials,* Stanley Thornes, Cheltenham, UK, **1998,**
183 E Tsyganova, I Didenkulova, V Shekunova, Y Aleksandrov. *Russian Journal of General Chemistry.* **2005,** 75 (9) pg 1354-1358
184 HS Kim, H Lee, KS Han, JH Kim, MS Song, MS Park, JY Lee, JK Kang. *J Phy. Chem. B.* **2005,** 109 (18) pg 8983-8986
185 M Boudart, AW Aldag, MA Vannice. *J Catal.* **1970,** 18 (1) pg 46-51

186 A Lueking, RT Yang. *J Catal.* **2002,** 206 (1) pg 165-168
187 PN Rylander. *Catalytic hydrogenation over platinum metals,* Academic Press, New York, **1967,**
188 T Belin, R Epron. *Materials Science and Engineering B-Solid State Materials for Advanced Technology.* **2005,** 119 (2) pg 105-118
189 C Pham-Huu, N Keller, VV Roddatis, G Mestl, R Schlogl, MJ Ledoux. *Physical Chemistry Chemical Physics.* **2002,** 4 (3) pg 514-521
190 YM Xie, PMA Sherwood. *Chemistry of Materials.* **1990,** 2 (3) pg 293-299
191 RTK Baker, N Rodriguez, A Mastalir, U Wild, R Schlogl, A Wootsch, Z Paal. *J Phy. Chem. B.* **2004,** 108 (38) pg 14348-14355
192 DR Olander, M Balooch. *J Catal.* **1979,** 60 (1) pg 41-56
193 RG Pearson. *Chemical Reviews.* **1985,** 85 (1) pg 41-49
194 A Zuttel. *Materials Today.* **2003,** 6 (9) pg 24-33
195 MC Roman-Martinez, D Cazorla-Amoros, A Linares-Solano, CS-M De Lecea, H Yamashita, M Anpo. *Carbon.* **1995,** 33 (1) pg 3-13
196 RF Cracknell. *Molecular Physics.* **2002,** 100 (13) pg 2079-2086
197 PA Gauden, AP Terzyk, P Kowalczyk. *Journal of Colloid and Interface Science.* **2006,** 300 (2) pg 453-474
198 QY Wang, JK Johnson. *Journal of Chemical Physics.* **1999,** 110 (1) pg 577-586
199 A Lueking, RT Yang. *Aiche Journal.* **2003,** 49 (6) pg 1556-1568
200 M Hirscher, M Becher, M Haluska, U ttlaff-Weglikowska, A Quintel, GS Duesberg, YM Choi, P Downes, M Hulman, S Roth, I Stepanek, P Bernier. *Applied Physics A-Materials Science & Processing.* **2001,** 72 (2) pg 129-132
201 E Johansson, B Hjorvarsson, T Ekstrom, M Jacob. *Journal of Alloys and Compounds.* **2002,** 330 pg 670-675
202 JM Blackman, JW Patrick, CE Snape. *Carbon.* **2006,** 44 (5) pg 918-927
203 C Zhang, XS Lu, AZ Gu. *International Journal of Hydrogen Energy.* **2004,** 29 (12) pg 1271-1276
204 JM Blackman, JW Patrick, CE Snape. *Carbon.* **2006,** 44 (5) pg 918-927
205 PX Hou, ST Xu, Z Ying, QH Yang, C Liu, HM Cheng. *Carbon.* **2003,** 41 (13) pg 2471-2476
206 H Cheng. **2005,**
207 VN Popov. *Materials Science and Engineering: R: Reports.* **2004,** 43 (3) pg 61-102
208 R Strobel, J Garche, PT Moseley, L Jorissen, G Wolf. *Journal of Power Sources.* **2006,** 159 (2) pg 781-801
209 TG Ros, AJ van Dillen, JW Geus, DC Koningsberger. *Chem. Eur. J.* **2002,** 8 (5) pg 1151-1162
210 TB Flanagan, WA Oates. *Annual Review of Materials Science.* **1991,** 21 pg 269-304
211 MS Dresselhaus, G Dresselhaus. *Advances in Physics.* **2002,** 51 (1) pg 1-186
212 CH Chen, CC Huang. *International Journal of Hydrogen Energy.* **2007,** 32 (2) pg 237-246

APPENDIX 1 NOT COPIED

ON INSTRUCTION FROM

UNIVERSITY